Dynamics and Performance of Wind-Energy Systems in Unsteady Flow Conditions

Thesis by
Nathaniel James Wei

In Partial Fulfillment of the Requirements for the
degree of
Doctor of Philosophy

CALIFORNIA INSTITUTE OF TECHNOLOGY
Pasadena, California

2023
Defended 26 May 2023

Nathaniel James Wei
ORCID: https://orcid.org/0000-0001-5846-6485

Acknowledgements

"Though one may be overpowered, two can defend themselves. A cord of three strands is not quickly broken."

Ecclesiastes 4:12 (NIV)

When I reflect on my time in graduate school, the first thing that comes to mind is not the research I conducted or the results I found, but the people who have journeyed alongside me on the path to the Ph.D. Accordingly, these "acknowledgements" are not merely a series of courteous nods to those who helped in some way with my scientific and personal development. Rather, they assert that, without the communities that have supported and cared for me over the years, this dissertation would not exist. Science never happens in a vacuum, and though this thesis represents five years of my labors, the wind in my sails (or turbine blades) has always been the generosity, guidance, and grace of colleagues, collaborators, mentors, and friends. This work is a testament to their investments in me, and it is therefore only appropriate that my dissertation should begin with my grateful recognition of many of those who have shaped both me and my research over the span of my studies.

First, I am indebted to my advisor, John Dabiri, for allowing me to join his research group and benefit from his caring, supportive, and inspiring mentorship. I am grateful for his guidance over the years, which has profoundly shaped my growth as a researcher and as a member of the scientific community. John sets an incredibly high standard both for quality of research and for constructive participation in the scientific community and in broader society, and I hope to emulate his enthusiasm and integrity in my own career.

I am also grateful to the members of my dissertation committee, Beverley McKeon, Mory Gharib, and Tim Colonius, for their support of my research and vocational endeavors since coming to Caltech. Their feedback, advice, and wisdom have shaped my outlook on the field of fluid mechanics and my approach to tackling research problems, and I greatly appreciate the academic hospitality they all extended to me when I made the transition from Stanford to Caltech in the midst of the COVID-19 pandemic in 2020.

My friends and colleagues in the Dabiri Lab — Simon Anuszczyk, Ian Brownstein, Jen Cardona, Malaika Cordeiro, Matt Fu, Roni Goldshmid, Peter Gunnarson, Isabel Houghton, Mike Howland, Nina Mohebbi, Kelsi Rutledge, Valerie Troutman,

Nicole Xu, and Noa Yoder — have served as a continual source of inspiration and encouragement throughout every stage of my grad-school journey. We have run together, sung together, and dressed up in goofy lab Halloween costumes together, and these folks' positive attitudes, scintillating senses of humor, and perpetual willingness to go out of their way to help a labmate in need (even after having graduated and left the lab!) have brought immeasurable joy to my time in grad school.

I have additionally had the privilege of working with several fantastic collaborators, including Di Yang, Masoumeh Gharaati, and Shuolin Xiao (University of Houston), Dave Rival, Frieder Kaiser, Adnan El Makdah, Winston Hu, and Ryan Chan (Queen's University), and Omkar Shende (Stanford University). I am also deeply indebted to the research mentors who equipped me with the knowledge and skills I needed to make it through grad school: Greg Bewley, Marcus Hultmark, Daniel Floryan, Tyler Van Buren, Lex Smits, Tim Wei, Johannes Kissing, and Cameron Tropea. Additionally, during my Ph.D. I have benefited from helpful technical discussions with Mark Miller, Kostas Steiros, Nate Bristow, Peter Renn, Emile Oshima, Mike Howland and many others. I count myself blessed to be part of such a supportive and creative scientific community.

None of the research contained in this dissertation would have been possible without the tireless support of the impeccably effective administrative staff at Stanford and Caltech, including Susan Dorman, Jack Chiueh, Martha Salcedo, Sarah Pontes, Christine Ramirez, and Jamie Meighen-Sei — especially as they helped me navigate the challenges of the ever-changing pandemic situation. The excellent custodial crews at Stanford and Caltech took great care of our facilities and equipment, and I always appreciated Barry Reed's warm greetings in the halls of Guggenheim.

Though I could not have predicted at the start that my time in grad school would span two institutions and a global pandemic, these chaotic circumstances have served to connect me with an unexpectedly high number of independent communities filled with some of the most brilliant, passionate, and caring people I could have ever hoped to meet. (In other words, the principle of turbulent mixing applies to movements of people as well.) I owe much of my understanding of the theory and practice of fluid mechanics from Stanford faculty in Mechanical Engineering and the Environmental Fluid Mechanics Laboratory, including Sanjiva Lele, Nick Ouellette, Ali Mani, and Parviz Moin, as well as my friends and fellow fluid-mechanics fanatics in my first-year cohort, Building 500, and the EFML. I am particularly grateful for the ongoing friendship of Omkar Shende, Paul Yi, Kevin Griffin, Jack Guo, and many

others who have kept up with me long after my move. The GALCIT community was extraordinarily hospitable in welcoming me to Caltech. In particular, Tanner Harms, Miles Chan, and their entire cohort took me in as one of their own and were incredibly supportive in my move and adjustment. As campus slowly returned to in-person activities, I have enjoyed getting to know people from across Caltech, particularly through the chamber-music program and the Alpine Club trail-running community. Having known almost nobody in the area when I moved down in September 2020, I am immensely grateful for all of the people who have helped make me feel more at home in Pasadena.

Furthermore, I have been wonderfully blessed to have stumbled into several strong communities of faith that have inspired me, challenged me, and helped me to keep perspective throughout the long journey of the Ph.D. I am thankful for the gracious fellowship of my friends in Stanford IVGrad; our FIGS hangouts, steering-committee shenanigans, restful retreats, shared meals, and skiing, hiking, and tennis adventures are all major highlights of my time at Stanford. I am also thankful for all the prayer, support, and wisdom I received from Jon and Joy Chiew's small group at PBC. My understanding of the intersection of faith, science, culture, and vocation has never experienced more significant growth than in the Square-Inch discussion group (now known as DCM), and it has been a joy and privilege to grow alongside this cross-country community of committed Christian scholars in a shared appreciation of nuance, tough questions, and "complicated fun" — even as many of us have been scattered across the country. I was also extremely fortunate to weather the first several months of the pandemic with a group of steadfast, caring, and ever-entertaining housemates and brothers: Jeremy Dahl, Paul Falcone, and Jonathan Love. Our quarantine community in 519 will always hold a special place in my heart. Upon moving to Pasadena, I was quickly met with the earnest fellowship of folks from GCF and Missio Community Church. These communities have helped me keep my identity and focus grounded in what really matters during some of the more stressful and difficult stages of my Ph.D., and I am grateful for the discussions in GCF weekly meetings and tea times, Melanie and Nick Dzugan's neighborhood group, and Missio question-and-response times that have helped me wrestle with many difficult topics. And throughout my time in grad school, I have been constantly encouraged by faithful friends from previous communities, including Paul Yi, Allen Fang, Victor Hsiao, Nathaniel Gerthe, and many others.

Finally, I would like to thank my family for supporting me throughout my educational

journey, and for graciously giving me love, patience, and support that I never earned and could never repay. My sister has always inspired me with her creativity, depth of thinking, and passion for serving the needy and marginalized in society, and I am grateful for her ability to listen well and ask insightful questions. My mother continually amazes me with her tireless care for our family, as well as her efficient problem-solving capabilities, which she has deployed to great effect in the fields of engineering, education, and science communication. I like to think that much of my research acumen stems from her efficacy and ability to break down imposing challenges into manageable tasks. My father has been my forerunner and role model in experimental fluid mechanics for most of my life, having taught me the concepts of vorticity and conservation of angular momentum in the bathtub when I was three years old. I greatly admire his vision, thoughtfulness, and empathetic approach to research and mentoring, and it has been of incalculable value to have him as a role model for both application-driven research and faithful living. (For better or for worse, I also seem to have inherited some fraction of his sense of humor.) Lastly, I want to recognize the profound influence that my grandmother, Lee C. Wei, had on my intellectual and spiritual development. A lifelong learner herself, she encouraged my curiosity and imparted on me habits of learning, discipline, and play that became the foundations of my educational journey. She also cared deeply for those around her and constantly challenged me to find practical ways to love my neighbor as myself. She, as well as my other grandparents, would have loved to see me finish this degree. I hope that, not just in my work but also in the way I live my life, I can honor their legacy.

The completion of this dissertation represents the end of my journey through grad school, but it also represents the beginning of something new. Since I have been surrounded by such a great community of friends, colleagues, and mentors, I only hope to continue to run the race set before me faithfully. *Soli Deo Gloria.*

> "Unless the Lord builds the house,
> those who build it labor in vain.
> Unless the Lord watches over the city,
> the watchman stays awake in vain.
> It is in vain that you rise up early
> and go late to rest,
> eating the bread of anxious toil;
> for He gives to His beloved sleep."
>
> Psalm 127:1-2 (ESV)

Abstract

Wind energy is poised to play a considerable role in the global transition to clean-energy technologies within the next few decades. Modern wind turbines, like aircraft and other aerodynamic structures, are typically designed with the assumption that the flows they encounter will be uniform and steady. However, atmospheric flows are highly unsteady, and systems operating within them must contend with gust disturbances that can lead to performance losses and structural damage. Therefore, the next generation of wind-energy systems requires physics-informed design principles that effectively account for and even leverage these unsteady flow phenomena for enhanced power generation, robustness, and operational longevity. Accordingly, this work details experimental and analytical efforts to characterize unsteady aerodynamics in wind-turbine contexts. First, the effects of unsteady streamwise motion on turbine performance are studied, as recent work has suggested that these dynamics may enable time-averaged efficiencies that exceed the steady-flow Betz limit on turbine efficiency. The power production of and flow around a periodically surging wind turbine are thus investigated using wind-tunnel experiments, which suggest that turbines in these flow conditions could leverage unsteady surge motions for power-extraction gains of up to 6.4% over the stationary case. Linearized and nonlinear dynamical models of the response of the turbine to these time-varying flows are derived and validated against the experimental data. These models are also coupled with a potential-flow model of the upstream induction zone of the turbine in order to predict temporal variations in the flow velocities and pressures in this region. Unsteady contributions to the time-averaged efficiency are also considered through theoretical potential-flow derivations. Additionally, a novel three-dimensional particle-tracking velocimetry approach using artificial snow as seeding particles is deployed to obtain volumetric flow measurements in the wakes of full-scale vertical-axis wind turbines in field conditions. These measurements yield insights into the effects of unsteady vortex dynamics on the structure of the near wake, with implications for the performance of turbines in wind-farm arrays. These investigations provide the analytical and experimental foundations for future studies of unsteady atmospheric flows, and will lead to the development of principles and techniques for wind-farm siting, control, and optimization.

Published Content and Contributions

1. Nathaniel J. Wei and John O. Dabiri. "Phase-averaged dynamics of a periodically surging wind turbine". In: *Journal of Renewable and Sustainable Energy* 14.1 (2022). Publisher: American Institute of Physics, p. 013305. DOI: 10.1063/5.0076029

   N. J. W. made the primary contributions to experiment design, data acquisition and analysis, analytical modeling, and writing. J. O. D. contributed to the conceptualization of the study, funding acquisition, analysis and interpretation of the results, and feedback on the manuscript.

2. Nathaniel J. Wei and John O. Dabiri. "Power-generation enhancements and upstream flow properties of turbines in unsteady inflow conditions". In: *Journal of Fluid Mechanics* (2023). In press. DOI: 10.48550/ARXIV.2210.14466

   N. J. W. made the primary contributions to experiment design, data acquisition and analysis, analytical modeling, and writing. J. O. D. contributed to the conceptualization of the study, funding acquisition, analysis and interpretation of the results, and feedback on the manuscript.

3. Nathaniel J. Wei, Ian D. Brownstein, Jennifer L. Cardona, Michael F. Howland, and John O. Dabiri. "Near-wake structure of full-scale vertical-axis wind turbines". In: *Journal of Fluid Mechanics* 914 (2021), A17. DOI: 10.1017/jfm.2020.578

   N. J. W. made the primary contributions to data processing, data analysis, modeling, and writing, and also conducted the artificial-snow validation experiments described in the appendix of this work. I. D. B. oversaw the conceptualization, planning, and execution of the field experiments, and J. L. C. and M. F. H. assisted with data collection. J. O. D. contributed to the conceptualization of the study, funding acquisition, and analysis and interpretation of the results. All co-authors provided input on the final manuscript draft.

Table of Contents

List of Figures

List of Tables

Preface: A Brief Discourse on the Current Climate Crisis

Note: The ideas expressed in this section represent the opinions of the author, and are not intended to contribute to the technical content of this work.

It is high time that we as a species take responsibility for the world in which we live. Particularly in the colonial, industrial, and modern eras, we have treated the Earth and its resources as things we may possess, control, and use for our shortsighted purposes. The consequences of our aggrandizing tendencies are becoming more drastically apparent in the 21st century. The recently released Sixth Assessment Report of the Intergovernmental Panel on Climate Change (IPCC AR6) states that global temperature levels between 2011 and 2020 were on average 1.09°C higher than the average global temperature between 1850 and 1900 (IPCC, 2023). This report, which summarizes a vast collection of scientific findings from recent years, suggests that average global temperature levels exceeding 1.5 or 2°C will lead to significant and irreversible damages to ecosystems, climate patterns, agriculture, and human health. Many scientists have expressed skepticism that keeping average global temperature levels at or below 1.5°C above pre-industrial levels is achievable (Tollefson, 2021). According to the 2022 Emissions Gap Report of the United Nations Environment Programme, current global emissions policies provide "no credible pathway to 1.5°C," with projected average global temperature increases above pre-industrial levels of 2.4 to 2.8°C by the end of this century (UN, 2022).

In addition to the ecological and environmental crises instigated by human activities and their resulting climate impacts, climate change represents a fundamental threat to human flourishing worldwide. According to the IPCC AR6 investigation, "approximately 3.3–3.6 billion people live in contexts that are vulnerable to climate change" (IPCC, 2023). Detrimental impacts of climate change on human livelihoods and health include severe weather, food and water shortages, rising sea levels, increased disease transmission, and the decimation of local wildlife. These consequences are largely felt by low-income communities around the world, particularly in the Global South. Conversely, developed nations in the West have historically been responsible for the majority of carbon emissions and unsustainable resource-consumption practices, in addition to the exploitative and dehumanizing approach these countries often took toward other people groups. Thus, the crisis of climate change is inextricably tied to systemic problems of injustice on a global scale.

Since anthropogenic climate change is such a pressing global problem, the approach to mitigating its deleterious effects must involve a concerted effort from all nations, communities, industries, and vocations. Solutions will need to incorporate justice-focused policy and legislation, economic incentives, public outreach and education, financial and medical support for those directly affected by climate disasters, sociological and ethical analyses of the impacts of climate change on human flourishing, and many other contributions from diverse fields and perspectives. While it is not the intention of this dissertation to prescribe particular approaches for these initiatives, this broader perspective is included at the outset to remind scientists and engineers that technical advancements represent only one facet of the solution space to humanity's most significant challenges. Western cultures steeped in scientific positivism tend to overestimate the scope and capabilities of technology, and several philosophical, cultural, and corporate movements in the past few centuries have sought solutions to the world's most persistent problems exclusively through logical reasoning, empirical investigations, and scientific innovation. Those of us in science and engineering, however, would do well to remember that science and technology are just as often contributors to global problems as they are solutions. For instance, the rapid industrialization of the modern era, coupled with its philosophical prioritizations of mass production and efficiency, have fueled unchecked increases in global emissions, dehumanizing labor conditions in developing nations, and rampant cycles of consumerism and waste generation. Scientists and engineers are thus neither innocent in the origins of the climate crisis nor solely responsible for its resolution.

These considerations are provided to properly contextualize the work presented in this dissertation in light of the current state of the climate crisis. Though the contributions of renewable-energy technologies such as wind power are well-established and will greatly reduce our dependence on high-carbon energy sources in the future, they should not be touted as the ultimate solutions to our climate woes. Our world is a complex and interconnected system, and our approaches to global-scale problems should reflect and respect this complexity. This dissertation investigates a microcosm of that coupling – the relationship between wind-energy systems and unsteady flows in the atmosphere. More broadly, however, I hope that research explorations such as these will inspire a deeper appreciation for the interconnected nature of global climate and human activities, leading to more robust cross-disciplinary conversations and collaborations, and ultimately to a more unified and comprehensive global effort to care for our planet and its inhabitants.

Chapter 1

Introduction

"The Earth is what we all have in common."

Wendell Berry, *The Unsettling of America: Culture & Agriculture*

1.1 Wind power as a sustainable solution to global energy demands

Climate change poses an existential threat to human and ecological flourishing worldwide. Carbon-neutral sources of energy are urgently needed to satisfy growing global energy demands while also reducing the harmful impacts of anthropogenic emissions, pollution, and waste on vulnerable human populations and ecological regions. Given these challenges, the progress of wind power over the past few decades is encouraging. Wind energy has grown rapidly, climbing to 906 GW of installed capacity by the end of 2022; 77.6 GW was installed in 2022 alone (Hutchinson and Zhao, 2023). In 2021, wind energy accounted for 6.5% of all electricity generated worldwide, representing 23.5% of the total contributed by renewables (BP, 2022). Some countries, such as Germany, are generating over a quarter of their electricity with wind power (Burger, 2023). Additionally, the levelized cost of energy (LCOE) of wind, a function of the lifetime cost of an installation divided by its total energy production, has decreased sharply over time. The global weighted average LCOE of onshore wind has sunk below the minimum values for fossil-fuel plants since 2018, and offshore wind is not far behind (IRENA, 2022). Offshore wind in particular represents a promising avenue for growth in the near future, as favorable wind resource off the eastern and western coasts of the US attract increased attention (Shaw *et al.*, 2022), while similar investments are already underway off the coasts of east Asia and northern Europe. Therefore, wind-energy systems are becoming increasingly more important to characterize and optimize as the world seeks to transition to zero-carbon energy infrastructure.

Wind-energy systems have come a long way from their origins in Persia around the 9^{th} century C.E. (Lucas, 2006). Today's wind turbines are larger and more efficient than ever before, with rotor diameters in excess of 140 m and power-extraction

efficiencies (relative to the power available in the incident wind) approaching 50%. These engineering feats are due in large part to advances in materials and manufacturing technologies, as well as the fact that winds tend to be stronger with increasing altitude (Veers *et al.*, 2019). In addition to traditional land-based horizontal-axis wind turbines (HAWTs), several turbine variants are currently being explored. Offshore wind turbines, for example, can be larger than their land-based counterparts to take advantage of strong offshore winds at higher altitudes. For offshore applications where the water depth makes fixed-bottom turbines prohibitively expensive, turbines mounted on floating platforms can serve as a depth-independent alternative (Gueydon *et al.*, 2020). To capitalize on stronger winds at even higher altitudes, turbines mounted to tethered aerial kites have been proposed and tested (Jonkman, 2021). Departing from the horizontal-axis design paradigm, vertical-axis wind turbines (VAWTs) have shown potential for achieving high power densities in closely packed arrays (Dabiri, 2011). Non-rotating energy-harvesting systems consisting of pitching and plunging airfoils have also been explored, particularly for hydrokinetic applications in rivers and tidal zones (Young *et al.*, 2014). Finally, oscillating energy harvesters that convert vortex-induced vibrations to energy either mechanically (Bernitsas and Raghavan, 2009) or using piezoelectric elements (Abdelkefi, 2016) may have fewer moving parts than traditional turbines and can operate at smaller scales and lower flow speeds.

Despite this extensive array of wind-energy technologies, the growth rate of the wind-energy sector is only projected to meet 68% of the estimated capacity required by 2030 to keep pace with the 1.5°C pathway instituted by the Paris Agreement, with a fivefold increase in annual capacity installation needed to meet 2030 targets (Hutchinson and Zhao, 2023). As this would require a 250% increase in total installed capacity within the next seven years, these goals cannot be achieved solely by building more wind turbines. Rather, as wind farms expand into more diverse and complex flow environments, such as offshore areas and terrestrial sites with uneven terrain, more work needs to be done to improve the ways in which wind-energy systems respond to and leverage these flows. The response of wind turbines to gusts, wakes, temporary lulls in wind speed, and other turbulent or unsteady flow phenomena is particularly important, as these disturbances may lower an array's aggregate performance below its rated capacity. The structural elements of the turbines, such as blades, gearboxes, and towers, also need to be resilient against fluctuating wind loads, as unanticipated fatigue cycles can decrease a turbine's operational lifespan and slow the expansion of wind energy in regions with variable

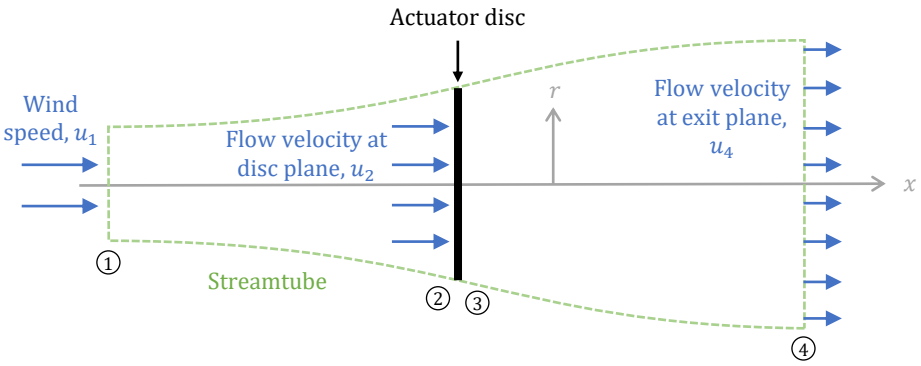

Figure 1.1: Schematic of the control-volume modeling approach of Betz (1920). Circled numbers denote streamwise interrogation locations (1 through 4). The pressure is assumed to be discontinuous across the disc, and is taken to be p_∞ at locations 1 and 4.

atmospheric conditions. In light of these considerations regarding the operation of wind turbines in complex flows, it is apparent that future wind-energy systems will need to comprehensively account for the impact of unsteady flow phenomena on their performance and longevity.

1.2 Wind-energy systems and unsteady fluid mechanics

Wind turbines are typically designed under the assumption of steady-flow conditions (Hau, 2013a; Hansen, 2015), but some extensions to unsteady flows do exist. We will now define steady, unsteady, and quasi-steady dynamics in the context of wind-energy systems, and review modeling and diagnostic tools that have been used to study and characterize these dynamics.

1.2.1 Steady, unsteady, and quasi-steady flows in wind-energy systems

The canonical steady-flow analysis of a general device that harnesses energy from a moving fluid was developed in the early 1900s by several engineers and mathematicians, including Lanchester, Betz, Joukowsky, Froude, and others (cf. Van Kuik, 2007). The energy-harvesting system is modeled as an actuator disc, and the flow through it is bounded by a streamtube (shown schematically in Figure 1.1). The flow is assumed to be incompressible, irrotational, inviscid, and steady. A control-volume analysis is conducted, and flow quantities are referenced at four streamwise

locations: far upstream of the disc (1), immediately upstream and downstream of the disc (2 and 3), and far downstream of the disc (4). The power-conversion efficiency of the actuator disc is given by the coefficient of power, which is defined as the power extracted by the device from the flow, $\mathcal{P}$, normalized by the available power in the incident wind, i.e.

$$C_p = \frac{\mathcal{P}}{\frac{1}{2}\rho\pi R^2 u_1^3}. \tag{1.1}$$

Further, an axial induction factor (or induction coefficient) may be defined to parameterize the difference in velocities between locations 1 and 2:

$$a = \frac{u_1 - u_2}{u_1}. \tag{1.2}$$

Applying conservation laws for mass and momentum, as well as the Bernoulli relation between velocities and pressures along a streamline, we find that

$$C_p = 4a(1-a)^2, \tag{1.3}$$

and maximizing this expression for a gives $C_{p,max} = 16/27 \approx 59.3\%$ at $a = 1/3$. This theoretical limit on the efficiency of any wind-energy or hydrokinetic system is known as the Betz limit (Betz, 1920). The limit appears empirically valid, as the most efficient turbines today have maximum efficiencies of around 50%. The theoretical analysis has also been applied to airborne wind-energy systems (De Lellis *et al.*, 2018) and flapping-foil power generators (Young *et al.*, 2020).

However, as mentioned in the preceding section, the flows encountered by wind-energy systems need not conform to the steady-flow assumption enforced by this analytical framework. This is particularly the case in the atmospheric boundary layer in which wind-turbines operate, where turbulence, gusts, and other unsteady phenomena are the rule rather than the exception. In this work, we define an unsteady process as a behavior whose dynamics involve a non-negligible time evolution of a quantity of interest, i.e. $\frac{\partial}{\partial t} \neq 0$. As outlined in Table 1.1, unsteady dynamics can appear in wind-energy systems either as a function of local atmospheric flow conditions or as a consequence of their own operation. Unsteady flow disturbances, such as axial gusts for ground-fixed turbines or platform oscillations for floating offshore systems, introduce a time-varying inflow condition to the turbine that will affect both its dynamics and power generation. Conversely, a turbine operating in a steady wind may still excite unsteady dynamics. The blades of a vertical-axis wind turbine, for example, experience local flow conditions that vary as a function of azimuthal position within a single rotation cycle. Thus, unsteady flow phenomena

Source of unsteadiness	**Inflow condition**	**Turbine dynamics**	**Examples**
Steady flow (Betz)	Constant	Steady	HAWT in steady flow
External disturbance	Time-varying	Quasi-steady or unsteady	HAWT in axial gust; FOWT with platform motion (Chs. 2 and 3)
Turbine operation	Constant	Unsteady	VAWT blades in steady flow (Ch. 4); HAWT with time-varying generator load or blade pitch

Table 1.1: Overview of scenarios involving unsteady flows in wind-energy contexts: 1) steady flow (baseline case), 2) unsteady dynamics due to an external disturbance), and 3) unsteady dynamics due to time-varying turbine operating conditions (e.g. changing generator load or blade pitch angle). HAWT stands for horizontal-axis wind turbine, FOWT stands for floating offshore wind turbine, and VAWT stands for vertical-axis wind turbine.

such as dynamic stall and vortex shedding occur on the blades, and these signatures are convected downstream into the wake of the turbine. Similarly, changes in the blade pitch angle or generator load of a wind turbine can induce changes in the turbine rotation rate and power extraction that affect the surrounding flow field in an unsteady manner. As these unsteady effects are propagated within the wake of the turbine, they may then act as unsteady inflow disturbances for downstream turbines in an array. Both of these types of unsteady dynamics will affect the performance and operation of wind-energy systems, and thus the wind-energy sector stands to benefit from improved parameterizations of these phenomena.

The so-called *quasi-steady* approximation is often invoked to simplify the unsteady contribution to a system's dynamics. A quasi-steady approximation assumes a local static equilibrium at every instant in time that is independent from all other instances. A separate steady-flow relation can then be solved independently at each timestep. This modeling approach often stems from the assumption that the time-varying forcing is slow or small enough that terms involving time derivatives become negligibly small, and thus this approximation is often applied when nondimensional forcing frequencies such as the reduced frequency or Strouhal number lie below a certain threshold (cf. Leishman, 2006).

Practically, there are different ways to implement a quasi-steady approximation in a model. One could hypothesize that a given input parameter does not change

appreciably as a function of time and treat it as a constant, as done by Johlas *et al.* (2021) for the coefficient of power of a turbine in an oscillating inflow. Alternatively, a hybrid quasi-steady/unsteady model can be applied, in which some time-dependent characteristics are considered and others are neglected. Take, for instance, an application of Newton's second law for rotation:

$$J\frac{d\omega}{dt} = \tau_1(t) - \tau_2(t), \tag{1.4}$$

where J is the rotational moment of inertia, ω is the rotation rate, and τ_1 and τ_2 are opposing torques, which themselves may include unsteady contributions. (This example, known in the turbine literature as the swing equation, will be explored in detail in Chapter 2.) A fully quasi-steady approach would neglect $\frac{d\omega}{dt}$ and the unsteady components of τ_1 and τ_2 and compute a separate value of ω for every instance of $\tau_1(t) \approx \tau_2(t)$. It is also possible, however, to neglect the unsteady components of the torques and retain the unsteady rotational-acceleration term. This model would be considered quasi-steady with respect to the torques and unsteady with respect to the rotation rate. The term "quasi-steady" is therefore somewhat ambiguous, and care must be taken to clarify the dynamics that are targeted when such an approximation is made.

These distinctions may seem pedantic, but their importance lies in the interpretation of the models they describe. A fully unsteady model will capture different mechanisms and dynamics than a quasi-steady model of the same system, and their regimes of applicability will differ accordingly. Thus, to extend the oft-quoted aphorism that "All models are wrong but some are useful,"[1] we might add that the usefulness of a model depends primarily on its assumptions and its applications. If we are careful to specify the nature of the dynamics that are captured by a set of models, and which are neglected by assumption, we will be more successful in using these models to describe and predict the response of wind-energy systems in real-world flow conditions.

1.2.2 Models and measurements of unsteady aerodynamics in wind-energy systems

With these considerations and caveats in place, we may now survey the range of modeling approaches that have been applied to unsteady dynamics in wind-energy contexts, as well as the numerical and experimental techniques that have been developed to validate these approaches.

[1] This proverb is generally attributed to the British statistician George E. P. Box.

Models seeking to capture unsteady effects in wind-energy systems span a wide range of fidelities. Unsteady actuator-disc models have been proposed to parameterize the effects of unsteady inflow conditions on the performance of a turbine and the dynamics of its wake (e.g. Chattot, 2014). These models often treat the wake of the turbine as a cylindrical vortex tube, and map the effects of flow unsteadiness onto the circulation of the sheet (Yu *et al.*, 2016). Multiple vortex tubes can also be used to model the effects of radially nonuniform circulation profiles, stemming from spanwise differences in the bound circulation on the turbine blade sections (Branlard and Gaunaa, 2015). For a time-resolved characterization of the wake, free-vortex wake models can be employed (e.g. Sebastian and Lackner, 2012). For example, de Vaal *et al.* (2014b) developed a model in which discrete vortex rings are shed with each blade passing and are advected into the wake via Biot-Savart induction. More granular models invoke blade-element momentum (BEM) computations to determine the forces on and shed circulation from radial blade sections; commonly applied models include those of Pitt and Peters (1980) and Snel and Schepers (1995). Combinations of BEM models and free-vortex wake simulations, such as QBlade, are widely used in turbine-design applications today (Marten, 2020). Finally, unsteady-aerodynamics models may be employed to parameterize unsteady forces on two-dimensional blade sections, in cooperation with BEM codes. Analytical models derived from potential-flow theory can be used for small-perturbation disturbances, such as transverse gusts (Sears, 1941; Atassi, 1984), streamwise gusts (Greenberg, 1947), airfoil oscillations (Theodorsen, 1934), and combinations of these disturbances (Wei and Shende, 2023). This class of models has been extensively validated in experiments, and in some cases can capture the lift response of unsteady airfoils even outside of the ideal-flow small-perturbation regime (e.g. Baik *et al.*, 2012; Wei *et al.*, 2019). Semi-empirical models are also widely used to capture the flow-separation and reattachment properties associated with the phenomenon of dynamic stall, including the ONERA (Tran and Petot, 1980), Beddoes-Leishman (Leishman and Beddoes, 1989), and Øye (Øye, 1991) models.

These models give physical insights into the unsteady dynamics of wind-energy systems, but because of their reduced-order nature, they are limited by their assumptions. A higher-fidelity approach is to use numerical simulations in tandem with these modeling frameworks. Direct numerical simulation (DNS) of the Navier-Stokes equations is generally not feasible for full-scale wind-energy systems, as the number of grid points required for a fully resolved simulation scales with $Re^{9/4}$, and the Reynolds number of a utility-scale turbine is on the order of 10^6 to 10^8.

Blade-resolved large-eddy simulation (LES) studies are more feasible than DNS (Sprague *et al.*, 2020), but the complex fluid-structure interactions involved make actuator-line and actuator-disc models that parameterize the coupling between the flow and the turbine blades more practical for simulations of individual turbines and turbine arrays (Stevens and Meneveau, 2017). For instance, NREL's OpenFAST code captures the dynamics of the entire turbine system, including aerodynamics, structural dynamics, control and electrical systems, and floating-platform hydrodynamics (Jonkman *et al.*, 2018), and it can be coupled with LES or Reynolds-Averaged Navier-Stokes (RANS) solvers such as OpenFOAM (Churchfield *et al.*, 2012) and Nalu-Wind (Ananthan *et al.*, 2019).

While high-fidelity numerical simulations continue to grow in their predictive capabilities, questions still arise regarding their ability to effectively capture unsteady flow phenomena such as separation and fluid-structure coupling. These numerical tools are thus complemented by an array of experimental techniques for studying wind-energy systems at laboratory and field scales. Conventional facilities include water channels (e.g. Strom *et al.*, 2022) and wind tunnels (e.g. Tescione *et al.*, 2014), in which optical flow-field measurements using particle-image velocimetry (PIV) can be carried out. Turbines can be operated in freely rotating or driven states (Araya and Dabiri, 2015); alternatively, for studies of turbine arrays, the turbines can be replaced by porous discs (e.g. Howland *et al.*, 2016; Kurelek *et al.*, 2023). For studies of unsteady flows, turbines can be moved in specified velocity profiles to mimic the effects of axial gusts or floating-platform motions (Bayati *et al.*, 2017; El Makdah *et al.*, 2019), or unsteady flows can be generated upstream using an active grid (Berger *et al.*, 2022). While these studies can shed light on flow mechanisms, the length scales in these facilities are typically orders of magnitude lower than full-scale systems. To replicate the flow conditions experienced by full-scale turbines in terms of nondimensional aerodynamic parameters, the Reynolds number, tip-speed ratio, and tip Mach number, given by

$$Re_D = \frac{\rho U_\infty D}{\mu}, \quad \lambda = \frac{\omega R}{U_\infty}, \quad \text{and} \quad Ma = \frac{\omega R}{U_{ss}} \tag{1.5}$$

respectively, must be matched. (Here, ρ is the fluid density, U_∞ is the free-stream flow velocity, D is the turbine diameter, μ is the dynamic viscosity of the fluid, R is the turbine radius, and U_{ss} is the speed of sound in the fluid.) Though the tip-speed ratio and tip Mach number are not strictly fluid-mechanical inputs of the system, since they depend on the control torque applied to the turbine shaft, they are nonetheless important for capturing turbine-blade aerodynamics and the resulting

power-generation characteristics of the turbine. One solution to this dynamic-similarity problem is to use pressurized air, which increases the Reynolds number without modifying the tip-speed ratio or the Mach number, since the speed of sound is a weak function of pressure. Miller, Duvvuri, Brownstein, *et al.* (2018) and Miller *et al.* (2019) utilized this approach to study the dynamics of vertical- and horizontal-axis turbines at full-scale Reynolds numbers in lab-scale experiments. However, controlling other atmospheric parameters such as unsteady gusts, boundary-layer turbulence, and atmospheric stability are still difficult in these types of facilities. Field experiments are therefore important tools for ascertaining the performance of wind-energy systems in real-world flow conditions. Structural diagnostics such as strain gauges and vibration sensors can be deployed to monitor the health and response of turbine blades and support elements (Sun *et al.*, 2022). Power measurements from the turbines themselves can also be used in conjunction with reduced-order models to test novel flow-control schemes such as wake steering (Howland *et al.*, 2019). Flow measurements are possible using LiDAR systems (e.g. Larsen and Hansen, 2014), meteorological masts (e.g. Kinzel *et al.*, 2012), and even fleets of drones (Wetz and Wildmann, 2023). These systems, however, are relatively limited in their ability to resolve unsteady flow phenomena and spatial inhomogeneities. By contrast, Hong *et al.* (2014) used natural snowfall to perform PIV measurements near a full-scale horizontal-axis wind turbine, and were able to resolve the evolution of tip vortices shed from the turbine blades. Recent advances in three-dimensional particle-tracking velocimetry (3D-PTV), such as Shake-The-Box PTV (Schanz *et al.*, 2016), are making three-dimensional volumetric flow-field measurements more feasible at the larger scales required for field campaigns. For example, Bristow *et al.* (2023) were able to measure the trajectories of falling snow particles in a $4\times4\times6$-m^3 volume. These techniques have also been used successfully in lab-scale experiments to quantify vortical structures in the wakes of VAWT pairs (Brownstein *et al.*, 2019), but since full-scale turbines span length scales on the order of tens to hundreds of meters, three-dimensional flow measurements around operational wind turbines in field conditions are still absent in the literature.

1.3 Aims and scope of the dissertation

The overview in the preceding section highlights the diversity of modeling and diagnostic tools available for the study of unsteady-flow effects on wind-energy systems. However, there still remain significant questions regarding the correspon-

dence of models of varying fidelity and experimental measurements, particularly when analyzing full-scale systems in real atmospheric flow conditions. The assumptions embedded in different modeling frameworks often require experimental validation to determine the conditions in which they apply, even for steady-flow analyses. Several models also have parameters that require empirical fitting and experimental calibration, which limits their generality. Additionally, field-scale flow measurements are only now starting to be able to sample spatial and temporal flow variations at scales large enough to be relevant for modern wind-energy systems. Therefore, there exists a pressing need for experimentally validated, physically interpretable models, as well as experimental techniques that can identify signatures of unsteady flow physics around active utility-scale wind turbines.

Furthermore, a conceptual paradigm shift in our approach to wind-energy technologies may be warranted. Rather than treating unsteady flows as annoying complications that need to be controlled or rejected, there is much potential in viewing unsteady flows as integral to the design and operation of the next generation of wind-energy systems. The lower atmosphere is fundamentally an unsteady place; perhaps our design methodologies should reflect this fact, rather than dismiss it. Wind-energy technologies that can account for and even creatively utilize unsteady dynamics may unlock new levels of energy-conversion performance and operational longevity, thereby accelerating the growth of the wind-energy sector and bringing the world closer to its climate goals.

This dissertation thus seeks to develop modeling frameworks, experiments, and measurement techniques to investigate and leverage unsteady fluid mechanics in wind-energy systems. First, the effects of streamwise unsteadiness on a horizontal-axis wind turbine are considered, since, as discussed previously, studies by Dabiri (2020), Johlas *et al.* (2021), and others have suggested that this mode of unsteadiness can lead to power-extraction gains over the steady-flow case. In Chapter 2, torque and power data from wind-tunnel experiments with a periodically surging turbine are presented, and the results are parameterized using a linearized dynamical model of the system. Time-averaged power-extraction enhancements of up to 6.4% above the steady reference case are also observed. In Chapter 3, a more general nonlinear dynamical model is proposed to clarify the mechanisms behind these power enhancements, and a potential-flow model is derived for the flow properties upstream of the surging turbine and is coupled to the nonlinear dynamical model. These analytical tools are validated using turbine-power and flow measurements. A theoretical

consideration of the contributions of an unsteady velocity potential is also outlined. Finally, Chapter 4 details the deployment of a field-scale 3D-PTV measurement system that uses artificial snow as seeding particles. This technique is used to obtain volumetric measurements of the flow fields in the wakes of utility-scale vertical-axis wind turbines with straight and helical blades. An unsteady vortex-shedding mechanism is proposed to qualitatively describe trends observed in the data. The conclusions and implications of these studies, as well as potential opportunities for future research, are laid out in Chapter 5.

Chapter 2

Linearized Dynamics of a Periodically Surging Wind Turbine

The contents of this chapter have been adapted from Wei and Dabiri (2022), published in the Journal of Renewable and Sustainable Energy under the title "Phase-averaged dynamics of a periodically surging wind turbine." As the first author, Nathan Wei made the primary contributions to experiment design, data acquisition and analysis, analytical modeling, and writing. Co-author John Dabiri contributed to the conceptualization of the study, funding acquisition, analysis and interpretation of the results, and feedback on the manuscript.

Abstract

The unsteady power generation of a wind turbine translating in the streamwise direction is relevant to floating offshore wind turbines, kite-mounted airborne wind turbines, and other non-traditional wind-energy systems. To study this problem experimentally, measurements of torque, rotor speed, and power were acquired for a horizontal-axis wind turbine actuated in periodic surge motions in a fan-array wind tunnel at the Caltech Center for Autonomous Systems and Technologies (CAST). Experiments were conducted at a diameter-based Reynolds number of $Re_D = 6.1 \times 10^5$ and at tip-speed ratios between 5.2 and 8.8. Sinusoidal and trapezoidal surge-velocity waveforms with maximum surge velocities up to 23% of the free-stream velocity were tested. A model in the form of a linear ordinary differential equation (first-order in time) was derived to capture the time-resolved dynamics of the surging turbine. Its coefficients were obtained using torque measurements from a stationary turbine, without the need for unsteady calibrations. Its predictions compared favorably with the measured amplitude- and phase-response data. Furthermore, increases in the period-averaged power of up to 6.4% above the steady reference case were observed in the experiments at high tip-speed ratios and surge velocities, potentially due to unsteady or nonlinear aerodynamic effects. Conversely, decreases in mean power with increased surge velocity at low tip-speed ratios were likely a result of the onset of stall on the turbine blades. These results inform the development of strategies to optimize and control the unsteady power

generation of periodically surging wind turbines, and motivate further investigations into the unsteady aerodynamics of wind-energy systems.

2.1 Introduction

New innovations in wind energy technology motivate the study of wind-turbine performance in previously unexplored operational regimes. In particular, while traditional land-based wind turbines are fixed in place, wind-energy systems such as floating offshore wind turbines (FOWTs) and airborne wind turbines undergo streamwise oscillations that may potentially complicate the aerodynamics of these systems. The periodic motions of the turbine rotor in these situations introduce additional dynamics that can affect the power generation of the wind turbines and the fatigue loading on their blades, thereby impacting their contribution to global energy demands. Therefore, this study investigates the dynamics of a periodically surging wind turbine through analytical modeling and laboratory-scale experiments.

2.1.1 Current progress in surging-turbine aerodynamics

Previous studies have generally considered surge motions typical of wave-driven FOWTs (Gueydon *et al.*, 2020), which are of increasing relevance as the emerging offshore-wind sector continues to expand. The majority of attention regarding turbine aerodynamics has been focused on time-averaged quantities. Using a model FOWT in a wind tunnel and wave tank, Farrugia *et al.* (2014) found that the time-averaged coefficient of power, $\overline{C_p}$, increased above the steady case by 1% when oscillations in the turbine were present. A similar increase in $\overline{C_p}$ by 1% was observed in wind-tunnel experiments by Khosravi *et al.* (2015) and free-vortex wake simulations by Shen *et al.* (2018). Farrugia *et al.* (2016) showed using free-vortex wake simulations that $\overline{C_p}$ increased with surge frequency at tip-speed ratios above the rated value by up to 13.7%, but decreased with surge frequency at tip-speed ratios below the rated value. Independent simulations by Wen *et al.* (2017) yielded similar results. Johlas *et al.* (2021) suggested that the increases in average power with surge velocity can be described by a simple quasi-steady model, where the term "quasi-steady" refers to effects for which successive instances in time can be considered as being in independent states of local equilibrium. Since the model is derived from the cubic dependence of power on the incident inflow velocity at the rotor, the relative power gains over the steady value of C_p from surge motions in the upwind direction outweigh the relative losses from surge motions in the downwind

direction. Their model agrees well with the time-averaged power results from their numerical simulations of a surging turbine, but the validity of the model has not yet been evaluated over a wide range of surge velocities and operating conditions. A fully characterized, quantitatively accurate explanation for the observed increases in $\overline{C_p}$ thus remains elusive.

The time-resolved dynamics of a turbine in surge have been explored as well. These unsteady dynamics determine the unsteady loads on the turbine and its support structures, and therefore inform the design of FOWT control systems. The presence of fluctuations in turbine thrust, torque, and power at the same frequency as the imposed surge motion is well-documented in the literature (Farrugia *et al.*, 2014; Farrugia *et al.*, 2016; Shen *et al.*, 2018; Tran and Kim, 2016; Wen *et al.*, 2017; Johlas *et al.*, 2021). These fluctuations increase in amplitude as the surge frequency is increased (Farrugia *et al.*, 2016). Mancini *et al.* (2020), however, showed in wind-tunnel experiments with a surging turbine that the relationship between torque amplitude and surge frequency increases above the prediction of their linear quasi-steady model at high frequencies. They attributed this to mechanical resonance, and not to a breakdown of their linearization of power as a function of the surge velocity or the influence of unsteady aerodynamics. By contrast, torque amplitudes measured in wind-tunnel experiments by Sant *et al.* (2015) were much lower than those computed by quasi-steady and dynamic-inflow codes.

The phase response of the turbine similarly lacks a single consistent characterization in the literature. The model developed by Johlas *et al.* (2021) predicts that the instantaneous power from the turbine will be in phase with the surge velocity. The linear quasi-steady model of Mancini *et al.* (2020) supports the same prediction. Some computational (Farrugia *et al.*, 2016; Tran and Kim, 2016; Wen *et al.*, 2017; Wen, Tian, *et al.*, 2018) and experimental (Mancini *et al.*, 2020) results, however, have shown phase differences in excess of 90°, while others displayed close to zero phase offset (Micallef and Sant, 2015; Shen *et al.*, 2018; Wen, Dong, *et al.*, 2018). The discrepancies in the literature regarding the amplitude and phase of the torque and power output of surging turbines motivates the current study.

The lack of consensus with respect to mean quantities and their amplitude and phase stems in large part from unanswered questions regarding the relative importance of quasi-steady and unsteady effects. The models of Johlas *et al.* (2021) and Mancini *et al.* (2020) can be classified as purely quasi-steady models that neglect unsteady effects. Other models have incorporated unsteady effects directly. For example, de

Vaal *et al.* (2014a) compared the results of different dynamic inflow models, which include corrections for time-varying inflow velocity and acceleration, that were paired with blade-element momentum (BEM) simulations of a surging turbine. They concluded that these engineering models were capable of capturing global forces on FOWTs in typical offshore conditions. In a different approach, Fontanella *et al.* (2020) derived a state-space model that maps linearized turbine aerodynamics and wave dynamics to the time derivatives of the kinematic parameters of the turbine. The model was shown to perform well both in simulations and as the basis for control systems (Fontanella *et al.*, 2021). In addition to these models, others have suggested various unsteady flow phenomena that could influence the turbine dynamics. For instance, several of the aforementioned studies have considered the effects of airfoil stall, particularly at the blade root, on time-averaged and fluctuating quantities (Farrugia *et al.*, 2016; Tran and Kim, 2016; Wen *et al.*, 2017; Wen, Tian, *et al.*, 2018). In addition to blade stall, Sebastian and Lackner (2013) postulated the formation of unsteady recirculation regions in or downstream of the rotor plane during turbine surge, as a result of slip-stream violations. Furthermore, Wen, Tian, *et al.* (2018) attributed the phase differences observed in their simulations to added-mass effects, blade-wake interactions, and unsteady aerodynamics. These unsteady flow phenomena may affect the structure, dynamics, and recovery of the wake of a surging turbine (Rockel *et al.*, 2016; Tran and Kim, 2016; Bayati *et al.*, 2017; Lee and Lee, 2019; Kopperstad *et al.*, 2020; Rezaeiha and Micallef, 2021). However, it still remains to be seen which (if any) of these unsteady effects must be accounted for in a model to capture the torque and power production of real surging turbines, or whether existing quasi-steady models are sufficient for this purpose.

Lastly, since nearly all existing work on surging-turbine aerodynamics has been conducted in the context of surge oscillations typical of FOWTs under normal operating conditions, the dynamics of wind turbines surging through larger amplitudes or higher frequencies remain relatively unexplored. Larger surge oscillations would be relevant not only to FOWTs in more extreme conditions, but also to airborne wind turbines mounted to aircraft or crosswind kites (Cherubini *et al.*, 2015). Crosswind kites generally fly through large periodic orbits with length scales much greater than the size of the aircraft itself (Jonkman, 2021). Turbines mounted to these kites would therefore undergo surge motions at amplitudes far larger than those experienced by FOWTs. In addition, Dabiri (2020) recently suggested that streamwise unsteadiness could be leveraged to increase the efficiency of wind-energy systems above the theoretical steady limit. Since increases in time-averaged power have already

been observed at the relatively low levels of unsteady motion typical of FOWTs, an investigation of higher surge amplitudes and frequencies could provide insights toward the practical realization of these theoretical efficiency gains.

2.1.2 Research objectives

This study aims to address several open questions regarding the time-resolved dynamics of a wind turbine in surge. The amplitude and phase of torque and power relative to the surge motions are investigated in wind-tunnel experiments. Trends in the data are parameterized by a model that accounts for quasi-steady aerodynamic torques and unsteady generator torques. The model is first-order in time and linear in the turbine surge velocity and rotor speed; thus, it shall henceforth be referred to as a first-order linear model. An important feature of the model is that its coefficients can be computed from measurements obtained under steady conditions; no data from actual surge tests are required to obtain time-resolved torque and power predictions. The experiments span higher levels of unsteadiness than previous studies in the literature, with scaled amplitudes up to $A^* = A/D = 0.51$ and nondimensional surge velocities up to $u^* = fA/u_1 = 0.23$, where A is the surge amplitude, f is the surge frequency in radians per second, u_1 is the free-stream velocity, and D is the turbine diameter. By contrast, the highest values reported in the literature are $A^* = 0.13$ (Tran and Kim, 2016) and $u^* = 0.42$ (Wen, Tian, *et al.*, 2018) in simulations, and $A^* = 0.15$ (Sant *et al.*, 2015) and $u^* = 0.079$ (Mancini *et al.*, 2020) in experiments. These values are all relatively high compared to the motion amplitudes measured on the Hywind Demo floating offshore turbine, which in calm seas underwent average surge amplitudes of $A^* \approx 0.03$ and surge-velocity amplitudes of $u^* \approx 0.06$ (Skaare *et al.*, 2015). When the controller on the floating platform was removed, amplitudes of up to $u^* \approx 0.16$ were reported. The numerical simulations of Johlas *et al.* (2021) produced similar results, with average surge-velocity amplitudes of $u^* \approx 0.09$ and maximum values of $u^* \approx 0.23$ in higher-amplitude wave conditions. The findings in the present study may thus be generalized to FOWTs operating under extreme conditions, as well as novel airborne wind-energy systems and other emergent technologies. The combined analytical and experimental results presented in this work provide a foundation upon which questions regarding the influence of unsteadiness and nonlinearity, including the dependence of the mean torque and power on surge kinematics, may be more comprehensively investigated in future work.

The paper is structured as follows. In Section 2.2, a first-order linear model is derived that enables a disambiguation between aerodynamic and generator torques.

Its amplitude and phase characteristics are also analyzed. In Section 2.3, the experimental apparatus is described, and methods for computing the coefficients of the analytical model from measurements in steady conditions are given. Phase-averaged results from experiments with sinusoidal and trapezoidal surge-velocity waveforms are presented in Section 2.4, and the results are compared with model predictions. Finally, a discussion regarding model capabilities and limitations, nonlinear and unsteady effects, and application to full-scale wind turbines is provided in Section 2.5.

2.2 Analytical model

In this section, we derive a model for the torque generated by a surging horizontal-axis turbine from an ordinary differential equation that is first-order in time and linear in the turbine surge velocity and rotor speed (or rotation rate). We linearize the aerodynamic torque with respect to the inflow velocity and rotor speed, and combine it with a model for the generator torque to obtain a differential equation for the rotor speed of the turbine. We then derive transfer functions in the frequency domain to characterize the amplitude and phase relative to the surge-velocity waveform of the aerodynamic and generator torque. A notable advantage of this model is that the model coefficients can be extracted directly from torque and rotation-rate measurements of the turbine in steady conditions (i.e. without surge motions); these methods will be described in Section 2.3.4 for the turbine used in these experiments.

2.2.1 Aerodynamic-torque model

A first-order linear model for the aerodynamic torque can be derived using a local linearization with respect to the inflow velocity and rotor speed:

$$\tau_{aero} \approx \tau_0 + \left.\frac{\partial \tau}{\partial u}\right|_{u=u_1,\omega=\overline{\omega}} (u - u_1) + \left.\frac{\partial \tau}{\partial \omega}\right|_{u=u_1,\omega=\overline{\omega}} (\omega - \overline{\omega}), \tag{2.1}$$

where $u = u_1 + U(t)$ is the instantaneous inflow velocity relative to the turbine, $U(t)$ is the turbine surge velocity in a stationary frame of reference, ω is the rotor speed, and τ_0 is the steady aerodynamic torque, i.e. the mean torque measured on a stationary turbine at a wind speed of u_1. In this work, bars denote time averages over a single streamwise-motion oscillation period for time-dependent variables in the case of unsteady streamwise motion, while the subscript 0 denotes the value of a variable in the reference case corresponding to a steady inflow at speed u_1. We

then define the performance coefficients

$$K_\ell = \frac{\partial \tau}{\partial u}\Big|_{u=u_1,\omega=\overline{\omega}} \tag{2.2}$$

and

$$K_d = -\frac{1}{R}\frac{\partial \tau}{\partial \omega}\Big|_{u=u_1,\omega=\overline{\omega}}, \tag{2.3}$$

where R is the radius of the turbine. These coefficients qualitatively correspond to lift and drag terms in a blade-element expression for aerodynamic torque. Values for these constants can be obtained empirically from measurements of the turbine torque taken with a stationary turbine over a range of wind speeds and loading conditions (cf. Section 2.3.4). Simplifying the above expression yields the following model:

$$\tau_{aero} \approx K_\ell U - K_d R(\omega - \overline{\omega}) + \tau_0. \tag{2.4}$$

The accuracy of this aerodynamic model depends on whether τ is sufficiently linear in u and ω in the neighborhood of the steady operating condition ($u = u_1$ and $\omega = \overline{\omega}$). Since the model is inherently quasi-steady, its accuracy will also depend on whether any unsteady effects such as dynamic stall on the turbine blades are present.

2.2.2 Generator-torque model

The torque applied by the generator (τ_{gen}) in opposition to the aerodynamic torque (τ_{aero}) represents the torque that is converted to usable power at each instant in time. It thus also represents the mechanically measurable torque on the turbine shaft (τ_{meas}). The generator torque is not necessarily equal to the aerodynamic torque in the case of unsteady rotation, with any difference between the two inducing a change in the angular velocity of the rotor.

The equations of motion for a permanent-magnet generator are identical in principle to those for a permanent-magnet motor, which is frequently modeled as a first-order ordinary differential equation in time (Concordia, 1951):

$$\tau_{gen} = \tau_{meas} = K_2\frac{d\omega}{dt} + K_1\omega + K_0, \tag{2.5}$$

where K_2 is the moment of inertia of the generator about its rotational axis, K_1 is the generator constant, and K_0 is an empirical zero-speed offset. Since the generator torque is proportional to the current through the generator coils, K_1 and K_0 scale

inversely with the resistive load applied to the generator (Concordia, 1951). Hence, a higher resistive load applied to the generator corresponds to a lower physical load on the turbine. This formulation assumes that the generator is directly driven by the turbine; a gear-ratio scaling could be incorporated to map the rotor speed to the generator rotation rate for turbines with gearboxes.

Additionally, the generator model in its current form does not include any effects of control, such as tip-speed ratio control systems that are typically present in utility-scale wind turbines. For the purposes of this study, the use of a direct-drive generator with fixed resistive loading and no speed control simplify the modeling of the turbine dynamics and subsequent model validation against experimental data. However, the linear form of the model means that linear or linearized tip-speed ratio controllers can readily be incorporated using classical analytical techniques.

2.2.3 Governing equation and its transfer functions

The dynamics of a turbine under the influence of competing aerodynamic and generator torques are given by the swing equation (Stevenson and Grainger, 1994),

$$J\frac{d\omega}{dt} = \tau_{aero} - \tau_{gen}, \tag{2.6}$$

where J is the moment of inertia of the turbine, its shaft assembly, and the generator about the axis of rotation, and is thus in practice much larger than K_2. Deviations of the instantaneous aerodynamic torque away from equilibrium, if not immediately matched by the generator torque, will lead to a change in the rotor speed until the generator torque overcomes inertia and restores the torque balance. This implies that the torque measured by a torque transducer, and consequently the power measured from the generator, will lag behind the aerodynamic torque.

Substituting Equations 2.4 and 2.5 into the above relation, we arrive at the equation of motion

$$J\frac{d\omega}{dt} = (K_\ell U - K_d R(\omega - \overline{\omega}) + \tau_0) - \left(K_2\frac{d\omega}{dt} + K_1\omega + K_0\right). \tag{2.7}$$

In the limit of equilibrium, in which all time-derivatives are zero, the steady aerodynamic torque τ_0 must equal the generator torque, i.e. $\tau_0 = K_1\overline{\omega} + K_0$. We can therefore simplify the model into a more informative form:

$$J\frac{d\omega}{dt} = K_\ell U - K_d R(\omega - \overline{\omega}) - K_2\frac{d\omega}{dt} - K_1(\omega - \overline{\omega}). \tag{2.8}$$

The resulting model is conceptually similar to that of Fontanella *et al.* (2020), though in this work the linearization for the aerodynamic torque is obtained differently and the generator torque is an output, rather than an input, to the system. An additional benefit of the model in Equation 2.8 is that it requires no data from unsteady surge experiments to make time-resolved predictions, since all of its coefficients can be computed either from measurements in steady flow or from geometric properties of the turbine and generator. The model has the form of a linear time-invariant (LTI) system, which allows transfer functions of the aerodynamic and measured torques to be computed in order to quantify the phase and amplitude behavior of the system. Taking the Laplace transform of Equation 2.8 with respect to an arbitrary surge velocity U (input) and the resulting rotor speed ω (output) yields the transfer function

$$\frac{\omega(s)}{U(s)} = \frac{K_\ell}{(J + K_2)s + K_1 + K_d R}. \tag{2.9}$$

This transfer function has the form of a first-order low-pass filter with critical frequency $f_c = \frac{K_1 + K_d R}{J + K_2}$. Using this transfer function, we can also derive transfer functions for the aerodynamic and generator torques:

$$\frac{\tau_{aero}(s)}{U(s)} = K_\ell - K_d R\frac{\omega(s)}{U(s)} = K_\ell\frac{(J + K_2)s + K_1}{(J + K_2)s + K_1 + K_d R} \tag{2.10}$$

and

$$\frac{\tau_{gen}(s)}{U(s)} = (K_2 s + K_1)\frac{\omega(s)}{U(s)} = K_\ell\frac{K_2 s + K_1}{(J + K_2)s + K_1 + K_d R}, \tag{2.11}$$

which share the same critical frequency f_c. The frequency response can be computed from these transfer functions using the imaginary part of the Laplace variable s, i.e. $\mathrm{Im}(s) = f$. Phase and amplitude predictions from the model can thus be obtained analytically, and the mean torque is given by the steady-state value τ_0. Power can then be computed as $\mathcal{P} = \tau\omega$. The linear form of the model dictates that, for periodic surge motions with zero net displacement, the period-averaged mean torque and power are not functions of the surge motions. According to this model, then, unsteady surge motions will not affect the period-averaged power generation

of the turbine. The model thus forgoes the ability to predict time-averaged quantities in favor of an analytical formulation of the time-resolved turbine dynamics. The consequences of this tradeoff will be discussed in Section 2.5.2.

The transfer functions suggest that the relevant nondimensional parameters for the surge dynamics are the nondimensional surge velocity, $u^* = fA/u_1$, and the normalized surge frequency, $f^* = f/f_c$. The analysis suggests that the amplitude of the unsteady torque oscillations scales directly with u^*, with a frequency dependence dictated by f^*. Either the reduced frequency $k = fD/u_1$ or the nondimensional surge amplitude $A^* = A/D$ would complete the nondimensional parameterization by including the length scale of the turbine, but in contrast to suggestions in the literature (Bayati *et al.*, 2017; Wen *et al.*, 2017), these parameters do not appear to follow directly from the transfer-function formulation of the model.

2.3 Experimental methods

In this section, the experimental apparatus used to study the torque and power production of a wind turbine in periodic surge motions is described. First, the wind tunnel and turbine apparatus are described. Then, the parameter space explored in these experiments is presented, and the experimental procedure is outlined. Finally, methods for empirically determining values for the scaling coefficients of the analytical model derived in the previous section and an overview of sources of uncertainty are provided.

2.3.1 Experimental apparatus

Experiments were conducted in a large open-circuit fan-array wind tunnel at the Caltech Center for Autonomous Systems and Technologies (CAST). The fan array was composed of 2,592 computer fans arranged in two counter-rotating layers within a 2.88×2.88 m frame, mounted 0.61 m above the floor of the facility (cf. Figure 2.1). The open-air test section downstream of the fan array vented directly to the atmosphere, while the other three sides and ceiling of the arena were enclosed with walls or awnings to mitigate the effects of atmospheric disturbances. The experiments in this study were carried out at a free-stream velocity of $u_1 = 8.06 \pm 0.16$ ms^{-1}, corresponding to a diameter-based Reynolds number of approximately $Re_D = 6.13 \times 10^5$. The relevance of this study to Reynolds numbers typical of utility-scale wind turbines is discussed in Section 2.5.3. The turbulence intensity in the tunnel, represented by the standard deviation of the velocity fluctuations normalized

by the average streamwise velocity, was measured to be 2.20 ± 0.17%. These measurements were obtained with an ultrasonic anemometer (Campbell Scientific CSAT3B) placed at the hub height and streamwise zero position of the wind turbine. Because the facility was exposed to the atmosphere and experiments were conducted over a range of atmospheric conditions and times of day, temperature and relative-humidity readings were recorded with measurement precisions of ±1°C and ±5% from a portable weather station (Taylor Precision Products model 1731) so that the air density could be calculated accordingly.

The turbine apparatus was constructed on an aluminum frame (80/20 1515 T-slotted profile) that was bolted to the floor and secured with sandbags. The frame was 2.00 m long, 0.69 m wide, and 0.87 m tall. Two 2-m long rails with two ball-bearing carriages each (NSK NH252000AN2PCZ) were mounted on top of the frame, parallel to the streamwise direction and spaced 0.65 m apart in the cross-stream direction. A traverse was mounted on the ball-bearing carriages, which supported a 0.99-m tall, 0.038-m wide turbine tower. The wind-turbine shaft assembly was placed on top of this tower at a hub height of 1.97 m above the floor. The origin of the surge motions of the turbine was located 3.09 m downstream of the fan array, and the rails afforded a maximum surge stroke of 1.52 m upstream of the origin. A schematic of the apparatus and its position relative to the wind tunnel is given in Figure 2.1.

A three-bladed horizontal-axis wind turbine (Primus Wind Power AIR Silent X) with a rotor diameter of $D = 1.17$ m and hub diameter of 0.127 m was attached to a 25.4-mm diameter steel shaft supported by two axially mounted shaft bearings (Sealmaster NP-16T). The blade chord ranged from 100 mm at the root to 32 mm at the tip. The blades were constructed from a laminated carbon-fiber composite. A rotary encoder (US Digital EM2-2-4096-I) with a resolution of 4096 counts per revolution was attached between the shaft bearings. A rotary torque transducer (FUTEK TRS300, 20 Nm torque rating) was connected to the turbine shaft on one end and to the turbine generator (Primus Wind Power AIR 30, 48V) by means of a floating 19.0-mm diameter steel shaft on the other. The shaft assembly was surrounded by a 4.76-mm thick acrylic nacelle ($0.610 \times 0.152 \times 0.152$ m) with a slanted rear section intended to reduce bluff-body separation effects in the turbine wake. The estimated blockage of the swept area of the turbine and all support structures, relative to the fan-array surface area, was 14%.

The load on the turbine was controlled electrically with resistors. The three-phase

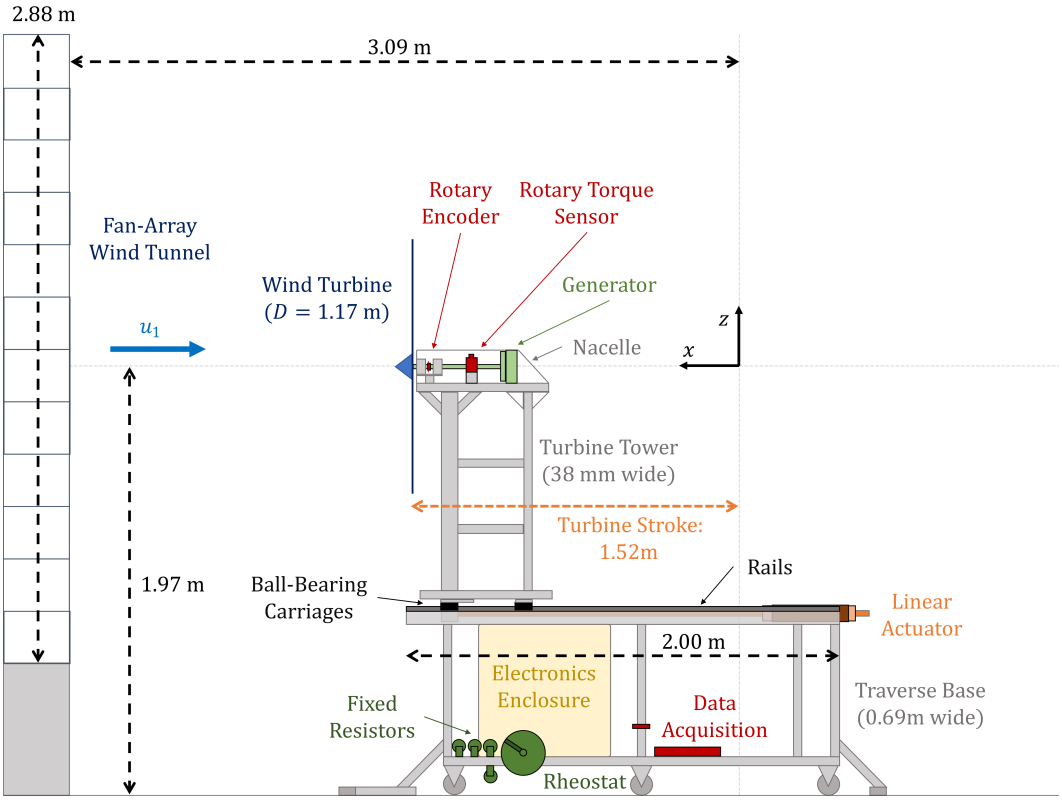

Figure 2.1: Schematic of the experimental apparatus, including fan-array wind tunnel (left) and surging turbine (center-right). The turbine is illustrated at its maximum upstream position relative to the origin. The estimated blockage of the swept area of the turbine and all support structures, relative to the fan-array surface area, is 14%.

alternating current produced by the generator was converted to DC by a bridge rectifier (Comchip Technology SC50VB80-G) and passed to a bank of resistors. Different combinations of fixed 10-Ohm resistors (TE Connectivity TE1000B10RJ) in series or parallel and an 8-Ohm rheostat (Ohmite RRS8R0E) were used to achieve a range of loading conditions that spanned the operational envelope of the turbine. An emergency short-circuit switch built from a solid-state relay (Crydom D1D12) and a 12-A fuse (Schurter 4435.0368) were included in the circuit for safety purposes.

The turbine traverse was driven in the streamwise direction by a piston-type magnetic linear actuator (LinMot PS10-70x320U-BL-QJ). Its sliding cylinder was attached to the traverse at rail height and its stator was mounted to the downstream end of the frame. The motions of the traverse were controlled by a servo driver (LinMot E1450-LU-QN-0S) with an external position sensor (LinMot MS01-1/D) mounted

along one of the two rails for increased repeatability. Power for the system was provided by a step-up transformer (Maddox MIT-DRY-188). Motion profiles were loaded onto the driver, and a TTL pulse was used to start each successive motion period. In these experiments, the maximum surge velocity was $U = 2.40$ ms^{-1} and the maximum surge acceleration was $\frac{dU}{dt} = 23.7$ ms^{-2}, while the average absolute position error was 0.68 mm and the average absolute velocity error was 8.33×10^{-3} ms^{-1}.

Data were collected from the rotary encoder and torque transducer using a data acquisition card (National Instruments USB-6221), as well as an amplifier (FUTEK IAA100) for the raw torque voltage signals. Data collection occurred at a sampling rate of 1 kHz. A LabVIEW control program coordinated data collection and triggering for the linear actuator. It was also used to adjust the resistance of the rheostat remotely via a stepper motor (Sparkfun ROB-13656). After each experiment, the program converted the raw voltage signals from the amplifier to dimensional values by interpolating between calibrated points, and it performed a fourth-order central-difference scheme on the angular measurements from the encoder to obtain a rotation-rate signal. Furthermore, the measured torque signals were filtered using a sixth-order Butterworth filter with a cutoff frequency of 100 Hz to reduce the influence of electrical noise.

2.3.2 Experimental parameters

The apparatus described in the previous section was used to investigate the unsteady torque and power production of a wind turbine actuated in surge motions. Surge amplitudes between $A = 0.150$ and 0.600 m ($A^* = A/D = 0.128$ and 0.514) were tested in combination with motion periods between $T = 0.5$ and 12 s. These combinations resulted in reduced frequencies $k = fD/u_1$ between 0.079 and 1.821 and nondimensional surge velocities $u^* = fA/u_1$ between 0.039 and 0.234. The specific combinations of A and T explored in this study, and their respective values of u^*, are given in Table 2.1. Sinusoidal and trapezoidal surge-velocity waveforms served as motion profiles for these experiments. The trapezoidal waveforms consisted of alternating segments of constant acceleration and constant velocity. The relative duration of the constant-acceleration phases was parameterized by ξ, defined as the total time of nonzero acceleration in a single cycle divided by the cycle period. Hence, $\xi = 0$ corresponded to a square wave, while $\xi = 1$ corresponded to a triangle wave. The types of waveforms used in these experiments are shown in Figure 2.2.

u^*	$A^* = 0.128$	$A^* = 0.257$	$A^* = 0.385$	$A^* = 0.514$
$T = 12$ s	–	–	–	0.039
$T = 6$ s	–	–	–	0.078
$T = 3$ s	–	–	–	0.156
$T = 2$ s	–	0.117	0.175	0.234
$T = 1$ s	–	0.234	–	–
$T = 0.5$ s	0.234	–	–	–

Table 2.1: Combinations of nondimensional amplitude $A^* = A/D$ and motion period T tested in this study, tabulated with their respective nondimensional surge velocities u^*.

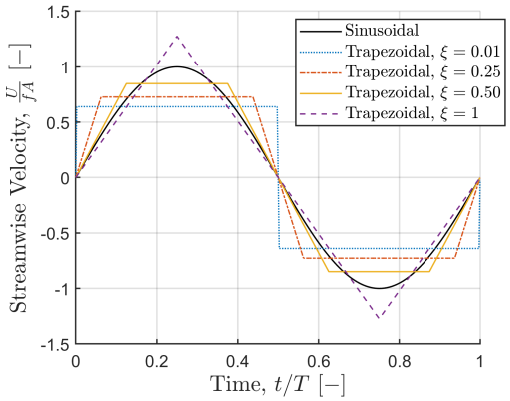

Figure 2.2: Surge-velocity waveforms used in these experiments. Sinusoidal profiles and four types of trapezoidal profiles (parameterized by ξ) were tested.

The wind turbine was tested with resistive loads of 7.39, 7.48, 9.80, 10, 20, and 40 Ohms. The first three loads were attained using the rheostat and fixed resistors, and the second three were achieved using fixed 10-Ohm resistors in series. These corresponded to steady tip-speed ratios $\lambda_0 = R\omega_0/u_1$ between 5.21 ± 0.22 and 8.77 ± 0.35, and coefficients of power $C_{p,0} = \mathcal{P}_0/\frac{\pi}{2}\rho R^2 u_1^3$ between 0.176 ± 0.010 and 0.288 ± 0.013. A summary of the loading conditions and their corresponding steady nondimensional parameters is given in Table 2.2. Additionally, a power curve consisting of a collection of measurements at different wind speeds and loading conditions is shown in Figure 2.3. Each of these steady measurements was conducted 3.09 m downstream of the fan array and over a duration of at least two minutes.

Resistive Load	7.39 Ω	7.48 Ω	9.80 Ω	10 Ω	20 Ω	40 Ω
Case Identifier	●	●	●	●	●	●
λ_0, sinusoidal cases	5.21 ± 0.22	5.34 ± 0.22	6.11 ± 0.25	6.21 ± 0.25	7.72 ± 0.31	8.64 ± 0.35
λ_0, trapezoidal cases	–	–	6.11 ± 0.25	6.27 ± 0.26	7.67 ± 0.31	8.77 ± 0.35
$C_{p,0}$, sinusoidal cases	0.261 ± 0.013	0.270 ± 0.012	0.264 ± 0.011	0.288 ± 0.013	0.250 ± 0.012	0.181 ± 0.009
$C_{p,0}$, trapezoidal cases	–	–	0.264 ± 0.011	0.286 ± 0.014	0.249 ± 0.012	0.176 ± 0.010
K_ℓ $\left[\text{kg}\frac{\text{m}}{\text{s}}\right]$, sinusoidal cases	0.458	0.456	0.445	0.444	0.422	0.409
K_ℓ $\left[\text{kg}\frac{\text{m}}{\text{s}}\right]$, trapezoidal cases	–	–	0.445	0.443	0.423	0.407
K_d $\left[\text{kg}\frac{\text{m}}{\text{s}}\right]$, sinusoidal cases	0.0262	0.0264	0.0276	0.0278	0.0302	0.0317
K_d $\left[\text{kg}\frac{\text{m}}{\text{s}}\right]$, trapezoidal cases	–	–	0.0276	0.0279	0.0301	0.0319
K_1 $\left[\text{kg}\frac{\text{m}^2}{\text{s}}\right]$	–	0.0141	0.0111	0.0112	0.00649	0.00376
K_0 [Nm]	–	0.153	0.125	0.119	0.0850	0.0676

Table 2.2: Performance characteristics and model constants for the six loading conditions investigated in this study. The values of K_1 and K_0 were not measured directly for the 7.39 Ω case; the values from the 7.48 Ω case were used instead.

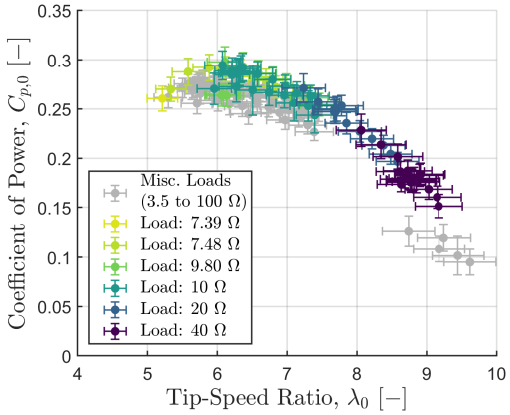

Figure 2.3: Steady power curve for the turbine used in this study, measured over a range of resistive loads (3.5 to 100 Ω) and wind speeds (6.05 to 12.09 ms^{-1}).

2.3.3 Experimental procedure

Experiments were conducted in the CAST fan-array wind tunnel between May and July 2021. A zero-offset reading was taken for the torque sensor at the start of every day of measurements. To bring the turbine from rest to its prescribed operating condition, a higher wind speed was initially applied for at least two minutes to mitigate the effects of startup hysteresis in the shaft assembly. Each unsteady experiment was paired with a corresponding steady reference case, conducted within one hour of the unsteady case to minimize the influence of changing atmospheric conditions. The steady measurements were taken 3.09 m downstream of the fan array, defined as $x = 0$ (where x is positive in the upstream direction). In the unsteady experiments, the turbine moved between $x = 0$ and $x = 2A$ at a prescribed frequency $f = 2\pi/T$. Each unsteady test began with five to ten startup periods to allow the system to reach cycle-to-cycle equilibrium. After these initial cycles, torque and rotation-rate measurements were recorded over 100 successive motion periods. For the shortest motion periods ($T = 0.5$ s), 200 motion periods were measured. The torque data were filtered and numerical derivatives of the angular-encoder readings were obtained, and these data were used to compute temporal means and time-resolved, phase-averaged profiles. The amplitudes and phases of these phase-averaged profiles were calculated by means of a fast Fourier transform. Finally, the aerodynamic torque was inferred via Equation 2.6, where τ_{gen} was supplied by the phase-averaged measured torque and $\frac{d\omega}{dt}$ was computed using a second-order central differencing scheme and was filtered using a sixth-order Butterworth filter with a cutoff frequency of 100 Hz to attenuate numerical-differentiation errors.

2.3.4 Computing model constants

To compare the experimental results with the model derived in Section 2.2, empirical methods were developed to compute the coefficients of the model. Both the generator constants K_1 and K_0 and the aerodynamic model coefficients K_ℓ and K_d were computed from steady torque measurements, without requiring any information from unsteady tests.

The generator constants K_1 and K_0 were obtained by applying a constant resistive load to the turbine and measuring torque over a range of wind speeds. From these data, linear fits for the generator torque as a function of rotor speed could be extracted for each loading condition. The fit coefficients corresponded directly with the generator constants K_1 and K_0 from Equation 2.5. The calculated values are

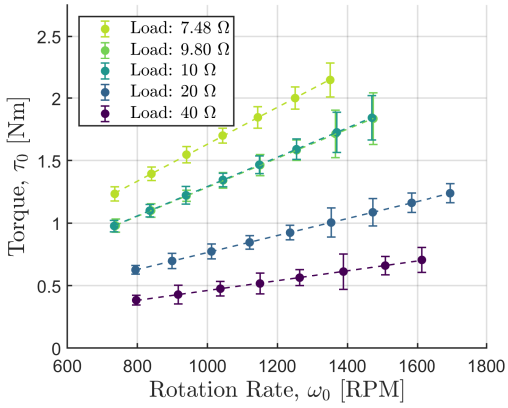

Figure 2.4: Measured torque from steady experiments with different resistive loads, plotted against rotor speed. The two coefficients from the linear fits (shown as dashed lines, $R^2 > 0.999$) correspond to the generator constants K_1 and K_0.

reported in Table 2.2 above, and, as expected for this type of generator, they scaled inversely with resistance. The accuracy of the generator-torque model depends primarily on the linearity of the generator within the typical operating conditions of the turbine. As evidenced by the data and linear fits shown in Figure 2.4, the generator used in this study fulfilled this condition well ($R^2 > 0.999$ in all cases).

The same steady torque data were used to compute the aerodynamic model coefficients K_ℓ and K_d. The steady torque data was plotted as a three-dimensional set of points with respect to the wind speed and rotor speed, and a second-order polynomial surface fit was applied to the points. The fit equation gave an analytical expression for the partial derivatives with respect to u_1 and ω_0 at any point, from which the coefficients K_ℓ and K_d were calculated by means of the definitions given in Equations 2.2 and 2.3. The accuracy of the method as a quasi-steady aerodynamic representation is limited by the topology of the torque surface and the fidelity of the applied surface fit. For the turbine used in this study, the second-order polynomial surface (shown in Figure 2.5) was only weakly quadratic and fit the data with $R^2 > 0.999$, so the model was expected to perform well over the range of conditions tested in these experiments.

The moment of inertia of the generator was estimated from manufacturer specifications of the mass and radius of its rotor to be $K_2 = 6.96 \times 10^{-4}$ kg m^2. The moment of inertia of the turbine and shaft assembly (including the generator), J, could be estimated in this manner as well. However, given the number of parts and nontrivial geometries in the assembly, a more empirical approach was taken. A 3D-printed spool with a diameter of 6 cm was attached to the turbine shaft, and the generator

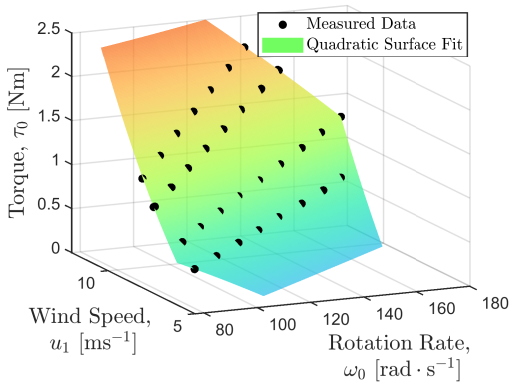

Figure 2.5: Measured torque from steady experiments with different resistive loads, plotted against both wind speed and rotor speed. A second-order polynomial surface ($R^2 > 0.999$) was fitted to the points to facilitate the computation of the linearized sensitivities K_ℓ and K_d.

circuit was disconnected. A string was wrapped around the spool and connected to a weight, suspended from the turbine tower by means of a pulley. The weight was dropped ten times, and using the average measured torque and a fit based on the measured rotation-rate signal and the equation of motion of the system, an average moment of inertia was found to be $J = 0.0266 \pm 0.0008$ kgm^2. This value aligned with the results of geometric estimates.

Thus, the only information required to obtain first-order predictions of the dynamics of a surging turbine were two moments of inertia and a series of steady torque measurements over a range of rotor speeds and wind speeds. Using the constants obtained from these prerequisites, the amplitude and phase of the aerodynamic and measured torques could be calculated analytically using the transfer functions given in Equations 2.10 and 2.11. To predict the time-resolved dynamics of the turbine for general surge-velocity waveforms, a numerical integration of the model as an initial-value problem was required. This was carried out using a fourth-order Runge-Kutta integration scheme with a time step of 10^{-3} s over ten motion periods, with the rotor speed initialized at $\omega\big|_{t=0} = \omega_0$. The final period served as a representation of the steady-state model prediction.

2.3.5 Sources of uncertainty

Before the results of the experiments can be discussed in detail, the nature of the experimental facility requires a consideration of the sources of uncertainty in the measurements. These sources can be divided into two types: those that occurred over short time scales relative to a single test case, and those that occurred over

longer time scales and were thus not captured in the error estimates computed from each data set.

Sources of uncertainty that occurred over short time scales contributed to the error bounds that will be shown in the figures in the following section. The standard deviation of the wind speed in the tunnel, measured over five minutes, was 2.20 ± 0.17% of the average wind speed. This variability includes fluctuations due to turbulence and short-period fluctuations in the bulk flow velocity due to atmospheric disturbances. Though external winds were generally stronger during the afternoon, no corresponding increase in torque or rotation-rate uncertainty was evident for measurements conducted under these conditions. Therefore, despite the exposure of the facility to local atmospheric conditions, gusts and pressure fluctuations had a small influence on the results compared to other factors. Electrical noise from the torque sensor also contributed to measurement uncertainties, though these effects were reduced by the 100-Hz lowpass filter applied to the raw torque signal. Lastly, a slight misalignment in the turbine shaft was responsible for small variations in the measured torque within every full rotation of the turbine. These intracycle variations accounted for much of the uncertainty on the mean-torque measurements, and were occasionally visible in the phase-averaged torque and rotation-rate profiles. However, since their time scales were dictated by the rotor speed and were thus one to two orders of magnitude faster than the time scales of the surge oscillations, they did not directly affect the surge dynamics that were the focus of this study.

The open-air nature of the facility, however, meant that changing conditions throughout the day and across multiple days introduced additional sources of uncertainty that were not explicitly captured in the error estimates computed directly from each data set. Measurements of the wind speed at a single location over temperatures between 24.7 and 31.9°C showed a mild dependence of wind speed on temperature (R^2 = 0.535), resulting in a 3.0% overall difference in wind speed. Given that temperatures in the facility ranged from 16.8 to 32.6°C across all experiments, a linear model would predict an uncertainty in the wind speed of ±3.2%. However, since no wind-speed measurements were taken at temperatures below 24°C, the fidelity of a linear model across the entire range of temperatures could not be directly confirmed. Because of these uncertainties, no temperature corrections were applied *a posteriori* to the wind-speed data. This source of uncertainty complicated comparisons of mean torque and power between test cases, though this was to some extent ameliorated by normalizing the mean data from unsteady tests by a temporally

proximal steady case. By contrast, the amplitude and phase depended primarily on the surge kinematics, which were comparably repeatable on account of the precision of the linear actuator, and were thus less affected by relatively small differences in wind speed.

In addition, the zero offset of the torque sensor exhibited a hysteretic dependence on temperature. To test this, the torque sensor was left in the facility for a period of 28 hours, and a voltage measurement was recorded every ten minutes. After the measurements were completed, during which the temperature in the facility ranged from 19.5 to 33.3°C, the difference between the initial and final voltage measurements corresponded to a torque difference of 0.014 Nm. Compared to the average torque measurements reported in this study, this represented a total shift of 1.2 to 2.9%. Since the torque sensor was zeroed at the start of every day of experiments, this served as an upper bound on the uncertainty introduced by the zero-offset drift. This additional uncertainty again primarily obfuscated the mean measured torque, without affecting the amplitude and phase.

Finally, the intracycle torque variations described previously increased in magnitude in the tests conducted during June and July 2021, increasing the reported experimental error of the longest-period tests (T = 6 and 12 s). Higher temperatures and direct sunlight on the apparatus during these experiments may have caused the shaft assembly materials to expand, thereby exacerbating the rotational asymmetries in shaft friction responsible for the torque variations. This temperature dependence of friction could have influenced both the mean torque and power as well as their amplitude.

To demonstrate the cumulative effect of these sources of uncertainty, a series of 13 test cases, composed of six sinusoidal motion profiles at two different loading conditions, and a single sinusoidal motion profile at a third loading condition, was tested twice at different times of day. All of these data were included in the results presented in the following section for visual comparison. These thus serve as qualitative indicators of the influence of environmental conditions and system hysteresis on the results and analysis. As suggested previously, the effects of these factors will be most evident in the mean torque and power measurements, and to a lesser extent in the measured torque amplitudes.

2.4 Experimental results

Experiments were conducted with 32 different sinusoidal waveforms over 6 loading conditions and 42 different trapezoidal waveforms over 4 loading conditions and 4 values of the waveform parameter ξ. As mentioned previously, 13 of the sinusoidal cases were repeated at different times of day to convey the additional uncertainty due to changing conditions in the facility: 6 at $\lambda_0 = 6.11$, 6 at $\lambda_0 = 8.64$, and 1 at $\lambda_0 = 7.72$. The data from these experiments are presented in this section, in terms of torque amplitude, torque phase, and mean power. A selection of phase-averaged power measurements and their associated model predictions are provided as Figures A.1 through A.5 in Appendix A.1.

2.4.1 Torque amplitude response

Aerodynamic-torque amplitudes, referenced to their respective surge-velocity amplitudes $U = fA$, are shown for sinusoidal and trapezoidal waveforms in Figure 2.6, while similar plots for the generator (measured) torque are given in Figure 2.7. The transfer-function magnitudes were normalized by the steady torque for each case τ_0 and the wind speed u_1. The aerodynamic torque was predicted by the model to increase in amplitude and asymptotically approach a maximum value above $f^* \approx 1$. The generator torque predictions showed behavior more characteristic of a low-pass filter, where the amplitude decreased with increased frequency. The data for both the aerodynamic torque and generator torque showed good agreement with the model predictions for low values of f^*, except for the two lowest tip-speed ratios in the sinusoidal-waveform cases. Excluding these tip-speed ratios and the highest three values of f^*, the average relative error between the model predictions and measured data was 2.79% and 2.13% for the aerodynamic and generator torque amplitudes, respectively. At the two lowest tip-speed ratios, the turbine was close to stall, a flow regime not accounted for in the model. Decreasing the resistive load by 0.1 Ω in the steady case caused the turbine to stall completely, slowing to a rotor speed of less than 10 rads^{-1}. Unsteady tests undertaken at these two loading conditions with higher amplitudes and frequencies than those shown also caused the turbine to stall completely. Therefore, it was likely that the downstream surge motions caused the turbine to experience stall due to a reduction in the incident wind velocity relative to the turbine, thus decreasing the amplitude of the torque oscillations. A less severe decrease in amplitude could be seen at steady tip-speed ratios close to $\lambda_0 \approx 6.2$, which represented the optimal operating condition for the turbine (cf. Figure 2.3). At normalized frequencies approaching $f^* = 1$, the amplitude began to drop below

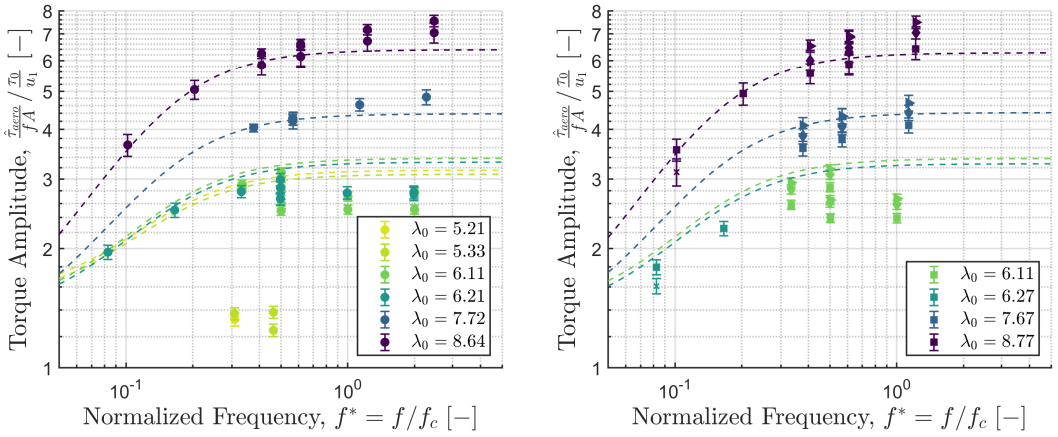

(a) (b)

Figure 2.6: Aerodynamic torque amplitude data (markers), compared with model predictions (dashed lines), for (a) sinusoidal and (b) trapezoidal surge-velocity waveforms. For these and all following figures in this section, circular markers (○) represent sinusoidal waveform cases, while non-circular markers represent trapezoidal-waveform cases with ξ = 0.01 (×), 0.25 (□), 0.5 (◇), and 1 (▷).

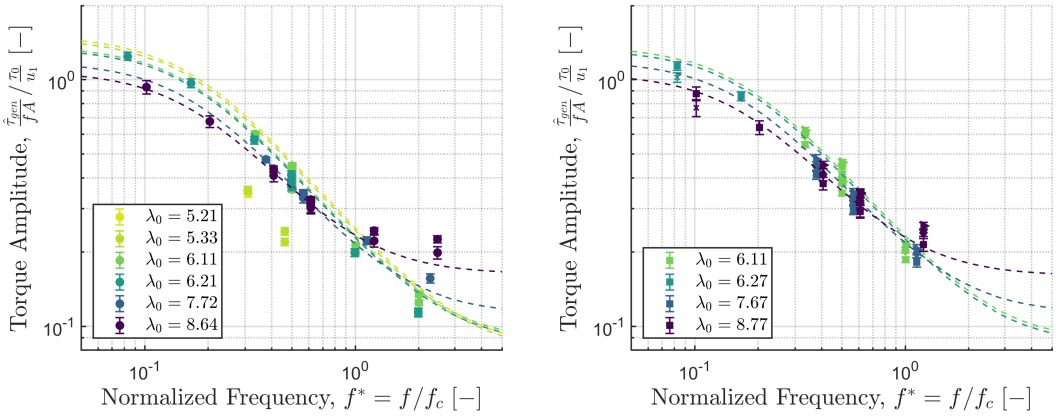

(a) (b)

Figure 2.7: Generator torque amplitude data (markers), compared with model predictions (dashed lines), for (a) sinusoidal and (b) trapezoidal surge-velocity waveforms.

the model prediction. Given the evidence of stall at lower tip-speed ratios, it is likely that this deviation was an effect of stall onset along a portion of the turbine blades as well. This conjecture is also in agreement with the simulations of Tran and Kim (2016), who suggested that large surge motions at low to intermediate tip-speed ratios can cause stall to occur at the roots of the turbine blades and propagate radially outwards.

In contrast to the decreases in amplitude observed at low tip-speed ratios, the

amplitudes at higher normalized frequencies ($f^* > 1$) and tip-speed ratios above the optimal value increased above the model predictions. Increases in amplitude were also correlated with increasing ξ (i.e. increasing proportions of streamwise acceleration within each motion cycle) in the trapezoidal-waveform experiments. The higher tip-speed ratios implied that the local angle of attack along the turbine blades was lower in these cases, reducing the likelihood that these increases in amplitude were due to stall phenomena. Since the model appeared to accurately capture the torque amplitudes at lower frequencies, it could be hypothesized that these trends were evidence of additional dynamics that became more salient at higher levels of unsteadiness. The specific nature of these dynamics cannot be identified definitively in the absence of flow measurements or a higher-order model for validation, but the present measurements do permit speculation as to the source of the observed discrepancies with the model. These considerations will be discussed in Section 2.5.2.

2.4.2 Torque phase response

The aerodynamic and generator phase-response data for the same experimental cases shown in Figures 2.6 and 2.7 are given in Figures 2.8 and 2.9 and are compared with model predictions. The generator torque phase lagged behind the forcing signal $U(t)$ across all tested frequencies, while the aerodynamic torque phase led the forcing signal for all cases except those at the lowest two tip-speed ratios. Excluding the lowest two tip-speed ratios, the average difference between the model predictions and measured data was 3.59° and 3.21° for the aerodynamic and generator torque phase, respectively. The phase in the anomalous cases showed an approximately 20° lag relative to the predictions of the model, suggesting again that the turbine blades were experiencing the effects of stall under these conditions. The tests conducted at higher tip-speed ratios followed the qualitative trends predicted by the model, though the model slightly overpredicted the aerodynamic and generator torque phase by around 6° at low normalized frequencies. Unlike the torque amplitude, the torque phase was relatively insensitive to changes in the trapezoidal-waveform parameter ξ.

2.4.3 Mean power

While the amplitude and phase responses of the aerodynamic and generator torque were nontrivial, the first-order linear model predicted zero change in the mean torque and power for all surge motions. The period-averaged measured torque and power, however, diverged from these predictions as the surge motions became more

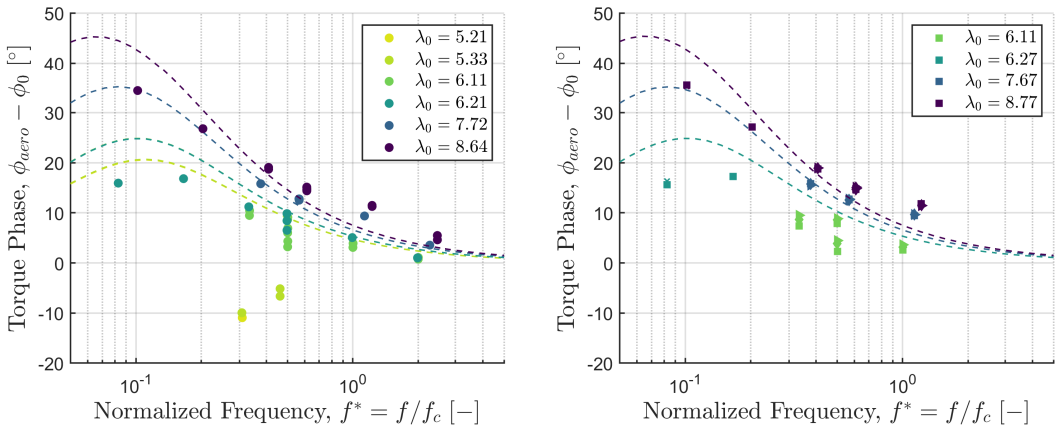

(a) (b)

Figure 2.8: Aerodynamic torque phase data (markers), compared with model predictions (dashed lines), for (a) sinusoidal and (b) trapezoidal surge-velocity waveforms.

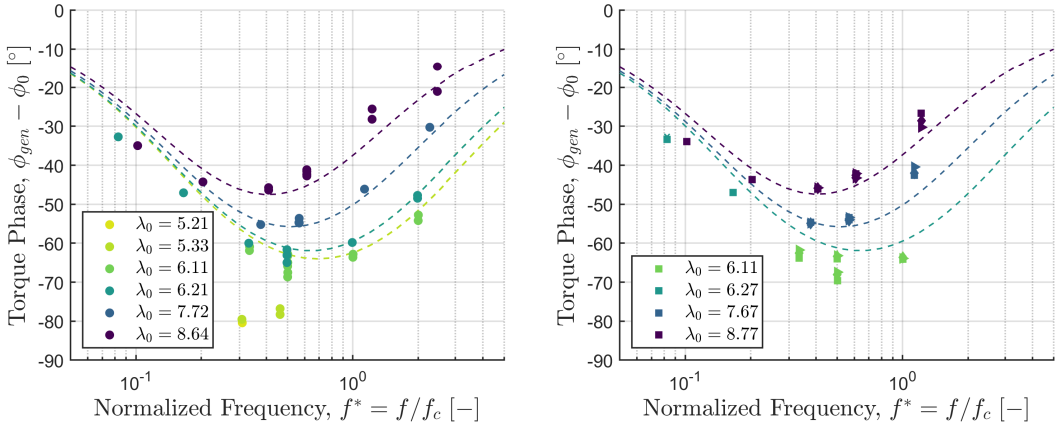

(a) (b)

Figure 2.9: Generator torque phase data (markers), compared with model predictions (dashed lines), for (a) sinusoidal and (b) trapezoidal surge-velocity waveforms.

pronounced. When plotted against the nondimensional surge velocity u^* and a nondimensional surge acceleration defined as $a^* = f^2 A / \frac{u_1^2}{D}$ (cf. Figure 2.10), the normalized period-averaged measured power $\overline{\mathcal{P}}/\mathcal{P}_0$ diverged from unity at higher levels of unsteadiness. For tip-speed ratios at or below the optimal operating point, the average power decreased with increasing surge velocity and acceleration. This was especially the case for the lowest two tip-speed ratios tested; at higher surge velocities than those shown, the turbine stalled completely and the normalized average power dropped nearly to zero. It is thus reasonable to infer that the occurrence of stall along portions of the turbine blades was responsible for the decrease in power observed at lower tip-speed ratios and higher surge velocities.

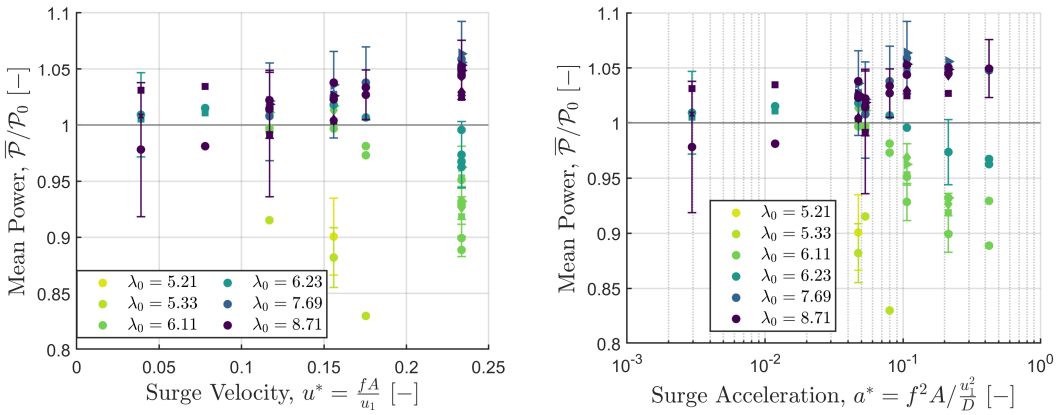

(a) (b)

Figure 2.10: Period-averaged measured power $\overline{\mathcal{P}}$, normalized by the reference steady power $\mathcal{P}_0$, plotted for all cases against (a) the nondimensional surge velocity u^* and (b) the nondimensional surge acceleration a^*. Circular markers (○) represent sinusoidal waveform cases; non-circular markers represent trapezoidal-waveform cases with $\xi = 0.01$ (×), 0.25 (□), 0.5 (◇), and 1 (▷). For the sake of clarity, error bars are only plotted for every sixth point.

For higher tip-speed ratios, the average power increased with increasing surge velocity and acceleration, with a maximum measured value of $\overline{\mathcal{P}}/\mathcal{P}_0 = 1.064 \pm 0.045$. The increases appeared well-correlated with these surge parameters, whereas the specific type of waveform did not appear to significantly affect the results. Furthermore, the apparent consistency in trend over a range of testing conditions and times of day suggests that these results cannot simply be attributed to long-period variations in the conditions in the facility. These trends were similar to those shown by Farrugia *et al.* (2016) (cf. Fig. 8 in their paper) and Wen *et al.* (2017) (cf. Fig. 15b in their paper), though those studies focused on the reduced frequency as the unsteady parameter of interest. These large deviations from the predictions of the first-order linear model will be discussed in the following section.

2.5 Discussion

2.5.1 Performance of the model

As shown in Sections 2.4.1 and 2.4.2, as well as in the results presented in Appendix A.1, the first-order linear model was able to capture trends in amplitude and phase for torque and power, using only *a priori* measurements from the turbine under steady-flow conditions. The time-resolved model predictions for power were qualitatively similar to the measured phase-averaged data shown in Figures A.1

through A.5 for all surge-velocity waveform types, both sinusoidal and trapezoidal. The model was also able to account for the effects of changes in the aerodynamic and generator parameters of the system, particularly through the characteristic frequency f_c. These results demonstrated that while the aerodynamic torque tends to increase in amplitude with frequency up to $f^* \approx 1$ and leads the input surge-velocity waveform, the generator acts as a low-pass filter on the measured torque and power, leading to decreases in amplitude and phase lags.

The nontrivial phase prediction is particularly noteworthy, since previous studies showed little consensus in the phases of their torque and power data. The existing quasi-steady models in the literature (e.g. Mancini *et al.*, 2020; Johlas *et al.*, 2021) predicted zero phase difference with the input surge-velocity waveform. The present results have demonstrated that the aerodynamic and generator characteristics of the system produce phase differences of up to 60°, with greater differences observed in cases at low tip-speed ratios where stall is purported to have an effect. The success of the first-order linear model in recovering these trends over a wide range of loading conditions, surge frequencies, and surge amplitudes suggests that the model can help explain the variation in phase trends reported in the literature, and serve as an analytical foundation for future studies involving the time-resolved dynamics and control of surging turbines.

2.5.2 Discrepancies between measurements and model predictions

Though the model showed good agreement with the measured data in terms of amplitude and phase, some discrepancies were still evident. The model tended to overpredict the torque amplitude at low tip-speed ratios and high surge frequencies and underpredict the torque amplitude at high tip-speed ratios and high surge frequencies. The model also did not correctly predict the trends in period-averaged power at high surge velocities. These deviations and their implications merit further discussion.

The observed decreases in torque amplitude and phase, as well as period-averaged power, were attributed to the onset of stall on the turbine blades. The turbine was close to static stall at the two lowest tip-speed ratios tested, as any slight decrease in the resistive load or inflow velocity would cause its rotor speed to fall to nearly zero. This observed behavior is in accordance with the assumption that the turbine blades were designed to maximize their lift-to-drag ratio near the optimal operating

condition of $\lambda_0 \approx 6.2$, as lower tip-speed ratios would imply higher induced angles of attack that would bring the blade sections closer to the static stall angle. If this was the case, then at tip-speed ratios near or below the optimal operating condition of the turbine, increased induced angles of attack on the blades through the addition of unsteady surge motions could be expected to increase the local angle of attack above the static stall angle. This explanation aligns well with the observed decreases in the amplitude, phase and time-averaged responses of the system with increasing normalized frequency and decreasing tip-speed ratio. It would be useful to verify this conjecture with flow measurements or numerical simulations in the future.

The discrepancies in which the model underpredicts the measured data, by contrast, have physical sources that are more difficult to identify given the present data. For the two highest tip-speed ratios tested, the torque amplitude data exceeded the model predictions at higher normalized frequencies. Furthermore, in the trapezoidal-waveform cases shown in Figure 2.6b, the torque amplitudes for cases with identical surge frequencies and amplitudes consistently increased with increasing ξ (i.e. an increasing proportion of surge acceleration within each motion cycle). These increases in amplitude run counter to the predictions of classical unsteady-aerodynamic theory for an isolated, two-dimensional airfoil. The Sears function, an analytical transfer function for the unsteady lift response of a two-dimensional airfoil in a transverse gust, predicts a decrease in the lift amplitude relative to the quasi-steady case for a turbine blade section undergoing surge motions (Sears, 1941). A reduction in torque amplitude with increasing reduced frequency would thus be expected if the Sears function is a sufficient model for the unsteady aerodynamics of a surging turbine. Since the opposite trend is observed in the data, additional dynamics must be involved to account for the divergence from the model predictions, such as spanwise flow along the blades, blade-wake interactions, or other unsteady effects.

The divergence in the period-averaged power data from the model further underscores the need to appeal to additional dynamics. The linear nature of the model dictated that the period-averaged power for a periodically surging turbine would never differ from the steady reference power, irrespective of surge kinematics. Thus, the increases in the period-averaged power over the steady reference case observed at higher levels of unsteadiness must have been the result of effects that were not accounted for in the linear model.

Either the assumption of linear aerodynamics or the assumption of quasi-steady

aerodynamics could be called into question to explain the observed enhancements in torque amplitude and period-averaged power. For instance, the quasi-steady model of Johlas *et al.* (2021), which is derived from the scaling of power with the cube of the incident wind velocity and is thus nonlinear, predicts that the period-averaged power should scale with $(u^*)^2$. This trend qualitatively agrees with the average-power data shown in Figure 2.10a, though their model does not capture the time-resolved turbine dynamics. This observation suggests that an incorporation of the nonlinear dependence of power on u^3 into the first-order linear model could better account for the improvements in period-averaged power with increasing u^*.

Alternatively, the enhancements in torque amplitude and average power in the unsteady cases at high tip-speed ratios could be the result of unsteady fluid mechanics. As a proxy for flow unsteadiness, we briefly consider the surge acceleration. Returning to the apparently systematic increases in torque amplitude with increasing ξ, we recall that higher values of the parameter ξ corresponded to waveforms in which segments of constant acceleration occupied a larger fraction of each period (with $\xi = 1$ representing one half-cycle of constant acceleration, followed by one half-cycle of constant deceleration). Therefore, the increase in torque amplitude with ξ could be interpreted as an effect of surge acceleration. To extend this point further, the relative error between the measured and modelled torque amplitude was plotted with respect to the nondimensional surge velocity u^* and surge acceleration a^* in Figure 2.11. While the data in Figure 2.11a became multi-valued at the highest value of u^*, more uniform trends were evident when the data were plotted against a^* in Figure 2.11b, suggesting that the surge acceleration was a more robust indicator of the difference between measured and predicted torque amplitudes. Finally, the apparent lack of scatter in the period-averaged power data when plotted against a^* might similarly suggest that the surge acceleration could play a systematic role in producing the increases in average power, though the strength of this argument is limited by the fact that the definition of a^* involves the same kinematic parameters as that of u^*. The role of surge acceleration cannot necessarily be accounted for in a linear sense, since adding a linear acceleration-dependent term to the existing model would introduce a 90° phase lead that would disrupt the accuracy of the model with respect to phase (cf. Figures 2.8 and 2.9). Still, these observations do suggest that the discrepancies with respect to the first-order linear model are systematic, and that the physics behind these systematic deviations may include unsteady effects.

Flow-field measurements at both the blade and rotor scale would greatly facilitate

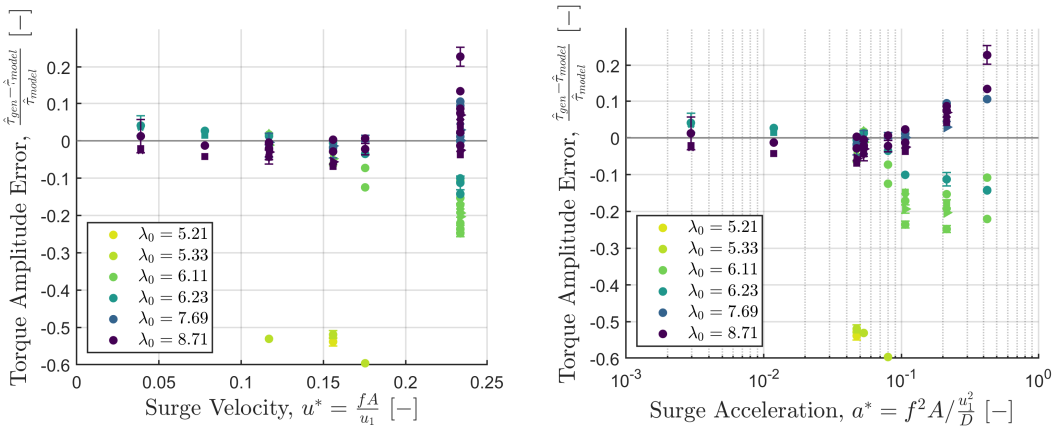

(a) (b)

Figure 2.11: Relative error between measured and modelled torque amplitudes, plotted for all cases against (a) the nondimensional surge velocity u^* and (b) the nondimensional surge acceleration a^*. Circular markers (○) represent sinusoidal waveform cases; non-circular markers represent trapezoidal-waveform cases with $\xi = 0.01$ (×), 0.25 (□), 0.5 (◇), and 1 (▷). For the sake of clarity, error bars are only plotted for every sixth point.

the identification of unsteady contributions to the turbine dynamics. El Makdah *et al.* (2019) provided some evidence of unsteady effects in their investigations of the wake structure of an accelerating low-inertia rotor, which were conducted in a water channel using planar particle-image velocimetry. A similar study at higher Reynolds numbers and involving periodic rather than unidirectional surge motions, and with the first-order linear model derived in this study as a baseline for torque and power comparisons, would be informative for establishing the relative influence of nonlinear and unsteady effects. Without such quantitative flow measurements, however, it is difficult to definitively conclude at this stage that either quasi-steady nonlinear effects or purely unsteady aerodynamic effects are responsible for the observed enhancements in torque amplitude and period-averaged power. The main conclusion to be drawn from these speculative considerations is that enhancements in torque and power due to unsteady streamwise motions are possible, and that these scale systematically with the surge kinematics. If unsteady fluid mechanics do play a role in these enhancements, as Dabiri (2020) has suggested analytically, then additional experimental and modelling studies could uncover novel solutions that leverage these unsteady effects to produce higher period-averaged turbine efficiencies.

2.5.3 Applications to full-scale wind turbines

Though these experiments were conducted at diameter-based Reynolds numbers that were one to two orders of magnitude smaller than those encountered in modern full-scale wind turbines, the dual analytical-empirical nature of the first-order linear model should in principle allow for a seamless extension to operational systems in field conditions. The topology of the torque space spanned by u_1 and ω will be different for full-scale systems, given the differences in full-scale turbine design and aerodynamics. A lack of Reynolds-number invariance in these results may also play a role in the precise topology of the torque space, since the chord-based Reynolds numbers encountered in these experiments ($5.6 \times 10^4 \lesssim Re_c \lesssim 9.2 \times 10^4$) were much lower than the invariance criterion of $Re_c \geq 3.5 \times 10^6$ proposed by Miller *et al.* (2019). Still, as long as a sufficiently reliable local linearization is possible, the procedure outlined in Section 2.3.4 for computing the aerodynamic constants K_ℓ and K_d should continue to give accurate predictions of time-resolved dynamics. Methods for characterizing the generator constants K_0, K_1, and K_2 may differ for full-scale generators, and gearbox effects may need to be taken into account, but these do not represent fundamental challenges to the validity of the model at scale. Thus, while to our knowledge no experiments with surging full-scale wind turbines have been carried out, the first-order linear model derived in this work should allow the dynamics of full-scale systems to be predicted solely on the basis of information from steady measurements, which may be readily obtained from onshore or fixed-bottom offshore turbines.

For floating offshore wind turbines, the surge amplitudes and velocities experienced due to typical surface-wave forcing patterns will likely be much smaller than the largest motions investigated in this study. Still, even for small perturbations, the disambiguation between aerodynamic and generator torque that the first-order linear model provides could inform design considerations and control strategies that leverage generator and turbine inertia or dynamic load-control schemes to reduce surge-induced fatigue loads on the turbine blades. These strategies could also be used to mitigate the effects of blade stall that may be encountered even in small surge motions if the turbine blades are operating at high static angles of attack.

In the extreme cases in which large surge excursions do occur, the surge motions of a FOWT would be coupled with large tilt disturbances, an effect not covered in this study. Therefore, it is questionable whether a FOWT will experience the large pure-surge oscillations represented by the maximally unsteady cases in these

experiments. However, these kinds of surge kinematics may be possible in more nascent wind-energy technologies, such as kite-based airborne wind turbines. In these contexts, the large surge motions could be leveraged to increase the efficiency of the turbines above their steady values. The first-order linear model would inform decisions regarding trade-offs between surge-induced efficiency gains and the onset of stall at high surge-velocity amplitudes, as well as the aerodynamic design of the turbine blades themselves for these inherently unsteady environments.

Finally, the potential of the time-averaged power enhancement empirically demonstrated in this study should not be missed. The increasing size of wind turbines and wind farms, combined with logistical difficulties involving siting for new wind-power plants, makes traditional wind power increasingly challenging to implement on a global scale. The theoretical limitation of the efficiency of wind-energy devices to 59.3% (Betz, 1920) also remains a fundamental roadblock to the engineering and economic efficacy of wind power. Thus, if the overall capacity of wind power is to be expanded over the next few decades, then innovative solutions for increasing the efficiency of wind-energy systems must be considered. The land-independent nature of floating offshore wind farms and airborne wind-energy systems already represents an appealing solution to the problem of land-based siting. If the unsteady surge motions inherent to these systems and other nascent technologies could be leveraged for increased efficiency, the constraints on both efficiency and large-scale implementation could potentially be circumvented.

2.6 Conclusions

In this study, the torque, rotor speed, and power of a horizontal-axis wind turbine undergoing periodic surge motions were investigated. A first-order linear model was derived to explain trends in amplitude and phase, and the experimental results compared favorably with the predictions of the model. Deviations from the model predictions were observed at low tip-speed ratios, a behavior that was attributed to the onset of stall on the turbine blades. At high tip-speed ratios, enhancements in the torque amplitude and period-averaged power were observed at high normalized surge frequencies. While the relative contributions of unsteady and nonlinear effects to these enhancements cannot be separated based on these experiments, it is nonetheless noteworthy that periodic surge motions can lead to increased period-averaged turbine efficiencies relative to the steady case. The trends captured by the model and data are expected to hold qualitatively for utility-scale wind turbines, both in the floating-

offshore context and in novel applications that inherently leverage unsteady flow physics for increased power-conversion efficiencies.

Acknowledgements

The authors gratefully acknowledge the assistance of several people, without whom the construction and operation of the experimental apparatus would not have been possible: J. Benson, who graciously provided machine-shop access during the pandemic; G. Juarez and M. Vega, who installed the power systems for the linear actuator; M. Miller, K. Bankord, and J. Kissing for technical consultation regarding the turbine power-control system and linear actuator; A. Kiani and E. Tang for machining key components of the apparatus; N. Esparza-Duran and R. Nemovi, who oversaw operations at CAST; M. Veismann and P. Renn for wind-tunnel support; and J. Cardona, E. Tang, P. Gunnarson, M. Fu, and R. Goldschmid for providing assistance and safety supervision for the experiments.

This work was funded by the National Science Foundation (grant CBET-2038071) and the Caltech Center for Autonomous Systems and Technologies. N. Wei was supported by a Stanford Graduate Fellowship and a National Science Foundation Graduate Research Fellowship.

Chapter 3

Nonlinear and Unsteady Mechanisms for Power-Generation Enhancements of Turbines in Unsteady Flow Conditions

The contents of this chapter have been adapted from Wei and Dabiri (2023), which has been accepted for publication in the Journal of Fluid Mechanics under the title "Power-generation enhancements and upstream flow properties of turbines in unsteady inflow conditions." As the first author, Nathan Wei made the primary contributions to experiment design, data acquisition and analysis, analytical modeling, and writing. Co-author John Dabiri contributed to the conceptualization of the study, funding acquisition, analysis and interpretation of the results, and feedback on the manuscript.

Abstract

Energy-harvesting systems in complex flow environments, such as floating offshore wind turbines, tidal turbines, and ground-fixed turbines in axial gusts, encounter unsteady streamwise flow conditions that affect their power generation and structural loads. In some cases, enhancements in time-averaged power generation above the steady-flow operating point are observed. To characterize these dynamics, a nonlinear dynamical model for the rotation rate and power extraction of a periodically surging turbine is derived and connected to two potential-flow representations of the induction zone upstream of the turbine. The model predictions for the time-averaged power extraction of the turbine and the upstream flow velocity and pressure are compared against data from experiments conducted with a surging-turbine apparatus in an open-circuit wind tunnel at a diameter-based Reynolds number of $Re_D = 6.3 \times 10^5$ and surge-velocity amplitudes of up to 24% of the wind speed. The combined modeling approach captures trends in both the time-averaged power extraction and the fluctuations in upstream flow quantities, while relying only on data from steady-flow measurements. The sensitivity of the observed increases in time-averaged power to steady-flow turbine characteristics is established, thus clarifying the conditions under which these enhancements are possible. Finally, the influence of unsteady fluid mechanics on time-averaged power extraction is ex-

plored analytically. The theoretical framework and experimental validation provide a cohesive modeling approach that can drive the design, control, and optimization of turbines in unsteady flow conditions, as well as inform the development of novel energy-harvesting systems that can leverage unsteady flows for large increases in power-generation capacities.

3.1 Introduction

Energy-harvesting turbines in atmospheric and oceanic flows are routinely exposed to unsteady flow conditions from gusts, tides, turbulent fluctuations, and other strongly time-dependent fluid motions. These unsteady effects induce time-varying forces and loads on the turbine components, which impact the time-averaged efficiency and operational lifespans of these systems. Oscillations in the streamwise velocity incident on the turbine are thus of major concern for conventional ground-fixed turbines in axial gusts, hydrokinetic turbines in tidal flows, and turbines mounted to airborne kites, which may undergo rapid changes in incident wind speed as they sweep through atmospheric flow gradients. These dynamic-inflow conditions are also related by means of a reference-frame transformation to the problem of a turbine moving in periodic linear surge motions in a steady inflow. This problem is of particular interest for emerging offshore-wind technologies, such as floating offshore wind turbines (FOWTs). Since these turbines are not fixed to the ocean floor, they can move under the influence of wind gusts and surface waves. Of these motions, the linear-surge oscillation mode tends to exhibit larger amplitudes relative to other degrees of freedom of motion (Johlas *et al.*, 2019). In certain forcing scenarios and platform configurations the velocity amplitude of the turbine motions may exceed 25% of the wind speed (Wayman, 2006; Larsen and Hanson, 2007; de Vaal *et al.*, 2014a). In spite of these complicating factors, FOWTs have the potential to enable wind-energy conversion in areas of the ocean whose depths prohibit the installation of conventional fixed-bottom systems, thereby creating additional avenues for the expansion of wind power as a contributor to global energy demands. They can capitalize on strong offshore wind resources, are by nature located close to coastal urban centers, and have fewer constraints on size and placement compared to their land-based and seafloor-mounted counterparts. The characterization of the aerodynamics of oscillating turbines, in addition to that of stationary turbines in oscillatory inflow conditions, is thus of critical importance to the design and control of the next generation of wind-energy technologies.

Unsteady streamwise flow conditions are particularly intriguing from both a fluid-mechanics and engineering perspective because they have the potential to yield substantial increases in the time-averaged power extraction of an energy-harvesting system. The one-dimensional (1D) axial momentum theory developed by Betz (1920) (as well as Lanchester, Joukowski, and others) posits that the power-conversion efficiency of an energy-harvesting system may not exceed $C_{p,Betz} = 16/27 \approx 59.3\%$, but this analysis was conducted under the assumption of steady flow. Dabiri (2020) recently relaxed that assumption and suggested that the contribution of an unsteady velocity potential could lead to theoretical efficiencies in excess of the so-called Betz limit. In parallel with this prediction, several studies have shown relative power enhancements over the steady operating power for turbines in surge motions or unsteady flows, both experimentally (Farrugia *et al.*, 2014; El Makdah *et al.*, 2019; Mancini *et al.*, 2020; Wei and Dabiri, 2022) and in simulations of varying fidelity (Farrugia *et al.*, 2016; Wen *et al.*, 2017; Johlas *et al.*, 2021). However, the extent to which unsteady flow physics contributed to these observed power enhancements is unclear. For example, Wen *et al.* (2017) and Johlas *et al.* (2021) found that a quasi-steady model for the time-averaged power could qualitatively describe the trends in the power enhancements. Mancini *et al.* (2020), by contrast, found that data from wind-tunnel experiments exceeded the predictions of their quasi-steady solution, though this solution differed from that of Johlas *et al.* (2021). Additionally, both Farrugia *et al.* (2016) and Wei and Dabiri (2022) found that the magnitude of the power enhancements depends on the turbine tip-speed ratio, and that under certain conditions, time-averaged power losses relative to the steady case are also possible. A full explanation and parameterization of these divergent observations remains lacking in the literature, and is urgently needed if the floating offshore wind-turbine technologies currently under development are to take advantage of these effects for increased power-generation capabilities.

The 1D axial momentum theory of Betz also asserts that the deceleration of the upstream flow approaching a wind turbine, or induction, is coupled with the operation and power output of a turbine. This induction effect dictates the flow and loading conditions encountered by the blades of a turbine and is directly related to the turbine's thrust force and efficiency. The induction zone, defined roughly as the region in which the flow velocity along the turbine's centerline is below 95% of the free-stream velocity, extends at least two turbine diameters upstream of the turbine itself (Medici *et al.*, 2011). These reduced velocities can thus bias tower-based estimates of the true wind speed by anemometers and LiDAR systems (e.g. Larsen

and Hansen, 2014; Howard and Guala, 2016; Simley *et al.*, 2016; Borraccino *et al.*, 2017; Mann *et al.*, 2018). For floating turbines, the coupling between incident wind conditions, blade-pitch control systems, and turbine thrust can also yield negatively damped (i.e. unstable) streamwise surge oscillations that increase fatigue loading on the turbine blades (Larsen and Hanson, 2007; Jonkman, 2008; López-Queija *et al.*, 2022). It is therefore instructive for turbine modeling and control to quantify the coupling between unsteady streamwise flow conditions, the dynamics of the turbine, and the flow properties in the upstream induction region.

The flow deceleration upstream of a stationary horizontal-axis wind turbine has been thoroughly studied in the literature, and several parameterizations of the induction region exist. One frequently used modeling approach treats the wake of the turbine as a cylindrical vortex sheet (Branlard and Gaunaa, 2015). This model lends itself well to free-vortex wake simulations (Sarmast *et al.*, 2016), and shows good agreement with experimental data (Medici *et al.*, 2011; Howard and Guala, 2016; Bastankhah and Porté-Agel, 2017; Borraccino *et al.*, 2017). It has also been extended to unsteady inflow conditions (Chattot, 2014; Yu *et al.*, 2019). Rather than rely on assumptions regarding near-wake structure, alternative approaches model the induction effect of the turbine using potential-flow objects such as Rankine half-bodies (Araya *et al.*, 2014; Gribben and Hawkes, 2019; Meyer Forsting *et al.*, 2021) or porous discs (Modarresi and Kirchhoff, 1979). These models reflect the common practice in both numerical and experimental studies of modeling the turbine as an actuator disc. Other models, such as the self-similar solution of Troldborg and Meyer Forsting (2017), are better able to capture the radial dependence of the streamwise flow velocity in the induction region. To the authors' knowledge, these models have not yet been extended to dynamically varying streamwise inflow conditions, such as axial gusts or turbine surge motions, as most existing studies involving these flow conditions do not investigate the upstream induction region.

The lack of parameterizations for the time-averaged power enhancements of turbines in unsteady inflow conditions and their coupled upstream flow properties motivates the present theoretical and experimental study. The work is structured as follows. First, in Section 3.2, a nonlinear dynamical model for the power extraction of a periodically surging turbine is derived, and a method is proposed that couples the time-varying power generated by the turbine to the turbine induction. This modeling framework is combined with two induction models to yield time-resolved predictions of the flow field upstream of the surging turbine. These predictions

rely solely on turbine data obtained from steady-flow measurements, namely the turbine power curve and the streamwise velocity averaged radially across the face of the rotor. A brief note on the dynamic equivalence between a surging turbine in a steady inflow and a stationary turbine in an oscillatory inflow is also presented. In Section 3.3, velocity and pressure measurements upstream of a surging-turbine apparatus are described, and the time-averaged power extraction and flow measurements are compared with the predictions of the modeling framework in Section 3.4. Additional analyses of the sensitivity of the modeling framework to the steady-flow aerodynamics of the turbine and the role of unsteady fluid mechanics are presented in Section 3.5. Finally, implications of the findings for the design, optimization, and control of turbines in unsteady flow environments are discussed.

3.2 Nonlinear dynamics of a periodically surging turbine

In this section, we derive a nonlinear dynamical model for the power extraction and flow properties upstream of a periodically surging turbine. We present a nonlinear ordinary differential equation for the turbine rotation rate as a function of known steady-flow turbine-aerodynamics and generator characteristics. This model can predict the time-varying and time-averaged rotation rate, torque, and power of the turbine. By applying 1D momentum theory, the axial induction factor of the turbine can be estimated from the instantaneous turbine power, and coupling this estimate with flow models allows the flow velocity and pressure at any point upstream of the turbine to be predicted. The modeling framework captures the unsteady dynamics of the surging-turbine problem using a quasi-steady parameterization of the turbine aerodynamics; potential contributions from unsteady fluid dynamics are explored later in Section 3.5.2.

In our notation, time-averaged quantities are marked with overbars, steady-flow or quasi-steady quantities are labeled with a zero subscript (e.g. $\mathcal{P}_0$), spatial averages are denoted with angle brackets, and amplitudes are denoted with a circumflex (e.g. $\hat{u}$). Additionally, if a flow variable lacks a specified radial dependence, it refers to a quantity measured on the turbine centerline (i.e. $r = 0$).

3.2.1 A nonlinear model for turbine rotation rate and power extraction

We build upon the linear modeling approach of Wei and Dabiri (2022), who describe the time-varying dynamics of a turbine using the swing equation (i.e. Newton's second law for rotation),

$$J\frac{d\omega}{dt} = \tau_{aero} - \tau_{gen}, \tag{3.1}$$

where J is the moment of inertia of the turbine system about its axis of rotation and ω is the rotation rate of the turbine. Deviations from equilibrium between the aerodynamic and generator torques τ_{aero} and τ_{gen} produce changes in the turbine rotation rate. Wei and Dabiri (2022) model the generator torque using the ordinary differential equation for the torque from a permanent-magnet motor,

$$\tau_{gen} = K_2\frac{d\omega}{dt} + K_1\omega + K_0, \tag{3.2}$$

where K_2 is the moment of inertia of the generator about its axis of rotation, K_1 is the generator constant, and K_0 is an empirical offset. These parameters can be established empirically for a given generator over a range of resistive loads.

While Wei and Dabiri (2022) utilized a linearized model for the aerodynamic torque, in this work we explicitly include the nonlinear relationship between the turbine coefficient of power,

$$C_p = \frac{\mathcal{P}}{\frac{1}{2}\rho\pi R^2 u_\infty^3}, \tag{3.3}$$

and the tip-speed ratio,

$$\lambda = \frac{R\omega}{u_\infty}, \tag{3.4}$$

where $\mathcal{P}$ is the power extracted by the turbine from the flow, ρ is the fluid density, R is the radius of the turbine, and u_∞ is the free-stream flow velocity. While the aforementioned linearization incorporates the wind speed and rotation rate as separate input parameters (cf. Figure 2.5), the present parameterization collapses these dependencies onto a single manifold, known as the turbine power curve. For a specified blade-pitch angle, any given turbine has a power curve defined as

$C_p = C_{p,0}(\lambda)$, which has a local maximum at a power-maximizing tip-speed ratio λ_{opt}. In this work, we will use the subscript 0 to refer to steady-flow quantities. Since the turbine power is determined by the product of the torque on the turbine and its rotation rate, the torque on the turbine can be written in terms of the power curve as

$$\tau = \frac{1}{2}\rho\pi R^2 u_\infty^3 \frac{C_{p,0}(\lambda)}{\omega}. \tag{3.5}$$

For a given surge-velocity profile $U(t)$, the effective free-stream velocity is $u_\infty = u_1 - U(t)$, where we define u_1 as the far-field wind speed relative to a ground-fixed frame. Thus, we may write the aerodynamic torque as

$$\tau_{aero} = \tau_{aero}(\omega, U, t) = \frac{1}{2}\rho\pi R^2 \frac{(u_1 - U(t))^3}{\omega} C_{p,0}\left(\frac{R\omega}{u_1 - U(t)}\right). \tag{3.6}$$

Substituting Equations 3.2 and 3.6 into Equation 3.1 results in a nonlinear ordinary differential equation for the turbine rotation rate that is first-order in time and depends on the surge velocity as an input forcing parameter:

$$\frac{d\omega}{dt} = \frac{1}{J + K_2}\left[\frac{1}{2}\rho\pi R^2 \frac{(u_1 - U(t))^3}{\omega} C_{p,0}\left(\frac{R\omega}{u_1 - U(t)}\right) - K_1\omega - K_0\right]. \tag{3.7}$$

This model is a nonlinear and nonautonomous ordinary differential equation, which precludes straightforward mathematical characterization, but it can be integrated forward in time from an initial condition $\omega(t = 0)$ until it reaches a period-averaged equilibrium. The model can therefore yield numerical predictions of the time-varying and time-averaged rotation rate, torque, and power of a turbine under surge motions or dynamic inflow conditions. This stands in contrast to the linearized model developed by Wei and Dabiri (2022), which can be written as a transfer function for convenient analysis but is unable to capture changes in time-averaged quantities.

As a limiting case, we may consider a quasi-steady solution to the model in which $\frac{d\omega}{dt} = 0$ and $C_{p,0}$ is constant as a function of time. The time-averaged power is defined as $\overline{\mathcal{P}} = \overline{\tau_{gen}\omega} = K_1\overline{\omega^2} + K_0\overline{\omega}$, which suggests that for a sinusoidal surge-velocity waveform with amplitude $u^* = \hat{U}/u_1$, the time-averaged power is

$$\overline{\mathcal{P}} = \frac{f}{2\pi}\int_0^{\frac{2\pi}{f}} \frac{1}{2}\rho\pi R^2 C_{p,0}\left(u_1 - U(t)\right)^3 dt = \mathcal{P}_0\left(1 + \frac{3}{2}u^{*2}\right). \tag{3.8}$$

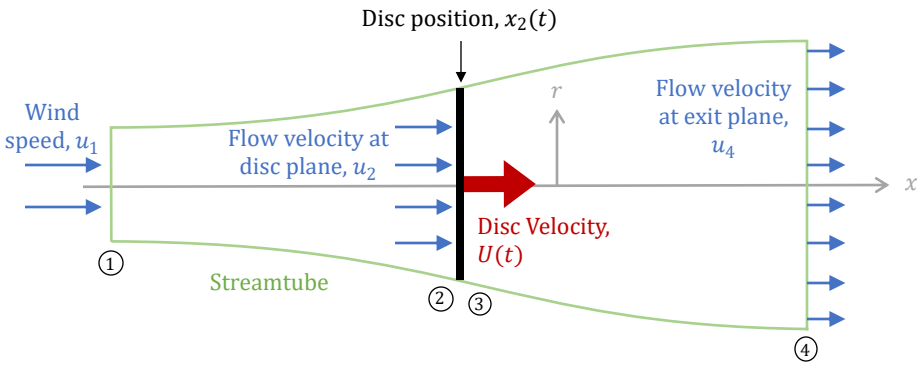

Figure 3.1: Schematic of the parameters and control volumes referenced in Section 3.2. The actuator disc is located instantaneously at $x_2(t)$ and moves with velocity $U(t)$ relative to the inertial frame defined by the x- and r-axes. Circled numbers denote streamwise interrogation locations (1 through 4).

This result is identical to that derived by Wen *et al.* (2017) and Johlas *et al.* (2021) for a surging turbine, and is equivalent to that of a stationary turbine with constant C_p in an oscillating inflow.

3.2.2 Modeling the relationship between turbine dynamics and upstream flow conditions

The 1D momentum theory derived by Betz (1920) can be used to infer flow properties upstream of the turbine rotor plane from the power extracted by the turbine. This theoretical framework employs conservation relations over a control volume composed of an axisymmetric streamtube surrounding the turbine, which is modeled as an actuator disc. An axial induction factor, representing the decrease in velocity from far upstream of the turbine to the upstream face of the actuator disc (i.e. location 2 in Figure 3.1), is defined as

$$a = \frac{u_1 - u_2}{u_1}. \tag{3.9}$$

The induction factor is the single free parameter needed to compute the coefficient of power within this framework, which is given by

$$C_p = 4a(1-a)^2. \tag{3.10}$$

This yields a theoretical maximum for the efficiency of a wind-energy system of $C_{p,Betz} = 16/27$, which is attained at $a = 1/3$. For the surging-turbine system, then,

we have the similar relation

$$\frac{\tau_{gen}\omega}{\frac{1}{2}\rho\pi R^2 u_1^3} = 4a(1-a)^2. \tag{3.11}$$

1D momentum theory assumes that the flow is inviscid, incompressible, irrotational, and steady. Upstream of the turbine rotor plane, the first three assumptions are reasonable to make. If we further assume that the flow upstream of the turbine can be modeled in a quasi-steady manner, we can use the rotation rate given by Equation 3.7 to compute an instantaneous coefficient of power $C_p(\omega, t)$, and by inverting Equation 3.11, we can estimate the time-varying induction factor $a(t)$. Since the induction factor is physically constrained as $a \in [0, 1]$, two solutions are possible for $C_p < C_{p,Betz}$. The upper solution for a represents a heavily loaded turbine, and for $a \gtrsim 0.37$ the theoretical framework breaks down (Wilson and Lissaman, 1974). In a majority of cases, including the experiments presented in this work, the turbine is not heavily loaded, and thus the lower solution for a is assumed to represent the system.

Equations 3.7 and 3.11 therefore connect the time-varying dynamics of a turbine under dynamic axial-flow conditions to the flow properties just upstream of the rotor disc. To propagate these predictions further upstream, an induction model for the turbine is needed. As mentioned previously, a common modeling approach involves representing the wake of the turbine as a cylindrical vortex sheet and performing Biot-Savart integration to compute the induced velocity from this wake model at any point in the domain (Johnson, 1980; Branlard and Gaunaa, 2015). This is known as vortex-sheet or vortex-cylinder theory (hereafter abbreviated as VCT). Evaluating this integral upstream of the turbine along its rotational axis yields a model for the induced velocity along the upstream centerline of the turbine (Medici *et al.*, 2011):

$$\frac{u(r=0,x)}{u_\infty} = 1 - a\left[1 + \frac{x-x_2}{R}\left(1 + \left(\frac{x-x_2}{R}\right)^2\right)^{-1/2}\right], \tag{3.12}$$

where x is the streamwise coordinate along the axis of the turbine (originating at the turbine and positive downstream) and x_2 is the instantaneous location of the turbine, as shown in Figure 3.1. For a surging turbine, the induction effect in the second term should scale with the effective free-stream velocity $u_1 - U(t)$, since in the limiting case where the turbine is moving downstream at velocity $U(t) = u_1$, the turbine should have no effect on the flow, and the flow everywhere upstream of the turbine should be equal to u_1. Involving the time-varying induction factor $a(t)$

provided by 1D momentum theory, we thus obtain the flow velocity at any upstream location $x < x_2$ and at any time as

$$u(r=0,x,t) = u_1 - a(t)(u_1 - U(t))\left[1 + \frac{x - x_2(t)}{R}\left(1 + \left(\frac{x - x_2(t)}{R}\right)^2\right)^{-1/2}\right]. \tag{3.13}$$

To complete the description of flow properties upstream of the surging turbine, the pressure along the centerline may be modeled by substituting the model for $u(r=0,x,t)$ into the steady Bernoulli equation,

$$p(r=0,x) = p_1 + \frac{1}{2}\rho\left({u_1}^2 - u\,(r=0,x,t)^2\right), \tag{3.14}$$

where ρ is the density of the fluid and p_1 is the ambient pressure in the free stream. If the velocity potential of the induction model is known, the unsteady Bernoulli equation may be applied instead. For the purposes of this work, however, we maintain quasi-steady assumptions for the flow physics in the induction zone, in keeping with the quasi-steady aerodynamics parameterized by the turbine model and 1D momentum theory. As mentioned previously, the effect of this unsteady potential will be considered in more detail in Section 3.5.2. While the expressions presented here have been confined to the centerline, Branlard and Gaunaa (2015) provide full relations for $u(r,x)$ that can be employed in place of Equation 3.12 to allow this modeling framework to cover the entire upstream induction zone.

Alternatively, we can model the effect of the surging turbine on the flow using a porous-disc representation in potential flow, which does not rely on parameterizations of the turbine wake geometry and vorticity. This is inspired by the work of Taylor (1944) and Koo and James (1973), which has recently been extended by Steiros and Hultmark (2018) for flat plates of arbitrary porosity and Bempedelis and Steiros (2022) for wind turbines at arbitrary loading conditions. The porous-disc approach, which has not been widely investigated in the wind-energy literature, is presented to demonstrate the robustness of the overall modeling framework put forth in this work to the choice of induction model. Its velocity potential is also more readily accessible than that of VCT, which will be advantageous when we consider the effects of unsteady fluid mechanics in Section 3.5.2. Finally, the model provides a convenient generalization to rotors with arbitrary radial distributions of streamwise velocity, which, though not explored in detail in this study, could be exploited to integrate this model with blade-element momentum (BEM) computations

that generate radially varying induction-factor profiles. We will refer to the model throughout this paper as the porous-disc theory (PDT).

3.2.3 A porous-disc induction model for a surging turbine

We first consider a circular porous disc with radius R located at streamwise coordinate $\xi = 0$, represented as a distribution of sources with a velocity potential of $\phi(r, \xi = 0) = C\sqrt{R^2 - r^2}$ for $r < R$ and $\phi(r, \xi = 0) = 0$ for $r > R$, where $C > 0$ is an arbitrary constant that represents the aggregate strength of the source distribution. Using this distribution as a boundary condition at $\xi = 0$, we may solve the Laplace equation $\nabla^2\phi = 0$ in cylindrical coordinates to obtain the velocity potential of a porous disc (cf. Lamb, 1916; Tranter, 1968):

$$\phi\,(r, \xi) = -\sqrt{\frac{\pi}{2}} C R^{3/2} \int_0^\infty s^{-1/2} J_{3/2}(Rs) J_0(rs) e^{-s\xi} ds;\ \xi > 0. \tag{3.15}$$

Here, $J_\nu(z)$ is a Bessel function of the first kind, and s is a dummy integration variable. The choice of $C = \frac{2}{\pi}V$ gives the velocity potential of a solid disc moving at axial velocity V in a quiescent fluid (Lamb, 1916, §102.4). More generally, the velocity V represents the velocity of the disc relative to that of the fluid in the far field. For a porous disc, we may define a representative source term a, directly corresponding to the induction factor defined in Equation 3.9, such that $C = \frac{2}{\pi}aV$. The choice of a dictates the porosity of the disc: $a = 0$ represents a fully permeable disc, $a = 1$ yields a fully solid disc, and intermediate values ($0 < a < 1$) reduce the source strength from the solid-disc solution so that a nonzero mass flux through the disc is established. Evaluating Equation 3.15 along the centerline yields

$$\phi\,(r = 0, \xi) = -aV\frac{2}{\pi}\left[R - \xi \arctan\left(\frac{R}{\xi}\right)\right];\ \xi > 0. \tag{3.16}$$

This solution is only valid for $\xi > 0$. To describe the other half of the domain as well, one might follow the ansatz of Taylor (1944) and use the even extension of ϕ to represent $\xi < 0$. The velocity discontinuity across the disc that this extension creates could then be removed using the base-suction correction of Steiros and Hultmark (2018). However, since in this work we are only concerned with the upstream region, we leave these derivations for future consideration.

We differentiate the velocity potential with respect to ξ to obtain the streamwise velocity along the centerline:

$$u\,(r = 0, \xi) = -aV\frac{2}{\pi}\left[\frac{R\xi}{\xi^2 + R^2} - \arctan\left(\frac{R}{\xi}\right)\right];\ \xi > 0. \tag{3.17}$$

This relation emphasizes the effect of the porosity parameter (or equivalently, the induction factor) on the behavior of the model. For $a = 0$, the flow is everywhere unaffected by the motion of the disc. For $a = 1$, $u(r = 0, \xi \rightarrow 0^+) = V$, which satisfies the surface boundary condition for a moving solid disc.

We now apply this expression in an inertial frame containing a uniform flow with free-stream velocity u_1, in which the disc translates at velocity $U(t)$ relative to the frame. In this frame, we define the downstream-oriented axial coordinate x and the instantaneous position of the disc $x_2(t)$ as shown in Figure 3.1, such that $\xi = x_2 - x$ and $U(t) = \frac{dx_2}{dt}$. The velocity of the disc relative to the far-field flow velocity is thus $V = U(t) - u_1$. Applying these definitions to Equation 3.17, we arrive at the following model for the centerline velocity in the upstream induction zone ($x < x_2$):

$$u\left(r = 0, x, t\right) = u_1 - a(t)\left(u_1 - U(t)\right)\frac{2}{\pi}\left[\frac{R(x - x_2(t))}{(x - x_2(t))^2 + R^2} - \arctan\left(\frac{R}{x - x_2(t)}\right)\right]. \tag{3.18}$$

We reiterate that the model cannot be used to predict the velocity downstream of the porous disc, given the constraint of $\xi > 0$ on the velocity potential. Additionally, though the solution is technically valid if the turbine moves downstream faster than the wind speed, i.e. $u_1 - U(t) < 0$, we expect that the model will cease to be valid in this case because the rotor will interact with its own wake.

As with the expression obtained from VCT, Equation 3.15 can in principle be integrated at any point upstream of the porous disc so that the velocity and pressure can be computed throughout the entire induction zone. In both models, the streamwise velocity u_2 on the upstream face of the rotor plane is predicted to be constant over r, i.e.

$$u(x = x_2, r) = u_1 - a(t)(u_1 - U(t)). \tag{3.19}$$

This is generally a poor approximation for real turbines, whose streamwise velocities typically increase toward the free-stream value with increasing radial distance from the hub (cf. Medici *et al.*, 2011; Troldborg and Meyer Forsting, 2017). An additional advantage of the porous-disc modeling approach is that arbitrary radial-velocity profiles can be modeled by changing the source-strength distribution in Equation 3.15. For example, if the turbine blade geometry is known, radial variations in the induction factor can be computed from blade-element momentum theory as a function $a(r)$ and integrated to obtain a modified velocity potential. A correction factor for the effects of nonuniform velocities at the disc face can then be derived by

defining a rotor-averaged induction factor,

$$\langle a \rangle = \frac{2}{R^2}\int_0^R a(r) r dr = \left[\frac{2}{R^2}\int_0^R \frac{a(r)}{a(r=0)} r dr\right] a(r=0) \equiv \kappa a(r=0). \quad (3.20)$$

The scaling constant κ, which maps the centerline induction factor to the equivalent rotor-averaged induction factor, can be computed from a known velocity-deficit radial profile, such as the self-similar solution of Troldborg and Meyer Forsting (2017) or a BEM computation. For a top-hat velocity-deficit profile, $\kappa = 1$. If the radial induction-factor distribution does not change much throughout the surge cycle (i.e. the velocity-deficit profile remains self-similar), κ can be assumed to be independent of the surge kinematics for a given loading condition, and thus can be treated as a constant for that particular wind speed and mean tip-speed ratio.

The distinction between the centerline and rotor-averaged induction factors is particularly important for a quantitative comparison between the 2D axisymmetric induction theories developed in this section and the 1D axial-momentum theory of Betz. Because 1D momentum theory by definition does not account for radial differences in streamwise velocity, the induction factor estimated using Equation 3.11 must represent the rotor-averaged induction factor. By the same logic, the induction factor in the VCT and PDT expressions for the streamwise velocity is the centerline induction factor, and is what will be measured by a point anemometer placed along the rotational axis of the turbine. The parameter κ thus serves as a bridge between the 1D and 2D analyses employed in this modeling framework.

For the remainder of this paper, we will focus on measurements taken along the rotational axis of the turbine ($r = 0$), and therefore the flow quantities $u(x)$, $p(x)$, and a will implicitly refer to these centerline quantities.

The modeling approach presented in this work may be summarized as follows:

1) Identify the turbine power curve $C_{p,0}(\lambda)$ and generator and inertia constants K_0, K_1, K_2, and J from steady-flow measurements and manufacturer specifications.

2) Integrate Equation 3.7 in time with a given surge-velocity forcing $U(t)$ to obtain the turbine rotation rate $\omega(t)$.

3) From $\omega(t)$, use Equations 3.2 and 3.11 to predict the coefficient of power $C_p(t)$ and the rotor-averaged induction factor $\langle a(t) \rangle$.

4) Calculate the centerline induction factor $a(t)$ using an analytical or empirical correction factor κ.

5) Include $a(t)$ in an induction model (e.g. Equation 3.13 for VCT or 3.18 for PDT) to obtain the velocity field upstream of the turbine.

6) Use the steady Bernoulli equation to obtain the pressure field from the velocity field.

We reiterate that this modeling framework invokes a quasi-steady assumption for the aerodynamics of the turbine, and the time dependence of the model comes from an unsteady treatment of the turbine rotation rate as a function of the aerodynamic and generator torques. The practical benefit of this approach is that time-resolved predictions of the turbine dynamics and upstream flow properties can be obtained solely on the basis of steady-flow measurements; the model does not depend on empirical calibrations from unsteady test cases. From a fluid-mechanics perspective, the approach provides an instructive disambiguation between the rotational dynamics of the turbine and the actuator-disc aerodynamics associated with the rotor and its motions. Furthermore, this analytical foundation allows the effects of unsteady flow physics to be more directly characterized.

3.2.4 On the problem of a stationary turbine in an oscillating inflow

The preceding analysis has focused on the case of a periodically surging turbine in a uniform inflow. From the work of Wen *et al.* (2017), El Makdah *et al.* (2019), Johlas *et al.* (2021), and others, it is apparent that the case of a stationary turbine in an axial gust can be made equivalent to the surging-turbine case by shifting from a ground-fixed to a turbine-fixed frame of reference. The time-averaged power is not affected by this transformation. To determine the effect of noninertial-frame accelerations, we consider the force on a body oscillating with velocity $W_i(t)$ in an oscillating inflow $U_i(t)$, which is given by Brennen (1982) as

$$F_i = -M_{ij}\frac{dW_j}{dt} + \left(M_{ij} + \rho V_D \delta_{ij}\right)\frac{dU_j}{dt};\ j = 1, 2, 3. \tag{3.21}$$

Here, M_{ij} is the added-mass tensor of the body, V_D is the volume of the body, δ_{ij} is the Kronecker delta operator, and the flow is assumed to be inviscid. This expression thus quantifies the influence of added-mass effects and an unsteady buoyancy force, which comes from the oscillating pressure gradient that drives the oscillating inflow (Granlund *et al.*, 2014). We assume that neither the added-mass tensor nor the volume of the body changes as a function of time for a porous disc, and that $U_i(t)$ and $W_i(t)$ are periodic. Since $U_i(t)$ and $W_i(t)$ are periodic, the time

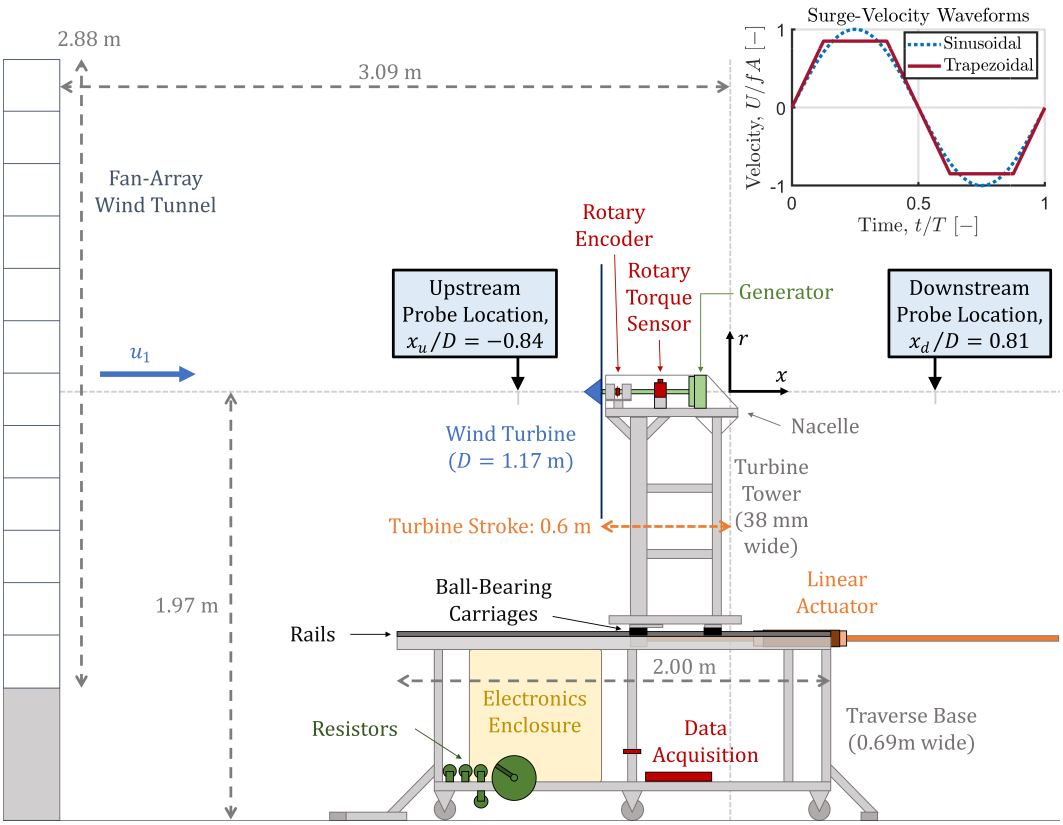

Figure 3.2: Schematic of the experimental apparatus, including the fan-array wind tunnel (left) and surging turbine (center-right). The turbine is illustrated at its maximum upstream position relative to the origin ($x = -0.6$ m). The inset figure (top right) shows the two types of surge-velocity waveforms used in these experiments.

averages over a single period of $\frac{dU_j}{dt}$ and $\frac{dW_j}{dt}$ are both zero. It thus follows that the time-averaged force on the body due to these two types of unsteady contributions is also zero, and therefore neither of these unsteady effects creates a theoretical difference between the time-averaged performance of an oscillating turbine and a stationary turbine in an oscillating inflow. Additionally, the volume of a 2D actuator disc is effectively zero, and thus the unsteady buoyancy force that differentiates the two scenarios should be negligible. These considerations do not exclude the possibility of additional differences between these two cases, for example due to viscous time-history effects, vortex dynamics, or other flow physics not captured by the potential-flow assumption.

3.3 Experimental methods

3.3.1 Experimental apparatus

To characterize the range of conditions over which the ideal-flow model holds, velocity and pressure measurements were conducted in a 2.88×2.88 m^2 open-circuit fan-array wind tunnel at the Caltech Center for Autonomous Systems and Technologies (CAST). A three-bladed, fixed-pitch horizontal-axis wind turbine (Primus Wind Power AIR Silent X) with a rotor diameter of $D = 1.17$ m was mounted on a traverse that translated along 2-m long rails (NSK NH-series) and was actuated by a magnetic piston-type linear actuator (LinMot PS10-70x320U). A diagram of this apparatus is given in Figure 3.2. The hub height of the turbine was 1.97 m above the floor of the facility, and the farthest-downstream position of the turbine (defined as $x = 0$) was 3.09 m downstream of the fan array. The electrical load on the turbine was provided by 10, 20, and 40-Ohm resistors (TE Connectivity TE1000-series). A rotary torque transducer (FUTEK TRS300) and rotary encoder (US Digital EM2) were used to measure the power produced by the turbine. The estimated blockage of the swept area of the turbine and all support structures, relative to the surface area of the fan array, was 14%. Further details regarding the dimensions and capabilities of the apparatus may be found in Wei and Dabiri (2022).

A constant-temperature hot-wire anemometry system (Dantec MiniCTA 54T42) and differential pressure transducer (MKS Baratron 398-series with Type 270B signal conditioner) were used to measure flow properties at two locations along the turbine centerline, one upstream of the turbine at $x_u = -0.840D$ and one downstream at $x_d = 0.810D$. The hot-wire probe was placed approximately on the centerline, while the input line of the pressure transducer was located 3.8 cm to the side. The transducer's reference line was placed in a shielded area outside the flow of the wind tunnel. Data were collected at a sampling rate of 20 kHz and were low-pass filtered using a sixth-order Butterworth filter with a cutoff frequency of 100 Hz. The hot-wire anemometer was calibrated in the wind tunnel against a Pitot probe using the same pressure transducer. Because the facility was exposed to the atmosphere, the temperature and relative humidity were recorded during all experiments to estimate the air density and correct the hot-wire calibration for temperature changes.

3.3.2 Experimental procedure

Experiments were conducted over two nights in March 2022, in which the free-stream velocities in the wind tunnel were $u_1 = 7.79 \pm 0.10$ and 7.96 ± 0.11 ms^{-1},

Resistive Load	10 Ω	20 Ω	40 Ω
Case Identifier	●	●	●
λ_0	6.48 ± 0.25	7.84 ± 0.28	8.77 ± 0.27
$C_{p,0}$	0.298 ± 0.013	0.248 ± 0.012	0.165 ± 0.010
K_1 $\left[\mathrm{kg\,m^2 s^{-1}}\right]$	0.0112	0.00649	0.00376
K_0 [Nm]	0.119	0.0850	0.0676
a_0 (VCT)	0.252	0.267	0.221
a_0 (PDT)	0.286	0.301	0.250
κ (VCT)	0.364	0.278	0.222
κ (PDT)	0.320	0.247	0.196

Table 3.1: Performance characteristics and model constants for the three loading conditions investigated in this study.

corresponding to an average diameter-based Reynolds number of $Re_D = 6.27 \times 10^5$. The hot-wire anemometer was calibrated at the beginning and end of each set of experiments. The turbine was operated at three tip-speed ratios, $\lambda_0 = 6.48 \pm 0.25$, 7.84 ± 0.28, and 8.77 ± 0.27, with corresponding coefficients of power of $C_{p,0} = 0.298 \pm 0.013 \approx C_{p,max}$, 0.248 ± 0.012, and 0.165 ± 0.010. The generator constants for these cases were obtained from the data of Wei and Dabiri (2022), as were the turbine and generator moments of inertia ($J = 0.0266 \pm 0.0008$ kg m^2; $K_2 = 6.96 \times 10^{-4}$ kg m^2). The operating parameters of the turbine are summarized in Table 3.1. The turbine was actuated in sinusoidal and trapezoidal motions (see inset, Figure 3.2) with an amplitude of $A = 0.3$ m ($0.257D$) and periods between $T = 1$ and 6 s, corresponding to nondimensional surge-velocity amplitudes between $u^* \equiv fA/u_1 = 0.039$ and 0.242. Data were phase-averaged over 100 motion periods. The amplitudes and phases of each quantity of interest were computed from an FFT of the phase-averaged signal. Upstream and downstream flow measurements were collected in separate tests. Additionally, a series of quasi-steady flow measurements were obtained for each tip-speed ratio by placing the turbine at six equally spaced streamwise locations between $x/D = -0.514$ and 0 and recording measurements over 120 s. To correct against differences in the ambient conditions between measurement sessions and facilitate more direct comparisons, quasi-steady measurements taken at $x/D = 0$ on both sessions were used to scale the measured velocities and pressures from one session to match those from the other session.

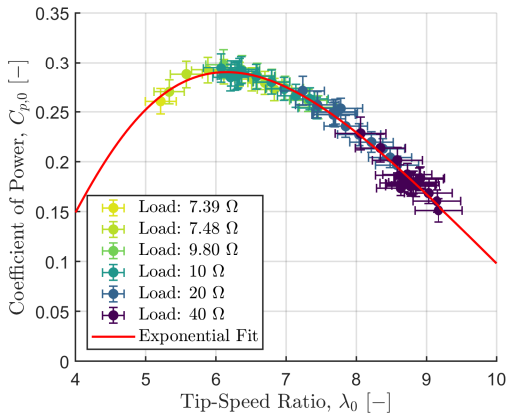

Figure 3.3: Steady power curve for the turbine used in these experiments, measured over a range of resistive loads and wind speeds. Some of these data points are reproduced from Wei and Dabiri (2022). The result of the exponential fit given by Equation 3.22 is shown as a solid red line.

3.3.3 Determination of model parameters from steady-flow measurements

3.3.3.1 Power-curve parameterization and model integration

To compare the analytical modeling framework with the experimental data, it was first necessary to parameterize the steady-flow power curve of the turbine, $C_{p,0}(\lambda)$. The data in the measured power curve of the turbine, shown in Figure 3.3, were fitted to a type of exponential function frequently used for wind-turbine modeling:

$$C_p = \left(\frac{c_1}{\lambda + c_2} - c_3\right) \exp\left(\frac{-c_4}{\lambda + c_2}\right). \tag{3.22}$$

Several coefficients from the general model form given by Heier (2014) were omitted to simplify the model; the four remaining fitted coefficients were $c_1 = 16.784$, $c_2 = -1.510$, $c_3 = 1.702$, and $c_4 = 8.764$. This parameterization was employed (as opposed to e.g. polynomial fits) to ensure that the slope and concavity at the extremes of the power curve would be captured reliably, since it will be shown in Section 3.4.1 that the performance of the modeling framework is sensitive to these factors.

To obtain time-resolved predictions of the turbine rotation rate, torque, and power, Equation 3.7 was numerically integrated over ten surge periods using a fourth-order Runge-Kutta scheme. Timesteps were kept no larger than $0.001T$ to maintain numerical stability and accuracy. The steady-flow turbine rotation rate ω_0 was used as the initial condition, and convergence was typically established within a few

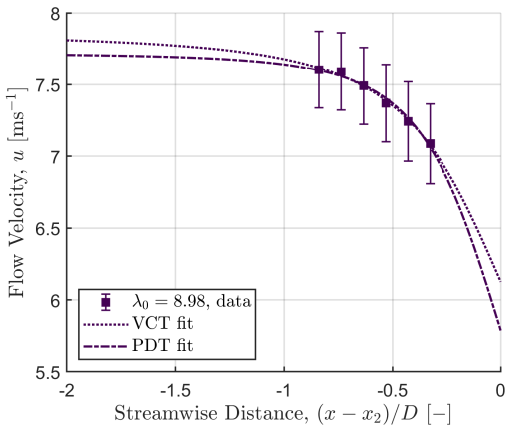

Figure 3.4: Streamwise-velocity measurements at six different streamwise distances upstream of the turbine for the highest tip-speed ratio tested, compared with two-parameter fits based on the VCT (dotted line) and PDT (dashed-dotted line) induction models. The PDT model shows a slightly more aggressive drop in streamwise velocity close to the turbine and a lower predicted free-stream velocity than the VCT model.

forcing periods. The model predictions for the amplitude, phase, and time-average of each quantity were computed from the final period in the simulation.

3.3.3.2 Steady-flow induction data

To estimate the steady induction-factor values of the turbine at the three tip-speed ratios tested in this study, quasi-steady measurements of the streamwise velocity $u(x)$ (described in Section 3.3.2) were plotted as a function of streamwise distance x/D, and two-parameter fits for the wind speed u_1 and centerline induction factor a_0 were applied to these data. Dimensional data for the highest tip-speed ratio tested are shown in Figure 3.4 with fits using the VCT (Equation 3.13) and PDT (Equation 3.18) models. This test case demonstrates the slight differences between the modeling frameworks: for the same data, the PDT model predicts a stronger induction effect (as $x/D \to 0$) and a slightly lower free-stream velocity ($x/D \leq -2$) than the VCT model. The fit results for all three tip-speed ratios are shown in Figures 3.5a (VCT) and 3.5b (PDT), where the measured and modeled flow velocities are normalized by the wind speeds identified by each two-parameter fit. These steady-flow tests demonstrate that, within the range of streamwise distances tested, the agreement of both models with the trends observed in the data is reasonably good.

The centerline induction-factor values shown in Figure 3.5 were compared with the rotor-averaged values estimated using Equation 3.11 and a C_p calculated from the average of the measured turbine torque and rotation rate over all six streamwise

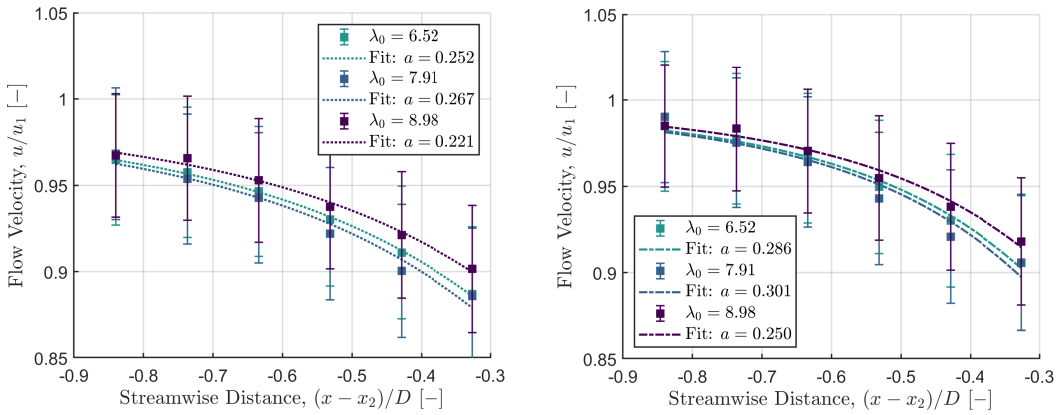

Figure 3.5: Streamwise-velocity measurements at six different streamwise distances upstream of the turbine and three tip-speed ratios, compared with fits based on the (a) VCT and (b) PDT induction models. The velocity data are normalized by the free-stream velocities obtained from the two-parameter fits.

locations. The ratio between these estimates of $\langle a_0 \rangle$ and the fitted values of a_0 gave an empirical estimate for the correction factor κ for each tip-speed ratio. The estimated values of a_0 and κ are given in Table 3.1 for the two induction-model frameworks. For comparison, an analytical correction factor can be calculated by integrating the self-similar solution of Troldborg and Meyer Forsting (2017), which yields $\kappa = 0.649$. This is larger than the empirically estimated values of κ. However, the ratio of the turbine hub diameter to the turbine diameter for the simulations used to calibrate the self-similar solution was 2.4%, whereas for the turbine used in this study the ratio was around 12%. It is therefore expected that the flow would decelerate more strongly along the centerline of this particular turbine, due to the increased blockage effect from the larger hub and nacelle, thus lowering the ratio between the rotor-averaged and centerline induction factors.

3.3.3.3 Wind-speed and pressure corrections

Since changes in the turbine tip-speed ratio correspond to changes in the thrust force on the turbine, the operation of the turbine in the open test section of the wind tunnel created a blockage effect that influenced the wind speed in the open test section — an effect that is well-documented in the literature (e.g. Eltayesh *et al.*, 2019). To correct against this additional source of error, a wind-speed correction was computed for each unsteady test case by comparing the mean of the streamwise-velocity measurements with the wind speeds measured by the hot-wire anemometer during calibration (where the turbine was present in the tunnel but was not rotating).

The average of these fitted wind speeds across all of the unsteady and quasi-steady tests for each tip-speed ratio was then used as an adjusted wind speed for normalizing the recorded velocity and pressure data.

Further corrections were implemented to reduce the influence of sources of uncertainty in the pressure data. Since the absolute pressure at the reference of the pressure transducer was unknown, the mean value of this pressure prediction was scaled to be equal to that of the data. Additionally, due to the long length of the tubes that connected the pressure transducer to the measurement location, a first-order low-pass filter with a cutoff frequency of 2.48 Hz was inferred from the phase of the measured pressure data relative to the velocity signal. This filter was then applied to the calculated model predictions for pressure. Remaining discrepancies between the measured and modeled pressure signals could be attributed to the true filtering effect of the tubes being of higher order than the first-order filter model (Bergh and Tijdeman, 1965).

3.4 Experimental results

In this section, the predictions of the nonlinear dynamical model derived in Section 3.2.1 are compared with experimental measurements of time-averaged and fluctuating quantities. The induction-factor estimates collected from the nonlinear dynamical model are then used to predict the streamwise velocity and pressure upstream of the surging turbine. Predictions based on vortex-cylinder theory (VCT) and porous-disc theory (PDT) are compared with flow measurements to demonstrate that the proposed modeling framework is able to reproduce trends observed in the measured response of the system.

3.4.1 Power generation

The predictions of the nonlinear ordinary differential equation given in Equation 3.7 are compared with rotation-rate, torque, and power data collected from the surging-turbine experimental apparatus. For this purpose, we reuse the experimental torque and power measurements of Wei and Dabiri (2022) and plot the results of the present modeling framework against these data. This dataset contained measurements at three lower tip-speed ratios, in addition to those investigated in the present study, and measurements were conducted over a wider range of surge-velocity amplitudes and frequencies.

Figure 3.6 shows the measured torque amplitude and phase from these data, plotted

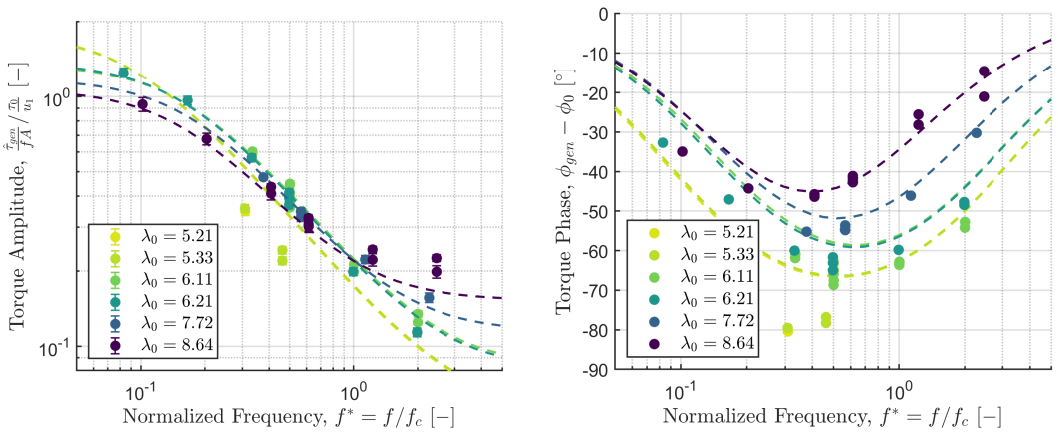

Figure 3.6: Generator-torque (a) amplitude and (b) phase for a series of sinusoidal surge-velocity waveforms, plotted against normalized frequency and compared with model predictions (dashed lines). Data are reproduced from Wei and Dabiri (2022).

against surge frequency. The torque amplitude was scaled by the surge-velocity amplitude $u^* = fA$ in the manner of a transfer-function gain, and this was nondimensionalized by the steady reference torque $\tau_{gen,0}$ and the free-stream velocity. The frequency was nondimensionalized by a characteristic frequency f_c derived from the linear model of Wei and Dabiri (2022). The trends in the data are relatively well-captured by the model predictions, and the nonlinear model shows some improvement over the linear model at the lowest tip-speed ratios tested (cf. Wei and Dabiri, 2022, Figures 7a and 9a). This suggests that the nonlinear model derived in this work is an effective generalization of the linearization developed and validated in the preceding study.

The benefit of the nonlinear model is evident when predictions for time-averaged quantities of interest are required. According to the preceding linearized model, the time-averaged rotation rate and power of the turbine will not deviate from their corresponding steady-flow quantities. Departures from this ansatz are clearly evident in Figure 3.7, as the mean rotation rate and power decrease as a function of increasing surge-velocity amplitude for low tip-speed ratios, and increase for high tip-speed ratios. The predictions of the nonlinear model, however, are able to follow these trends. The largest enhancements in time-averaged power over the steady case are predicted at the highest tip-speed ratios, while the greatest decreases in time-averaged power occur at the lowest tip-speed ratios. The nonlinear model still overpredicts these power decreases; it is likely that these additional losses are a result of the inception of flow separation on the turbine blades. The turbine stalled

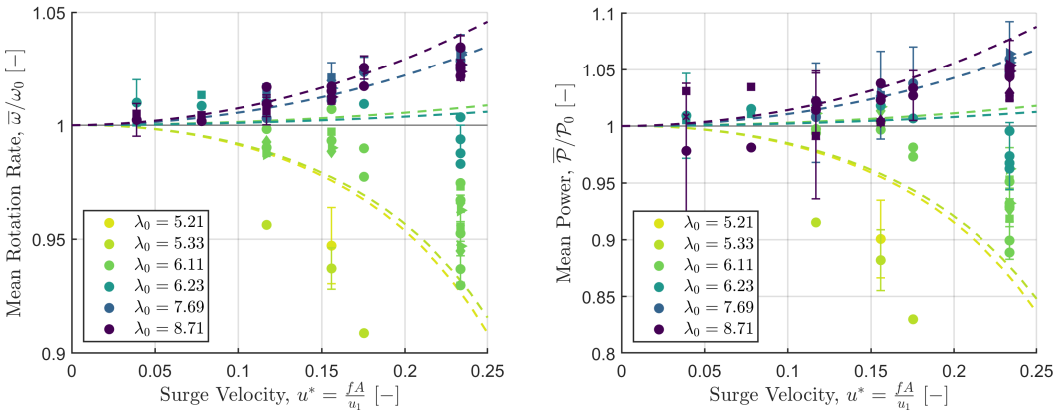

(a) (b)

Figure 3.7: Time-averaged (a) rotation rate and (b) power, plotted against surge-velocity amplitude. Data are reproduced from Wei and Dabiri (2022); model predictions derived from Equation 3.7 are plotted as dashed lines and colored by tip-speed ratio. Circles represent sinusoidal surge-velocity waveforms and diamonds and other markers represent trapezoidal waveforms. Error bars are plotted on every sixth point for the sake of clarity.

and stopped spinning when forced to operate at or below $\lambda_0 \approx 5$, and so the decrease in power as a function of decreasing tip-speed ratio was in reality much sharper than that suggested by the fit to the turbine power curve in Figure 3.3. The lack of a parameterization for these dynamics in the current modeling framework is thus probably responsible for the lack of quantitative agreement at lower tip-speed ratios.

The discussion of flow separation and the extent to which stall is captured in the turbine power curve emphasizes the key point that the critical nonlinearity in Equation 3.7 is the functional form of the power curve itself. In other words, the present quasi-steady modeling framework hinges on a reliable characterization of the turbine in steady flow conditions. This is a considerable advantage of the modeling approach, since it precludes the need for unsteady calibration and can thus be applied directly to the design of turbines in unsteady flow conditions when only steady-flow data are available. It also implies, however, that particular attention must be paid to the parameterization of the steady-flow power curve of the turbine. This dependence and its implications will be discussed in Section 3.5.1.

3.4.2 Upstream flow properties

We now investigate the extension of the nonlinear model for the turbine dynamics to the flow properties in the upstream induction region of the turbine. The unsteady and quasi-steady data from three selected experimental cases, all measured at $x = x_u$,

are shown in Figure 3.8. The streamwise-velocity signals showed a phase lead and increased amplitude with respect to the quasi-steady measurements. Also shown in these figures are the VCT and PDT model predictions, which align well with the shape of the phase-averaged data and anticipate the increased amplitudes and phase leads as well. For all of these cases, both models show good agreement with the velocity and pressure data, as well as with each other.

The differences between the induction predictions of the models is reflected in the induction factors estimated from the power data. The time-averaged induction factors estimated using the VCT and PDT models and correction factors are shown in Figures 3.9a and 3.9b, respectively. The induction factors all increase with increasing surge-velocity amplitude, but at different rates depending on tip-speed ratio. The trends are consistent between the two models; the main difference is that the estimated induction factors from the PDT model are slightly higher, in accordance with the model's sharper induction profile (noted previously in Figure 3.4).

The increases in time-averaged induction factor with surge-velocity amplitude are tied to increases in the thrust force exerted by the turbine on the incoming flow. According to 1D momentum theory, the thrust coefficient of the turbine is given as

$$C_t \equiv \frac{F_t}{\frac{1}{2}\rho\pi R^2 u_\infty^2} = 4\langle a\rangle\left(1-\langle a\rangle\right), \tag{3.23}$$

which, for the relatively low values of $\langle a\rangle$ considered in this study, increases with increasing $\langle a\rangle$. The induction-factor estimates in Figure 3.9 therefore suggest that the thrust force on the turbine increases with increasing surge-velocity amplitude.

This aligns with a simplified analysis of the thrust force of a turbine in an oscillating inflow. If C_t is held constant and the dimensional thrust is integrated over a sinusoidal surge-velocity waveform, as done for C_p in Equation 3.8, the time-averaged thrust enhancement is

$$\frac{\overline{F_t}}{F_{t,0}} = 1 + \frac{1}{2}u^{*2}, \tag{3.24}$$

which is also an increasing function with u^*. Although direct thrust measurements were not possible in this study due to the large inertial forces associated with the turbine motions, the induction-factor estimates and constant-C_t analysis both suggest that unsteady surge motions increase the time-averaged thrust loading on the turbine rotor. In accordance with the trends observed in the time-averaged power data in Figure 3.7b, the time-averaged thrust may decrease with increasing surge-velocity amplitudes for tip-speed ratios lower than those investigated here.

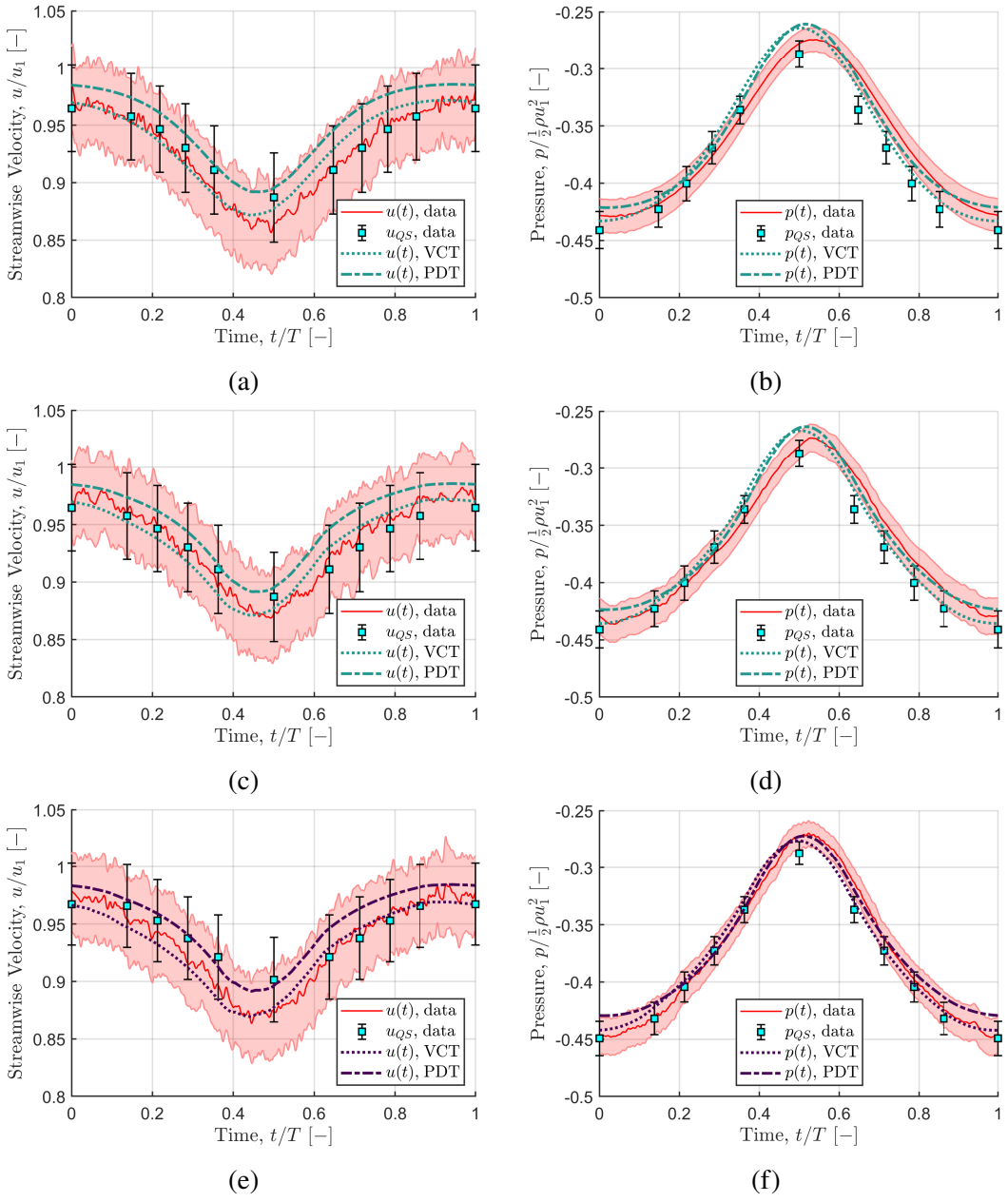

Figure 3.8: Phase-averaged velocity and pressure profiles for (a,b) a sinusoidal surge-velocity waveform with $\lambda_0 = 6.48$, (c,d) a trapezoidal waveform with $\lambda_0 = 6.48$, and (e,f) a trapezoidal waveform with $\lambda_0 = 8.77$. All surge-velocity waveforms had $u^* = 0.242$. The solid red lines represent unsteady measurements, the blue squares represent quasi-steady measurements, the dotted lines show the VCT model predictions, and the dashed-dotted lines show the PDT model predictions.

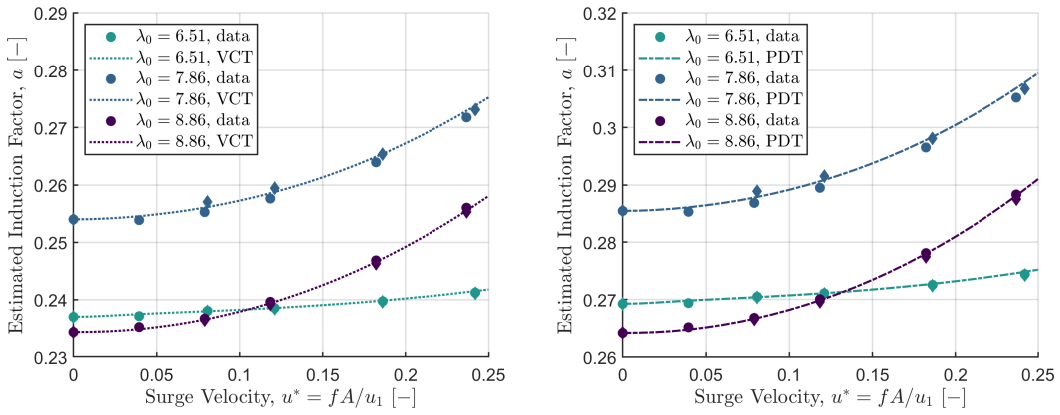

(a) (b)

Figure 3.9: Time-averaged induction-factor estimates from the (a) VCT and (b) PDT models. For these and all following figures, circles indicate sinusoidal-waveform data and diamonds denote trapezoidal-waveform data. Points are estimated from measured power data, while lines are estimated from the nonlinear dynamical model of the turbine.

The case studies in Figure 3.8 and induction-factor estimates in Figure 3.9 suggest that the VCT and PDT models produce quantitatively similar results. For the sake of clarity, Figures 3.10 through 3.12 will only show PDT predictions. The VCT predictions are qualitatively similar, and are provided for completeness in Appendix B.1.

In Figure 3.10, the amplitude and phase (relative to the surge-velocity waveform) of the estimated induction factors are presented as a function of surge-velocity amplitude. The induction-factor amplitudes and phase offsets decrease in magnitude with increasing tip-speed ratio; the highest amplitudes observed in the measured data do not exceed 12% of the time-averaged values. Good agreement between the estimates from the measured data and the estimates from the nonlinear dynamical model is observed.

Good agreement between the model predictions and measured data is also observed in the streamwise-velocity data, shown in terms of amplitude and phase (relative to the quasi-steady measurements) in Figure 3.11. As noted previously, the surge motions slightly increase the amplitude of the velocity oscillations above the quasi-steady case, and a slight phase lead accrues with increasing surge-velocity amplitude. There is some quantitative mismatch between the phase measurements and model predictions, including a plateau in the phase data at the highest surge-velocity amplitude that is not reflected by the model. Given the large experimental uncertainties in

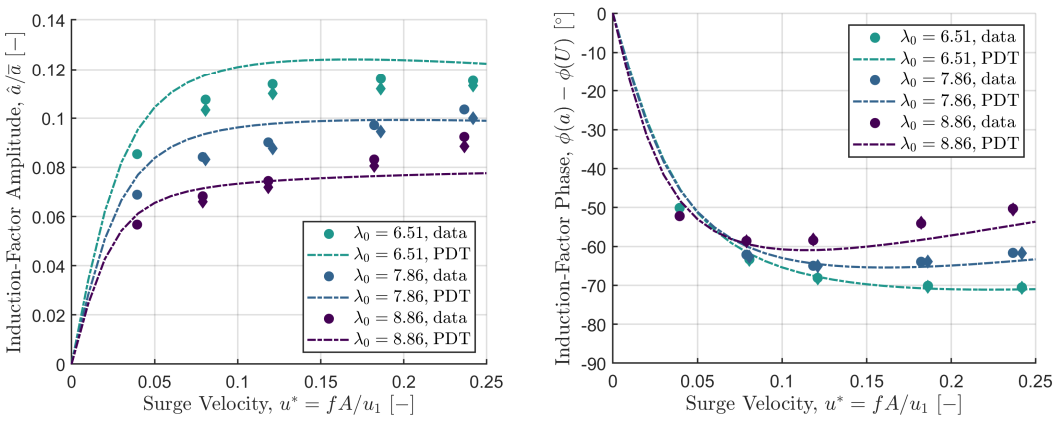

(a) (b)

Figure 3.10: (a) Amplitude and (b) phase of the estimated induction factors using the PDT model, plotted against surge-velocity amplitude. Model predictions are given as dashed-dotted lines.

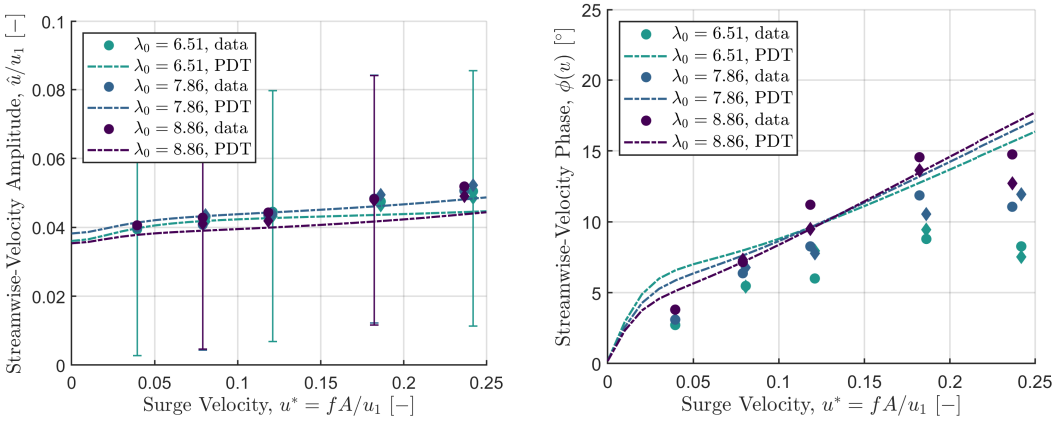

(a) (b)

Figure 3.11: (a) Amplitude and (b) phase of the measured flow velocity at $x = x_u$, plotted against surge-velocity amplitude. PDT model predictions are given as dashed-dotted lines. Error bars are plotted on every fourth point for clarity.

the streamwise-velocity measurements, this is not surprising. However, the slopes of the model-prediction lines still align with the slopes of the measured data (except for the highest surge-velocity amplitude tested), which differ slightly across tip-speed ratios. This suggests that the modeling framework is able to capture some of the more subtle differences in flow properties in the upstream induction region as the tip-speed ratio of the turbine changes.

Similar agreement in trend is observed in the pressure data, shown in amplitude and phase (relative to the quasi-steady measurements) in Figure 3.12. The slight increase in pressure amplitude as a function of surge-velocity amplitude is generally

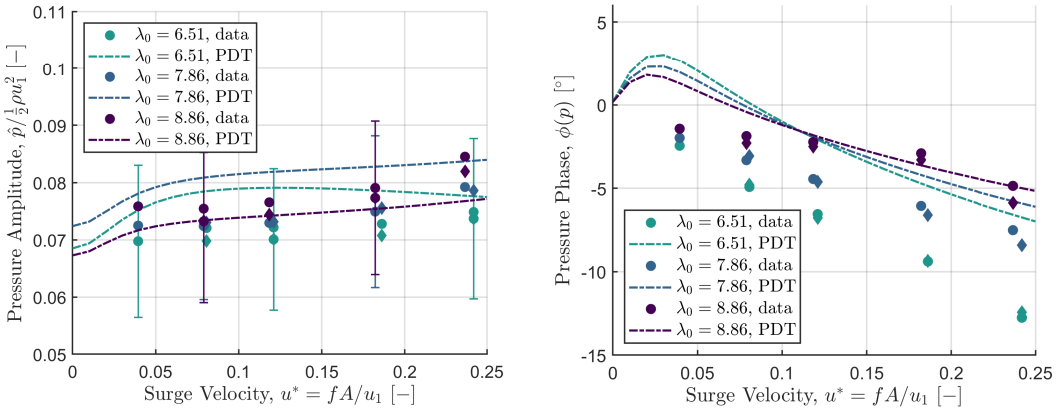

(a) (b)

Figure 3.12: (a) Amplitude and (b) phase of the measured relative pressure at $x = x_u$, plotted against surge-velocity amplitude. PDT model predictions are given as dashed-dotted lines. Error bars are plotted on every fourth point.

reflected in the model predictions, and as in the streamwise-velocity phase data, the model predictions of the pressure phase follow similar slopes to those evident in the data. Again, some quantitative differences are apparent in the plots, but given the measurement uncertainties and the relatively small magnitude of the signals being quantified and predicted, the qualitative agreement between the model predictions and measured data suggests that the modeling framework is parameterizing the salient dynamics of the system.

Finally, the time-averaged difference between the upstream and downstream pressure measurements at $x = x_u$ and $x = x_d$, respectively, is shown as a function of surge-velocity amplitude in Figure 3.13 for both the VCT and PDT models. The corresponding model predictions are calculated by evaluating the model at $x = x_u$ and $x = -x_d$, and assuming that the pressure exhibits odd symmetry about the turbine rotor plane so that $p(x = -x_d) = -p(x = x_d)$, as is the case for 1D momentum theory. For a real turbine with a low-pressure wake region, this is likely not a tenable assumption. However, the model predictions still follow the trends in the data within measurement uncertainty. The measured pressure difference can be understood as an analogue to the thrust force on the turbine, and as previously implied by the time-averaged induction-factor estimates, it increases with increasing surge-velocity amplitude. As well as further demonstrating the predictive capabilities of the modeling framework, these data suggest that the model could also be extended to serve as an initial condition for wake models of the surging turbine, which will depend on the thrust force and pressure drop across the rotor.

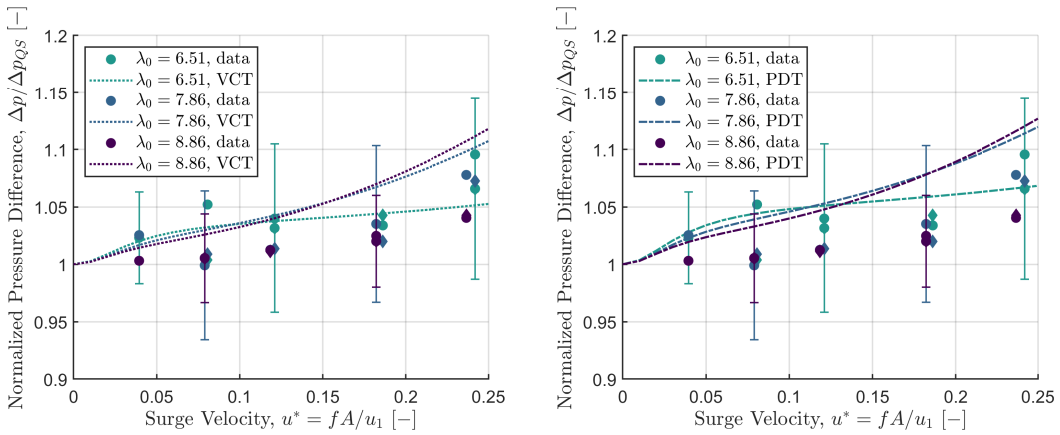

(a) (b)

Figure 3.13: Pressure difference across the turbine, $\Delta p = p(x = x_u) - p(x = x_d)$, normalized by the quasi-steady pressure difference and plotted against surge-velocity amplitude. Model predictions are given as dotted lines for the VCT model in (a) and as dashed-dotted lines for the PDT model in (b). Error bars are shown on every fourth point.

In summary, both induction-model frameworks are able to reproduce the trends observed in the centerline flow measurements recorded upstream of the turbine, and the modeling approach may have some bearing on the near-wake region downstream of the turbine as well. This observed agreement implies that the proposed modeling framework is capturing the dominant dynamics of the surging-turbine system, in spite of only incorporating empirical data from the turbine power curve and the induction-factor correction parameter κ — both of which can be obtained from steady-flow theories, simulations, or experiments. While the nonlinear dynamical model accounts for unsteady rotation accelerations of the turbine, the aerodynamics of the turbine itself are treated in a quasi-steady manner, as a function of the power curve and the induction models. The fact that this quasi-steady first-principles model still manages to align with data collected from a real surging turbine might suggest that unsteady flow physics are not unambiguously present in this system. However, the uncertainties in these experiments preclude us from ruling out this possibility, and we will thus present a theoretical analysis of the effects of unsteady flows in Section 3.5.2.

3.5 Further theoretical considerations

The experimental results presented in Section 3.4 establish the predictive capabilities of the modeling framework outlined in Section 3.2. In this section, we address

remaining considerations regarding the sensitivity of the unsteady turbine performance to its steady-flow aerodynamics and the influence of unsteady flow physics on the system. These analyses highlight potential design strategies for maximizing unsteady power enhancements with wind-energy systems in dynamic-inflow conditions.

3.5.1 Time-averaged power enhancements

The results presented in Section 3.4.1 suggested that the amount of enhancement in the time-averaged power extraction of a surging turbine relative to the steady case depends on the characteristics of the power curve of the turbine. To explore this connection further, a parametric survey using simulations of the turbine model from Equation 3.7 with simplified power curves was instantiated. For four known equilibrium points along the power curve, corresponding to four of the tip-speed ratios tested in experiments, local quadratic power curves were constructed with the form

$$C_p(\lambda) = C_p(\lambda_0) + \frac{dC_p}{d\lambda}|_{\lambda_0}(\lambda - \lambda_0) + \frac{1}{2}\frac{d^2C_p}{d\lambda^2}(\lambda - \lambda_0)^2, \tag{3.25}$$

where the local slope $\frac{dC_p}{d\lambda}|_{\lambda_0}$ was taken from the fitted power curve in Equation 3.22 and the concavity $\frac{d^2C_p}{d\lambda^2}$ was varied between -0.1 and 0.02. The four tip-speed ratios used in this exploration were $\lambda_0 = 5.47$, 6.33, 7.67, and 8.69, and the local slope of the second tip-speed ratio was approximated as zero. This parameterization created a set of power curves for each equilibrium point with identical local slope but different concavities, and the effect of changing local slope could be ascertained by comparing the simulation results across tip-speed ratios. A fixed surge-velocity amplitude of $u^* = 0.24$ was used for the simulations; other relevant parameters were $u_1 = 8$ ms^{-1}, $\rho = 1.19$ kgm^{-3}, and $\Delta t = 0.001$ s. As before, a fourth-order Runge-Kutta scheme was used to integrate the model forward in time over ten surge-oscillation periods. A strict convergence metric required the difference between successive periods to decrease monotonically; test cases that failed this criterion were deemed unstable and were not plotted.

The results of these simulations are shown in Figure 3.14, where the relative power enhancement $\overline{C_p}/C_{p,0} - 1$ is plotted as a function of power-curve concavity for the four selected tip-speed ratios. Filled circles show the concavity of the full power curve from Equation 3.22, corresponding approximately to the power gains and losses observed in Figure 3.7b at $u^* \approx 0.24$. At zero slope and zero concavity, the system reduces to the quasi-steady prediction derived by Wen *et al.* (2017) and

Johlas *et al.* (2021) (Equation 3.8, shown as a red $\times$ in the figure). Where the concavity is zero, differences are still evident across local slopes: the two highest tip-speed ratios have negative local slopes and larger power enhancements relative to the constant-C_p case. Conversely, the lowest tip-speed ratio (which has a positive local slope) exhibits the lowest power enhancement. As concavity decreases from zero, these power gains decrease and eventually become losses, finally becoming unstable below some critical concavity. Positive concavities, by contrast, show increasing power enhancements.

The influence of power-curve concavity can be understood geometrically. The dynamics of the turbine are constrained in the present model to its power curve, and thus periodic forcings represent periodic excursions along the power curve centered at some equilibrium point λ_0. First, let us assume that the local slope at λ_0 is zero. If the curve is concave-down in a neighborhood about λ_0, then the value of C_p at $\lambda_0 \pm \epsilon$ will be lower than $C_p(\lambda_0)$. Therefore, the integrated value over a periodic excursion away from λ_0 will be lower than the equilibrium value at λ_0. The opposite is true when the power curve is concave up; since $C_p(\lambda_0)$ is now a local minimum, nonzero perturbations away from λ_0 will lead to an increased time-averaged C_p. These arguments also hold qualitatively for a nonzero local slope at λ_0, though the local slope does have an influence on the time-averaged value across a periodic perturbation.

This analysis underscores the point that the geometry of the steady power curve and the equilibrium operating point of the turbine dictate the time-averaged power enhancements or losses that a surging turbine will experience relative to the steady-flow case. In general, it will be favorable to operate in regions of a power curve that have minimal concavity. In terms of turbine design, this implies that turbines whose power curves exhibit a relatively flat maximal region will benefit the most from time-averaged power enhancements relative to the steady case. Flattening the curve in this manner may be achieved through traditional turbine-design methods; alternatively, the pitch of the turbine blades could be varied within a single oscillation period to produce the same topological effect on the C_p manifold. Finally, while concave-up power curves are not typically found in current wind-energy systems, this analysis does suggest that such designs (if physically possible) would lead to even greater power enhancements in unsteady flow conditions.

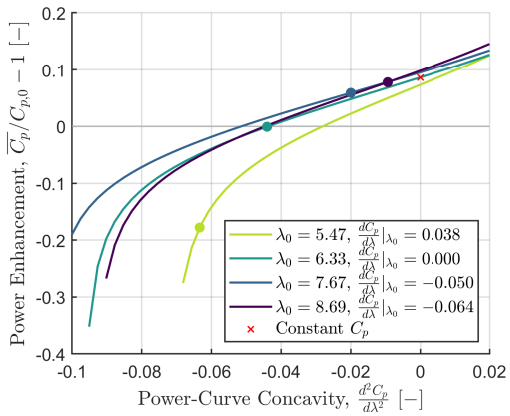

Figure 3.14: Fractional enhancements in the time-averaged coefficient of power, plotted against the concavity of the power curve (approximated as a quadratic function with fixed local slope and variable concavity), for four tip-speed ratios. A sinusoidal surge-velocity waveform with $u^* = 0.24$ was used for these simulations. The red $\times$ shows the constant-C_p solution given in Equation 3.8, and the solid circles denote the approximate concavity of the actual power curve at each reference tip-speed ratio.

3.5.2 The role of unsteady flow physics

Until this point, we have neglected the contribution of unsteady fluid mechanics to the system in question. We now investigate these effects analytically. The analysis in this section is purely theoretical, and is included to complete the conceptual picture of wind-energy systems in dynamic-inflow conditions that has been presented in this work. Thus, quantitative predictions and comparisons with the experimental results shown previously are not pursued.

3.5.2.1 Specifying velocity potentials for an unsteady extension to 1D momentum theory

To characterize the influence of streamwise unsteadiness on the theoretical efficiency of wind-energy systems, we extend the analytical framework of Dabiri (2020) using the potential-flow modeling approach proposed in Section 3.2.3. This unsteady extension to the 1D momentum theory of Betz uses the same control volume shown in Figure 3.1, but makes use of two additional unsteady terms:

$$\frac{d}{dt}\left[KE\right] = \frac{d}{dt}\left[-\frac{1}{2}\rho \iint_{A_2} \phi \hat{n} \cdot \nabla \phi dA\right], \tag{3.26}$$

which represents the unsteady power associated with changes in the streamwise kinetic energy of the actuator disc, and

$$\Phi_t = \frac{\partial \phi_2}{\partial t} - \frac{\partial \phi_3}{\partial t}, \tag{3.27}$$

which is the difference in the unsteady potential across the face of the actuator disc. These quantities are accounted for in energy-conservation relations to obtain expressions for the time-averaged unsteady power. Here, we use A_i to refer to the cross-sectional area at streamwise location i; this is not to be confused with the surge-motion amplitude A used elsewhere in this work.

By specifying a velocity potential for the moving actuator disc, we aim to close these two terms and parameterize the instantaneous and time-averaged coefficients of power as a function of the induction factor (as in the steady Betz analysis) and the surge kinematics of the actuator disc. For the sake of simplicity, we will assume that the induction factor a varies in a quasi-steady manner, and will not consider time-derivatives of a. Additionally, we only consider the velocity potential associated with the surge velocity $U(t)$, and assume that the velocity potential connected to the free-stream velocity u_1 has no unsteady contribution. We begin by completing the analysis for a moving porous disc, and then explore the effects of more general classes of velocity potentials. For the sake of brevity, we omit intermediate steps in the derivations here; several of these details are provided in Appendix B.2.

From Equation 3.15, the velocity potential for a moving porous disc located instantaneously at $x = x_2$ can be written as

$$\phi\,(r,x) = a(u_1 - U)\sqrt{\frac{2}{\pi}}R^{3/2}\int_0^\infty s^{-1/2}J_{3/2}(Rs)J_0(rs)e^{s(x-x_2)}ds;\ x < x_2, \quad (3.28)$$

and from this expression, the kinetic energy of the disc moving at velocity U can be derived as

$$KE_{disc} = \frac{4}{3}\rho a^2 U^2 R^3 \quad (3.29)$$

(cf. Lamb, 1916, Art. 102, Eq. 20). The time derivative is therefore

$$\frac{d}{dt}\left[KE_{disc}\right] = \frac{8}{3}\rho R^3 a^2 U\frac{dU}{dt}. \quad (3.30)$$

The unsteady-potential term Φ_t can be computed by applying the chain rule to Equation 3.28, which gives

$$\frac{\partial\phi_2}{\partial t} = -\frac{2}{\pi}a\sqrt{R^2 - r^2}\frac{dU}{dt} + aU^2. \quad (3.31)$$

Using the odd extension to model the region immediately downstream of the disc, we obtain an expression for $\frac{\partial\phi_3}{\partial t}$ that is identical except that the first term in positive. Averaging this over the area of the disc gives

$$\langle\Phi_t\rangle \equiv \Phi_{t,disc} = -\frac{8R}{3\pi}a\frac{dU}{dt}. \quad (3.32)$$

These results may now be introduced into the framework of Dabiri (2020), with some additional considerations that reduce the parameter space of the theory. The unsteady power associated with the motion of the disc leads to a difference between the available power upstream and downstream of the disc (cf. Dabiri, 2020, Eq. 11):

$$\frac{1}{2}\rho A_2\left(u_2^3 - u_3^3\right) = \frac{d}{dt}\left[KE\right]. \tag{3.33}$$

Defining additional induction factors $b = 1 - u_3/u_1$ and $c = 1 - u_4/u_1$, this expression can be written as

$$(1-a)^3 - (1-b)^3 = \frac{2}{\rho A_2 u_1^3}\frac{d}{dt}\left[KE\right], \tag{3.34}$$

which we can solve for b in terms of a:

$$b = 1 - \left[(1-a)^3 - \frac{2}{\rho A_2 u_1^3}\frac{d}{dt}\left[KE\right]\right]^{1/3}. \tag{3.35}$$

A nondimensional form of the momentum equation for this problem can be written by means of the unsteady Bernoulli equation as

$$-2c(1-a) = (1-c)^2 + (1-a)^2 - (1-b)^2 - 1 + \frac{2\Phi_t}{u_1^2}, \tag{3.36}$$

which can be solved for the remaining induction factor c as

$$c = a \pm \sqrt{2a - 1 + (1-b)^2 - \frac{2\Phi_t}{u_1^2}}. \tag{3.37}$$

In this expression, the larger root is taken to satisfy the physical requirement that the flow must slow down between locations 2 and 4, which implies $c > a$. Having written the additional induction factors b and c in terms of the original induction factor a and the known unsteady contributions $\frac{d}{dt}[KE]$ and Φ_t, we can find the instantaneous coefficient of power using the relation

$$C_p = \frac{1}{2}\left(4c - 4c^2 + c^3\right) + \frac{1}{2}(2-c)\left[(1-b)^2 - (1-a)^2\right] - (2-c)\left(\frac{\Phi_t}{u_1^2}\right). \tag{3.38}$$

This expression is limited by the physical constraints $b \in [0,1]$, $c \in [0,1]$, and $C_p \geq 0$, which enforce that the velocities at locations 3 and 4 cannot be negative or exceed the free-stream velocity, and that the power extracted from the actuator disc cannot be negative. This analysis does not account for quasi-steady changes in C_p due to the normalization by the effective inflow velocity $u_1 - U(t)$; therefore, changes in $\overline{C_p}$ predicted by this theoretical framework will appear in practice as adjustments to the time-averaged power predictions of the quasi-steady modeling approach outlined in Section 3.2.1.

3.5.2.2 Phase-plane analysis of a surging porous disc

While Dabiri (2020) assumed that the parameters a, b, c, and Φ_t were independent, we now have a theoretical framework that only depends on the induction factor a and the surge kinematics of the actuator disc, U and $\frac{dU}{dt}$. For a given induction factor, we may therefore use the system of equations described above to construct a phase portrait for C_p in terms of the surge kinematics. Contours of C_p in the U-$\frac{dU}{dt}$ phase plane are shown for four values of a (0.21, 0.27, 1/3, and 0.40) in Figure 3.15. The orange contour marks the Betz efficiency ($C_p/C_{p,Betz} = 1$), and grey regions represent locations in the phase plane where one of the physical constraints on C_p is violated.

If a is constant, a surge waveform will appear as a periodic loop in the phase plane that must be centered on the origin so that the turbine has no net displacement. A sinusoidal waveform will follow an elliptical trajectory about the origin, while a trapezoidal waveform will appear as a rectangular trajectory. The time-averaged coefficient of power is calculated by evaluating the line integral of C_p along one closed cycle of this trajectory. The depiction of C_p in the phase plane thus allows the effects of the unsteady velocity potential and power terms from the porous disc to be evaluated by topological reasoning.

To illustrate this line of argumentation, we consider the case where $a = 1/3$ (Figure 3.15c). A trajectory that is centered on the origin will experience instantaneous values of C_p in excess of the steady-flow Betz limit for positive surge accelerations, while C_p will decrease below $C_{p,Betz}$ for negative surge accelerations. However, the slope of the contours of C_p is greater below the Betz-limit contour than above it. Thus, for a nonzero surge trajectory, the lower C_p values sampled below the zero-acceleration axis will outweigh the higher C_p values sampled above the axis, and the time-averaged coefficient of power will be lower than the steady coefficient of power. This mathematical effect is qualitatively similar to the concavity-based arguments described above in Section 3.5.1.

For values of a that are above or below the steady-flow optimal value of $1/3$, the same arguments hold: the topology of C_p in the phase plane implies that nontrivial surge motions will yield a decrease in time-averaged efficiency as a result of unsteady effects. Furthermore, if a is allowed to vary in a quasi-steady manner, the surge trajectory will exist in a three-dimensional phase space spanned by U, $\frac{dU}{dt}$, and a. Ascertaining the precise differences in time-averaged power extraction may be done numerically for a given profile of $a(t)$, e.g. one obtained from the amplitude and

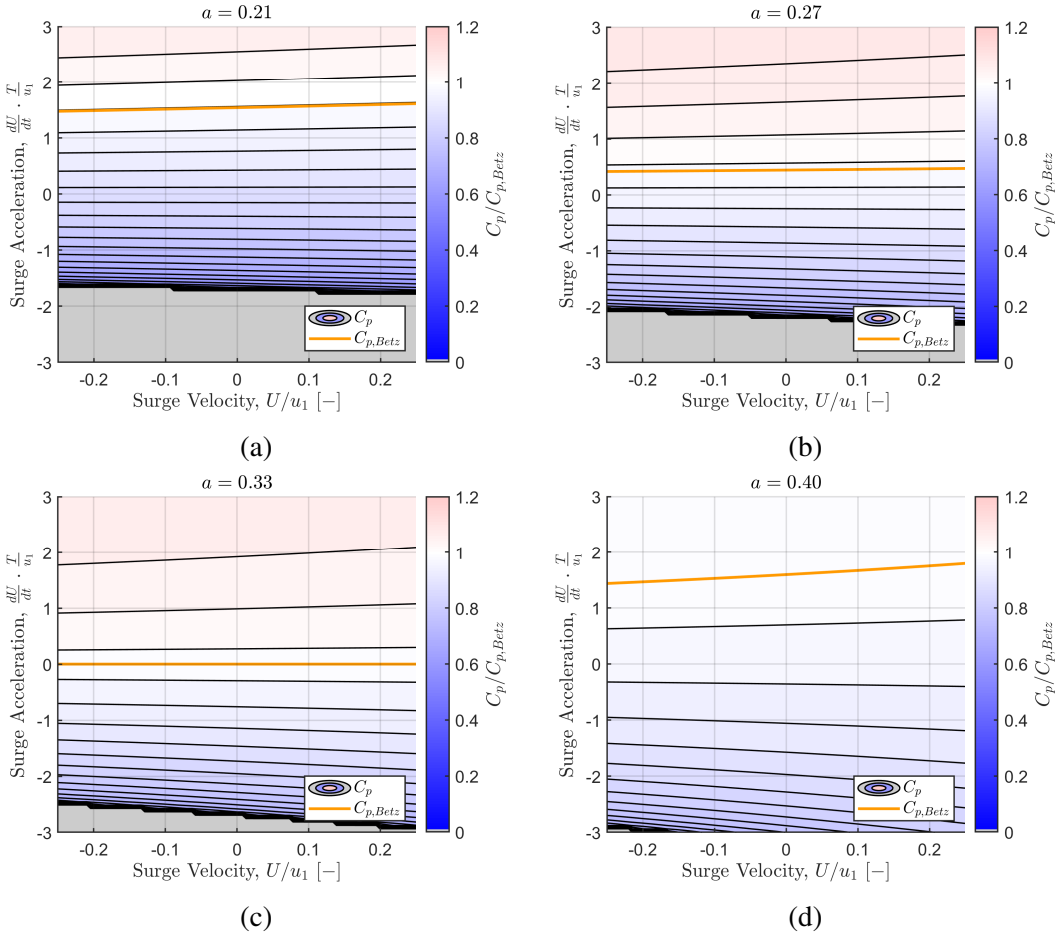

Figure 3.15: Contours of $C_p/C_{p,Betz}$ calculated from Equation 3.38 for a moving porous disc, plotted in the surge-kinematics phase plane as a function of surge velocity and acceleration for induction factors of (a) 0.21, (b) 0.27, (c) 1/3, and (d) 0.40. The orange line indicates $C_p = C_{p,Betz}$, and grey regions denote dynamics that violate one or more assumptions of the theoretical framework. To nondimensionalize the surge acceleration, T is taken to be 1 s.

phase data shown in Figure 3.10. Still, as the region in the phase plane where efficiencies above the steady Betz limit occur moves away from the origin for $a \neq 1/3$, it is apparent that oscillations in a will further decrease the time-averaged efficiency of the system.

3.5.2.3 General velocity potentials and the effects of fore-aft asymmetry

We have shown that the unsteady contribution to the time-averaged efficiency of a wind-energy system modeled as a surging porous disc is negative. However, efficiency enhancements may be attained with a different choice of velocity potential. Consider a general velocity potential for a moving body with translation velocity **U**,

angular velocity $\mathbf{\Omega}$, and circulation Γ, located instantaneously at a point $\mathbf{x} = \mathbf{x_0}$ in an otherwise quiescent fluid:

$$\phi(\mathbf{x}) = \mathbf{U} \cdot \mathbf{\Xi} + \mathbf{\Omega} \cdot \mathbf{\Theta} + \Gamma \left(\frac{\theta}{2\pi} + \psi \right) \tag{3.39}$$

(Batchelor, 2000, Eq. 6.4.10). Here, boldfaced variables refer to vectors in 3-space. The functions $\mathbf{\Xi}$, $\mathbf{\Theta}$, and ψ are geometric descriptors that only depend on location relative to the body, $\mathbf{x} - \mathbf{x_0}$. For bodies producing zero circulation, $\Gamma = 0$. We also ignore the effect of rotation and set $\mathbf{\Omega} = 0$. (The effect of rotation is explained in Appendix B.2.) The translational kinetic energy associated with such a moving body scales as U^2, and thus the unsteady power term will always scale as

$$\frac{d}{dt}[KE] \sim U \frac{dU}{dt}, \tag{3.40}$$

irrespective of the body geometry parameterized by the function $\mathbf{\Xi}$.

The time derivative of the velocity potential, on the other hand, is affected by body geometry. This can be written as

$$\frac{\partial \phi}{\partial t} = \frac{d\mathbf{U}}{dt} \cdot \mathbf{\Xi} - \mathbf{U} \cdot \mathbf{u} \tag{3.41}$$

(Batchelor, 2000, Eq. 6.4.22), where $\mathbf{u}$ is the local flow velocity at $\mathbf{x}$. To compute Φ_t from the unsteady theoretical framework, we assume that the local flow velocity in the quiescent-fluid frame at streamwise locations 2 and 3 scales with the velocity of the body, U. Additionally, since the velocity on either side of the translating body must decrease with increasing distance from the body, the geometric function $\mathbf{\Xi}$ must exhibit odd symmetry about the body plane.

For a translating symmetric body in potential flow, $\mathbf{u}$ on either side of the body will be identical. Therefore, when taking the difference of the unsteady-potential terms upstream and downstream of the body, the $\mathbf{U} \cdot \mathbf{u}$ term will cancel. The odd symmetry of the geometric function $\mathbf{\Xi}$ will retain the acceleration-dependent term, and thus for a symmetric body, we have

$$\Phi_t \sim R \frac{dU}{dt}. \tag{3.42}$$

For a body that exhibits fore-aft asymmetry about its flow-normal center plane, however, $\mathbf{u}$ may differ across the upstream and downstream sides of the body. In this case, the quadratic velocity term may not cancel, suggesting that

$$\Phi_t \sim R \frac{dU}{dt} \pm U^2. \tag{3.43}$$

The additional dependence on U^2 will change the topology of C_p in the phase plane and affect the time-averaged coefficients of power that are possible in the theoretical framework.

To illustrate these effects, we conduct a phase-plane analysis by assuming the existence of a velocity potential for a moving asymmetric body that yields

$$\Phi_t = -\frac{8}{3\pi} a \left(R \frac{dU}{dt} + U^2 \right). \tag{3.44}$$

We keep the same scaling coefficients as for the surging porous disc for the sake of comparison, and use the same expression for the kinetic energy of the body (Equation 3.30). Contours of C_p for the same four values of a shown previously are given for this representative model in Figure 3.16. We again first consider the case where $a = 1/3$ (Figure 3.16c). Here, we observe that the addition of the U^2 term in the expression for Φ_t has curved the contours of C_p such that the region where $C_p > C_{p,Betz}$ now extends below the zero-acceleration axis. This implies that a trajectory centered on the origin can have a time-averaged efficiency that exceeds the steady Betz limit. This may also be possible if we allow for small oscillations in a, depending on the surge kinematics applied and their corresponding trajectories in the phase space.

If the sign of the U^2 term in Equation 3.44 were reversed, the concavity of the contours would also be reversed, leaving the region where $C_p > C_{p,Betz}$ on the interior of a concave-up parabola with respect to the surge velocity. In this scenario, a periodic trajectory will spend less time in the efficiency-enhancing region relative to the efficiency-depleting region, and the time-averaged efficiency will therefore drop below the steady Betz limit. Thus, fore-aft asymmetry in the velocity potential is a necessary but not sufficient condition for enhancements in the time-averaged efficiency of a periodically translating actuator body.

This conceptual exercise demonstrates that, for symmetric bodies in potential flow, the unsteady contribution to time-averaged efficiency will be negative. As the modeling efforts and experiments presented previously seem to suggest that a moving porous-disc model captures the dominant dynamics of a periodically surging horizontal-axis wind turbine, it is likely that unsteady effects would act against the time-averaged power enhancements described in Section 3.5.1 above. This hypothesis appears to be consistent with the time-averaged power data shown in Figure 3.7b, which at high surge-velocity amplitudes tend to be overpredicted by the nonlinear turbine model (which assumes quasi-steady aerodynamics). However,

wind-energy systems need not be symmetric. Streamwise asymmetries across the rotor plane could be introduced either mechanically, through the geometry of the turbine, or dynamically, through intracycle blade-pitch or generator-load control. These non-traditional design and control paradigms could create beneficial asymmetries in the equivalent velocity potential of the system that could be leveraged to achieve higher time-averaged efficiencies than steady-flow or quasi-steady analyses would suggest. In the case of dynamic induction-control schemes, the influence of unsteady induction-factor variations $\frac{da}{dt}$ may no longer be negligible, and the analysis presented here would need to be expanded to include these variations in a four-dimensional phase space. Still, the present analysis can serve as a helpful theoretical framework for characterizing trends in unsteady contributions to the efficiency of wind-energy systems.

3.6 Conclusions

In this work, a nonlinear dynamical model for the power generation of a periodically surging wind turbine was paired with a potential-flow model for the flow properties upstream of the turbine. This modeling framework was shown to reproduce trends in experimental measurements of both the time-averaged power extraction and upstream flow-velocity and pressure, at surge-velocity amplitudes of up to 24% of the wind speed. These results are posited to be equally applicable to stationary turbines in dynamically varying inflow conditions, such as axial gusts. A key advantage of this approach is that the entire modeling approach is calibrated only by steady-flow quantities: the turbine power curve and the radial induction profile of the turbine at the rotor plane. The theoretical analyses also identified and parameterized contributions to power-extraction enhancements over the steady-flow case, such as a dependence on the local concavity of the turbine power curve and the role of streamwise asymmetries in unsteady power gains. This work thus not only informs the design, characterization, and control of wind and hydrokinetic turbines in unsteady flow environments, such as floating offshore wind farms and tidal currents, but also yields fundamental insights into the relative influences of quasi-steady and unsteady fluid mechanics in energy-harvesting systems.

While similar theoretical tools have been widely applied to the analysis of wind turbines in steady flow, a major contribution of this work is the extension of these methods to unsteady flow contexts. The porous-disc model is also similar in principle to the actuator-disc models often used in numerical simulations of large wind

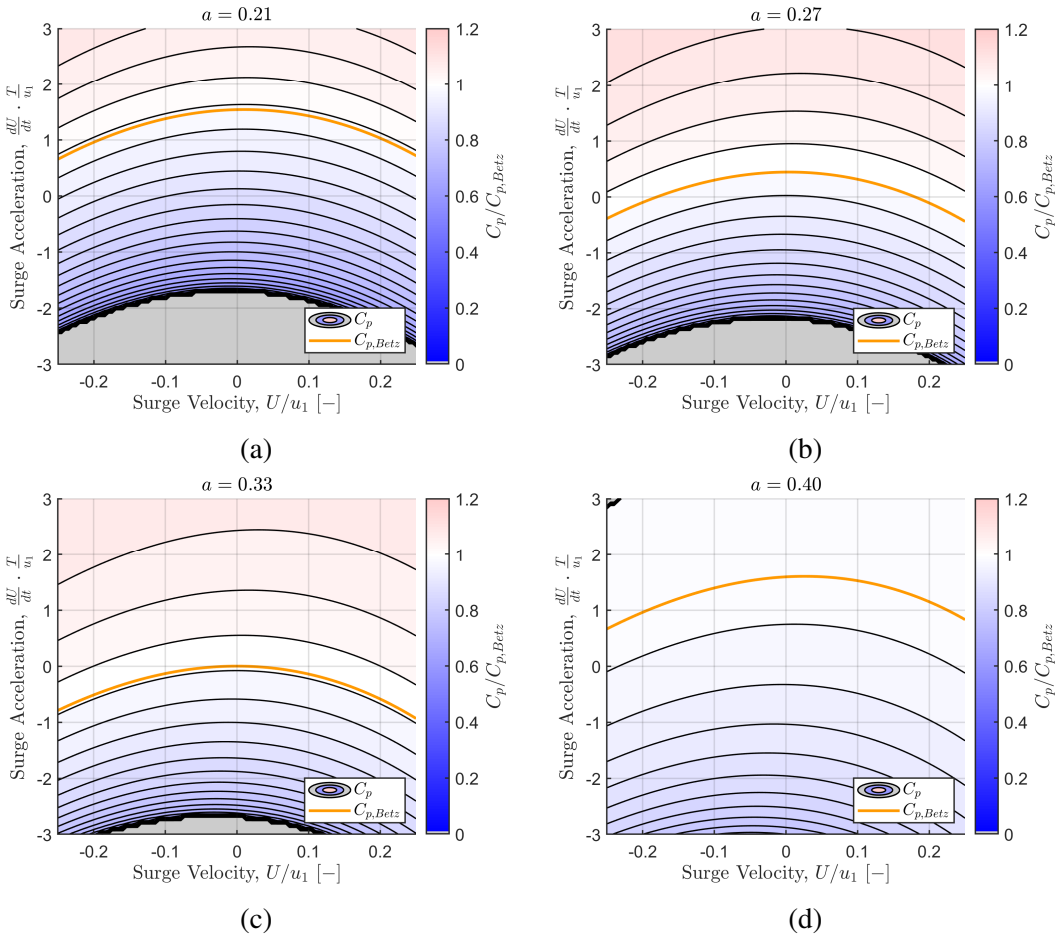

Figure 3.16: Contours of $C_p/C_{p,Betz}$ for a moving porous asymmetric body (parameterized by Equation 3.44), plotted in the surge-kinematics phase plane as a function of surge velocity and acceleration for induction factors of (a) 0.21, (b) 0.27, (c) 1/3, and (d) 0.40. The orange line indicates $C_p = C_{p,Betz}$, and grey regions denote dynamics that violate one or more assumptions of the theoretical framework.

farms (e.g. Calaf *et al.*, 2010; Stevens and Meneveau, 2017), and thus this study could inform modifications of existing actuator-disc simulations for surging-turbine or dynamic-inflow conditions. This may be particularly useful for large-eddy simulations (LES) of floating offshore turbine arrays, where the analytical turbine model can help to parameterize the coupling between turbine inflow conditions, sea-surface waves, and floating-platform dynamics. Additionally, the induction and thrust-force predictions of this modeling framework could be used as initial conditions for wake models of turbines in dynamic inflow conditions, which could further improve parameterizations of turbine aerodynamics in numerical simulations. Such a connection was recently developed for yawed turbines by Heck *et al.* (2023), whose modeling philosophy was influential in the development of the present analytical

approach. These wake-modeling initiatives would further benefit from the work of Steiros and Hultmark (2018) and Bempedelis and Steiros (2022), particularly for capturing wake-pressure effects in highly loaded turbine configurations.

This work has several implications for full-scale wind-energy systems in real-world flow conditions. First, the analytical model for flow properties upstream of a surging turbine can be used in conjunction with nacelle-mounted LiDAR units for improved load control and wind-speed estimation in floating offshore applications. The same principles can be applied to stationary turbines in gusty environments and kite-mounted aerial turbines. Secondly, these analytical and experimental results reinforce and parameterize the evidence collected by Wen *et al.* (2017), El Makdah *et al.* (2019), Johlas *et al.* (2021), and Wei and Dabiri (2022) that streamwise unsteadiness (either in the flow or in the turbine itself) can lead to increases in power extraction above the reference steady case. The present investigations suggest both quasi-steady and unsteady mechanisms that can be exploited to capitalize on these power-extraction enhancements. Future work can investigate turbine design and control strategies, such as active blade pitching and intracycle load control (e.g. Strom *et al.*, 2017), that may further increase the time-averaged power extraction of floating offshore wind turbines and other systems that can operate in inherently unsteady flows. The modeling framework also provides a means to estimate thrust loads on turbines from dynamic inflow conditions, which may increase fatigue loading on turbine blades and support structures. The analytical tools outlined in this study can inform control strategies that anticipate the changes in thrust and blade loading as a function of changing inflow conditions and dynamically adjust the blade pitch or generator load to mitigate the unsteady loads of unwanted disturbances and oscillations. Whether these models are used to enhance unsteady power-conversion gains or extend the operational lifespan of energy-harvesting systems by controlling unsteady loads, this work makes the case that unsteady flow phenomena should be at the forefront of design considerations for structures operating in the atmosphere and ocean.

Acknowledgements

The authors would like to thank Michael Howland for several enlightening conversations regarding the development of the nonlinear dynamical model and its connection to induction effects. The authors also would like to thank Konstantinos Steiros for sharing resources that helped with the derivation of the porous-disc

model, and the three anonymous referees assigned by the *Journal of Fluid Mechanics* for their feedback and suggestions, which greatly strengthened the analysis and conclusions of this study. The authors additionally appreciate the assistance and safety supervision of Malaika Cordeiro, Matthew Fu, and Peter Gunnarson during the experiments. Finally, the authors recognize discussions with David Rival, Tim Colonius, and Paul Dimotakis that helped clarify the reference-frame considerations described in Section 3.2.4.

This work was supported by the National Science Foundation (grant number CBET-2038071) and the Caltech Center for Autonomous Systems and Technologies. Nathaniel Wei was supported by a National Science Foundation Graduate Research Fellowship.

Chapter 4

Field Measurements of the Near-Wake Structure of Full-Scale Vertical-Axis Wind Turbines

The contents of this chapter have been reproduced from Wei *et al.* (2021), published in the Journal of Fluid Mechanics under the title "Near-wake structure of full-scale vertical-axis wind turbines." As the first author, Nathan Wei made the primary contributions to data processing, data analysis, modeling, and writing, and also conducted the artificial-snow validation experiments described in the appendix of this work. Ian Brownstein oversaw the conceptualization, planning, and execution of the field experiments, and Jen Cardona and Mike Howland assisted with data collection. John Dabiri contributed to the conceptualization of the study, funding acquisition, and analysis and interpretation of the results. All co-authors provided input on the final manuscript draft.

In addition, large-eddy simulations of the field-experiment scenario were conducted by collaborators from the University of Houston and have been published in the Journal of Renewable and Sustainable Energy (Gharaati *et al.*, 2022). Though these results are not discussed in this chapter, many qualitative similarities can be observed between the experimental and simulation data, and the simulations provide time-resolved evidence of the vortex-motion mechanisms described in this work. Nathan Wei contributed to the conceptualization of the numerical study, the interpretation of its results, and feedback on the manuscript.

Abstract

To design and optimize arrays of vertical-axis wind turbines (VAWTs) for maximal power density and minimal wake losses, a careful consideration of the inherently three-dimensional structure of the wakes of these turbines in real operating conditions is needed. Accordingly, a new volumetric particle-tracking velocimetry method was developed to measure three-dimensional flow fields around full-scale VAWTs in field conditions. Experiments were conducted at the Field Laboratory for Optimized Wind Energy (FLOWE) in Lancaster, CA, using six cameras and ar-

tificial snow as tracer particles. Velocity and vorticity measurements were obtained for a 2-kW turbine with five straight blades and a 1-kW turbine with three helical blades, each at two distinct tip-speed ratios and at Reynolds numbers based on the rotor diameter D between 1.26×10^6 and 1.81×10^6. A tilted wake was observed to be induced by the helical-bladed turbine. By considering the dynamics of vortex lines shed from the rotating blades, the tilted wake was connected to the geometry of the helical blades. Furthermore, the effects of the tilted wake on a streamwise horseshoe vortex induced by the rotation of the turbine were quantified. Lastly, the implications of these dynamics for the recovery of the wake were examined. This study thus establishes a fluid-mechanical connection between the geometric features of a VAWT and the salient three-dimensional flow characteristics of its near-wake region, which can potentially inform both the design of turbines and the arrangement of turbines into more efficient arrays.

4.1 Introduction

Wind turbines are becoming increasingly important contributors to global energy supplies, as they represent a low-carbon alternative to traditional power-generation technologies that rely on the combustion of fossil fuels. If wind power is to comprise a larger share of global energy production, the efficiency and power density of wind farms will need to be improved (Jacobson and Archer, 2012). The critical limitation of these large arrays is not the efficiency of individual wind turbines, which already operate at efficiencies approaching their theoretical maximum (Betz, 1920), but rather the dynamics of wind-turbine wakes and their effects on downstream turbines (Stevens and Meneveau, 2017). The efficiency of the large-scale deployment of wind power thus depends largely on a more careful consideration of the wake dynamics of wind turbines.

Horizontal-axis wind turbines (HAWTs) typically have long wakes that extend up to 20 turbine diameters (D) downstream of the turbine itself (Vermeer *et al.*, 2003; Meyers and Meneveau, 2012; Hau, 2013b; Stevens and Meneveau, 2017), although wake persistence may vary with field conditions (e.g. Nygaard and Newcombe, 2018). HAWTs placed in closely packed arrays therefore generally incur significant losses from the wakes of upstream turbines (e.g. Barthelmie *et al.*, 2007; Barthelmie and Jensen, 2010; Barthelmie *et al.*, 2010). Vertical-axis wind-turbine (VAWT) wakes, by contrast, have been observed to recover their kinetic energy within 4 to 6 D downstream of the turbine, albeit with lower individual coefficients of thrust

and power (Kinzel *et al.*, 2012; Kinzel *et al.*, 2015; Ryan *et al.*, 2016). VAWTs can also be arranged in pairs, to capitalize on synergistic fluid interactions between the turbines (e.g. Rajagopalan *et al.*, 1990; Brownstein *et al.*, 2016; Ahmadi-Baloutaki *et al.*, 2016; Hezaveh *et al.*, 2018; Brownstein *et al.*, 2019). Taken together, these factors imply that arrays of VAWTs can potentially achieve power densities an order of magnitude higher than those of conventional wind farms (Dabiri, 2011).

The dynamics of VAWT wakes are therefore relevant to the design of large-scale wind farms with higher energy densities, and accordingly have been analyzed in several recent studies. The replenishment of momentum in both HAWT and VAWT wakes has been shown to be dependent on turbulent entrainment of fluid from above the turbine array, through modeling (Meneveau, 2012; Luzzatto-Fegiz and Caulfield, 2018), simulations (Calaf *et al.*, 2010; Hezaveh and Bou-Zeid, 2018), wind-tunnel experiments (Chamorro and Porté-Agel, 2009; Cal *et al.*, 2010), and field experiments (Kinzel *et al.*, 2015). VAWTs also exhibit large-scale vortical structures in their wakes that may further augment wake recovery. These vortex dynamics have been observed in scale-model studies of varying geometric fidelity, from rotating circular cylinders (Craig *et al.*, 2016) to complete rotors (e.g. Tescione *et al.*, 2014; Brownstein *et al.*, 2019). The inherently three-dimensional nature of these vortical structures, coupled with the high Reynolds numbers of operational VAWTs, complicates experimental and numerical studies of the dynamics of VAWT wakes.

Accordingly, numerical simulations with varying levels of complexity have been applied to study VAWT wakes. For studies of wake interactions within arrays, two-dimensional (2D) Reynolds-averaged Navier-Stokes (RANS) simulations have often been employed (e.g. Bremseth and Duraisamy, 2016; Zanforlin and Nishino, 2016). Large-eddy simulation (LES) studies have generally used actuator-line models to approximate the effects of the individual blades on the flow (e.g. Shamsoddin and Porté-Agel, 2014; Shamsoddin and Porté-Agel, 2016; Abkar and Dabiri, 2017; Hezaveh and Bou-Zeid, 2018; Abkar, 2018). Posa *et al.* (2016) and Posa and Balaras (2018) were able to resolve the unsteady vortex shedding of individual blades in the spanwise component of vorticity using LES with periodic boundary conditions in the spanwise direction, which meant that tip-vortex shedding was not captured. More recently, Villeneuve *et al.* (2020) used delayed detached-eddy simulations (DDES) and a fully three-dimensional turbine model in a rotating overset mesh to study the effects of end plates on VAWT wakes, resolving 3D vortex shedding and

the wake dynamics up to 10 D into the wake. Numerical simulations have thus continued to improve in their capacity to resolve the salient dynamics in the wakes of VAWTs.

Laboratory- and field-scale experiments have been extensively employed to characterize the wake dynamics of HAWTs over a large range of configurations and inflow conditions (e.g. Chamorro and Porté-Agel, 2009; Bastankhah and Porté-Agel, 2017; Schottler *et al.*, 2017; Bartl *et al.*, 2018), and similar laboratory-scale experiments have proved invaluable for the analysis of the wake structures of VAWTs as well. Experiments with VAWTs, however, have generally been limited to planar measurements in the laboratory (e.g. Brochier *et al.*, 1986; Ferreira *et al.*, 2009; Battisti *et al.*, 2011). The deployment of stereoscopic particle-image velocimetry (stereo-PIV) has allowed some three-dimensional effects to be captured (Tescione *et al.*, 2014; Rolin and Porté-Agel, 2015; Rolin and Porté-Agel, 2018), as has the use of planar PIV with multiple imaging planes (Parker and Leftwich, 2016; Parker *et al.*, 2017; Araya *et al.*, 2017). These planar techniques have been successful in identifying characteristic vortex phenomena, such as dynamic stall on turbine blades (Ferreira *et al.*, 2009; Dunne and McKeon, 2015; Buchner *et al.*, 2015; Buchner *et al.*, 2018) and tip-vortex shedding from the ends of individual blades (Hofemann *et al.*, 2008; Tescione *et al.*, 2014). Generally, however, it is difficult to compute all three components of vorticity or the circulation of vortical structures with purely planar measurements. The analysis of the three-dimensional character of vortical structures in the wake is therefore greatly facilitated by fully three-dimensional flow-field measurements. Such experiments have only recently been carried out in laboratory settings. Using tomographic PIV, Caridi *et al.* (2016) resolved the three-dimensional structure of tip vortices shed by a VAWT blade within a small measurement volume with a maximum dimension of 5.5 blade chord lengths. Ryan *et al.* (2016) obtained 3D time-averaged velocity and vorticity measurements of the full wake of a model VAWT using magnetic-resonance velocimetry (MRV). Most recently, Brownstein *et al.* (2019) used 3D particle-tracking velocimetry (PTV) to obtain time-averaged measurements of the wakes of isolated and paired VAWTs. These studies were all carried out at laboratory-scale Reynolds numbers, which fell between one and two orders of magnitude below those typical of operational VAWTs. Miller, Duvvuri, Brownstein, *et al.* (2018) attained Reynolds numbers up to $Re_D = 5 \times 10^6$ using a compressed-air wind tunnel, and their measurements of the coefficients of power demonstrated a Reynolds-number invariance for $Re_D > 1.5 \times 10^6$. These power measurements suggest that Reynolds numbers on the order of 10^6 may be required

to fully capture the wake dynamics of field-scale turbines. As an alternative to laboratory experiments at lower Re_D, experiments in field conditions at full scale are possible, but these have been limited to pointwise anemometry (Kinzel *et al.*, 2012; Kinzel *et al.*, 2015) or 2D planar velocity measurements (Hong *et al.*, 2014). Thus, for the validation and extension of existing experimental work on the wake dynamics of VAWTs, 3D flow measurements around full-scale VAWTs in field conditions are desirable.

The additional benefit of 3D flow measurements is that they enable the effects of complex turbine geometries on wake structures to be investigated. This is particularly useful for VAWTs, since several distinct geometric variations exist. Because of the planar constraints of most experimental and numerical studies, VAWTs with straight blades and constant spanwise cross-sections have primarily been studied due to their symmetry and simplicity of construction. However, there exist several VAWT designs that incorporate curved blades. Large-scale Darrieus-type turbines have blades that are bowed outward along the span, and these have historically reached larger sizes and power-generation capacities than straight-bladed turbines (Möllerström *et al.*, 2019). Similarly, many modern VAWTs have helical blades that twist around the axis of rotation, following the design of the Gorlov Helical Turbine (Gorlov, 1995), to reduce fatigue from unsteady loads on the turbine blades. Relatively few studies have investigated the flow physics of these helical-bladed VAWTs in any kind of detail. Schuerich and Brown (2011) used a vorticity-transport model for this purpose, and Cheng *et al.* (2017) approached the problem using unsteady RANS, 2D LES, and wind-tunnel experiments. Aliferis *et al.* (2019) studied the 2D planar wake structure of a Savonius-type VAWT with helical blades using a Cobra probe on a traverse. Lastly, Ouro *et al.* (2019) analyzed turbulence quantities in the wake of a helical-bladed VAWT in a water channel using pointwise velocity measurements from an anemometer on a traverse. A full treatment of the effects of the helical blades on the three-dimensional vorticity fields and corresponding vortical structures in the wake has yet to be undertaken.

Thus, the purpose of this work is to study the three-dimensional flow features of operational VAWTs in the field. The work revolves around two primary contributions: the development of a field-deployed 3D-PTV measurement system, and the analysis of topological and dynamical characteristics of vortical structures in the wakes of full-scale VAWTs. First, the characterization of the artificial-snow-based technique for obtaining three-dimensional, three-component measurements of velocity and

vorticity in field experiments around full-scale VAWTs will be documented (Section 4.2). Experiments with two VAWTs, one with straight blades and one with helical blades and each at two tip-speed ratios, will then be outlined. Velocity and vorticity fields from these experiments will be presented, and a difference in the three-dimensional structure of the wake between the two types of turbines will be identified (Sections 4.3.1 and 4.3.2). This tilted-wake behavior will be analyzed further, to establish a connection between blade geometry and wake topology (Section 4.3.3). The results from these analyses shed light on the dynamics that govern the near wake of VAWTs (up to $\sim 3\ D$ downstream, cf. Araya *et al.*, 2017), and implications of these findings for future studies and for the design and optimization of VAWT wind farms will be discussed (Sections 4.3.4 and 4.3.5). This work represents the first full-scale, fully three-dimensional flow-field study on operational VAWTs in field conditions, and therefore provides fundamental insights into the wake dynamics at high Reynolds numbers and the fluid mechanics of wind energy.

4.2 Experimental methods

In this section, the setup of the field experiments is outlined, and a novel technique for 3D-PTV measurements in field conditions is introduced. The experimental procedure is discussed, and the post-processing steps for computing velocity and vorticity fields are described. Additional details and characterizations of the measurement system are given in appendices C.1 and C.2.

4.2.1 Field site and turbine characterization

Experiments were carried out during the nights of 9-11 August 2018 at the Field Laboratory for Optimized Wind Energy (FLOWE), located on a flat, arid segment of land near Lancaster, California, USA. Details regarding the geography of the site are provided by Kinzel *et al.* (2012). Wind conditions at the site were measured with an anemometer (First Class, Thies Clima) and a wind vane (Model 024A, Met One), which recorded data at 1 Hz with accuracies of ±3% and ±5°, respectively. These were mounted on a meteorological tower (Model M-10M, Aluma Tower Co.) at a height of 10 m above the ground. The tower also recorded air temperature, which was used to interpolate air density from a density-temperature table. A datalogger (CR1000, Campbell Scientific) recorded these data at 1- and 10-minute intervals. The height difference between the anemometer and the VAWTs was corrected using a fit of an atmospheric boundary-layer profile to data collected previously at the

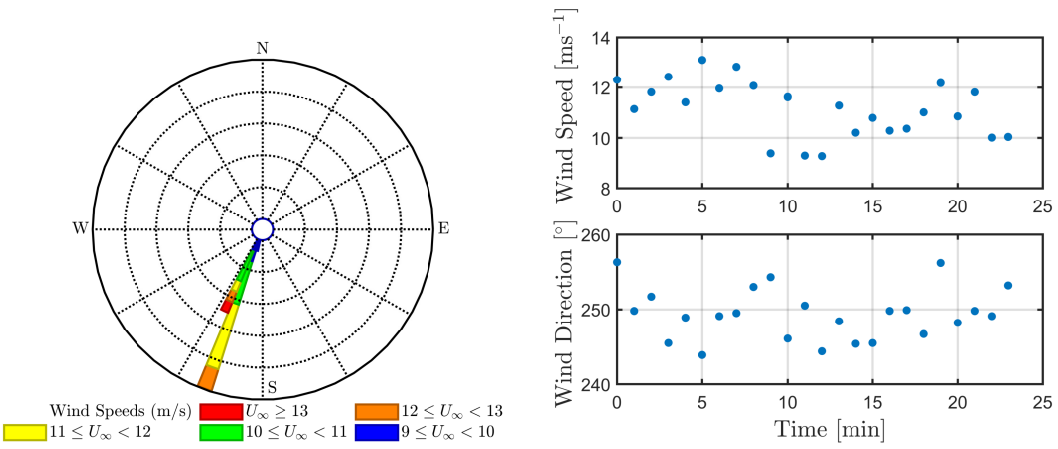

(a) (b)

Figure 4.1: (a) Wind rose for conditions during experiments (9-11 August 2018). The plotted wind speeds and directions are those recorded by the tower-mounted anemometer, located 10 m above the ground, and have been binned in ten-minute averages by 1 ms^{-1} and 5°, respectively. (b) Wind speeds and directions, from a single experiment (three eight-minute data sets), binned in one-minute averages.

site at multiple heights (cf. Kinzel *et al.*, 2012). The correction resulted in a 3% change in the free-stream velocity, which compared more favorably with the particle-based flow-field measurements than the uncorrected readings. The measured wind conditions at the site during experiments were uniform in both magnitude and direction: the wind speed was 11.01 ± 1.36 ms^{-1}, and the wind direction was from the southwest at $248 \pm 3°$. These statistics were calculated from sensor data that had been averaged by the datalogger into ten-minute readouts, and are summarized in the wind rose shown in Figure 4.1a.

For these experiments, two types of VAWTs were employed. A 1-kW, three-bladed VAWT with helical blades, built by Urban Green Energy (UGE), was compared with a 2-kW, five-bladed VAWT with straight blades from Wing Power Energy (WPE). The blades of both turbines had constant cross-sectional geometries. The blade twist of the helical-bladed turbine, representing the angle of twist with respect to the axis of rotation per unit length along the span of the turbine, was $\tau = 0.694$ rad $\cdot$ m^{-1}. Photos and details of these two turbines, referred to in this work by their manufacturer's acronyms (UGE and WPE), are given in Figure 4.2. Each turbine was tested at two different tip-speed ratios, defined as

$$\lambda = \frac{\omega R}{U_\infty}, \tag{4.1}$$

Helical-Bladed Turbine (UGE)	
Manufacturer	Urban Green Energy
Model	VisionAir 3
Rated Power	1 kW
Number of Blades	3
Turbine Radius	0.9 m
Turbine Span	3.2 m
Blade Chord	0.511 m
Solidity (σ)	0.271 ± 0.030

Straight-Bladed Turbine (WPE)	
Manufacturer	Wing Power Energy
Model	N/A
Rated Power	2 kW
Number of Blades	5
Turbine Radius	1.1 m
Turbine Span	3.7 m
Blade Chord	0.483 m
Solidity (σ)	0.349 ± 0.020

Figure 4.2: Photographs (left) and specifications (right) of the helical-bladed UGE turbine (top) and the straight-bladed WPE turbine (bottom). The blade twist of the UGE turbine is $\tau = 0.694$ rad $\cdot$ m^{-1}.

where ω is the rotation rate of the turbine (rad $\cdot$ s^{-1}), R is the radius of the turbine (m), and U_∞ is the magnitude of the free-stream velocity (ms^{-1}). The turbines had different solidities, quantified as the ratio of the blade area to the swept area of the rotating blades. This was defined as

$$\sigma = \frac{nc}{\pi D}, \tag{4.2}$$

where n is the number of blades, c is the chord length of each blade, and D is the turbine diameter. The parameters for the four experiments presented in this work are given in Table 4.1.

The turbines were mounted on the same tower for experiments, setting the mid-span location of each at a height of 8.2 m above the ground. A Hall-effect sensor (Model 55505, Hamlin) on the tower measured the rotation rate of the WPE turbine by recording the blade passing frequency. This method could not be implemented with the UGE turbine due to its different construction. Therefore, the rotation rate of the UGE turbine was calculated from videos of the turbine in operation, taken at 120 frames per second with a CMOS camera (Hero4, GoPro), by autocorrelating

Case Identifier	▲	▼	■	♦
Turbine	UGE	UGE	WPE	WPE
Wind Speed, U_∞ (ms^{-1})	11.15 ± 1.37	11.39 ± 1.25	12.76 ± 1.54	10.10 ± 1.29
Duration, T (s)	1393	1343	1453	1393
Duration, $T^* = T\frac{U_\infty}{D}$ (–)	8627	8491	8423	6396
Reynolds Number, $Re_D \times 10^6$	1.26 ± 0.15	1.29 ± 0.14	1.81 ± 0.22	1.43 ± 0.18
Tip-Speed Ratio, λ	1.19 ± 0.13	1.40 ± 0.14	0.96 ± 0.10	1.20 ± 0.16
Solidity, σ	0.271 ± 0.030	0.271 ± 0.030	0.349 ± 0.020	0.349 ± 0.020

Table 4.1: Experimental parameters for the four test cases presented in this work. From the left, the first two experiments were carried out on 9 August 2018, the third on 10 August, and the fourth on 11 August. The nondimensional duration T^* represents the number of convective time units D/U_∞ captured by each experiment. Uncertainties from the average values represent one standard deviation over time.

the pixel-intensity signal to establish a blade passing time. Electrical power outputs from the turbines were measured and recorded in 10-minute intervals using a second datalogger (CR1000, Campbell Scientific). The coefficient of power was then calculated as

$$C_p = \frac{P}{\frac{1}{2}\rho S D {U_\infty}^3}, \tag{4.3}$$

where P is the power produced by the turbine, ρ is the density of air, and S is the turbine span. The computed coefficients of power of the two turbines for each of the tested tip-speed ratios are shown in Figure 4.3. The C_p values for both turbines agree with measurements from previous experiments at the FLOWE field site reported by Miller, Duvvuri, Brownstein, *et al.* (2018) that suggested that the optimal tip-speed ratio for maximizing C_p was on the order of $\lambda \approx 1$ for the WPE turbine. This operating tip-speed ratio is low compared to those of larger-scale VAWTs with lower solidities (cf. Möllerström *et al.*, 2019), but is consistent with those of turbines of the same power-production class (e.g. Han *et al.*, 2018). The results also agree with the findings of other studies that the optimal tip-speed ratio for power production decreases with increasing solidity (Miller, Duvvuri, Kelly,

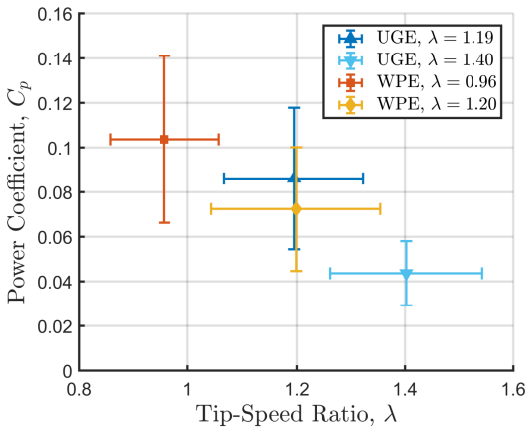

Figure 4.3: Coefficient of power as a function of tip-speed ratio for the four experiments outlined in Table 4.1.

et al., 2018; Rezaeiha *et al.*, 2018).

4.2.2 Particle-tracking velocimetry

A new method for volumetric flow measurements in field conditions was developed to obtain three-dimensional velocity measurements in a large measurement volume encapsulating the near wake of full-scale turbines. Because of the arid climate at the field site, natural precipitation could not be relied on to populate the required measurement volume with seeding particles (cf. Hong *et al.*, 2014). Therefore, to quantify the flow around the turbines, artificial snow particles were used as seeding particles for the flow. These were produced by four snow machines (Silent Storm DMX, Ultratec Special Effects) that were suspended by cables from two poles approximately four turbine diameters (D) upstream of the turbine tower. The machines could be raised to different heights with respect to the turbine, to adjust the distribution of particles in the measurement volume. The particles were illuminated by two construction floodlights (MLT3060, Magnum), so that their images contrasted the night sky. Six CMOS video cameras (Hero4, GoPro) were mounted on frames and installed in a semicircle on the ground to capture the particles in the turbine wake from several different angles. The layout of the entire experiment (excluding the upstream meteorological tower) is shown in Figure 4.4. The low seeding density and high visibility of the particles under these conditions meant that unambiguous particle trajectories could be extracted from the camera images, making PTV a natural choice for obtaining three-dimensional, three-component volumetric velocity measurements.

The degree to which the artificial snow particles follow the flow was an important

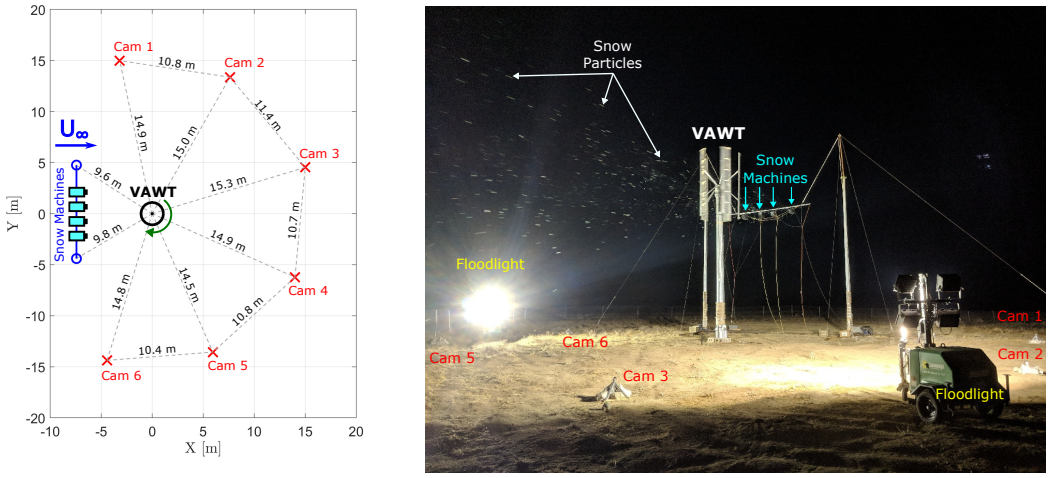

(a) (b)

Figure 4.4: Schematic (a) and photograph (b) of the field experiment. The snow machines in (a) are not drawn to scale. The video cameras are labeled as Cam 1 through Cam 6. The direction of rotation for the turbine in the diagram is clockwise, and the Z-coordinate points vertically upward from the ground. The WPE turbine ($S = 3.7$ m) is shown in the photo. The artificial snow particles are visible moving with the flow toward the left of the frame.

factor for the accuracy of the PTV measurements, and their aerodynamic characteristics were accordingly considered in detail. The particles were composed of an air-filled soap foam with an average effective diameter of $d_p = 11.2 \pm 4.2$ mm and an average density of $\rho = 6.57 \pm 0.32$ kgm^{-3}. Since the particles were relatively large and non-spherical, experiments were conducted in laboratory conditions to establish their aerodynamic characteristics. A detailed description of the experiments, results, and analyses regarding particle response and resulting experimental error is given in appendix C.1. By releasing the particles into a wind tunnel as a jet in cross-flow and tracking them using 3D-PTV with four cameras, the particle-response time scale τ_p and slip velocity V_s were computed. Comparing τ_p with the relevant flow time scale, $\tau_f = D/U_\infty$, yielded a particle Stokes number of $Sk = \tau_p/\tau_f \approx 0.23$. The worst-case slip velocities for the field experiments were estimated to be $V_s \lesssim 0.170$ ms^{-1}, or less than 2% of the average wind speed. Therefore, the particles were found to follow the flow with sufficient accuracy to resolve the large-scale structures encountered in VAWT wakes in the field.

To ensure that the entire measurement domain was sampled with sufficient numbers of particles, multiple iterations of each experimental case were conducted, focusing on different regions of the measurement volume. This was accomplished by raising

the snow machines to three distinct heights with respect to the turbine: at the turbine mid-span, above the turbine mid-span, and at the top of the turbine (approximately 8 m, 9 m, and 10 m above the ground, respectively). Vector fields obtained from the data for each case were combined, so that each experiment listed in Table 4.1 represents the combination of three separate recording periods. The effects of time averaging are further discussed in Section 4.2.4.

The six video cameras were arranged in a semicircle around the near-wake region of the turbines, up to 7 to 8 D downstream of the turbine. They recorded video at 120 frames per second and a resolution of 1920×1080 pixels, with an exposure time of 1/480 s and an image sensitivity (ISO) of 6400. The test cases outlined in Table 4.1 thus represent between 161,000 and 175,000 images per camera of the measurement volume. Because the cameras were all positioned on the downstream side of the turbine, some flow regions adjacent to the turbine were masked by the turbine itself, and thus could not be measured. This, however, did not affect the measurement of the wake dynamics downstream of the turbine. The total measurement volume was approximately 10 m $\times$ 7 m $\times$ 7 m, extending up to 2 D upstream of the turbine and at least 3 D downstream into the wake.

To achieve the 3D reconstruction of the artificial snow particles in physical space from the 2D camera images, a wand-based calibration procedure following that of Theriault *et al.* (2014) was carried out. A description of the procedure and its precision is included in appendix C.2.1. The two calibrations collected at the field site resulted in reconstruction errors of distances between cameras of $0.74 \pm 0.39\%$ and $0.83 \pm 0.41\%$, and reconstruction errors in the spans of the turbines of 0.21% and 0.32%. The calibrations therefore allowed particle positions to be triangulated accurately in physical space.

4.2.3 Experimental procedure

The collection of data for the field experiments was undertaken as follows. The rotation rate of the turbine was controlled via electrical loading to change the tip-speed ratio between experiments. The snow machines were hoisted to the desired height relative to the turbine, and artificial snow particles were advected through the measurement domain by the ambient wind. All six cameras were then initiated to record 420 to 560 seconds of video. Wind speed and direction measurements from the meteorological tower were averaged and recorded in one-minute bins over the duration of the recording period. The procedure was then repeated for the three

different snow-machine heights listed in Section 4.2.2, corresponding to three data sets in total for each experimental case.

4.2.4 Data processing and analysis

The procedure and algorithms used to obtain accurate time-averaged velocity fields from the raw camera images are presented in detail in appendix C.2.2, along with an analysis of the statistical convergence of the averaged data. An overview of the procedure is given here.

Particles were isolated in the raw images through background subtraction and masking. Because the cameras were not synchronized via their hardware, the images from the camera views were temporally aligned using an LED band (RGBW LED strip, Supernight) that was mounted on the turbine tower below the turbine blades and flashed at one-minute intervals. Particles were then identified in the synchronized images by thresholding based on pixel intensities. The particles were mapped to 3D locations in physical space using epipolar geometry (Hartley and Zisserman, 2003). A multi-frame predictive-tracking algorithm developed by Ouellette *et al.* (2006) and Xu (2008) computed Lagrangian particle trajectories and velocities from these locations. Velocity data recorded with the snow machines set at different heights were combined into a single unstructured volume of instantaneous velocity vectors. This field was averaged into discrete cubic voxels with side lengths of 25 cm. The standard deviation of the velocity magnitude over all vectors in these voxels was below 5% of the average value for over 50% of the voxels in the measurement domain. This quantity can be interpreted as an analogue for measurement precision, though some variation due to turbulence across vectors within the voxels was expected. In the wake of the turbine, the volume of interest for the analyses presented in this work, 87% of voxels had standard deviations below 5%, with 58% having values below 2%. The best-case precision for the most densely sampled voxels was below 1%. A more thorough account of these statistical-convergence studies is provided in appendix C.2.2. The velocity fields were finally filtered to enforce a zero-divergence condition (Schiavazzi *et al.*, 2014) and were used to compute vorticity fields.

It is important to briefly consider the effect of time averaging, which was inherent to this PTV method. Temporal averaging removed the presence of turbulence fluctuations in the data, and thus the resulting velocity and vorticity fields necessarily contained only flow phenomena that were present in the mean flow. Conjectures regarding the effects of turbulence fluctuations on momentum transfer into the

wake are therefore not possible based on these measurements. These effects are expected to dominate the far wake, whereas the near wake is characterized by large-scale vortical structures. Therefore, for the purposes of this study, it was deemed acceptable to forgo the resolution of turbulence fluctuations. Similarly, unsteady vortex dynamics were not resolved in these experiments. However, the effects of vortex dynamics occurring at large scales can still be observed in the time-averaged flow fields, as will be shown in the following section. It is thus possible to infer connections between the time-averaged results of these experiments and the underlying unsteady dynamics observed in previous studies (e.g. Battisti *et al.*, 2011; Tescione *et al.*, 2014; Parker and Leftwich, 2016; Araya *et al.*, 2017; Rolin and Porté-Agel, 2018).

4.3 Experimental results

In this section, the results of the field experiments described in the previous section are presented and further analyzed. First, the velocity fields for the four experimental cases given in Table 4.1 are shown to highlight three-dimensional flow features. Next, the vorticity fields for these cases are presented, and a tilted wake is observed for the helical-bladed turbine. The tilted wake is then analyzed further, and a connection between turbine-blade geometry and wake tilt is established. Finally, the dynamics of the identified vortical structures are considered, and the implications of the results for arrays of VAWTs are outlined.

4.3.1 Velocity fields

Velocity fields for the time-averaged streamwise-velocity component U on three orthogonal planar cross-sections are given in Figures 4.5 and 4.6 for the helical-bladed (UGE) and straight-bladed (WPE) turbines at tip-speed ratios of $\lambda = 1.19$ and $\lambda = 1.20$, respectively. The wake structure was not observed to change significantly with the changes in λ achieved in these experiments. A more detailed analysis of the wake velocity fields for both turbines, including comparisons with previous wake studies at lower Re_D, is provided in appendix C.3.1. As this study seeks to ascertain the effects of turbine-blade geometry on the 3D structure of the near wake, two key differences between the velocity fields of the two turbines are highlighted.

First, in YZ cross-sections of U downstream of the turbine, topological differences were evident in the wake region, where the local streamwise velocity fell below the free-stream velocity. This region was observed to tilt in the clockwise direction

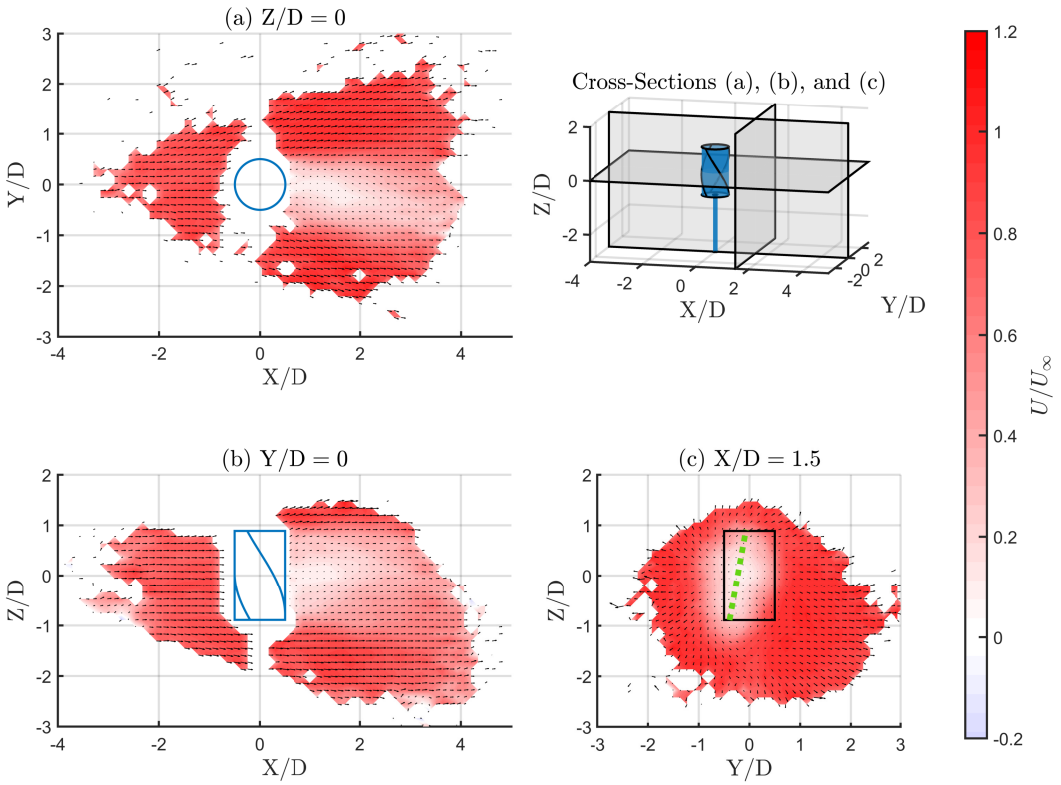

Figure 4.5: Three orthogonal time-averaged planar fields of the streamwise velocity U for the helical-bladed turbine, taken at $Z/D = 0$, $Y/D = 0$, and $X/D = 1.5$ (counter-clockwise, from top left). A slight tilt from the vertical in the clockwise direction, shown by a fit to minima in the streamwise velocity (dashed green line), is visible in the velocity-deficit region in the YZ cross-section.

when viewed from downstream in the case of the helical-bladed turbine (Figure 4.5), while no such tilt was observed in the case of the straight-bladed turbine (Figure 4.6). This tilted-wake behavior will be analyzed in detail in Section 4.3.3, and it will be shown that this topological difference was a consequence of the blade shape of the helical-bladed turbine.

Secondly, a slice of the time-averaged vertical-velocity component W through the central axis of the turbine further implied the existence of more complex three-dimensional dynamics in the wake of the helical-bladed turbine (Figure 4.7). The vector field at $Y/D = 0$ for the straight-bladed turbine showed a downward sweep of fluid from above the turbine and an upward sweep of fluid from below the turbine, as would be expected from a bluff body in cross-flow (Figure 4.7b). The corresponding field for the helical-bladed turbine showed a qualitatively different scenario, in which a uniform central updraft was present (Figure 4.7a). At planar slices of Y/D on either side of $Y/D = 0$, corresponding uniform downward motions of fluid were observed.

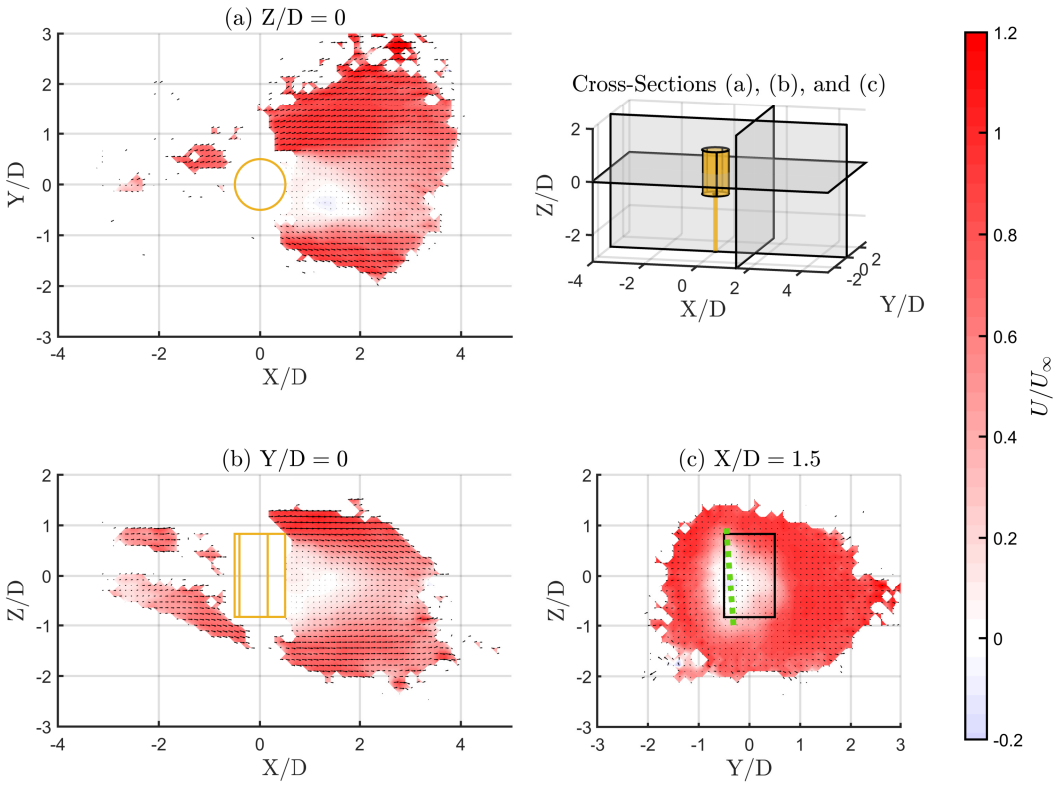

Figure 4.6: Three orthogonal time-averaged planar fields of the streamwise velocity U for the straight-bladed turbine, taken at $Z/D = 0$, $Y/D = 0$, and $X/D = 1.5$ (counter-clockwise, from top left). In contrast to Figure 4.5, no wake tilt is present in the YZ cross-section, as evidenced by the relatively vertical alignment of the fit to the wake profile (dashed green line).

These differences in the vertical-velocity fields implied that the 3D structure of the helical-bladed turbine had an effect on the wake dynamics that could not be resolved simply by examining the velocity fields. A three-dimensional analysis of the vortical structures present in the wakes of these VAWTs is required to explain these observed differences. This will be provided in Section 4.3.2.

4.3.2 Vortical structures and wake topology

An analysis of the vortical structures in the streamwise direction (ω_x) demonstrates the importance of three-dimensional considerations to the wake dynamics of these VAWTs. Streamwise planar slices of ω_x are shown in Figures 4.8 and 4.9. The structures visible in these plots comprised a horseshoe-shaped vortex induced by the rotation of the turbine, observed previously by Rolin and Porté-Agel (2018) and Brownstein *et al.* (2019). While in the case of the straight-bladed turbine, the two branches of the vortex were symmetric about the mid-span of the turbine, the

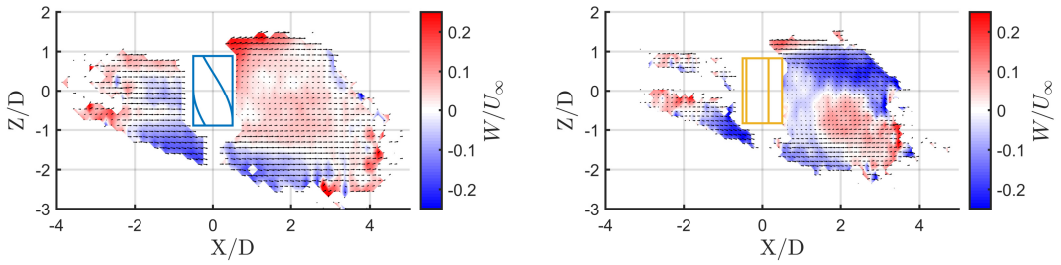

Figure 4.7: Time-averaged planar fields of the vertical velocity W for (a) the helical-bladed turbine at $\lambda = 1.19$ and (b) the straight-bladed turbine at $\lambda = 1.20$, taken at $Y/D = 0$. The wake of the straight-bladed turbine is characterized by symmetric sweeps of high-momentum fluid into the wake from above and below. In contrast, the wake of the helical-bladed turbine exhibits a uniform updraft at $Y/D = 0$. This difference suggests that the helical blades have a pronounced three-dimensional effect on the wake structure.

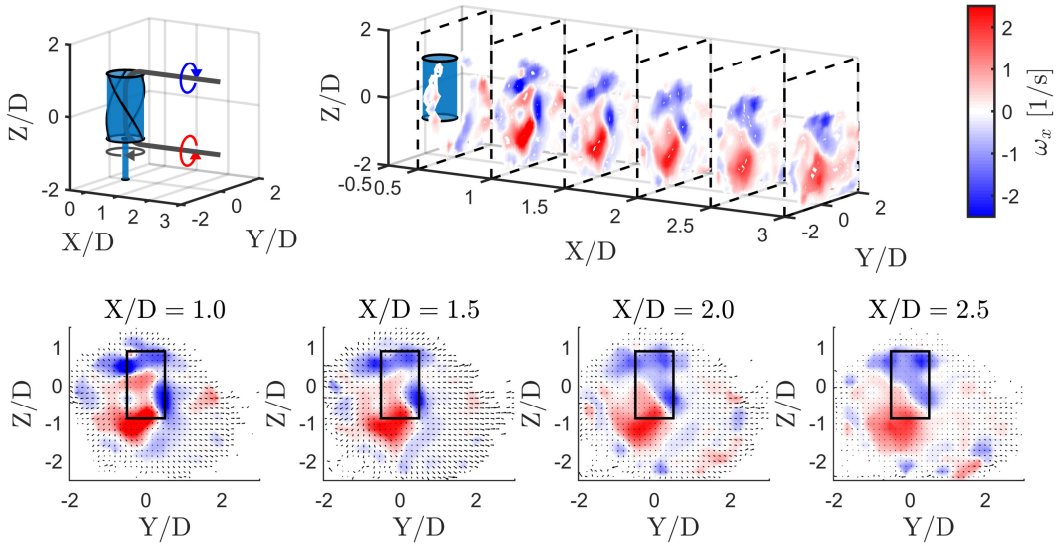

Figure 4.8: Streamwise slices of the streamwise vorticity ω_x in the case of the helical-bladed turbine for $\lambda = 1.19$. The X-axis is stretched on $0.5 \leq X/D \leq 3$ to show the slices more clearly. These fields show marked asymmetry and a vertical misalignment in the two branches of the horseshoe vortex induced by the rotation of the turbine, compared to those shown in Figure 4.9.

corresponding structure for the helical-bladed turbine was asymmetric. The offset of the upper branch with respect to the lower branch induced the central updraft of fluid observed in Figure 4.7a. It will be argued in Section 4.3.3 that this asymmetry was a result of the blade twist of the helical-bladed turbine, which skewed the overall wake profile and thereby affected the alignment of the streamwise vortical structures.

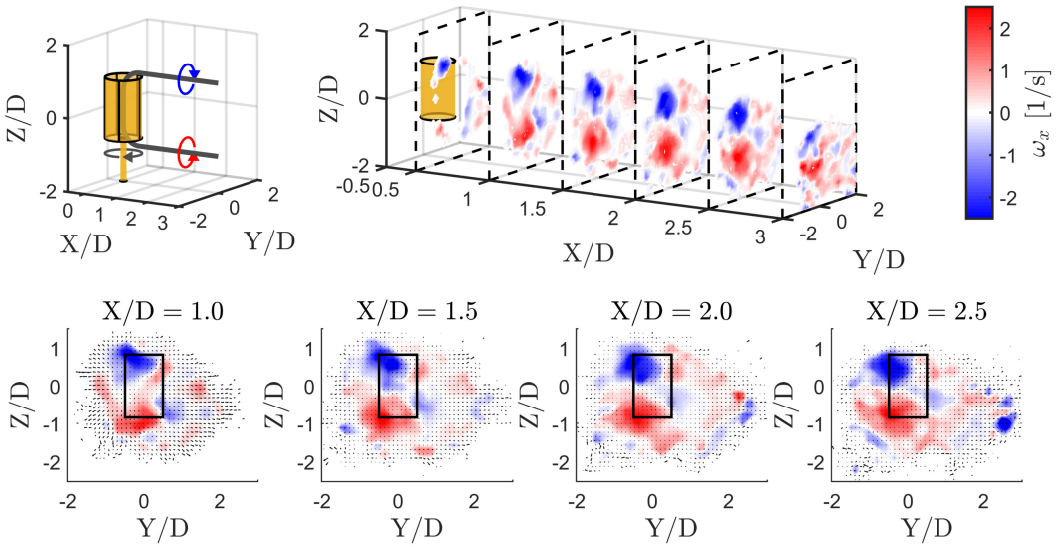

Figure 4.9: Streamwise slices of the streamwise vorticity ω_x in the case of the straight-bladed turbine for $\lambda = 1.20$. The X-axis is stretched on $0.5 \leq X/D \leq 3$ to show the slices more clearly. Compared to the wake of the helical-bladed turbine (Figure 4.8), the streamwise vortical structures are symmetric about the $Z/D = 0$ plane. Small counter-rotating secondary vortices are also present to the right of each main streamwise vortex, possibly similar to those observed in full-scale HAWTs by Yang *et al.* (2016).

Similar asymmetric behavior in the wake of the helical-bladed turbine was observed in the vertical vortical structures (ω_z), shown in streamwise slices in Figures 4.10 and 4.11. In both cases, the structure with positively signed vorticity initially had a linear shape and was oriented vertically, while the structure with negatively signed vorticity was bent toward the positive Y direction. This initial geometry was related to the mechanics of formation of these vortices. The positively signed structure was composed of vortices shed from turbine blades as they rotated into the wind, which formed a vortex line that was advected downstream. These vortices have been observed in two dimensions for straight-bladed turbines by Tescione *et al.* (2014), Parker and Leftwich (2016), and Araya *et al.* (2017), and in 3D simulations of straight-bladed turbines by Villeneuve *et al.* (2020). The arched shape of the negatively signed structures was a consequence of the low-velocity wake region. Behind the straight-bladed turbine, these two structures remained vertically oriented and relatively parallel. In contrast, behind the helical-bladed turbine, these structures began to tilt with respect to the vertical as they were advected downstream. This tilt was analogous to that observed in the horseshoe vortex (Figure 4.8). Since the structures in ω_z were formed by vortex shedding from the turbine blades, we

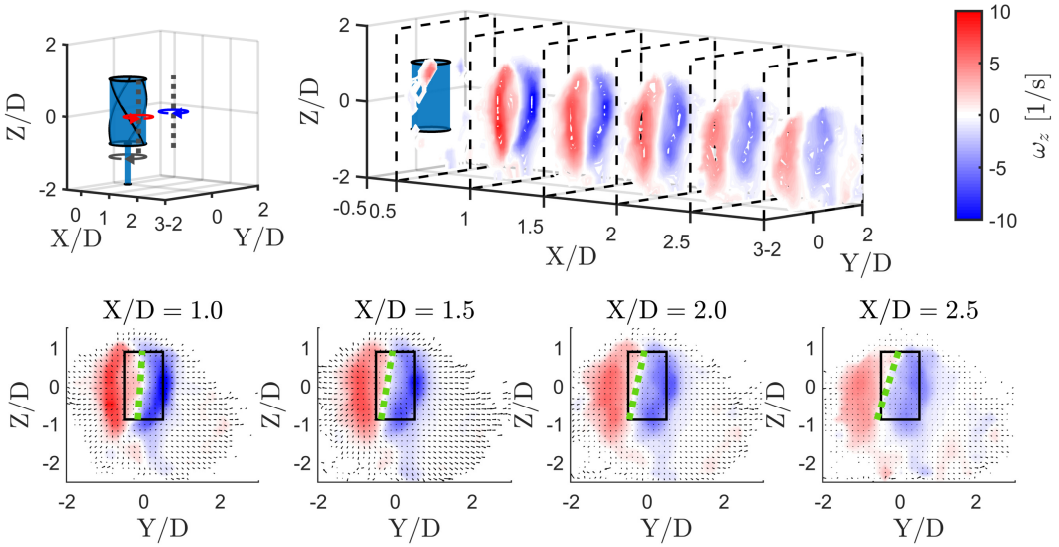

Figure 4.10: Streamwise slices of the vertical vorticity ω_z downstream of the helical-bladed turbine for $\lambda = 1.19$. As in the previous figures, the X-axis is stretched on $0.5 \leq X/D \leq 3$. These structures exhibit a tendency to tilt with increasing streamwise distance from the turbine, as evidenced by fits to the zero-vorticity region between the structures (dashed green lines).

hypothesize that the helical blades of the UGE turbine were the cause of this observed asymmetric wake behavior.

The spanwise vortical structures (ω_y) did not show any significant signs of asymmetry (appendix C.3.2, Figures C.13 and C.14). These structures represented time-averaged tip vortices shed by the passing turbine blades, as documented by Tescione *et al.* (2014), and were thus not expected to change in geometry in these experiments. Together, the blade-shedding structures in ω_y and ω_z bounded the near wake. Their time-averaged profiles outlined and encapsulated the regions of streamwise-velocity deficit in the wake shown in Figures 4.5 and 4.6. This topological correspondence suggested that vortex shedding from the turbine blades has a dominant effect on the overall shape of the near wake.

4.3.3 Effect of blade twist

In the previous section, connections between vortex shedding from VAWT blades and the 3D topology of VAWT wakes were observed. A more thorough investigation of the tilted wake is now undertaken to develop a more comprehensive description of the dynamics in the near wake.

The results presented thus far have shown that the wake of the helical-bladed turbine

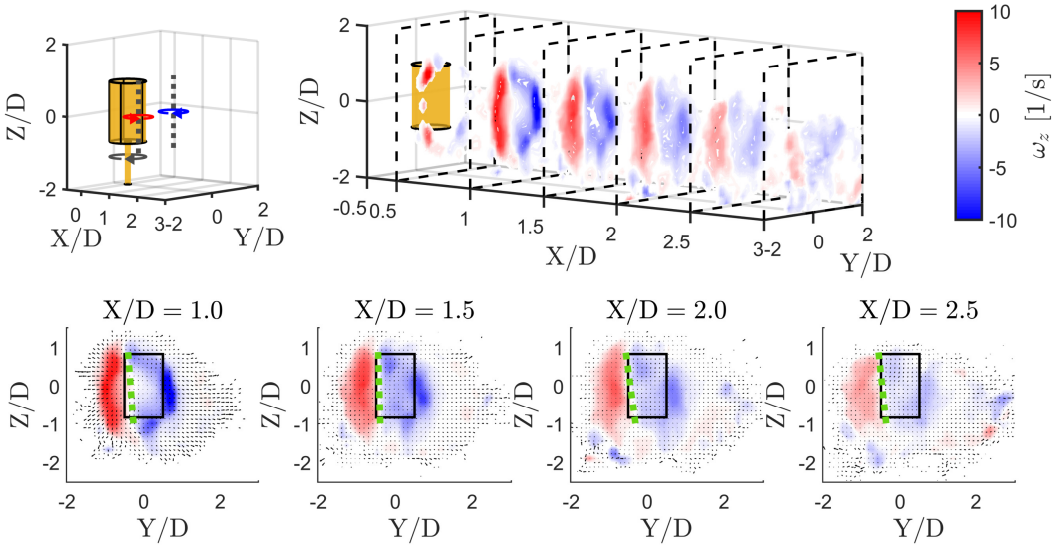

Figure 4.11: Streamwise slices of the vertical vorticity ω_z downstream of the straight-bladed turbine for $\lambda = 1.20$. The X-axis is again stretched on $0.5 \leq X/D \leq 3$. These structures remain upright with respect to the vertical (again denoted by dashed green lines), in contrast to their counterparts from the helical-bladed turbine.

was tilted at some angle with respect to the vertical, whereas the wake of the straight-bladed turbine was not. To quantify this effect, two measures were employed: the angle of the velocity-deficit region, and the angle of the region of zero vorticity between the two vertical vortical structures. These two measures were selected on the premise that the dynamics of the vertical vortical structures are tied to the geometry of the near wake. Both were computed on slices parallel to the YZ plane, taken at several streamwise positions downstream of each turbine. For the first measure, the location of minimum velocity was identified at every Z-position in each slice, and a linear fit through these points on each slice was computed to approximate the slope of the velocity-deficit region. For the second measure, the location of minimum vorticity between the two vertical vortical structures was identified at every Z-position in each slice using linear interpolation, and a linear fit through these points on each slice represented the orientation of the structures. For both measures, confidence intervals of one standard deviation on the slope of the linear fit served as error bounds. The results of this procedure are shown in Figure 4.12a for the velocity-deficit measure and Figure 4.12b for the vortical-structure measure. The results demonstrated that the wake orientation of the straight-bladed turbine did not exhibit a strong deviation from the vertical in the near-wake region. In contrast, the wake orientation of the helical-bladed turbine increased monotonically with streamwise distance for both of the tip-speed ratios tested in the experiments.

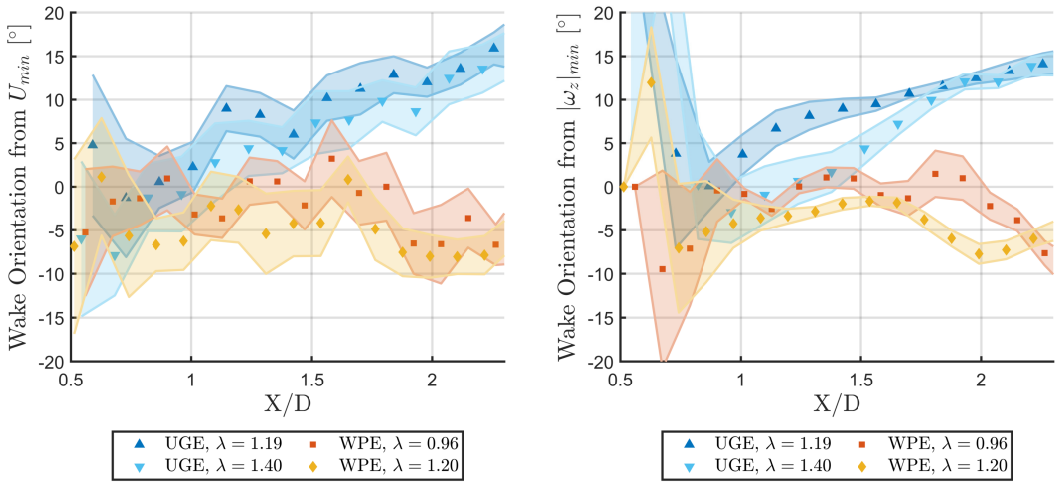

(a) (b)

Figure 4.12: Wake orientation measurements from all four experimental cases, computed from (a) the locations of minima in the velocity-deficit region, U_{min}, and (b) the coordinates of the zero-vorticity strip between the two vertical vortical structures, $|\omega_z|_{min}$. The wake orientation of the helical-bladed turbine increases monotonically, while that of the straight-bladed turbine does not exhibit a strong trend away from zero.

These measures thus quantified the various observations from the previous section regarding changes in the wake topology between the two turbines.

The wake-orientation measurements shed light on the mechanism responsible for the tilted wake observed for the helical-bladed turbine. First, the orientation profiles were consistent between the two measures, supporting the hypothesis that the shape of the near wake is directly tied to the dynamics of the vertical vortical structures. Additionally, the profiles did not show a strong dependence on turbine solidity, and no significant dependence on tip-speed ratio over the limited range of λ tested in these experiments was observed. Though the measurements did separate into two classes corresponding to the two turbine geometries, the three-dimensional nature of the tilted-wake behavior made it unlikely that solidity, which is not defined using three-dimensional geometric parameters, was the dominant factor. These results thus isolate the geometry of the turbine blades as the primary contributing factor to the observed differences in wake topology.

A mechanism by which turbine-blade geometry can affect the wake topology is now proposed. As described previously, the vortical structures visible in the time-averaged fields of ω_z represent the profiles of vortex lines shed from the rotating turbine blades and advected away from the turbine by the free stream. We expect

that the shape of these vortex lines will depend on the shape of the blades: a straight blade will shed a straight vortex line, while a helical blade will shed a vortex line with non-zero curvature. The latter hypothesis is drawn from the fact that a helical blade, in contrast to a straight blade, is yawed relative to the incoming flow and experiences a range of local angles of attack along its span as it rotates around the turbine. A yawed or swept blade with respect to the incoming flow exhibits three-dimensional vortex shedding in dynamic stall (Visbal and Garmann, 2019), due in part to a net transport of vorticity along the span of the blade (Smith and Jones, 2019). A linearly increasing spanwise angle-of-attack profile in dynamic stall similarly induces a spanwise transport of vorticity that affects the stability of the leading-edge vortex and thus the character of the vortex shedding from the blade (Wong *et al.*, 2017). Given these observations, we conclude that the spanwise non-uniformity of the flow over helical VAWT blades makes the vortex lines shed by the dynamic-stall mechanism inherently nonlinear and three-dimensional.

To model the evolution of these vortex lines as they are advected downstream, the principle of Biot-Savart self-induction can be applied. In an inviscid flow field, the self-induced velocity at any point $\mathbf{r}$ on a single vortex line with finite core size μ, defined by the curve $\mathbf{r}'$ and parameterized by the arc length s', can be written as

$$\frac{\partial \mathbf{r}}{\partial t} = -\frac{\Gamma}{4\pi} \int \frac{(\mathbf{r} - \mathbf{r}') \times \frac{\partial \mathbf{r}'}{\partial s'}}{(|\mathbf{r} - \mathbf{r}'|^2 + \mu^2)^{3/2}} ds', \tag{4.4}$$

where the integration is performed over the length of the vortex line (Leonard, 1985). This model for the self-induced deformation of curved vortex lines has been studied numerically using both approximate methods (Arms and Hama, 1965) and exact simulations (Moin *et al.*, 1986). The quantity $(\mathbf{r} - \mathbf{r}') \times \frac{\partial \mathbf{r}'}{\partial s'}$ in the numerator of the integrand is only non-zero when the displacement vector between two points on the vortex line does not align with the direction of the vortex line. Therefore, a vortex line with curvature or piecewise changes in alignment will undergo deformation under self-induction, while a purely linear vortex line will not. Self-induced deformations of a similar nature have been observed in curved and tilted vortex lines in numerous computational and experimental contexts (e.g. Hama and Nutant, 1961; Boulanger *et al.*, 2008).

Given that the precise shape of the curved vortex lines shed by the helical-bladed turbine cannot be extracted from the time-averaged vorticity fields, Equation 4.4 cannot be applied quantitatively in this case. However, it can still be used qualita-

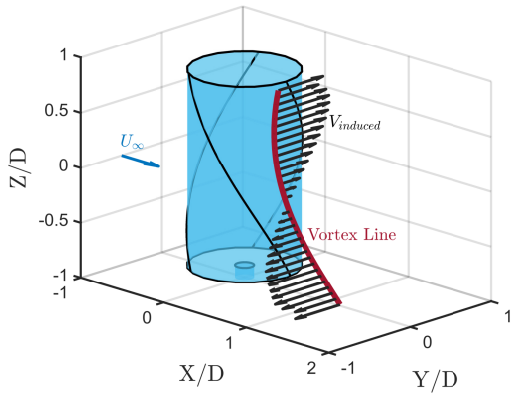

Figure 4.13: Schematic of the Y component of the induced velocities, $V_{induced}$, along a helical vortex line due to Biot-Savart self-induction (Equation 4.4). The scale of the vectors and the streamwise location of the vortex line are both arbitrary, and the streamwise and vertical components of the induced velocity are not shown for clarity. The stretching induced on the vortex line matches the behavior of the tilted wake.

tively to connect the development of the tilted wake to blade geometry. We therefore consider a helical vortex line that corresponds to the helical shape of the UGE turbine blades, shed from a blade as it rotates upstream into the prevailing wind. This model system accounts for the three-dimensional blade geometry while abstracting the precise dynamics of the vortex-shedding mechanism on the blades. The curve is parameterized for $Z \in [-S/2, S/2]$ as $X = -aR\sin(\tau Z)$ and $Y = -R\cos(\tau Z)$. The constant a accounts for stretching of the vortex line in the streamwise direction due to differences between the tip-speed velocity of the turbine and advection from the free stream. The selection $a = 1/\lambda$, for example, recovers the expected asymptotic result that the curved vortex line will become a straight vertical line as $\lambda \to \infty$. The initial induced velocities along this vortex line, computed numerically from Equation 4.4, apply a stretching in the Y direction that corresponds directly with the previous observations of the tilted wake (Figure 4.13). The streamwise and vertical induced velocities are not addressed in this analysis since they do not contribute to the tilted wake. The computed vectors also do not represent the full time evolution of the vortex line, as only the initial induced velocities $\mathbf{u}\left(\mathbf{r}(t=0)\right)$ are given. The demonstration shows qualitatively that the mechanism of Biot-Savart self-induction provides a direct connection between blade geometry and the evolution of the wake topology.

Based on these results, the propagation of the influence of turbine-blade geometry in the dynamics of the near wake can be outlined. The shape of the blades determines

the shape of the vortex lines shed by the blades as they rotate around the turbine. The shape of these vortex lines in turn drives their evolution downstream of the turbine. As these structures bound the wake region, topological changes in the vortex lines are reflected in the shape of the velocity-deficit region of the wake. These developments affect the shape of the horseshoe vortex, which is not directly affected by differences in blade geometry but is necessarily bound to the shape of the wake region. The connection between blade twist and wake tilt described in this section therefore provides a unifying framework that accounts for the trends previously observed in the wake velocity and vorticity fields.

4.3.4 Wake dynamics

In the previous section, it was hypothesized that the shape of VAWT blades dictates the near-wake topology through Biot-Savart self-induction of shed vortex lines. The wake dynamics are now analyzed in detail, to quantify the evolution of the vortical structures in the wake and to identify their contributions to wake recovery. The circulation of the wake structures in each direction, Γ_i, was calculated as a function of downstream distance from the turbine. The circulation was computed at a series of streamwise positions X/D by integrating the vorticity component in question over a square $D \times D$ window, which was oriented normal to the direction of the vorticity component. This window was placed at the center of the vortex at several points along the vortex line. The center was identified at each point by applying a threshold based on the standard deviation of the vorticity field and computing the center of mass of the isolated vorticity distribution. The values of the circulation along the vortex line, computed with these windows, were averaged to obtain a representative circulation for the structure. Error bars were determined by propagating the standard deviations of the components of individual velocity vectors from the particle trajectories in each voxel through the curl operator and the circulation integration. This computation was done independently for the positively and negatively signed vortical structures. The resulting circulations in X, Y, and Z are plotted on $0.5 \leq X/D \leq 2.3$ in Figures 4.14, 4.15a, and 4.15b, respectively. Circulation measurements downstream of this region were inconclusive due to measurement noise, or possibly as a result of atmosphere-induced unsteady modulations in the wake similar to those observed in full-scale HAWTs (Abraham and Hong, 2020).

The circulations of the streamwise structures (Γ_x, Figure 4.14) appeared to extend farther into the wake than the vortical structures in Y and Z, whose circulations declined monotonically after $X/D \approx 1.5$ (as shown in Figure 4.15). This difference

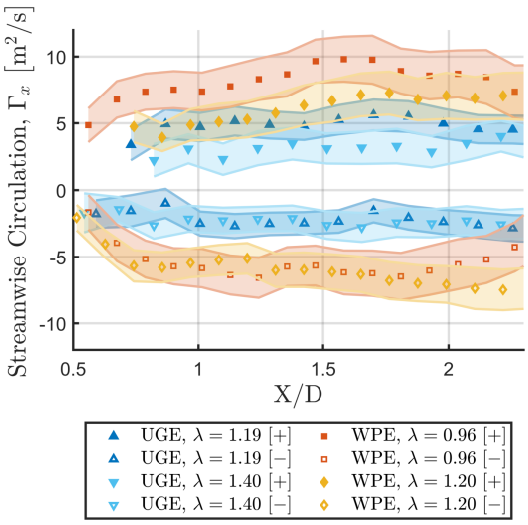

Figure 4.14: Circulation of the positive and negative streamwise vortical structures, Γ_x, for all four experimental cases. Compared to the plots of Γ_y and Γ_z shown in Figure 4.15, Γ_x did not decay as significantly with increasing streamwise distance, and the horseshoe vortex was thus hypothesized to extend farther into the wake than the structures induced by vortex shedding from the blades.

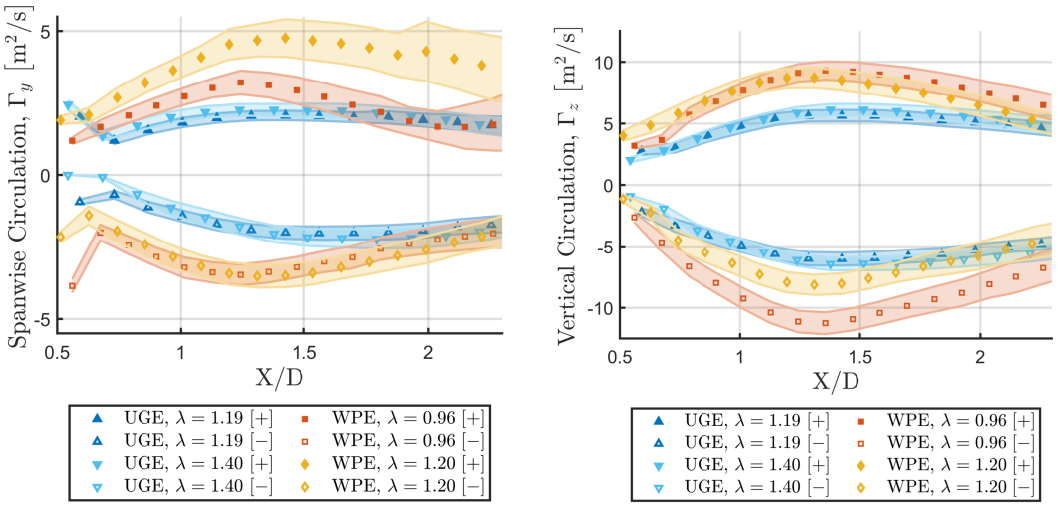

(a) (b)

Figure 4.15: Circulations of the positive and negative (a) spanwise vortical structures (Γ_y) and (b) vertical vortical structures (Γ_z) for all four experimental cases. The circulation profiles collapse approximately by turbine, implying that turbine solidity is a dominant factor in these dynamics. The decaying trends of the profiles past $X/D \approx 1.5$ show that these structures are only influential in the near wake.

in dynamical behavior agrees with the previously stated hypothesis that the horseshoe vortex is induced by the rotation of the turbine rather than unsteady vortex shedding from the turbine blades. Furthermore, the streamwise circulation at the lowest tip-speed ratio ($\lambda = 0.96$) began to decline at $X/D \approx 1.7$, prior to those at higher tip-speed ratios, which suggests that the persistence of the horseshoe vortex in the wake increases with increasing λ. Given the limited range of tip-speed ratios and streamwise locations considered in these experiments, a definitive relation between Γ_x and λ cannot be isolated from these results. Still, the comparatively long-lived coherence of the horseshoe vortex in the wake does imply that it plays an important role in the dynamics of wake recovery, considering its influence on vertical velocities in the wake and thus the entrainment of momentum into the wake (Figure 4.7). Additionally, the difference in the alignment of the branches of the horseshoe vortex between the helical- and straight-bladed turbines suggests that the wake recovery will also differ as a function of blade geometry.

The circulations of the structures corresponding to vortex shedding from the turbine blades (Γ_y and Γ_z, shown in Figures 4.15a and 4.15b) exhibited uniform behavior for both turbines. Taken together with the time-resolved results of Araya *et al.* (2017), these trends confirm that the vortex-shedding dynamics that contribute to the wake structure are only active in shaping the near wake ($X/D \lesssim 2$). An apparent dependence on turbine solidity is evident in these data, as the circulation profiles separated into groups by turbine rather than by tip-speed ratio. This trend is likely not a function of three-dimensional blade shape, because the measurements of Γ_y and Γ_z were averaged in Y and Z, respectively. Again, because of the limited number of turbine geometries considered in this study, a definitive relation between Γ_y, Γ_z, and σ cannot be established from these data. These results, however, do indicate that the contributions of the blade-shedding structures to wake recovery will not differ significantly between the two turbine geometries considered in this study.

The main conclusion from the circulation analysis presented in this section is that the horseshoe vortex extends farther into the wake than the vortical structures in the Y and Z directions, which begin to decay in strength soon after they are shed from the turbine blades. These results thus suggest that, though the vortex lines shed by the turbine blades define the topology of the near wake, the horseshoe vortex has a larger contribution to wake recovery due to its comparative longevity in the wake. The analysis also noted possible dependencies of Γ_x on λ and of Γ_y and Γ_z on σ. The contributions of vortex breakdown and turbulent entrainment of

momentum from the free stream to wake recovery have not been considered here, because of the time-averaged nature of the experimental data. These effects become more significant downstream of the limit of our measurement domain, and thus will also be affected by the mean-flow dynamics identified in this work.

4.3.5 Implications for turbine arrays

The findings of this study have parallels in recent studies of the wake dynamics of HAWTs that highlight the implications of the present results for the arrangement of VAWTs in closely packed arrays. In both experiments with a porous disc and large-eddy simulations with actuator-disc and actuator-line models, Howland *et al.* (2016) reported an alteration to the shape of the wake profile, known as a curled wake, behind HAWTs yawed with respect to the incoming flow caused by counter-rotating streamwise vortices that are induced by the yawed turbine. Bastankhah and Porté-Agel (2016) and Shapiro *et al.* (2018) modelled this topological phenomenon analytically, leading to new estimates of the wake deflection and available power downwind of a yaw misalignment wind turbine. Fleming *et al.* (2017) confirmed the existence of these vortices for yawed turbines in field conditions. Additionally, Fleming *et al.* (2018) demonstrated that these changes in wake topology affect the performance of downstream and adjacent turbines in an array. Howland *et al.* (2019) and Fleming *et al.* (2019) then utilized these analytic models to demonstrate the potential for wake steering control in field experiments of HAWTs at full scale. Given the qualitative similarities in the dynamics of the tilted wake observed in this study and the curled wake observed in HAWTs, the ramifications of the tilted wake for arrays of VAWTs could be analogous as well.

The performance of VAWTs downstream of a given turbine will be affected by the dynamics identified in this study. The strong vortex shedding in the near wake of a VAWT ($X/D \lesssim 2$) will lead to a severe decrease in the performance of downstream turbines placed in this region. Brownstein *et al.* (2019) observed this effect in experiments with turbine pairs. For greater streamwise separations, the horseshoe vortex will be the primary large-scale mean-flow vortical structure encountered by downstream turbines. At these distances, the effects of helical blades on wake recovery will be more evident, and will affect the overall performance of the VAWT array. The tilted wake will also lead to a modified wake profile that will affect the optimal placement of helical-bladed turbines in arrays by at least one turbine radius, in a manner similar to that reported by Bossuyt *et al.* (2016) for HAWTs.

The performance of adjacent VAWTs will also be affected, especially for turbines placed in close proximity to each other for the enhancement of power production. The mean-flow mechanisms observed by Brownstein *et al.* (2019) will be altered by the presence of the three-dimensional vortex shedding from helical-bladed turbines, and it is thus likely that these turbines would experience a different degree of performance enhancement observed in that work for straight-bladed turbines.

Lastly, the vortical structures and topological effects isolated in this study are expected to hold for vertical-axis wind turbines in general, with variations for different turbine geometries. The horseshoe vortex, in particular, is expected to be enhanced for VAWTs that operate at higher tip-speed ratios than those employed in these experiments. The significance of the tilted wake for helical-bladed turbines will vary with aspect ratio and blade twist. The 3D effects of blade geometry will also need to be reconsidered for the bowed blades of the large-scale Darrieus-type turbines studied by Klimas and Worstell (1981). Particular differences notwithstanding, it can be inferred that the three-dimensional dynamics identified here will have significant effects on the dynamics and topology of the wake for VAWTs of all designs and power outputs, and thereby affect the aerodynamics and overall efficiency of VAWT arrays.

4.4 Conclusions

In this study, a novel method for conducting volumetric three-dimensional, three-component flow-field measurements in field conditions was developed and used to quantify the wake dynamics of two full-scale vertical-axis wind turbines. This 3D-PTV setup demonstrated sufficient precision and resolution to resolve large-scale vortical structures in the wakes of the turbines. Time-averaged velocity and vorticity fields showed a tilted wake downstream of helical-bladed turbines, compared to the wake profile of straight-bladed turbines. A fully three-dimensional analysis of the vortical structures present in the near wakes of VAWTs was undertaken, and demonstrated that the topology of the near wake is dependent primarily on the mechanics of vortex shedding from the turbine blades. The connection between blade geometry and wake dynamics was clarified by considering the Biot-Savart self-induction of curved vortex lines. Measurements of the circulation of the vortical structures in the wake revealed that the vortical structures shed by the blades decay in influence relatively quickly but affect the topology of the horseshoe vortex, which extends farther into the wake and is thus related to wake recovery. Therefore, a line

of influence was established between blade geometry, vortex shedding, near-wake topology, the horseshoe vortex, and wake recovery.

A major point of emphasis in this work is that three-dimensional effects are significant to the dynamics and evolution of VAWT wakes. Many of the flow phenomena observed in this study would be difficult to resolve completely by planar measurement techniques; the vorticity and circulation measurements in particular required three-component 3D data to collect. The experimental method for obtaining time-averaged velocity and vorticity measurements in field conditions and high Reynolds numbers is therefore well suited to further analyses of wind-turbine wake dynamics at full scale. The method is also flexible enough in its deployment to be applied to other large-scale flow phenomena and atmosphere-structure interactions.

While this study focused on differences in flow topology that stemmed from the use of helical blades in VAWTs, the connection between object geometry and vortex dynamics proposed in this work could be applied in wider aerodynamic contexts, such as rotorcraft, flapping flight, and more complex fluid-structure interaction problems. This study provides both an experimental method and a theoretical framework for wake analysis that can be leveraged for future studies of the three-dimensional vortex dynamics in engineering-scale wakes.

The limited number of test cases in this study precluded the execution of a full scaling analysis of the vortical structures and circulation profiles with respect to turbine solidity and tip-speed ratio. A larger series of test cases, involving different turbine geometries and a wider range of tip-speed ratios, would allow these relationships to be established more quantitatively. In addition, a larger measurement volume would allow the wake-topology observations of this study to be extended into the far wake, so that the effects of the tilted wake and the streamwise vortical structures on wake recovery could be more thoroughly investigated. Given the size of the measurement domain that would be required for these kinds of experiments, as well as the range of parameters involved, it may be more feasible to carry out this analysis in a laboratory or computational setting. This study can thus provide validation cases to demonstrate that flow phenomena observed in VAWT wakes in laboratory experiments and numerical simulations are representative of those present in the wake of operational turbines in field conditions.

Acknowledgements

The authors gratefully acknowledge funding from the Gordon and Betty Moore Foundation through Grant No. 2645, the National Science Foundation through Grant No. FD-1802476, the Stanford University TomKat Center for Energy Sustainability, and the Stanford Graduate Fellowships in Science and Engineering. The authors would also like to recognize Bob Hayes and Prevailing Wind Power for managing the operation and maintenance of the FLOWE field site, and Ryan McMullen for assisting with the field experiments. The authors extend their thanks to Snow Business International & Snow Business Hollywood for assisting in the selection and supply of the snow machines and the snow fluid used, for providing troubleshooting during late night experiments, for allowing extended use of their machines, and for shipping a machine to Stanford for the laboratory experiments. Lastly, the authors would like to extend their appreciation to the reviewers from the Journal of Fluid Mechanics for their detailed feedback and helpful suggestions that significantly improved the presentation of this work.

Chapter 5

Conclusions

"We know truth, not only by reason, but also by the heart."

Blaise Pascal, *Pensées*

A comprehensive approach to the current climate crisis requires coordinated action from every sector of human society that appreciates the complex interconnections between regions, disciplines, and people groups. This dissertation seeks to explore one small portion of that broader interdisciplinary solution space, with the recognition that technological solutions alone do not have the power to solve these problems. In this section, the main findings of this work are reviewed, and several potential areas for future investigations are outlined. More generally, it is my hope that a more cohesive and constructive understanding of unsteady flows can lead to significant innovation and transformative design initiatives in the renewable-energy sector and beyond.

5.1 Summary of contributions

This series of studies was aimed at addressing gaps in the wind-energy literature in three major areas: unsteady flow modeling, experimental measurements of unsteady-flow models, and experimental techniques for resolving large-scale flow patterns in field applications. The first two sections of this work addressed linearized and nonlinear analytical frameworks for the dynamics and power extraction of a horizontal-axis wind turbine oscillating in periodic surge motions in the streamwise direction, whereas the third section described a novel field-scale measurement approach for quantifying flow fields in the wakes of utility-scale vertical-axis wind turbines.

Specifically, in Chapter 2, a linear ordinary differential equation was derived to model the time-varying dynamics of a surging turbine. The model coefficients were obtained from steady-flow torque measurements and *a priori* knowledge of the characteristics of the turbine and generator. The model predictions for fluctuating quantities such as torque, rotation rate, and power compared favorably with data collected from a surging-turbine apparatus in a fan-array wind tunnel. However,

changes in time-averaged quantities were not predicted by the linearized approach, while deviations from the steady-flow power output between −17% and +6.4% were observed in the data. The power decreases were hypothesized to be connected to flow separation on the turbine blades at low tip-speed ratios and high sectional angles of attack.

In Chapter 3, a nonlinear dynamical model was proposed as a generalization of the linear model. In keeping with the philosophy of the linear model, it only depended on knowledge of the steady-flow characteristics of the turbine, with the turbine power curve introducing the key nonlinearity. This model was able to capture the changes in the time-averaged power extraction of the turbine that the linear model could not, without significantly affecting the predictions of the fluctuating quantities. In addition, a potential-flow model was derived using a collection of point sources to represent a surging porous disc. This flow-field representation was coupled with the nonlinear dynamical model of the turbine via 1D axial-momentum theory to enable time-varying predictions of flow quantities in the upstream induction zone of the surging turbine. This modeling framework was validated using wind-tunnel experiments. Furthermore, the dependence of the power-extraction enhancements observed in the experiments on the local slope and concavity of the turbine power curve was investigated using simulations of the model, which clarified the conditions in which these enhancements are possible. Finally, fully unsteady contributions to the time-averaged power extraction of the turbine were considered through an extension of the theoretical framework of Dabiri (2020). These demonstrated that time-averaged unsteady power-extraction gains are only realizable for wind-energy systems with streamwise fore-aft asymmetry.

In Chapter 4, a three-dimensional particle-tracking velocimetry technique was developed for field-scale volumetric flow measurements in the wakes of utility-scale vertical-axis wind turbines. Artificial snow particles were used as flow seeding, and multiple ground-based cameras allowed the particle tracks to be quantified. Time-averaged velocity and vorticity fields in the near wakes of VAWTs with straight and helical blades were obtained. An unsteady vortex-shedding mechanism was proposed to explain differences observed in the wakes of the two types of turbines, thereby establishing a connection between VAWT blade geometry and wake dynamics.

The salient contributions of these studies to the understanding and quantification of the flow physics of wind-energy systems, as well as their implications, can be

summarized as follows.

1. **A linearized model for the dynamics of a turbine translating in the streamwise direction was developed and experimentally validated.** The model depends only on turbine and generator parameters that can be obtained from steady-flow measurements, and requires no unsteady calibration for use in practical applications. Therefore, it is directly applicable to the modeling and control of floating offshore wind turbines, aerial turbines, and traditional ground-fixed turbines in streamwise flow perturbations. The linear nature of the model can facilitate the implementation of classical control techniques, such as PID controllers, for mitigating fluctuations in torque, power, and resulting fatigue loads due to unsteady disturbances (cf. Fontanella *et al.*, 2020).

2. **Enhancements in the time-averaged power extracted by a periodically surging turbine of up to 6.4% above the steady reference case were measured experimentally and were parameterized by a nonlinear dynamical model.** These increases were observed at high tip-speed ratios, whereas mean power losses in excess of -17% relative to the steady case were incurred at low tip-speed ratios. The nonlinear dynamical model was able to parameterize these behaviors. The identified time-averaged power enhancements suggest that floating offshore wind farms, aerial wind turbines, and other wind-energy systems involving unsteady streamwise flows can achieve large power-generation gains over their steady-flow counterparts — provided the dependencies of these gains on the turbine power curve, tip-speed ratio, and surge kinematics discussed in Chapter 3 are taken into account. In today's burgeoning wind-energy market, even a single-percent increase in power generation could translate to gigawatts of additional energy for consumption and close to 800 million US dollars of additional revenue. These unsteady flow effects could give floating offshore wind farms an additional advantage over traditional ground-fixed installations.

   Conversely, the nonlinear dynamical model also suggests ways in which generator-load control (also known as induction control) or blade-pitch control can be used to mitigate power losses due to unsteady flow conditions when turbines are operating at low tip-speed ratios and high blade-section angles of attack. The model was not able to parameterize the effects of flow separation on the turbine blades, but as it predicted the correct trends in torque and power

at these tip-speed ratios, it can still be used as a reference for control strategies that seek to avoid blade stall in unsteady flows. This topic for future work will be particularly important for turbines operating in gusty environments near the cutoff wind speed.

3. **A potential-flow model coupled with the dynamical model for the turbine captures the time-varying behavior of flow properties in the upstream induction region of the turbine.** Such a connection, which spans potential-flow theory, 1D axial-momentum theory, and nonlinear turbine modeling, serves as a helpful analytical foundation for wind-energy systems in unsteady flows, as well as a demonstration of the continued relevance of simple fluid-mechanical modeling frameworks for parameterizing the dynamics of complex systems. The model can be used for real-time control and flow sensing in wind-energy systems where direct measurements of the far-field wind speed are not possible, for instance for individual turbines in large arrays. This could potentially be achieved by using the model in tandem with nacelle-mounted LiDAR systems or anemometers to infer the "true" incident wind speed, or even by inverting the model to infer the wind speed from the instantaneous torque and rotation rate of the turbine itself.

4. **The 3D-PTV technique allowed for the first volumetric flow-field measurements around utility-scale wind turbines.** This method was shown to be effective in resolving time-averaged flow structures in an unprecedentedly large 10 m $\times$ 7 m $\times$ 7 m volume. It does not depend on natural precipitation and involves relatively inexpensive components (compared to a LiDAR system or met tower), and can thus be used for general field measurements of full-scale structures in atmospheric flows. This method is limited to nocturnal use due to visibility constraints from the particles. However, recent developments in glare-point tracking using soap bubbles could allow similar 3D-PTV approaches to be employed using different seeding particles in daytime conditions, using sunlight as a light source (e.g. Hou *et al.*, 2021; Kaiser and Rival, 2022).

5. **The geometry of VAWT blades affects the vorticity distribution within and shape of the near wake of the turbine.** The symmetry-breaking effect of curved turbine blades introduces topological changes in the near wake, including a central updraft or downdraft along the turbine centerline that can potentially deflect the downstream evolution of the wake upwards or

downwards. (Though the far-wake effects were not shown directly in this work, the numerical study of Gharaati *et al.* (2022) demonstrated the connections between the near-wake dynamics observed here and far-wake characteristics.) These vortex-evolution and wake behaviors are particularly important for the design and optimization of closely packed VAWT arrays, as evidenced by the turbine-pair measurements of Brownstein *et al.* (2019).

5.2 Opportunities for further exploration

Taken together, the findings detailed in this work and their implications provide a foundation for future studies of unsteady fluid mechanics in wind-energy and climate contexts. In the future, combinations of large-scale flow-measurement campaigns and analytical modeling efforts will reveal further ways in which unsteady flows can be leveraged for performance and robustness improvements in wind-energy technologies, as well as other engineering systems that are exposed to atmospheric flows. Several possible directions for further exploration are listed in this section.

5.2.1 Dynamics and control of horizontal-axis wind turbines in unsteady flow conditions

The studies described in Chapters 2 and 3 involved actuated turbine motions. If the performance enhancements observed in these experiments are to be achieved in practical systems, self-excited and self-sustaining oscillations will need to be induced. The existing modeling framework provides an analytical foundation for a dynamical-systems analysis of the problem. For instance, the negatively damped platform-oscillation mode described by López-Queija *et al.* (2022) in floating offshore wind turbines could be excited and maintained by varying the turbine tip-speed ratio in controlled oscillations, thereby inducing changes in the thrust force of the rotor and taking advantage of the streamwise degree of freedom of the floating platform. Alternatively, without employing any time-varying turbine control schemes, the design of the floating platforms could be tuned to accentuate rather than damp out oscillations in the direction of the incident wind. Ambient wave forcings, then, would provide the disturbances required to achieve turbine oscillations and the accompanying additional power gains. In a sense, therefore, the floating offshore wind turbine in unsteady operation could be viewed as a dual wind and wave energy-harvesting device.

In a terrestrial system, a similar effect could be obtained using a turbine mounted to

the top end of an inverted pendulum, balanced by a counterweight below the point of rotation. Periodic changes in the generator load or blade pitch angle could be used to excite swinging oscillations of the pendulum system, which for relatively small angles can be approximated as linear surge motions at the location of the turbine. Simulations using either the linearized or nonlinear dynamical models described previously in this work, in combination with a control system and model for the floating-platform or pendulum dynamics, would give a preliminary indication of whether these oscillations could be incited and sustained, and whether they would lead to sizeable power-extraction enhancements.

It is also important to note that the experiments described in this work employed a turbine with fixed-pitch blades. The true power curve of a turbine, however, is a function of the blade pitch angle as well as the tip-speed ratio. This extra degree of freedom could therefore allow for additional control authority over the surge-induced power enhancements demonstrated in this work. For instance, varying the blade pitch angle within a surge-oscillation cycle could have the same effect as flattening the power curve of a fixed-pitch turbine, thereby leading to higher power-extraction gains. At low tip-speed ratios, blade-pitch control schemes could also be employed strategically to mitigate or avoid flow separation on the blades in critical phases of the surge-oscillation cycle. Since the dynamical models derived in this work give time-resolved predictions of the turbine rotation rate, the instantaneous angle of attack along the turbine blades can be calculated, and based on the steady lift polars of the blade sections, parts of the cycle in which the static stall angle may be exceeded can be identified. The blade pitch angle can then be modulated in these segments to reduce the local angle of attack and inhibit flow separation. Hypothetically, blade-pitch control could even be used to induce dynamic stall on the turbine blades, so that the extra lift provided by the roll-up of the leading-edge vortex could be leveraged for increased turbine power.

The ability to control the turbine generator load and blade pitch angle also suggests the possibility of integrating the dynamical models derived in this work into a feed-forward control system that includes built-in knowledge of the effects of unsteady flow disturbances. This kind of physics-informed controller could be used in floating offshore systems to maximize the time-averaged power enhancements as a function of unsteady surge motions. Alternatively, for ground-fixed turbines in unsteady flow environments, the control scheme could be used to anticipate the effects of incoming flow disturbances and mitigate their impact on structural components.

This application could be particularly useful for wind turbines operating near their cut-in wind speed, i.e. the wind speed below which the turbine would stop operating. The data presented in Chapter 2 suggest that turbines operating near the cut-in wind speed would be particularly sensitive to flow separation during axial-gust events, which could lead to power losses, unsteady fatigue loads, and an unstable decrease in turbine rotation rate leading to full turbine stall. A control scheme that can anticipate and mitigate the effects of unsteady flow disturbances could therefore ensure that turbines are able to more reliably operate at wind speeds just above the cut-in speed. This would in turn increase the capacity factor of these wind farms, by keeping more wind turbines producing power in low-wind conditions. Further analysis is needed to understand the effects of turbine inertia, the timescales of flow disturbances in these low wind speeds, and whether the control authority a turbine has over its operation would be strong enough to overcome the negative effects of these perturbations.

The present work also only investigated flow properties upstream of the surging turbine. The time-varying properties of the wake, however, are critical to the performance of downstream turbines in an array. The time-varying thrust force of the turbine rotor from streamwise flow disturbances or turbine surge oscillations will imprint a periodic unsteady forcing onto the near wake of the turbine, which will propagate downstream into the far wake and appear as an unsteady inflow condition to downstream turbines. An extension of the induction model into the near-wake region could be used as an initial condition for a turbulent far-wake model, as done by Heck *et al.* (2023) for yaw-misaligned turbines in steady flow. The effects of this unsteady wake on downstream turbines could then be studied in a computationally inexpensive manner, and the extended modeling framework could be used in the design and control of floating offshore wind farms and traditional ground-fixed farms in unsteady inflow conditions.

Furthermore, periodic fluctuations in a turbine's thrust and rotation rate could induce instabilities that would affect the evolution of the wake of the turbine. Brown *et al.* (2021) and Brown *et al.* (2022) have suggested that intracycle blade-pitch and rotor-speed oscillations for a turbine operating in steady flow can excite an instability in the tip vortex shed by the turbine, leading to vortex pairing that causes the wake to break down and recover faster than in the steady reference case. Though on slower timescales, the unsteady oscillations in the thrust and rotation rate of a surging turbine, or a turbine in an axial gust, could produce similar instabilities and

corresponding increases in the wake-recovery distance. This in turn could lead to shorter spacing increments between turbines in a floating offshore wind farm, thereby increasing the effective power density of the array. Still, Rockel *et al.* (2016) found that the uncontrolled rocking motions of model floating offshore turbines lead to decreased turbulent mixing within their wakes, implying that these turbines would need to be spaced farther apart than their fixed-bottom counterparts for effective operation in an array. Clearly, these questions require further clarification.

These open questions regarding the wake dynamics of turbines in unsteady flow conditions were the subject of a flow-measurement campaign with collaborators from David Rival's group at Queen's University in Kingston, Ontario during the summer of 2022. While the data have not been sufficiently analyzed to be included in this work, we anticipate that these measurements will shed light on some of the problems and hypotheses discussed above.

5.2.2 Dynamics and optimization of vertical-axis wind turbines in arrays

The field experiments and analysis given in Chapter 4 described qualitative mechanisms for unsteady vortex shedding from VAWT blades as a function of blade shape, as well as their effect on the near wake of the turbine. These phenomena were also visible in the large-eddy simulations of Gharaati *et al.* (2022), though the specific vortex dynamics and vortex-shedding mechanisms were not analyzed. The qualitative agreement between the field data and the numerical simulations lends credence to the proposed mechanism for wake deformation in turbines with curved blades. Further studies, however, could investigate these relationships with more granularity — particularly since the LES computations invoked actuator-line models for the effect of the turbine blades on the flow, and therefore were unable to fully capture the complex interactions of the blades with the local flow conditions they encountered in each rotation period.

The effects of the observed vortical structures on neighboring turbines in closely packed arrays could also be explored in more detail. The experiments of Brownstein *et al.* (2019) were able to visualize differences in strength and spatial arrangement of some of these vortical structures in paired arrangements of VAWTs; however, these time-averaged flow fields belie the complex fluid-structure interactions that the vortical structures shed by one turbine would have on its neighbor in a pair. The timing of these external influences may be particularly significant for the perfor-

mance of VAWTs, as dynamic stall is typically present on the turbine blades, and Strom *et al.* (2017) have shown that intracycle changes in the flow conditions experienced by VAWT blades can significantly affect the power extraction of the turbine. Three-dimensional blade shapes, such as the helical blades considered in this work, further complicate these dynamics, and the dynamic-stall process on these kinds of rotating surfaces needs to be more clearly understood. Overall, the unsteady aerodynamics of VAWT blades and their associated vortical structures continues to be an active area of research. Better parameterizations of these dynamics would enable flow-control schemes and wind-farm arrangements to be developed that improve aggregate efficiency, longevity, and robustness, while also strategically leveraging the shed vortical structures to enhance momentum transport into the wake and thereby increase the effective power density of the array.

5.2.3 Unsteady flow estimation in and around wind-energy installations

Finally, the modeling efforts and experiments presented in this work can inspire more ambitious efforts to quantify and leverage unsteady flows in real atmospheric conditions. As a first step, the feasibility of using wind turbines themselves to detect unsteady flow phenomena may be investigated. Since this work has presented modeling frameworks whose inputs are the time-varying flow conditions encountered by a turbine and whose outputs are the rotation rate, torque, and power of the turbine, it is reasonable to ask whether these models may be inverted, so that the rotation rate and power of a turbine might serve as indicators of unsteady flows. If the frequency, amplitude, and phase of the flow disturbance can be inferred from the inverted modeling framework, then the propagation of an unsteady event could be tracked across an array of turbines and its spatial and temporal variability could be estimated. If possible, this would give existing wind farms a method for characterizing the unsteady flow phenomena they typically encounter as a function of the specific topography and layout of the site, without requiring the installation of additional met towers or other flow sensors.

The wind-energy industry would also benefit from scalable and inexpensive methods for characterizing unsteady flows in remote areas, regions with complex terrain, and new and existing wind-farm sites. Existing methods for flow sensing, such as met towers, LiDAR systems, and point anemometers, tend to be expensive, limited in spatial and temporal resolution, and restricted in altitude. The 3D-PTV

technique described in Chapter 4 suggests that sparse Lagrangian flow measurements could allow much larger measurement domains to be sampled, while still encoding temporally resolved information about local flow statistics along a trajectory. For sampling the atmospheric flows relevant to wind-energy and environmental contexts, the objects used to seed the flow do not necessarily need to resolve the smallest scales of atmospheric turbulence, as large-scale flow structures will often dominate in terms of mixing, convection, and transport. Therefore, Lagrangian drifters such as balloons or passive gliders could be employed to traverse large regions of the atmosphere and collect flow information along their flight paths. Active airborne vehicles such as drones could also be used, provided that transfer functions for their response to quasi-steady and unsteady flow disturbances can be derived so that their dynamics can be decoupled from the flows they are trying to sense. These aircraft could carry onboard anemometers for mobile flow sensing, such as the MEMS system recently developed by Simon *et al.* (2022). Alternatively, since the length scales of the aircraft will be much smaller than those of the flows they are investigating, the aircraft themselves could be treated as flow sensors, as perturbations from their intended flight paths will contain information about the flow disturbances encountered at those points in space and time. The recent study by Wetz and Wildmann (2023) demonstrates a proof-of-concept application of this idea to *in-situ* measurements of wind-turbine wakes. At larger scales, these kinds of systems could be employed to better characterize the so-called *terra incognita* of atmospheric flows: submesoscale flow motions on the order of hundreds of meters to kilometers in length (Wyngaard, 2004). Overall, the scalability of sparse Lagrangian flow-sensing paradigms lends itself well to the study of unsteady flows at atmospheric scales, particularly in comparison to traditional Eulerian methods.

Afterword: On the Exploration of Scientific Questions in Community

Note: The ideas expressed in this section represent the opinions of the author, and are not intended to contribute to the technical content of this work.

As surveyed in the previous section, the topics explored in this work open several possibilities for further research and exploration. In light of these opportunities, I would like to conclude this dissertation by emphasizing that collaboration and community are essential to the practice of scientific and technological innovation in their most potent forms. Given the wide range of pressing issues facing modern society, and the ever-multiplying number of research problems motivated by these questions, robust dialogue and cross-disciplinary communication are indispensable for effectively prioritizing, approaching, and addressing the problems that are most critical to the promotion of human flourishing worldwide. To this end, I believe the full potential of the scientific enterprise can only be reached when people from diverse backgrounds are able to bring their unique perspectives, experiences, and worldviews — in other words, their whole human selves — to the table as we work together to tackle these problems. This is science for humanity and by humanity, and its practice requires empathy, humility, and compassion along with technical expertise and rigor. Only in this manner will we be able to meaningfully engage with the wounds and suffering of a broken and hurting world.

> "The practice of science is not some purely and generically human enterprise, nor some autonomous self-governing and self-sustaining enterprise; but an eminently concrete social-historical enterprise incorporating goals and standards and intuitions and values that people bring to it and that emerge from their interaction with each other after their induction into the practice. We enter the conversation of science as concrete beings of diverse convictions and commitments. We do not shed all our ordinary convictions and commitments at the door of the conversation room of science and enter nakedly human; nor do we shed them all to put on some pure white cloak of science. We enter as who we are; and we begin conversing on whatever is the topic in hand. When some disagreement turns up, we deal with that. We do not make sure that we have forestalled it in advance. Often we learn from our disagreements."
>
> Nicholas Wolterstorff, *Educating for Shalom*

Bibliography

[1] A. Abdelkefi. "Aeroelastic energy harvesting: A review". In: *International Journal of Engineering Science* 100 (2016), pp. 112–135. DOI: 10.1016/j.ijengsci.2015.10.006.

[2] Mahdi Abkar. "Impact of Subgrid-Scale Modeling in Actuator-Line Based Large-Eddy Simulation of Vertical-Axis Wind Turbine Wakes". In: *Atmosphere* 9.7 (2018), p. 257. DOI: 10.3390/atmos9070257.

[3] Mahdi Abkar and John O Dabiri. "Self-similarity and flow characteristics of vertical-axis wind turbine wakes: an LES study". In: *Journal of Turbulence* 18.4 (2017), pp. 373–389.

[4] Aliza Abraham and Jiarong Hong. "Dynamic wake modulation induced by utility-scale wind turbine operation". In: *Applied Energy* 257 (2020), p. 114003. DOI: 10.1016/j.apenergy.2019.114003.

[5] Mojtaba Ahmadi-Baloutaki, Rupp Carriveau, and David S-K Ting. "A wind tunnel study on the aerodynamic interaction of vertical axis wind turbines in array configurations". In: *Renewable Energy* 96 (2016), pp. 904–913.

[6] Alexander D. Aliferis, Marius Stette Jessen, Tania Bracchi, and R. Jason Hearst. "Performance and wake of a Savonius vertical-axis wind turbine under different incoming conditions". In: *Wind Energy* 22.9 (2019), pp. 1260–1273. DOI: 10.1002/we.2358.

[7] A. Aliseda, A. Cartellier, F. Hainaux, and J. C. Lasheras. "Effect of preferential concentration on the settling velocity of heavy particles in homogeneous isotropic turbulence". In: *Journal of Fluid Mechanics* 468 (2002). Publisher: Cambridge University Press, pp. 77–105. DOI: 10.1017/S0022112002001593.

[8] Shreyas Ananthan, Luigi Capone, Marc Henry De Frahan, Jonathan Hu, Jeremy Melvin, James Overfelt, Ashesh Sharma, Jay Sitaraman, Katarzyna Swirydowicz, Stephen Thomas, Ganesh Vijayakumar, Alan Williams, Shashank Yellapantula, and Michael Sprague. *Nalu-Wind and OpenFAST: A high-fidelity modeling and simulation environment for wind energy. Milestone ECP-Q2-FY19*. Tech. rep. SAND-2019-3687R, 674330. Sandia National Laboratories, 2019, SAND–2019–3687R, 1762093, 674330. DOI: 10.2172/1762093.

[9] Daniel B Araya, Tim Colonius, and John O Dabiri. "Transition to bluff-body dynamics in the wake of vertical-axis wind turbines". In: *Journal of Fluid Mechanics* 813 (2017), pp. 346–381.

[10] Daniel B Araya, Anna E Craig, Matthias Kinzel, and John O Dabiri. "Low-order modeling of wind farm aerodynamics using leaky Rankine bodies". In: *Journal of Renewable and Sustainable Energy* 6 (2014).

[11] Daniel B. Araya and John O. Dabiri. "A comparison of wake measurements in motor-driven and flow-driven turbine experiments". In: *Experiments in Fluids* 56.7 (2015), p. 150. DOI: 10.1007/s00348-015-2022-7.

[12] R. J. Arms and Francis R. Hama. "Localized-Induction Concept on a Curved Vortex and Motion of an Elliptic Vortex Ring". In: *The Physics of Fluids* 8.4 (1965), pp. 553–559. DOI: 10.1063/1.1761268.

[13] H. M. Atassi. "The Sears problem for a lifting airfoil revisited - new results". In: *Journal of Fluid Mechanics* 141 (1984), pp. 109–122. DOI: 10.1017/S0022112084000768.

[14] Yeon Sik Baik, Luis P. Bernal, Kenneth Granlund, and Michael V. Ol. "Unsteady force generation and vortex dynamics of pitching and plunging aerofoils". In: *Journal of Fluid Mechanics* 709 (2012). Publisher: Cambridge University Press, pp. 37–68. DOI: 10.1017/jfm.2012.318.

[15] R. J. Barthelmie, S. T. Frandsen, M. N. Nielsen, S. C. Pryor, P.-E. Rethore, and H. E. Jørgensen. "Modelling and measurements of power losses and turbulence intensity in wind turbine wakes at Middelgrunden offshore wind farm". In: *Wind Energy* 10.6 (2007), pp. 517–528. DOI: 10.1002/we.238.

[16] R. J. Barthelmie and L. E. Jensen. "Evaluation of wind farm efficiency and wind turbine wakes at the Nysted offshore wind farm". In: *Wind Energy* 13.6 (2010), pp. 573–586. DOI: 10.1002/we.408.

[17] R. J. Barthelmie, S. C. Pryor, S. T. Frandsen, K. S. Hansen, J. G. Schepers, K. Rados, W. Schlez, A. Neubert, L. E. Jensen, and S. Neckelmann. "Quantifying the Impact of Wind Turbine Wakes on Power Output at Offshore Wind Farms". In: *Journal of Atmospheric and Oceanic Technology* 27 (2010), pp. 1302–1317.

[18] Jan Bartl, Franz Mühle, Jannik Schottler, Lars Sætran, Joachim Peinke, Muyiwa Adaramola, and Michael Hölling. "Wind tunnel experiments on wind turbine wakes in yaw: effects of inflow turbulence and shear". In: *Wind Energy Science* 3.1 (2018). Publisher: Copernicus GmbH, pp. 329–343. DOI: https://doi.org/10.5194/wes-3-329-2018.

[19] M. Bastankhah and F. Porté-Agel. "Wind tunnel study of the wind turbine interaction with a boundary-layer flow: Upwind region, turbine performance, and wake region". In: *Physics of Fluids* 29.6 (2017). Publisher: American Institute of Physics, p. 065105. DOI: 10.1063/1.4984078.

[20] Majid Bastankhah and Fernando Porté-Agel. "Experimental and theoretical study of wind turbine wakes in yawed conditions". In: *Journal of Fluid Mechanics* 806 (2016), pp. 506–541. DOI: 10.1017/jfm.2016.595.

[21] G. K. Batchelor. *An Introduction to Fluid Dynamics*. Cambridge: Cambridge University Press, 2000. DOI: 10.1017/CBO9780511800955.

[22] L. Battisti, L. Zanne, S. Dell'Anna, V. Dossena, G. Persico, and B. Paradiso. "Aerodynamic Measurements on a Vertical Axis Wind Turbine in a Large Scale Wind Tunnel". In: *Journal of Energy Resources Technology* 133.3 (2011), p. 031201. DOI: 10.1115/1.4004360.

[23] I. Bayati, M. Belloli, L. Bernini, and A. Zasso. "Wind Tunnel Wake Measurements of Floating Offshore Wind Turbines". In: *Energy Procedia*. 14th Deep Sea Offshore Wind R&D Conference, EERA DeepWind'2017 137 (2017), pp. 214–222. DOI: 10.1016/j.egypro.2017.10.375.

[24] N. Bempedelis and K. Steiros. "Analytical all-induction state model for wind turbine wakes". In: *Physical Review Fluids* 7.3 (2022). Publisher: American Physical Society, p. 034605. DOI: 10.1103/PhysRevFluids.7.034605.

[25] F. Berger, L. Neuhaus, D. Onnen, M. Hölling, G. Schepers, and M. Kühn. "Experimental analysis of the dynamic inflow effect due to coherent gusts". In: *Wind Energy Science* 7.5 (2022), pp. 1827–1846. DOI: 10.5194/wes-7-1827-2022.

[26] H. Bergh and H. Tijdeman. *Theoretical and experimental results for the dynamic response of pressure measuring systems*. Tech. rep. NLR-TR F. 238. Nationaal Lucht- en Ruimtevaartlaboratorium, 1965. DOI: 10.13140/2.1.4790.1123.

[27] Michael M. Bernitsas and Kamaldev Raghavan. "Fluid motion energy converter". US7493759B2. 2009.

[28] Albert Betz. "Das Maximum der theoretisch möglichen Ausnützung des Windes durch Windmotoren". In: *Zeitschrift für das gesamte Turbinenwesen* 26 (1920), pp. 307–309.

[29] Hannes P. Böhm. "A General Equation for the Terminal Fall Speed of Solid Hydrometeors". In: *Journal of the Atmospheric Sciences* 46.15 (1988), pp. 2419–2427. DOI: 10.1175/1520-0469(1989)046<2419:AGEFTT>2.0.CO;2.

[30] Antoine Borraccino, David Schlipf, Florian Haizmann, and Rozenn Wagner. "Wind field reconstruction from nacelle-mounted lidar short-range measurements". In: *Wind Energy Science* 2.1 (2017). Publisher: Copernicus GmbH, pp. 269–283. DOI: 10.5194/wes-2-269-2017.

[31] Juliaan Bossuyt, Michael F. Howland, Charles Meneveau, and Johan Meyers. "Measurement of unsteady loading and power output variability in a micro wind farm model in a wind tunnel". In: *Experiments in Fluids* 58.1 (2016), p. 1. DOI: 10.1007/s00348-016-2278-6.

[32] Nicolas Boulanger, Patrice Meunier, and Stéphane Le Dizès. "Tilt-induced instability of a stratified vortex". In: *Journal of Fluid Mechanics* 596 (2008), pp. 1–20. DOI: 10.1017/S0022112007009263.

[33] Mickaël Bourgoin and Haitao Xu. "Focus on dynamics of particles in turbulence". In: *New Journal of Physics* 16.8 (2014). Publisher: IOP Publishing, p. 085010. DOI: 10.1088/1367-2630/16/8/085010.

[34] BP. *bp Statistical Review of World Energy 2022*. Tech. rep. London, UK: BP, 2022.

[35] E. Branlard and M. Gaunaa. "Cylindrical vortex wake model: right cylinder: Cylindrical vortex wake model: right cylinder". In: *Wind Energy* 18.11 (2015), pp. 1973–1987. DOI: 10.1002/we.1800.

[36] J. Bremseth and K. Duraisamy. "Computational analysis of vertical axis wind turbine arrays". In: *Theoretical and Computational Fluid Dynamics* 30.5 (2016), pp. 387–401. DOI: 10.1007/s00162-016-0384-y.

[37] C. E. Brennen. *A Review of Added Mass and Fluid Inertial Forces*. Tech. rep. CR 82.010. Port Hueneme, CA, USA: Naval Civil Engineering Laboratory, 1982.

[38] Nathaniel Bristow, Jiaqi Li, Peter Hartford, Michele Guala, and Jiarong Hong. "Imaging-based 3D particle tracking system for field characterization of particle dynamics in atmospheric flows". In: *Experiments in Fluids* 64.4 (2023), p. 78. DOI: 10.1007/s00348-023-03619-6.

[39] G Brochier, P Fraunie, and C Beguierj. "Water Channel Experiments of Dynamic Stall on Darrieus Wind Turbine Blades". In: *Journal of Propulsion* 2.5 (1986).

[40] Kenneth Brown, Daniel Houck, David Maniaci, Carsten Westergaard, and Christopher Kelley. "Accelerated Wind-Turbine Wake Recovery Through Actuation of the Tip-Vortex Instability". In: *AIAA Journal* 60.5 (2022), pp. 3298–3310. DOI: 10.2514/1.J060772.

[41] Kenneth Brown, Daniel Houck, David C. Maniaci, and Carsten Westergaard. "Rapidly Recovering Wind Turbine Wakes with Dynamic Pitch and Rotor Speed Control". In: *AIAA Scitech 2021 Forum*. VIRTUAL EVENT: American Institute of Aeronautics and Astronautics, 2021. DOI: 10.2514/6.2021-1182.

[42] I.D. Brownstein, M. Kinzel, and J.O. Dabiri. "Performance enhancement of downstream vertical-axis wind turbines". In: *Journal of Renewable and Sustainable Energy* 8.5 (2016), p. 053306.

[43] Ian D. Brownstein, Nathaniel J. Wei, and John O. Dabiri. "Aerodynamically Interacting Vertical-Axis Wind Turbines: Performance Enhancement and Three-Dimensional Flow". In: *Energies* 12.14 (2019), p. 2724. DOI: 10.3390/en12142724.

[44] A-J. Buchner, M. W. Lohry, L. Martinelli, J. Soria, and A. J. Smits. "Dynamic stall in vertical axis wind turbines: Comparing experiments and computations". In: *Journal of Wind Engineering and Industrial Aerodynamics* 146 (2015), pp. 163–171. DOI: 10.1016/j.jweia.2015.09.001.

[45] Abel-John Buchner, Julio Soria, Damon Honnery, and Alexander J. Smits. "Dynamic stall in vertical axis wind turbines: scaling and topological considerations". In: *Journal of Fluid Mechanics* 841 (2018), pp. 746–766. DOI: 10.1017/jfm.2018.112.

[46] Bruno Burger. *Öffentliche Nettostromerzeugung in Deutschland im Jahr 2022*. Tech. rep. Freiburg, Germany: Fraunhofer Institute for Solar Energy Systems ISE, 2023.

[47] Raúl Bayoán Cal, José Lebrón, Luciano Castillo, Hyung Suk Kang, and Charles Meneveau. "Experimental study of the horizontally averaged flow structure in a model wind-turbine array boundary layer". In: *Journal of Renewable and Sustainable Energy* 2 (2010).

[48] Marc Calaf, Charles Meneveau, and Johan Meyers. "Large eddy simulation study of fully developed wind-turbine array boundary layers". In: *Physics of Fluids* 22.1 (2010), p. 015110. DOI: 10.1063/1.3291077.

[49] Giuseppe Carlo Alp Caridi, Daniele Ragni, Andrea Sciacchitano, and Fulvio Scarano. "HFSB-seeding for large-scale tomographic PIV in wind tunnels". In: *Experiments in Fluids* 57.12 (2016), p. 190. DOI: 10.1007/s00348-016-2277-7.

[50] Leonardo P. Chamorro and Fernando Porté-Agel. "A Wind-Tunnel Investigation of Wind-Turbine Wakes: Boundary-Layer Turbulence Effects". In: *Boundary-Layer Meteorology* 132.1 (2009), pp. 129–149. DOI: 10.1007/s10546-009-9380-8.

[51] Jean-Jacques Chattot. "Actuator Disk Theory—Steady and Unsteady Models". In: *Journal of Solar Energy Engineering* 136.3 (2014), pp. 031012–031012–10. DOI: 10.1115/1.4026947.

[52] Qian Cheng, Xiaolan Liu, Ho Seong Ji, Kyung Chun Kim, and Bo Yang. "Aerodynamic Analysis of a Helical Vertical Axis Wind Turbine". In: *Energies* 10.4 (2017), p. 575. DOI: 10.3390/en10040575.

[53] Antonello Cherubini, Andrea Papini, Rocco Vertechy, and Marco Fontana. "Airborne Wind Energy Systems: A review of the technologies". In: *Renewable and Sustainable Energy Reviews* 51 (2015), pp. 1461–1476. DOI: 10.1016/j.rser.2015.07.053.

[54] Matthew Churchfield, Sang Lee, and Patrick Moriarty. *Overview of the simulator for wind farm application (SOWFA)*. 2012.

[55] Charles Concordia. *Synchronous Machines: Theory and Performance*. General Electric series. Wiley, 1951.

[56] Anna E. Craig, John O. Dabiri, and Jeffrey R. Koseff. "A Kinematic Description of the Key Flow Characteristics in an Array of Finite-Height Rotating Cylinders". In: *Journal of Fluids Engineering* 138.7 (2016), p. 070906. DOI: 10.1115/1.4032600.

[57] John O. Dabiri. "Potential order-of-magnitude enhancement of wind farm power density via counter-rotating vertical-axis wind turbine arrays". In: *Journal of Renewable and Sustainable Energy* 3.4 (2011), p. 043104. DOI: 10.1063/1.3608170.

[58] John O. Dabiri. "Theoretical framework to surpass the Betz limit using unsteady fluid mechanics". In: *Physical Review Fluids* 5.2 (2020). Publisher: American Physical Society, p. 022501. DOI: 10.1103/PhysRevFluids.5.022501.

[59] Marcelo De Lellis, Romeu Reginatto, Ramiro Saraiva, and Alexandre Trofino. "The Betz limit applied to Airborne Wind Energy". In: *Renewable Energy* 127 (2018), pp. 32–40. DOI: 10.1016/j.renene.2018.04.034.

[60] J. B. de Vaal, M. O. L. Hansen, and T. Moan. "Effect of wind turbine surge motion on rotor thrust and induced velocity". In: *Wind Energy* 17.1 (2014), pp. 105–121. DOI: 10.1002/we.1562.

[61] J. B. de Vaal, M. O. L. Hansen, and T. Moan. "Validation of a vortex ring wake model suited for aeroelastic simulations of floating wind turbines". In: *Journal of Physics: Conference Series* 555.1 (2014). Publisher: IOP Publishing, p. 012025. DOI: 10.1088/1742-6596/555/1/012025.

[62] Reeve Dunne and Beverley J. McKeon. "Dynamic stall on a pitching and surging airfoil". In: *Experiments in Fluids* 56.8 (2015), p. 157. DOI: 10.1007/s00348-015-2028-1.

[63] B Efron. "Bootstrap Methods: Another Look at the Jackknike". In: *The Annals of Statistics* 7.1 (1979), pp. 1–26.

[64] Adnan M. El Makdah, Sacha Ruzzante, Kai Zhang, and David E. Rival. "The influence of axial gusts on the output of low-inertia rotors". In: *Journal of Fluids and Structures* 88 (2019), pp. 71–82. DOI: 10.1016/j.jfluidstructs.2019.04.009.

[65] G. E. Elsinga, J. Westerweel, F. Scarano, and M. Novara. "On the velocity of ghost particles and the bias errors in Tomographic-PIV". In: *Experiments in Fluids* 50.4 (2010), pp. 825–838.

[66] Abdelgalil Eltayesh, Magdy Bassily Hanna, Francesco Castellani, A. S. Huzayyin, Hesham M. El-Batsh, Massimiliano Burlando, and Matteo Becchetti. "Effect of Wind Tunnel Blockage on the Performance of a Horizontal Axis Wind Turbine with Different Blade Number". In: *Energies* 12.10 (2019), p. 1988. DOI: 10.3390/en12101988.

[67] R. Farrugia, T. Sant, and D. Micallef. “A study on the aerodynamics of a floating wind turbine rotor”. In: *Renewable Energy* 86 (2016), pp. 770–784. DOI: 10.1016/j.renene.2015.08.063.

[68] R. Farrugia, T. Sant, and D. Micallef. “Investigating the aerodynamic performance of a model offshore floating wind turbine”. In: *Renewable Energy* 70 (2014), pp. 24–30. DOI: 10.1016/j.renene.2013.12.043.

[69] Carlos Simão Ferreira, Gijs van Kuik, Gerard van Bussel, and Fulvio Scarano. “Visualization by PIV of dynamic stall on a vertical axis wind turbine”. In: *Experiments in Fluids* 46 (2009), pp. 97–108.

[70] Paul Fleming, Jennifer Annoni, Matthew Churchfield, Luis A. Martinez-Tossas, Kenny Gruchalla, Michael Lawson, and Patrick Moriarty. “A simulation study demonstrating the importance of large-scale trailing vortices in wake steering”. In: *Wind Energy Science* 3.1 (2018), pp. 243–255. DOI: https://doi.org/10.5194/wes-3-243-2018.

[71] Paul Fleming, Jennifer Annoni, Andrew Scholbrock, Eliot Quon, Scott Dana, Scott Schreck, Steffen Raach, Florian Haizmann, and David Schlipf. “Full-Scale Field Test of Wake Steering”. In: *Journal of Physics: Conference Series* 854 (2017), p. 012013. DOI: 10.1088/1742-6596/854/1/012013.

[72] Paul Fleming, Jennifer King, Katherine Dykes, Eric Simley, Jason Roadman, Andrew Scholbrock, Patrick Murphy, Julie K. Lundquist, Patrick Moriarty, Katherine Fleming, Jeroen van Dam, Christopher Bay, Rafael Mudafort, Hector Lopez, Jason Skopek, Michael Scott, Brady Ryan, Charles Guernsey, and Dan Brake. “Initial results from a field campaign of wake steering applied at a commercial wind farm – Part 1”. In: *Wind Energy Science* 4.2 (2019), pp. 273–285. DOI: https://doi.org/10.5194/wes-4-273-2019.

[73] A. Fontanella, M. Al, D. van der Hoek, Y. Liu, J. W. van Wingerden, and M. Belloli. “A control-oriented wave-excited linear model for offshore floating wind turbines”. In: *Journal of Physics: Conference Series* 1618 (2020). Publisher: IOP Publishing, p. 022038. DOI: 10.1088/1742-6596/1618/2/022038.

[74] Alessandro Fontanella, Mees Al, Jan-Willem van Wingerden, and Marco Belloli. “Model-based design of a wave-feedforward control strategy in floating wind turbines”. In: *Wind Energy Science* 6.3 (2021). Publisher: Copernicus GmbH, pp. 885–901. DOI: 10.5194/wes-6-885-2021.

[75] T. F. Fric and A. Roshko. “Vortical structure in the wake of a transverse jet”. In: *Journal of Fluid Mechanics* 279 (1994). Publisher: Cambridge University Press, pp. 1–47. DOI: 10.1017/S0022112094003800.

[76] Masoumeh Gharaati, Shuolin Xiao, Nathaniel J. Wei, Luis A. Martínez-Tossas, John O. Dabiri, and Di Yang. “Large-eddy simulation of helical- and straight-bladed vertical-axis wind turbines in boundary layer turbulence”.

In: *Journal of Renewable and Sustainable Energy* 14.5 (2022), p. 053301. DOI: 10.1063/5.0100169.

[77] Shridhar Gopalan, Bruce M. Abraham, and Joseph Katz. "The structure of a jet in cross flow at low velocity ratios". In: *Physics of Fluids* 16.6 (2004). Publisher: American Institute of Physics, pp. 2067–2087. DOI: 10.1063/1.1697397.

[78] Alexander M. Gorlov. "United States Patent: 5451137 - Unidirectional helical reaction turbine operable under reversible fluid flow for power systems". 5451137. 1995.

[79] K. Granlund, B. Monnier, M. Ol, and D. Williams. "Airfoil longitudinal gust response in separated vs. attached flows". In: *Physics of Fluids* 26.2 (2014). Publisher: American Institute of Physics, p. 027103. DOI: 10.1063/1.4864338.

[80] J. Mayo Greenberg. *Airfoil in sinusoidal motion in a pulsating stream*. Tech. rep. 1947.

[81] Brian J Gribben and Graham S Hawkes. *A potential flow model for wind turbine induction and wind farm blockage*. Tech. rep. Frazer-Nash Consultancy, 2019, p. 13.

[82] S. Gueydon, I. Bayati, and E.J. de Ridder. "Discussion of solutions for basin model tests of FOWTs in combined waves and wind". In: *Ocean Engineering* 209 (2020), p. 107288. DOI: 10.1016/j.oceaneng.2020.107288.

[83] Francis R. Hama and John Nutant. "Self-Induced Velocity on a Curved Vortex". In: *The Physics of Fluids* 4.1 (1961), pp. 28–32. DOI: 10.1063/1.1706184.

[84] Dowon Han, Young Gun Heo, Nak Joon Choi, Sang Hyun Nam, Kyoung Ho Choi, and Kyung Chun Kim. "Design, Fabrication, and Performance Test of a 100-W Helical-Blade Vertical-Axis Wind Turbine at Low Tip-Speed Ratio". In: *Energies* 11.6 (2018), p. 1517. DOI: 10.3390/en11061517.

[85] Martin Hansen. *Aerodynamics of Wind Turbines*. 0th ed. Routledge, 2015. DOI: 10.4324/9781315769981.

[86] Richard Hartley and Andrew Zisserman. *Multiple View Geometry*. 2nd Edition. Cambridge University Press, 2003.

[87] Ernest F. Hasselbrink and M. G. Mungal. "Transverse jets and jet flames. Part 1. Scaling laws for strong transverse jets". In: *Journal of Fluid Mechanics* 443 (2001). Publisher: Cambridge University Press, pp. 1–25. DOI: 10.1017/S0022112001005146.

[88] Erich Hau. "Rotor Aerodynamics". In: *Wind Turbines: Fundamentals, Technologies, Application, Economics*. Ed. by Erich Hau. Berlin, Heidelberg: Springer, 2013, pp. 89–166. DOI: 10.1007/978-3-642-27151-9_5.

[89] Erich Hau. *Wind Turbines Fundamentals, Technologies, Application, Economics*. Springer, 2013.

[90] K.S. Heck, H.M. Johlas, and M.F. Howland. "Modelling the induction, thrust and power of a yaw-misaligned actuator disk". In: *Journal of Fluid Mechanics* 959 (2023), A9. DOI: 10.1017/jfm.2023.129.

[91] Siegfried Heier. *Grid Integration of Wind Energy: Onshore and Offshore Conversion Systems*. Chichester, UK: John Wiley & Sons, Ltd, 2014. DOI: 10.1002/9781118703274.

[92] Seyed Hossein Hezaveh and Elie Bou-Zeid. "Mean kinetic energy replenishment mechanisms in vertical-axis wind turbine farms". In: *Phys. Rev. Fluids* 3.094606 (2018).

[93] Seyed Hossein Hezaveh, Elie Bou-Zeid, John O. Dabiri, Matthias Kinzel, Gerard Cortina, and Luigi Martinelli. "Increasing the Power Production of Vertical- Axis Wind- Turbine- Farms using Synergistic Clustering". In: *Boundary Layer Meteorology* 169.2 (2018), pp. 275–296.

[94] Claudia Hofemann, Carlos Simão Ferreira, Kristian Dixon, Gerard Van Bussel, Gijs Van Kuik, and Fulvio Scarano. "3D Stereo PIV study of tip vortex evolution on a VAWT". In: *The proceedings of the European Wind Energy Conference and exhibition EWEC*. Brussels,Belgium: European Wind Energy Association EWEA, 2008.

[95] Jiarong Hong, Mostafa Toloui, Leonardo P. Chamorro, Michele Guala, Kevin Howard, Sean Riley, James Tucker, and Fotis Sotiropoulos. "Natural snowfall reveals large-scale flow structures in the wake of a 2.5-MW wind turbine". In: *Nature Communications* 5 (2014), p. 4216. DOI: 10.1038/ncomms5216.

[96] Jianfeng Hou, Frieder Kaiser, Andrea Sciacchitano, and David E. Rival. "A novel single-camera approach to large-scale, three-dimensional particle tracking based on glare-point spacing". In: *Experiments in Fluids* 62.5 (2021), p. 100. DOI: 10.1007/s00348-021-03178-8.

[97] Kevin B. Howard and Michele Guala. "Upwind preview to a horizontal axis wind turbine: a wind tunnel and field-scale study". In: *Wind Energy* 19.8 (2016), pp. 1371–1389. DOI: 10.1002/we.1901.

[98] Michael F. Howland, Juliaan Bossuyt, Luis A. Martínez-Tossas, Johan Meyers, and Charles Meneveau. "Wake structure in actuator disk models of wind turbines in yaw under uniform inflow conditions". In: *Journal of Renewable and Sustainable Energy* 8.4 (2016), p. 043301. DOI: 10.1063/1.4955091.

[99] Michael F. Howland, Sanjiva K. Lele, and John O. Dabiri. "Wind farm power optimization through wake steering". In: *Proceedings of the National Academy of Sciences* 116.29 (2019), pp. 14495–14500. DOI: 10.1073/pnas.1903680116.

[100] Mark Hutchinson and Feng Zhao. *Global Wind Report 2023*. Tech. rep. Brussels, Belgium: Global Wind Energy Council, 2023, p. 120.

[101] Miloš Ilak, Philipp Schlatter, Shervin Bagheri, and Dan S. Henningson. "Bifurcation and stability analysis of a jet in cross-flow: onset of global instability at a low velocity ratio". In: *Journal of Fluid Mechanics* 696 (2012). Publisher: Cambridge University Press, pp. 94–121. DOI: 10.1017/jfm.2012.10.

[102] IPCC. *Climate Change 2023: Synthesis Report*. A Report of the Intergovernmental Panel on Climate Change. Geneva, Switzerland: IPCC, 2023.

[103] Peter J. Ireland, Andrew D. Bragg, and Lance R. Collins. "The effect of Reynolds number on inertial particle dynamics in isotropic turbulence. Part 2. Simulations with gravitational effects". In: *Journal of Fluid Mechanics* 796 (2016). Publisher: Cambridge University Press, pp. 659–711. DOI: 10.1017/jfm.2016.227.

[104] IRENA. *Renewable Power Generation Costs in 2021*. Tech. rep. Abu Dhabi: International Renewable Energy Agency, 2022.

[105] Mark Z. Jacobson and Cristina Lozej Archer. "Saturation wind power potential and its implications for wind energy." In: *Proceedings of the National Academy of Sciences of the United States of America* 109.39 (2012), pp. 15679–15684. DOI: 10.1073/pnas.1208993109.

[106] H. M. Johlas, L. A. Martínez-Tossas, D. P. Schmidt, M. A. Lackner, and M. J. Churchfield. "Large eddy simulations of floating offshore wind turbine wakes with coupled platform motion". In: *Journal of Physics: Conference Series* 1256.1 (2019). Publisher: IOP Publishing, p. 012018. DOI: 10.1088/1742-6596/1256/1/012018.

[107] Hannah M. Johlas, Luis A. Martínez-Tossas, Matthew J. Churchfield, Matthew A. Lackner, and David P. Schmidt. "Floating platform effects on power generation in spar and semisubmersible wind turbines". In: *Wind Energy* 24.8 (2021), pp. 901–916. DOI: 10.1002/we.2608.

[108] Wayne Johnson. *Helicopter Theory*. Princeton University Press, 1980.

[109] Jason Jonkman. *Google / Makani Energy Kite Modeling: Cooperative Research and Development Final Report, CRADA Number CRD-17-00569*. Tech. rep. NREL/TP-5000-80635. National Renewable Energy Lab. (NREL), Golden, CO (United States), 2021. DOI: 10.2172/1813012.

[110] Jason Jonkman. "Influence of Control on the Pitch Damping of a Floating Wind Turbine". In: *46th AIAA Aerospace Sciences Meeting and Exhibit*. Aerospace Sciences Meetings NREL/CP-500-42589. American Institute of Aeronautics and Astronautics, 2008. DOI: 10.2514/6.2008-1306.

[111] Jason M. Jonkman, Alan D. Wright, Greg J. Hayman, and Amy N. Robertson. "Full-System Linearization for Floating Offshore Wind Turbines in OpenFAST". In: *ASME 2018 1st International Offshore Wind Technical Conference*. San Francisco, California, USA: American Society of Mechanical Engineers, 2018, V001T01A028. DOI: 10.1115/IOWTC2018-1025.

[112] Frieder Kaiser and David E. Rival. *Large-scale volumetric particle tracking using a single camera: Analysis of the scalability and accuracy of glare-point particle tracking*. preprint. 2022. DOI: 10.21203/rs.3.rs-2356060/v1.

[113] Ann R. Karagozian. "The jet in crossflow". In: *Physics of Fluids* 26.10 (2014). Publisher: American Institute of Physics, p. 101303. DOI: 10.1063/1.4895900.

[114] Morteza Khosravi, Partha Sarkar, and Hui Hu. "An Experimental Investigation on the Performance and the Wake Characteristics of a Wind Turbine Subjected to Surge Motion". In: *33rd Wind Energy Symposium*. American Institute of Aeronautics and Astronautics, 2015.

[115] Matthias Kinzel, Daniel B. Araya, and John O. Dabiri. "Turbulence in vertical axis wind turbine canopies". In: *Physics of Fluids* 27.11 (2015), p. 115102. DOI: 10.1063/1.4935111.

[116] Matthias Kinzel, Quinn Mulligan, and John O. Dabiri. "Energy exchange in an array of vertical-axis wind turbines". In: *Journal of Turbulence* 13 (2012), N38. DOI: 10.1080/14685248.2012.712698.

[117] Paul C Klimas and Mark H Worstell. "Effects of Blade Preset Pitch / Offset on Curved-Blade Darrieus Vertical Axis Wind Turbine Performance". In: *Sandia Report* (1981).

[118] L. Klotz, K. Gumowski, and J. E. Wesfreid. "Experiments on a jet in a crossflow in the low-velocity-ratio regime". In: *Journal of Fluid Mechanics* 863 (2019). Publisher: Cambridge University Press, pp. 386–406. DOI: 10.1017/jfm.2018.974.

[119] J.-K. Koo and David F. James. "Fluid flow around and through a screen". In: *Journal of Fluid Mechanics* 60.3 (1973). Publisher: Cambridge University Press, pp. 513–538. DOI: 10.1017/S0022112073000327.

[120] Karsten M. Kopperstad, Rajan Kumar, and Kourosh Shoele. "Aerodynamic characterization of barge and spar type floating offshore wind turbines at different sea states". In: *Wind Energy* 23.11 (2020), pp. 2087–2112. DOI: 10.1002/we.2547.

[121] John W. Kurelek, Alexander Piqué, and Marcus Hultmark. "Performance of the porous disk wind turbine model at a high Reynolds number: Solidity distribution and length scales effects". In: *Journal of Wind Engineering and Industrial Aerodynamics* 237 (2023), p. 105377. DOI: 10.1016/j.jweia.2023.105377.

[122] Sir Horace Lamb. *Hydrodynamics*. 4th ed. Cambridge: University Press, 1916.

[123] Gunner Chr Larsen and Kurt S. Hansen. "Full-scale measurements of aerodynamic induction in a rotor plane". In: *Journal of Physics: Conference Series* 555 (2014). Publisher: IOP Publishing, p. 012063. DOI: 10.1088/1742-6596/555/1/012063.

[124] T. J. Larsen and T. D. Hanson. "A method to avoid negative damped low frequent tower vibrations for a floating, pitch controlled wind turbine". In: *Journal of Physics: Conference Series* 75 (2007). Publisher: IOP Publishing, p. 012073. DOI: 10.1088/1742-6596/75/1/012073.

[125] Hakjin Lee and Duck-Joo Lee. "Effects of platform motions on aerodynamic performance and unsteady wake evolution of a floating offshore wind turbine". In: *Renewable Energy* 143 (2019), pp. 9–23. DOI: 10.1016/j.renene.2019.04.134.

[126] Gordon J. Leishman. *Principles of Helicopter Aerodynamics*. Cambridge University Press, 2006.

[127] J. G. Leishman and T. S. Beddoes. "A Semi-Empirical Model for Dynamic Stall". In: *Journal of the American Helicopter Society* 34.3 (1989), pp. 3–17. DOI: 10.4050/JAHS.34.3.3.

[128] Anthony Leonard. "Computing Three-Dimensional Incompressible Flows with Vortex Elements". In: *Annual Review of Fluid Mechanics* 17.1 (1985), pp. 523–559. DOI: 10.1146/annurev.fl.17.010185.002515.

[129] Javier López-Queija, Eider Robles, Josu Jugo, and Santiago Alonso-Quesada. "Review of control technologies for floating offshore wind turbines". In: *Renewable and Sustainable Energy Reviews* 167 (2022), p. 112787. DOI: 10.1016/j.rser.2022.112787.

[130] Adam Lucas. *Wind, Water, Work: Ancient and Medieval Milling Technology*. Leiden, The Netherlands: Brill, 2006. DOI: https://doi.org/10.1163/9789047417224.

[131] Paolo Luzzatto-Fegiz and Colm-cille P. Caulfield. "Entrainment model for fully-developed wind farms: Effects of atmospheric stability and an ideal limit for wind farm performance". In: *Physical Review Fluids* 3.9 (2018), p. 093802. DOI: 10.1103/PhysRevFluids.3.093802.

[132] Krishnan Mahesh. "The Interaction of Jets with Crossflow". In: *Annual Review of Fluid Mechanics* 45.1 (2013), pp. 379–407. DOI: 10.1146/annurev-fluid-120710-101115.

[133] Simone Mancini, Koen Boorsma, Marco Caboni, Marion Cormier, Thorsten Lutz, Paolo Schito, and Alberto Zasso. "Characterization of the unsteady aerodynamic response of a floating offshore wind turbine to surge mo-

tion". In: *Wind Energy Science* 5.4 (2020). Publisher: Copernicus GmbH, pp. 1713–1730. DOI: 10.5194/wes-5-1713-2020.

[134] Jakob Mann, Alfredo Peña, Niels Troldborg, and Søren J. Andersen. "How does turbulence change approaching a rotor?" In: *Wind Energy Science* 3.1 (2018). Publisher: Copernicus GmbH, pp. 293–300. DOI: 10.5194/wes-3-293-2018.

[135] David Marten. "QBlade: a modern tool for the aeroelastic simulation of wind turbines". Publisher: Technische Universität Berlin. PhD thesis. Berlin, Germany: Technische Universität Berlin, 2020.

[136] D. Medici, S. Ivanell, J.-Å. Dahlberg, and P. H. Alfredsson. "The upstream flow of a wind turbine: blockage effect". In: *Wind Energy* 14.5 (2011), pp. 691–697. DOI: 10.1002/we.451.

[137] Charles Meneveau. "The top-down model of wind farm boundary layers and its applications". In: *Journal of Turbulence* 13 (2012), N7. DOI: 10.1080/14685248.2012.663092.

[138] A Meyer Forsting, Os Rathmann, MP van der Laan, N Troldborg, B Gribben, G Hawkes, and E Branlard. "Verification of induction zone models for wind farm annual energy production estimation". In: *Journal of Physics: Conference Series* 1934.1 (2021), p. 012023. DOI: 10.1088/1742-6596/1934/1/012023.

[139] Johan Meyers and Charles Meneveau. "Optimal turbine spacing in fully developed wind farm boundary layers". In: *Wind Energy* 15.2 (2012), pp. 305–317. DOI: 10.1002/we.469.

[140] Daniel Micallef and Tonio Sant. "Loading effects on floating offshore horizontal axis wind turbines in surge motion". In: *Renewable Energy* 83 (2015), pp. 737–748. DOI: 10.1016/j.renene.2015.05.016.

[141] Mark A. Miller, Subrahmanyam Duvvuri, Ian Brownstein, Marcus Lee, John O. Dabiri, and Marcus Hultmark. "Vertical-axis wind turbine experiments at full dynamic similarity". In: *Journal of Fluid Mechanics* 844 (2018), pp. 707–720. DOI: 10.1017/jfm.2018.197.

[142] Mark A. Miller, Subrahmanyam Duvvuri, William D. Kelly, and Marcus Hultmark. "Rotor solidity effects on the performance of vertical-axis wind turbines at high Reynolds numbers". In: vol. 1037. IOP Conference Series. Milan, Italy: IOP Publishing, 2018.

[143] Mark A. Miller, Janik Kiefer, Carsten Westergaard, Martin O. L. Hansen, and Marcus Hultmark. "Horizontal axis wind turbine testing at high Reynolds numbers". In: *Physical Review Fluids* 4.11 (2019). Publisher: American Physical Society, p. 110504. DOI: 10.1103/PhysRevFluids.4.110504.

[144] K Modarresi and R H Kirchhoff. *The Flow Field Upstream Of A Horizontal Axis Wind Turbine*. Tech. rep. Paper 10. Amherst, MA: University of Massachusetts Wind Energy Center, 1979, p. 97.

[145] Parviz Moin, Anthony Leonard, and John Kim. "Evolution of a curved vortex filament into a vortex ring". In: *The Physics of Fluids* 29.4 (1986), pp. 955–963. DOI: 10.1063/1.865690.

[146] Erik Möllerström, Paul Gipe, Jos Beurskens, and Fredric Ottermo. "A historical review of vertical axis wind turbines rated 100 kW and above". In: *Renewable and Sustainable Energy Reviews* 105 (2019), pp. 1–13. DOI: 10.1016/j.rser.2018.12.022.

[147] Andras Nemes, Teja Dasari, Jiarong Hong, Michele Guala, and Filippo Coletti. "Snowflakes in the atmospheric surface layer: observation of particle–turbulence dynamics". In: *Journal of Fluid Mechanics* 814 (2017). Publisher: Cambridge University Press, pp. 592–613. DOI: 10.1017/jfm.2017.13.

[148] Nicolai Gayle Nygaard and Alexander Christian Newcombe. "Wake behind an offshore wind farm observed with dual-Doppler radars". In: *Journal of Physics: Conference Series* 1037 (2018), p. 072008. DOI: 10.1088/1742-6596/1037/7/072008.

[149] Nicholas T Ouellette, Haitao Xu, and Eberhard Bodenschatz. "A quantitative study of three-dimensional Lagrangian particle tracking algorithms". In: *Experiments in Fluids* 40 (2006), pp. 301–313.

[150] Pablo Ouro, Stefan Runge, Qianyu Luo, and Thorsten Stoesser. "Three-dimensionality of the wake recovery behind a vertical axis turbine". In: *Renewable Energy* 133 (2019), pp. 1066–1077. DOI: 10.1016/j.renene.2018.10.111.

[151] Stig Øye. "Dynamic stall simulated as time lag of separation". In: *Proceedings of the 4th IEA Symposium on the Aerodynamics of Wind Turbines*. Vol. 27. Rome, Italy, 1991, p. 28.

[152] Colin M Parker, Daniel B Araya, and Megan C Leftwich. "Effect of chord–to–diameter ratio on vertical–axis wind turbine wake development". In: *Experiments in Fluids* 58.168 (2017).

[153] Colin M Parker and Megan C Leftwich. "The effect of tip speed ratio on a vertical axis wind turbine at high Reynolds numbers". In: *Experiments in Fluids* 57.74 (2016).

[154] Alec J. Petersen, Lucia Baker, and Filippo Coletti. "Experimental study of inertial particles clustering and settling in homogeneous turbulence". In: *Journal of Fluid Mechanics* 864 (2019). Publisher: Cambridge University Press, pp. 925–970. DOI: 10.1017/jfm.2019.31.

[155] Dale M. Pitt and David A. Peters. "Theoretical Prediction of Dynamic-Inflow Derivatives". In: *6th European Rotorcraft and Powered Lift Aircraft Forum, Paper*. Vol. 47. Bristol, England, 1980.

[156] Antonio Posa and Elias Balaras. "Large Eddy Simulation of an isolated vertical axis wind turbine". In: *Journal of Wind Engineering & Industrial Aerodynamics* 172 (2018), pp. 139–151.

[157] Antonio Posa, Colin M Parker, Megan C Leftwich, and Elias Balaras. "Wake structure of a single vertical axis wind turbine". In: *International Journal of Heat and Fluid Flow* 61 (2016), pp. 75–84.

[158] R. Ganesh Rajagopalan, Ted L. Rickerl, and Paul C. Klimas. "Aerodynamic interference of vertical axis wind turbines". In: *Journal of Propulsion and Power* 6.5 (1990), pp. 645–653. DOI: 10.2514/3.23266.

[159] Abdolrahim Rezaeiha and Daniel Micallef. "Wake interactions of two tandem floating offshore wind turbines: CFD analysis using actuator disc model". In: *Renewable Energy* 179 (2021), pp. 859–876. DOI: 10.1016/j.renene.2021.07.087.

[160] Abdolrahim Rezaeiha, Hamid Montazeri, and Bert Blocken. "Towards optimal aerodynamic design of vertical axis wind turbines: Impact of solidity and number of blades". In: *Energy* 165 (2018), pp. 1129–1148. DOI: 10.1016/j.energy.2018.09.192.

[161] F. P. Ricou and D. B. Spalding. "Measurements of entrainment by axisymmetrical turbulent jets". In: *Journal of Fluid Mechanics* 11.1 (1961). Publisher: Cambridge University Press, pp. 21–32. DOI: 10.1017/S0022112061000834.

[162] Stanislav Rockel, Joachim Peinke, Michael Hölling, and Raúl Bayoán Cal. "Wake to wake interaction of floating wind turbine models in free pitch motion: An eddy viscosity and mixing length approach". In: *Renewable Energy* 85 (2016), pp. 666–676. DOI: 10.1016/j.renene.2015.07.012.

[163] V. Rolin and F. Porté-Agel. "Wind-tunnel study of the wake behind a vertical axis wind turbine in a boundary layer flow using stereoscopic particle image velocimetry". In: *Journal of Physics: Conference Series* 625 (2015), p. 012012. DOI: 10.1088/1742-6596/625/1/012012.

[164] Vincent F-C. Rolin and Fernando Porté-Agel. "Experimental investigation of vertical-axis wind-turbine wakes in boundary layer flow". In: *Renewable Energy* 118 (2018), pp. 1–13. DOI: 10.1016/j.renene.2017.10.105.

[165] Kevin J Ryan, Filippo Coletti, Christopher J Elkins, John O Dabiri, and John K Eaton. "Three–dimensional flow field around and downstream of a subscale model rotating vertical axis wind turbine". In: *Experiments in Fluids* 57.38 (2016).

[166] Tonio Sant, David Bonnici, Russell Farrugia, and Daniel Micallef. "Measurements and modelling of the power performance of a model floating wind turbine under controlled conditions". In: *Wind Energy* 18.5 (2015). _eprint: https://onlinelibrary.wiley.com/doi/pdf/10.1002/we.1730, pp. 811–834. DOI: 10.1002/we.1730.

[167] Sasan Sarmast, Antonio Segalini, Robert F. Mikkelsen, and Stefan Ivanell. "Comparison of the near-wake between actuator-line simulations and a simplified vortex model of a horizontal-axis wind turbine". In: *Wind Energy* 19.3 (2016), pp. 471–481. DOI: 10.1002/we.1845.

[168] Daniel Schanz, Sebastian Gesemann, and Andreas Schröder. "Shake-The-Box: Lagrangian particle tracking at high particle image densities". In: *Experiments in Fluids* 57.5 (2016), p. 70. DOI: 10.1007/s00348-016-2157-1.

[169] Daniele Schiavazzi, Filippo Coletti, Gianluca Iaccarino, and John K. Eaton. "A matching pursuit approach to solenoidal filtering of three-dimensional velocity measurements". In: *Journal of Computational Physics* 263 (2014), pp. 206–221. DOI: 10.1016/j.jcp.2013.12.049.

[170] Jannik Schottler, Nico Reinke, Agnieszka Hölling, Jonathan Whale, Joachim Peinke, and Michael Hölling. "On the impact of non-Gaussian wind statistics on wind turbines – an experimental approach". In: *Wind Energy Science* 2.1 (2017). Publisher: Copernicus GmbH, pp. 1–13. DOI: https://doi.org/10.5194/wes-2-1-2017.

[171] Frank Schuerich and Richard E. Brown. "Effect of Dynamic Stall on the Aerodynamics of Vertical-Axis Wind Turbines". In: *AIAA Journal* 49.11 (2011), pp. 2511–2521. DOI: 10.2514/1.J051060.

[172] William R. Sears. "Some aspects of non-stationary airfoil theory and its practical application". In: *Journal of the Aeronautical Sciences* 8.3 (1941), pp. 104–108. DOI: 10.2514/8.10655.

[173] T. Sebastian and M.A. Lackner. "Development of a free vortex wake method code for offshore floating wind turbines". In: *Renewable Energy* 46 (2012), pp. 269–275. DOI: 10.1016/j.renene.2012.03.033.

[174] Thomas Sebastian and Matthew A. Lackner. "Characterization of the unsteady aerodynamics of offshore floating wind turbines". In: *Wind Energy* 16.3 (2013), pp. 339–352. DOI: 10.1002/we.545.

[175] Sina Shamsoddin and Fernando Porté-Agel. "A Large-Eddy Simulation Study of Vertical Axis Wind Turbine Wakes in the Atmospheric Boundary Layer". In: *Energies* 9.5 (2016), p. 366. DOI: 10.3390/en9050366.

[176] Sina Shamsoddin and Fernando Porté-Agel. "Large Eddy Simulation of Vertical Axis Wind Turbine Wakes". In: *Energies* 7.2 (2014), pp. 890–912.

[177] Carl R. Shapiro, Dennice F. Gayme, and Charles Meneveau. "Modelling yawed wind turbine wakes: a lifting line approach". In: *Journal of Fluid Mechanics* 841 (2018). DOI: 10.1017/jfm.2018.75.

[178] William J. Shaw, Larry K. Berg, Mithu Debnath, Georgios Deskos, Caroline Draxl, Virendra P. Ghate, Charlotte B. Hasager, Rao Kotamarthi, Jeffrey D. Mirocha, Paytsar Muradyan, William J. Pringle, David D. Turner, and James M. Wilczak. "Scientific challenges to characterizing the wind resource in the marine atmospheric boundary layer". In: *Wind Energy Science* 7.6 (2022), pp. 2307–2334. DOI: 10.5194/wes-7-2307-2022.

[179] Xin Shen, Jinge Chen, Ping Hu, Xiaocheng Zhu, and Zhaohui Du. "Study of the unsteady aerodynamics of floating wind turbines". In: *Energy* 145 (2018), pp. 793–809. DOI: 10.1016/j.energy.2017.12.100.

[180] Eric Simley, Nikolas Angelou, Torben Mikkelsen, Mikael Sjöholm, Jakob Mann, and Lucy Y. Pao. "Characterization of wind velocities in the upstream induction zone of a wind turbine using scanning continuous-wave lidars". In: *Journal of Renewable and Sustainable Energy* 8.1 (2016). Publisher: American Institute of Physics, p. 013301. DOI: 10.1063/1.4940025.

[181] Nathaniel Simon, Alexander Piqué, David Snyder, Kyle Ikuma, Anirudha Majumdar, and Marcus Hultmark. "Fast-response hot-wire flow sensors for wind and gust estimation on UAVs". In: *Measurement Science and Technology* 34.2 (2022), p. 025109.

[182] Bjørn Skaare, Finn Gunnar Nielsen, Tor David Hanson, Rune Yttervik, Ole Havmøller, and Arne Rekdal. "Analysis of measurements and simulations from the Hywind Demo floating wind turbine: Dynamic analysis of the Hywind Demo floating wind turbine". In: *Wind Energy* 18.6 (2015), pp. 1105–1122. DOI: 10.1002/we.1750.

[183] Luke R. Smith and Anya R. Jones. "Measurements on a yawed rotor blade pitching in reverse flow". In: *Physical Review Fluids* 4.3 (2019), p. 034703. DOI: 10.1103/PhysRevFluids.4.034703.

[184] H Snel and J G Schepers. *Joint investigation of dynamic inflow effects and implementation of an engineering method*. Tech. rep. ECN-C-94-107. Netherlands: Netherlands Energy Research Foundation (ECN), 1995.

[185] M A Sprague, S Ananthan, G Vijayakumar, and M Robinson. "ExaWind: A multifidelity modeling and simulation environment for wind energy". In: *Journal of Physics: Conference Series* 1452.1 (2020), p. 012071. DOI: 10.1088/1742-6596/1452/1/012071.

[186] K. Steiros and M. Hultmark. "Drag on flat plates of arbitrary porosity". In: *Journal of Fluid Mechanics* 853 (2018). Publisher: Cambridge University Press. DOI: 10.1017/jfm.2018.621.

[187] Richard J.A.M. Stevens and Charles Meneveau. "Flow Structure and Turbulence in Wind Farms". In: *Annual Review of Fluid Mechanics* 49.1 (2017), pp. 311–339. DOI: 10.1146/annurev-fluid-010816-060206.

[188] William Stevenson and John Grainger. *Power System Analysis*. Google-Books-ID: NBIoAQAAMAAJ. McGraw-Hill Education, 1994.

[189] Benjamin Strom, Steven L. Brunton, and Brian Polagye. "Intracycle angular velocity control of cross-flow turbines". In: *Nature Energy* 2.8 (2017), p. 17103. DOI: 10.1038/nenergy.2017.103.

[190] Benjamin Strom, Brian Polagye, and Steven L. Brunton. "Near-wake dynamics of a vertical-axis turbine". In: *Journal of Fluid Mechanics* 935 (2022), A6. DOI: 10.1017/jfm.2021.1123.

[191] L. K. Su and M. G. Mungal. "Simultaneous measurements of scalar and velocity field evolution in turbulent crossflowing jets". In: *Journal of Fluid Mechanics* 513 (2004). Publisher: Cambridge University Press, pp. 1–45. DOI: 10.1017/S0022112004009401.

[192] Shilin Sun, Tianyang Wang, and Fulei Chu. "In-situ condition monitoring of wind turbine blades: A critical and systematic review of techniques, challenges, and futures". In: *Renewable and Sustainable Energy Reviews* 160 (2022), p. 112326. DOI: 10.1016/j.rser.2022.112326.

[193] G. I Taylor. *The aerodynamics of porous sheets*. Tech. rep. 2237. London, England: Aeronautical Research Council (Great Britain), 1944.

[194] G. Tescione, D. Ragni, C. He, C. J. Simão Ferreira, and G. J. W. van Bussel. "Near wake flow analysis of a vertical axis wind turbine by stereoscopic particle image velocimetry". In: *Renewable Energy*. Special issue on aerodynamics of offshore wind energy systems and wakes 70 (2014), pp. 47–61. DOI: 10.1016/j.renene.2014.02.042.

[195] Theodore Theodorsen. *General theory of aerodynamic instability and the mechanism of flutter*. Technical Report 496. National Advisory Committee for Aeronautics, 1934.

[196] Diane H. Theriault, Nathan W. Fuller, Brandon E. Jackson, Evan Bluhm, Dennis Evangelista, Zheng Wu, Margrit Betke, and Tyson L. Hedrick. "A protocol and calibration method for accurate multi-camera field videography". In: *Journal of Experimental Biology* 217 (2014), pp. 1843–1848.

[197] Jeff Tollefson. "Top climate scientists are sceptical that nations will rein in global warming". In: *Nature* 599.7883 (2021), pp. 22–24. DOI: 10.1038/d41586-021-02990-w.

[198] Federico Toschi and Eberhard Bodenschatz. "Lagrangian Properties of Particles in Turbulence". In: *Annual Review of Fluid Mechanics* 41.1 (2009), pp. 375–404. DOI: 10.1146/annurev.fluid.010908.165210.

[199] CT Tran and D Petot. "Semi-empirical model for the dynamic stall of airfoils in view of the application to the calculation of responses of a helicopter blade in forward flight". In: *Vertica* 5 (1980), pp. 35–53.

[200] Thanh Toan Tran and Dong-Hyun Kim. "A CFD study into the influence of unsteady aerodynamic interference on wind turbine surge motion". In: *Renewable Energy* 90 (2016), pp. 204–228. DOI: 10.1016/j.renene.2015.12.013.

[201] Clement John Tranter. *Bessel Functions with Some Physical Applications*. Hart Publishing Company, 1968.

[202] Niels Troldborg and Alexander Raul Meyer Forsting. "A simple model of the wind turbine induction zone derived from numerical simulations". In: *Wind Energy* 20.12 (2017), pp. 2011–2020. DOI: 10.1002/we.2137.

[203] UN. *Emissions Gap Report 2022: The Closing Window - Climate Crisis Calls for Rapid Transformation of Societies*. Tech. rep. United Nations Environment Programme, 2022.

[204] Gijs A.M. Van Kuik. "The Lanchester–Betz–Joukowsky limit". In: *Wind Energy* 10.3 (2007), pp. 289–291. DOI: 10.1002/we.218.

[205] Paul Veers, Katherine Dykes, Eric Lantz, Stephan Barth, Carlo L. Bottasso, Ola Carlson, Andrew Clifton, Johney Green, Peter Green, Hannele Holttinen, Daniel Laird, Ville Lehtomäki, Julie K. Lundquist, James Manwell, Melinda Marquis, Charles Meneveau, Patrick Moriarty, Xabier Munduate, Michael Muskulus, Jonathan Naughton, Lucy Pao, Joshua Paquette, Joachim Peinke, Amy Robertson, Javier Sanz Rodrigo, Anna Maria Sempreviva, J. Charles Smith, Aidan Tuohy, and Ryan Wiser. "Grand challenges in the science of wind energy". In: *Science* 366.6464 (2019), eaau2027. DOI: 10.1126/science.aau2027.

[206] L. J. Vermeer, J. N. Sørensen, and A. Crespo. "Wind turbine wake aerodynamics". In: *Progress in Aerospace Sciences* 39.6 (2003), pp. 467–510. DOI: 10.1016/S0376-0421(03)00078-2.

[207] Thierry Villeneuve, Matthieu Boudreau, and Guy Dumas. "Improving the efficiency and the wake recovery rate of vertical-axis turbines using detached end-plates". In: *Renewable Energy* 150 (2020), pp. 31–45. DOI: 10.1016/j.renene.2019.12.088.

[208] Miguel R. Visbal and Daniel J. Garmann. "Effect of Sweep on Dynamic Stall of a Pitching Finite-Aspect-Ratio Wing". In: *AIAA Journal* 57.8 (2019), pp. 3274–3289. DOI: 10.2514/1.J058206.

[209] Elizabeth N. Wayman. "Coupled dynamics and economic analysis of floating wind turbine systems". Accepted: 2007-01-10T16:56:13Z. Thesis. Massachusetts Institute of Technology, 2006.

[210] Nathaniel J. Wei, Ian D. Brownstein, Jennifer L. Cardona, Michael F. Howland, and John O. Dabiri. "Near-wake structure of full-scale vertical-axis wind turbines". In: *Journal of Fluid Mechanics* 914 (2021), A17. DOI: 10.1017/jfm.2020.578.

[211] Nathaniel J. Wei and John O. Dabiri. "Phase-averaged dynamics of a periodically surging wind turbine". In: *Journal of Renewable and Sustainable Energy* 14.1 (2022). Publisher: American Institute of Physics, p. 013305. DOI: 10.1063/5.0076029.

[212] Nathaniel J. Wei and John O. Dabiri. "Power-generation enhancements and upstream flow properties of turbines in unsteady inflow conditions". In: *Journal of Fluid Mechanics* (2023). In press. DOI: 10.48550/ARXIV.2210.14466.

[213] Nathaniel J. Wei, Johannes Kissing, Tom T. B. Wester, Sebastian Wegt, Klaus Schiffmann, Suad Jakirlic, Michael Hölling, Joachim Peinke, and Cameron Tropea. "Insights into the periodic gust response of airfoils". In: *Journal of Fluid Mechanics* 876 (2019), pp. 237–263. DOI: 10.1017/jfm.2019.537.

[214] Nathaniel J. Wei and Omkar B. Shende. *On the Lift of an Oscillating Airfoil Encountering Periodic Gust Disturbances*. Publisher: arXiv Version Number: 2. 2023. DOI: 10.48550/ARXIV.2212.14517.

[215] Binrong Wen, Xingjian Dong, Xinliang Tian, Zhike Peng, Wenming Zhang, and Kexiang Wei. "The power performance of an offshore floating wind turbine in platform pitching motion". In: *Energy* 154 (2018), pp. 508–521. DOI: 10.1016/j.energy.2018.04.140.

[216] Binrong Wen, Xinliang Tian, Xingjian Dong, Zhike Peng, and Wenming Zhang. "Influences of surge motion on the power and thrust characteristics of an offshore floating wind turbine". In: *Energy* 141 (2017), pp. 2054–2068. DOI: 10.1016/j.energy.2017.11.090.

[217] Binrong Wen, Xinliang Tian, Xingjian Dong, Zhike Peng, and Wenming Zhang. "On the power coefficient overshoot of an offshore floating wind turbine in surge oscillations". In: *Wind Energy* 21.11 (2018), pp. 1076–1091. DOI: 10.1002/we.2215.

[218] Tamino Wetz and Norman Wildmann. *Multi-Point In-Situ Measurements of Turbulent Flow in a Wind Turbine Wake and Inflow with a Fleet of UAS*. preprint. Fluid mechanics/Wakes and wind farm aerodynamics, 2023. DOI: 10.5194/wes-2023-6.

[219] R E Wilson and P B.S. Lissaman. "Applied aerodynamics of wind power machines". In: (1974).

[220] J. G. Wong, B. P. laBastide, and D. E. Rival. "Flow separation on flapping and rotating profiles with spanwise gradients". In: *Bioinspiration & Biomimetics* 12.2 (2017), p. 026008. DOI: 10.1088/1748-3190/aa594b.

[221] John C. Wyngaard. "Toward Numerical Modeling in the "Terra Incognita"". In: *Journal of the Atmospheric Sciences* 61.14 (2004). Place: Boston MA, USA Publisher: American Meteorological Society, pp. 1816–1826. DOI: https://doi.org/10.1175/1520-0469(2004)061<1816:TNMITT>2.0.CO;2.

[222] Haitao Xu. "Tracking Lagrangian trajectories in position–velocity space". In: *Measurement Science and Technology* 19.075105 (2008).

[223] Haitao Xu and Eberhard Bodenschatz. "Motion of inertial particles with size larger than Kolmogorov scale in turbulent flows". In: *Physica D: Nonlinear Phenomena*. Euler Equations: 250 Years On 237.14 (2008), pp. 2095–2100. DOI: 10.1016/j.physd.2008.04.022.

[224] Xiaolei Yang, Jiarong Hong, Matthew Barone, and Fotis Sotiropoulos. "Coherent dynamics in the rotor tip shear layer of utility-scale wind turbines". In: *Journal of Fluid Mechanics* 804 (2016). Publisher: Cambridge University Press, pp. 90–115. DOI: 10.1017/jfm.2016.503.

[225] John Young, Joseph C.S. Lai, and Max F. Platzer. "A review of progress and challenges in flapping foil power generation". In: *Progress in Aerospace Sciences* 67 (2014), pp. 2–28. DOI: 10.1016/j.paerosci.2013.11.001.

[226] John Young, Fang-Bao Tian, Zhengliang Liu, Joseph C. S. Lai, Nima Nadim, and Anthony D. Lucey. "Analysis of unsteady flow effects on the Betz limit for flapping foil power generation". In: *Journal of Fluid Mechanics* 902 (2020). Publisher: Cambridge University Press. DOI: 10.1017/jfm.2020.612.

[227] Wei Yu, Carlos Simao Ferreira, and Gijs van Kuik. "Analytical actuator disc solution for unsteady load". In: *34th Wind Energy Symposium*. AIAA SciTech Forum 34. American Institute of Aeronautics and Astronautics, 2016. DOI: 10.2514/6.2016-0751.

[228] Wei Yu, Delphine Tavernier, Carlos Ferreira, Gijs A. M. van Kuik, and Gerard Schepers. "New dynamic-inflow engineering models based on linear and nonlinear actuator disc vortex models". In: *Wind Energy* 22.11 (2019), pp. 1433–1450. DOI: 10.1002/we.2380.

[229] Stefania Zanforlin and Takafumi Nishino. "Fluid dynamic mechanisms of enhanced power generation by closely spaced vertical axis wind turbines". In: *Renewable Energy* 99 (2016), pp. 1213–1226.

Appendix A

Supplementary Material for Chapter 2

A.1 Phase-averaged power profiles

The plots shown in this section compare the measured, phase-averaged power over a single period (blue) with the prediction of the first-order linear model (orange) and the steady reference power (green). The model prediction was computed using a fourth-order Runge-Kutta time-integration scheme with a time-step of 10^{-3} s. Ten periods were simulated to attenuate startup effects, and the last period was extracted to represent the model prediction. The model did not capture the time-averaged power for the unsteady cases, but good agreement was still observed in terms of amplitude, phase, and waveform shape.

A set of four cases, consisting of two nondimensional surge amplitudes ($A^* = 0.257$ and 0.514), three reduced frequencies ($k = 0.304$, 0.455, and 0.911), and three nondimensional surge velocities $u^* = 0.117$, 0.156, and 0.234) are shown for comparison across waveform shapes and loading conditions. This set of parameters is presented for various loading conditions and waveform types: sinusoidal waveforms with a load of 10 Ω (Figure A.1), sinusoidal waveforms with a load of 40 Ω (Figure A.2), trapezoidal waveforms with a load of 9.8 Ω and $\xi = 0.25$ (Figure A.3), and trapezoidal waveforms with a load of 40 Ω and $\xi = 1$ (Figure A.4). Additionally, to highlight the accuracy of the model in predicting time-resolved dynamics, two trapezoidal cases with $\xi = 0.01$, $A^* = 0.257$, $k = 0.076$, and $u^* = 0.039$ and loads of 10 and 40 Ω are shown in Figure A.5. These cases are not hand-picked for agreement; they represent the general fidelity of the model with respect to the data in all of the cases presented in this study, with the exception of the cases involving the two lowest tip-speed ratios.

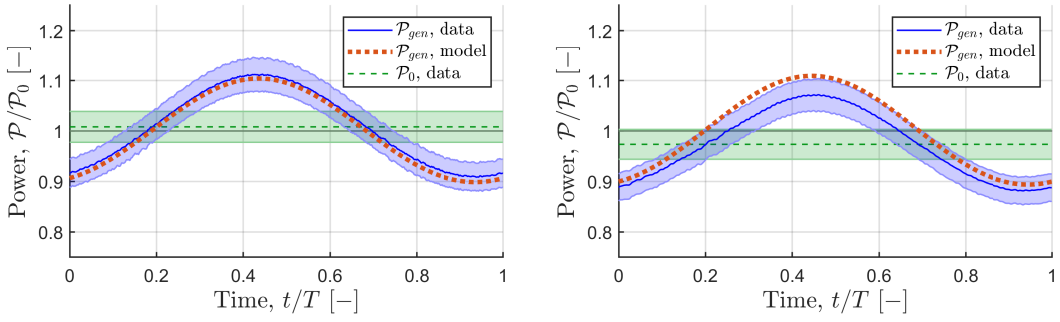

(a) $A^* = 0.257$, $k = 0.455$, $u^* = 0.117$

(b) $A^* = 0.257$, $k = 0.911$, $u^* = 0.234$

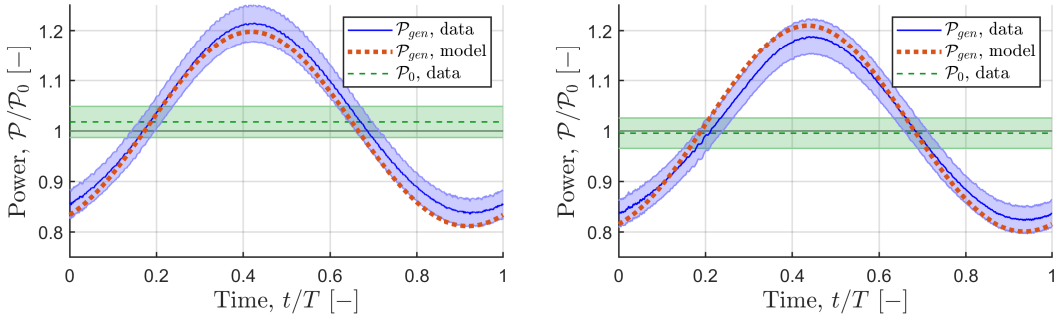

(c) $A^* = 0.514$, $k = 0.304$, $u^* = 0.156$

(d) $A^* = 0.514$, $k = 0.455$, $u^* = 0.234$

Figure A.1: Sinusoidal waveforms with a load of 10 Ω ($\lambda_0 = 6.21 \pm 0.25$), for four representative cases: (a) $A = 0.3$ m and $T = 2$ s, (b) $A = 0.3$ m and $T = 1$ s, (c) $A = 0.6$ m and $T = 3$ s, and (d) $A = 0.6$ m and $T = 2$ s.

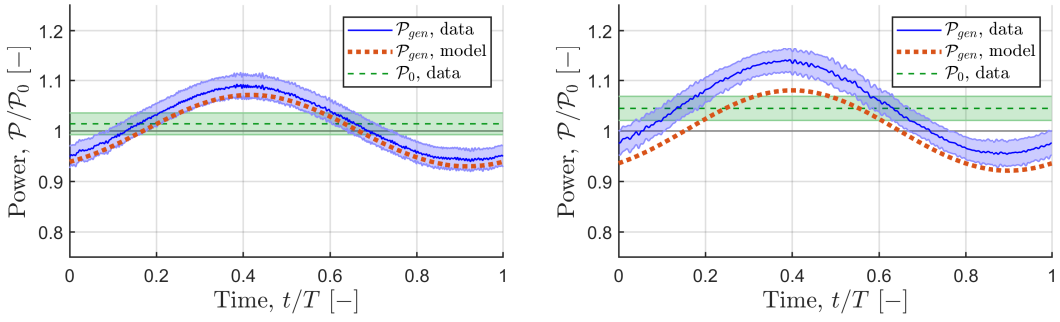

(a) $A^* = 0.257$, $k = 0.455$, $u^* = 0.117$

(b) $A^* = 0.257$, $k = 0.911$, $u^* = 0.234$

(c) $A^* = 0.514$, $k = 0.304$, $u^* = 0.156$

(d) $A^* = 0.514$, $k = 0.455$, $u^* = 0.234$

Figure A.2: Sinusoidal waveforms with a load of 40 Ω ($\lambda_0 = 8.64 \pm 0.35$), for four representative cases: (a) $A = 0.3$ m and $T = 2$ s, (b) $A = 0.3$ m and $T = 1$ s, (c) $A = 0.6$ m and $T = 3$ s, and (d) $A = 0.6$ m and $T = 2$ s.

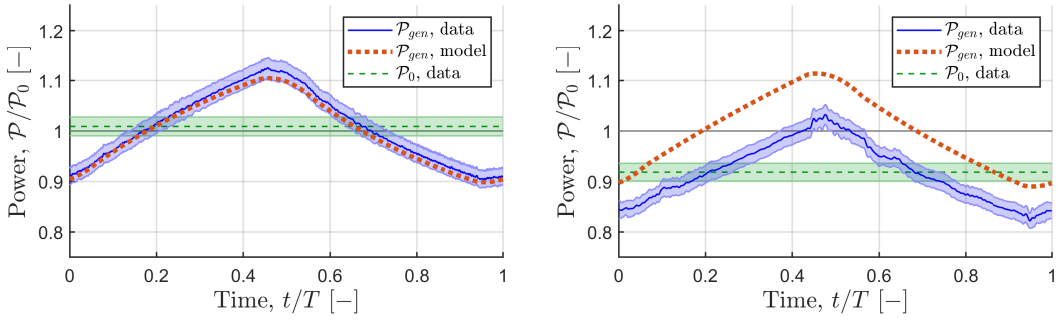

(a) $A^* = 0.257$, $k = 0.455$, $u^* = 0.117$

(b) $A^* = 0.257$, $k = 0.911$, $u^* = 0.234$

(c) $A^* = 0.514$, $k = 0.304$, $u^* = 0.156$

(d) $A^* = 0.514$, $k = 0.455$, $u^* = 0.234$

Figure A.3: Trapezoidal waveforms with $\xi = 0.25$ and a load of 9.8 Ω ($\lambda_0 = 6.11 \pm 0.25$), for four representative cases: (a) $A = 0.3$ m and $T = 2$ s, (b) $A = 0.3$ m and $T = 1$ s, (c) $A = 0.6$ m and $T = 3$ s, and (d) $A = 0.6$ m and $T = 2$ s.

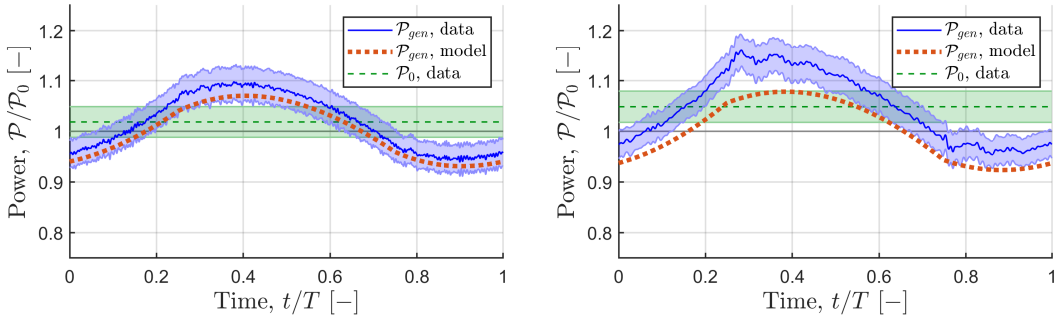

(a) $A^* = 0.257$, $k = 0.455$, $u^* = 0.117$

(b) $A^* = 0.257$, $k = 0.911$, $u^* = 0.234$

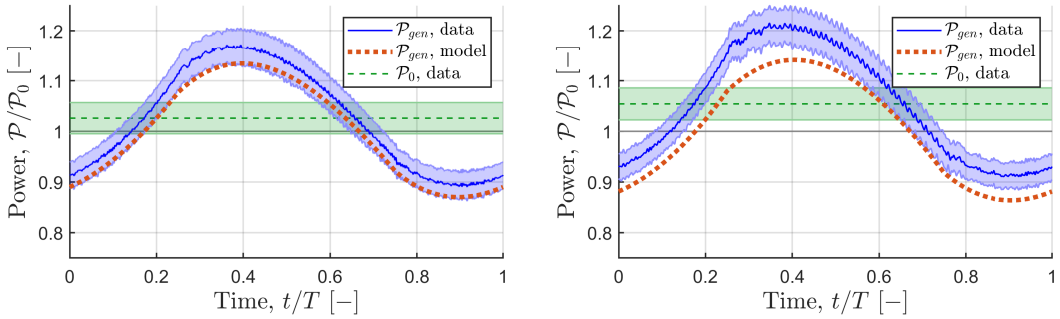

(c) $A^* = 0.514$, $k = 0.304$, $u^* = 0.156$

(d) $A^* = 0.514$, $k = 0.455$, $u^* = 0.234$

Figure A.4: Trapezoidal waveforms with $\xi = 1$ and a load of 40 Ω ($\lambda_0 = 8.77 \pm 0.35$), for four representative cases: (a) $A = 0.3$ m and $T = 2$ s, (b) $A = 0.3$ m and $T = 1$ s, (c) $A = 0.6$ m and $T = 3$ s, and (d) $A = 0.6$ m and $T = 2$ s.

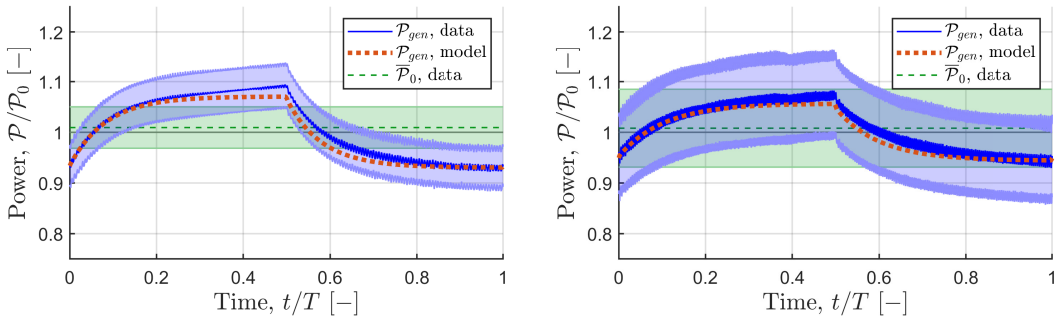

(a) Load: 10 Ω ($\lambda_0 = 6.27 \pm 0.26$)

(b) Load: 40 Ω ($\lambda_0 = 8.77 \pm 0.35$)

Figure A.5: Long-period trapezoidal waveforms with $\xi = 0.01$, $A^* = 0.257$, $k = 0.076$, and $u^* = 0.039$, for resistive loads of (a) 10 Ω ($\lambda_0 = 6.27 \pm 0.26$) and (b) 40 Ω ($\lambda_0 = 8.77 \pm 0.35$).

Appendix B

Supplementary Material for Chapter 3

B.1 Vortex-cylinder theory results

Since Figures 3.10, 3.11, and 3.12 in Section 3.4.2 omitted the predictions of VCT, these results are included in this appendix. The data in Figures B.1, B.2, and B.3 are identical to the aforementioned figures, but VCT model predictions are shown instead of PDT predictions. Similar trends are observed, though slight quantitative differences exist between the two sets of model predictions. Overall, both models appear to capture the trends observed in the data reasonably well.

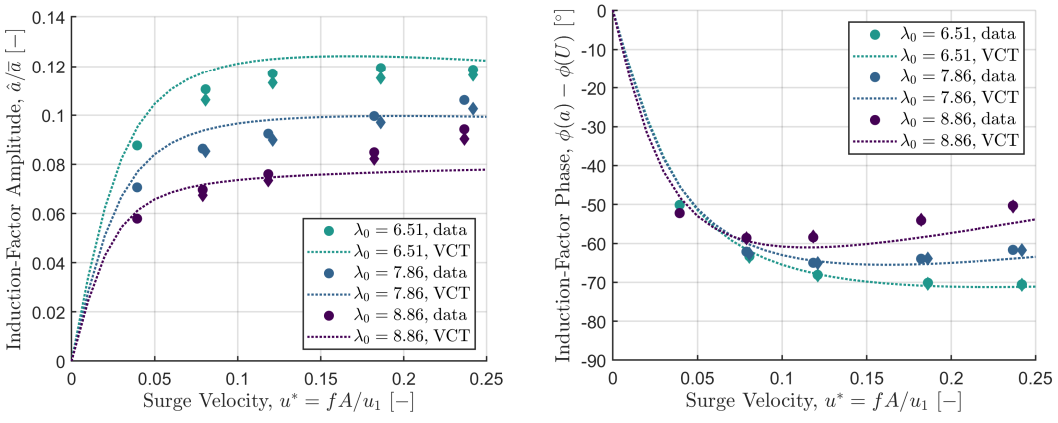

(a) (b)

Figure B.1: (a) Amplitude and (b) phase of the estimated induction factors using the VCT model, plotted against surge-velocity amplitude. Model predictions are given as dotted lines.

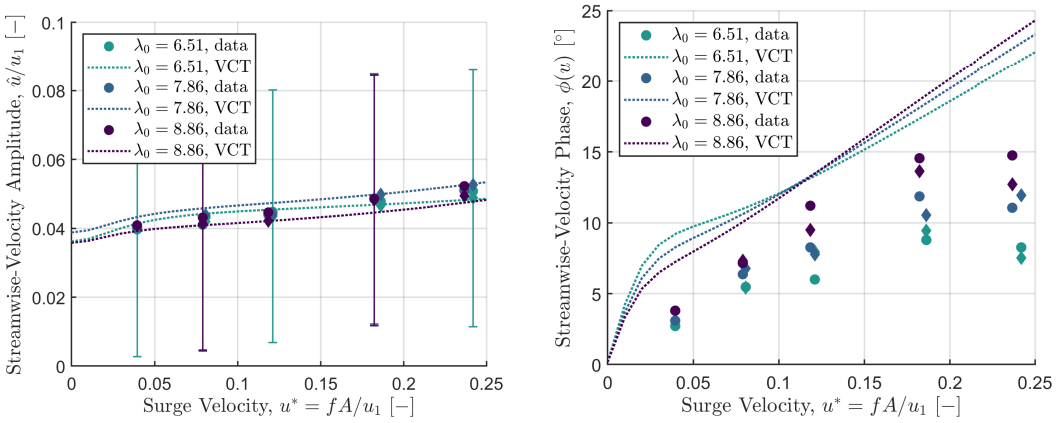

(a) (b)

Figure B.2: (a) Amplitude and (b) phase of the measured flow velocity at $x = x_u$, plotted against surge-velocity amplitude. VCT model predictions are given as dotted lines. Error bars are plotted on every fourth point.

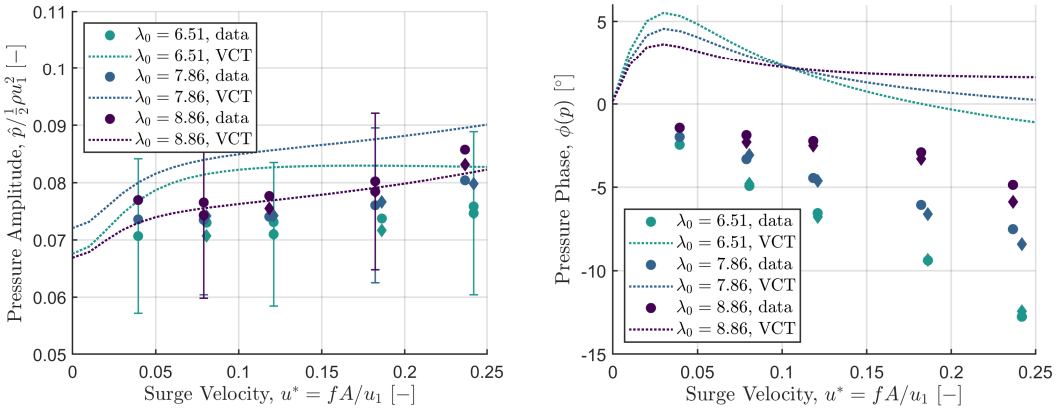

(a) (b)

Figure B.3: (a) Amplitude and (b) phase of the measured relative pressure at $x = x_u$, plotted against surge-velocity amplitude. VCT model predictions are given as dotted lines. Error bars are plotted on every fourth point.

B.2 Additional derivations from the unsteady theoretical analysis

B.2.1 Porous-disc derivations

The kinetic energy associated with the motion of a solid disc is given by

$$KE_{disc} = -\frac{1}{2}\rho \iint_A \phi \hat{n} \cdot \nabla\phi dA, \tag{B.1}$$

where the flux integral is taken on an infinitesimally thin control surface surrounding the disc. Across this surface, $\nabla\phi = U\hat{i}$. The kinetic energy of the disc can thus be written as

$$\begin{aligned} KE_{disc} &= -\frac{1}{2}\rho U \iint_A \phi \left(\hat{n} \cdot \hat{i}\right) dA \\ &= -\frac{1}{2}\rho U \left[-\int_0^R 4U\sqrt{R^2 - r^2} r dr - \int_0^R 4U\sqrt{R^2 - r^2} r dr \right] \\ &= 4\rho U^2 \int_0^R r\sqrt{R^2 - r^2} dr \\ &= \frac{4}{3}\rho U^2 R^3. \end{aligned} \tag{B.2}$$

The odd extension to the upstream velocity potential given in Equation 3.28 is

$$\phi(r, x) = -a(u_1 - U)\sqrt{\frac{2}{\pi}} R^{3/2} \int_0^\infty s^{-1/2} J_{3/2}(Rs) J_0(rs) e^{-s(x - x_2)} ds;\ x > x_2. \tag{B.3}$$

We may differentiate the expression for ϕ at streamwise location 3 in time, noting that x_3 represents a fixed spatial coordinate with zero time derivative, while x_2 represents the instantaneous position of the actuator disc such that $\frac{dx_2}{dt} = U$:

$$
\begin{aligned}
\frac{\partial \phi_3}{\partial t} &= a\frac{dU}{dt}\left[R\left(\frac{2R}{\pi}\right)^{1/2}\int_0^\infty s^{-1/2}e^{-s(x_3-x_2)}J_0(rs)J_{3/2}(Rs)ds\right] \\
&\quad + aU\frac{\partial}{\partial t}\left[R\left(\frac{2R}{\pi}\right)^{1/2}\int_0^\infty s^{-1/2}e^{-s(x_3-x_2)}J_0(rs)J_{3/2}(Rs)ds\right] \\
&= a\frac{2}{\pi}\sqrt{R^2-r^2}\frac{dU}{dt} + aUR\left(\frac{2R}{\pi}\right)^{1/2}\int_0^\infty s^{-1/2}\frac{d}{dt}\left[e^{-s(x_3-x_2)}\right]J_0(rs)J_{3/2}(Rs)ds \\
&= a\frac{2}{\pi}\sqrt{R^2-r^2}\frac{dU}{dt} + aUR\left(\frac{2R}{\pi}\right)^{1/2}\int_0^\infty s^{-1/2}\left[s\frac{dx_2}{dt}e^{-s(x_3-x_2)}\right]J_0(rs)J_{3/2}(Rs)ds \\
&= a\frac{2}{\pi}\sqrt{R^2-r^2}\frac{dU}{dt} + aUR\left(\frac{2R}{\pi}\right)^{1/2}\int_0^\infty s^{1/2}Ue^{-s(x_3-x_2)}J_0(rs)J_{3/2}(Rs)ds \\
&= a\frac{2}{\pi}\sqrt{R^2-r^2}\frac{dU}{dt} + aU^2.
\end{aligned}
\tag{B.4}
$$

The following integrals are used in this derivation:

$$
\int_0^\infty s^{-1/2}J_0(rs)J_{3/2}(Rs)ds = \sqrt{\frac{2}{\pi}}\sqrt{R^2-r^2}R^{-3/2},\ 0 \le r \le R \tag{B.5}
$$

and

$$
\int_0^\infty s^{1/2}J_0(rs)J_{3/2}(Rs)ds = \sqrt{\frac{\pi}{2}}R^{-3/2},\ 0 \le r \le R. \tag{B.6}
$$

By a similar process, we obtain

$$
\frac{\partial \phi_2}{\partial t} = -a\frac{2}{\pi}\sqrt{R^2-r^2}\frac{dU}{dt} + aU^2. \tag{B.7}
$$

Combining these two unsteady potentials, we arrive at the relation

$$
\Phi_t = -\frac{4}{\pi}a\sqrt{R^2-r^2}\frac{dU}{dt}, \tag{B.8}
$$

which may be averaged across the face of the actuator disc to obtain

$$
\langle \Phi_t \rangle = \frac{2\pi}{A_2}\int_0^R\left[-\frac{4}{\pi}a\sqrt{R^2-r^2}\frac{dU}{dt}\right]rdr = -\frac{8R}{3\pi}a\frac{dU}{dt} \equiv \Phi_t. \tag{B.9}
$$

B.2.2 Rotating actuator bodies

We consider the case of a purely rotating actuator body, for which $\mathbf{U} = 0$ and $\mathbf{\Omega} \neq 0$. Equation 3.39 becomes

$$
\phi(\mathbf{x}) = \mathbf{\Omega} \cdot \mathbf{\Theta}, \tag{B.10}
$$

where $\mathbf{\Omega}$ is an axial vector. The kinetic energy of the rotating body scales as $|\mathbf{\Omega}|^2$, so that in the quasi-1D formulation, we find

$$\frac{d}{dt}(KE) \sim \Omega \frac{d\Omega}{dt}, \tag{B.11}$$

ignoring geometric constants. This is analogous to the case of a purely translating body, for which the time derivative of the kinetic energy scales as $U\frac{dU}{dt}$.

Taking the time derivative of Equation B.10 yields

$$\frac{\partial \phi}{\partial t} = \frac{\partial \mathbf{\Omega}}{\partial t} \cdot \mathbf{\Theta} + \mathbf{\Omega} \cdot \frac{\partial \mathbf{\Theta}}{\partial t} = \frac{\partial \mathbf{\Omega}}{\partial t} \cdot \mathbf{\Theta} + \mathbf{\Omega} \cdot \left(\frac{\partial (\mathbf{x} - \mathbf{x_0})}{\partial t} \cdot \nabla \mathbf{\Theta} \right). \tag{B.12}$$

Noting that $\frac{\partial (\mathbf{x}-\mathbf{x_0})}{\partial t} = -\mathbf{U} = 0$, the second term vanishes. For the quasi-1D case, we write the vector-valued functions $\mathbf{\Omega}$ and $\mathbf{\Theta}$ as scalar-valued functions and obtain the result

$$\frac{\partial \phi}{\partial t} = \Theta \frac{d\Omega}{dt}. \tag{B.13}$$

Comparing Equations B.11 and B.13 with the previously obtained results for a purely translating body with a locally symmetric flow field, we see that there is no symmetry-breaking term for a purely rotating body that will yield time-averaged efficiencies in excess of the Betz limit. This aligns with intuition, as changes in the rotation rate of an actuator body should affect the flow on either side of the body symmetrically, which, as we have seen, will not lead to net improvements in efficiency. It is possible that, in a real wind turbine, changes in the rotation rate would lead to unsteadiness at the turbine-blade level, potentially due to dynamic stall or other kinds of vortex-shedding events. These effects, however, would manifest themselves as streamwise unsteadiness (e.g. changes in induced velocities) rather than rotational unsteadiness. Thus, streamwise unsteadiness remains the primary parameter of interest for these investigations.

Appendix C

Supplementary Material for Chapter 4

C.1 Dynamics of artificial snow particles

Since the choice of flow seeding particles is critical to the accuracy of PTV measurements, the generation and characterization of the artificial snow particles used in these experiments were carefully considered. Natural snowfall had been used successfully by Hong *et al.* (2014) as seeding particles for 2D particle-image velocimetry in the wake of a full-scale HAWT. In the present experiments, artificial snow was used due to the lack of natural snowfall at the FLOWE site. The artificial snow used in these experiments was composed of an air-filled soap foam (ProFlake Falling Snow Fluid, Snow Business), which formed irregularly shaped particles with a range of sizes. The particles that were visible in the images from the field site had diameters of $d_p = 11.2 \pm 4.2$ mm and an average density of $\rho = 6.57 \pm 0.32$ kgm^{-3}. Smaller particles would have been more ideal as 'tracer' particles, but these were difficult to visually identify and isolate in the recorded videos and were thus unfeasible for these experiments. The settling velocity of these particles in quiescent air was measured to be $W_s = 0.60 \pm 0.18$ ms^{-1}, which corresponds to a particle Reynolds number $Re_p = \frac{W_s d_p}{\nu}$ of 448. Since this Reynolds number is outside the Stokes-flow regime, the relative influence of inertial effects on the ability of the particles to follow the flow had to be ascertained. A considerable body of research documents the dynamics of various types of inertial particles in turbulence (e.g. Böhm, 1988; Aliseda *et al.*, 2002; Xu and Bodenschatz, 2008; Toschi and Bodenschatz, 2009; Bourgoin and Xu, 2014; Ireland *et al.*, 2016; Nemes *et al.*, 2017; Petersen *et al.*, 2019). Regardless, the foam-based composition and irregular shapes of the artificial snow particles meant that laboratory experiments were required to more accurately characterize their dynamics.

In this section, a series of laboratory experiments are detailed that allowed the flow response of the artificial snow particles to be quantified. This is followed by a qualitative analysis based on scaling arguments that confirms the findings of the laboratory experiments in the field data.

C.1.1 Laboratory experiments with a snow machine

Laboratory experiments in a wind tunnel were designed to determine the aerodynamic response characteristics of the artificial snow particles used in the field experiments. To measure the particle response to a step change in velocity, a snow machine was arranged to release particles normal to the flow in the wind tunnel, creating a jet in cross-flow. As this canonical flow has been studied extensively in experiments, simulations, and analytical investigations (cf. Fric and Roshko, 1994; Gopalan *et al.*, 2004; Su and Mungal, 2004; Mahesh, 2013; Karagozian, 2014), it served as a well-documented baseline against which the particle dynamics could be evaluated. The spanwise discrepancy between the profile of the jet in cross-flow and the particle trajectories could then be analyzed to establish a particle relaxation time and quantify the effects of particle inertia on flow fidelity. The dynamics of the large particles used in the field experiments were therefore compared with the behavior of smaller, more regularly shaped particles generated by increasing the blower flow rate and decreasing the fluid injection rate in the snow machine. The response of each particle type was studied at two distinct free-stream velocities. The impulse response and slip velocity of the particles were then calculated from the measured jet profiles.

Experiments to characterize the dynamics of particles produced by a single snow machine (Silent Storm DMX, Ultratec Special Effects) were conducted in an open-circuit wind tunnel with flow driven by a 4×4 grid of fans at the inlet of the tunnel. The test section was 4.88 m long in the streamwise direction (X), 2.06 m in width (Y), and 1.97 m in height (Z). The tunnel was operated with free-stream velocities of 5.64 ± 0.45 ms^{-1} and 6.58 ± 0.45 ms^{-1}, as measured with a hot-film anemometer. A full description of the wind-tunnel facility is given by Brownstein *et al.* (2019).

The snow machine was positioned on a platform 2.8 m downstream of the tunnel inlet, so that the output nozzle was perpendicular to the centerline of the tunnel (cf. Figure C.1). The end of the nozzle was offset at $Y = -0.2$ m in the spanwise direction from the center of the tunnel. The blockage from this configuration was less than 5%. Four hardware-synchronized cameras (N-5A100, Adimec) were positioned around the tunnel, with one located directly above the measurement volume. These cameras captured a measurement volume of approximately 1.2 m $\times$ 0.5 m $\times$ 0.5 m in the X, Y, and Z directions, respectively. The cameras recorded images at a resolution of 2048×1008 pixels and a frequency of 250 frames per second, with an exposure of 600 μs.

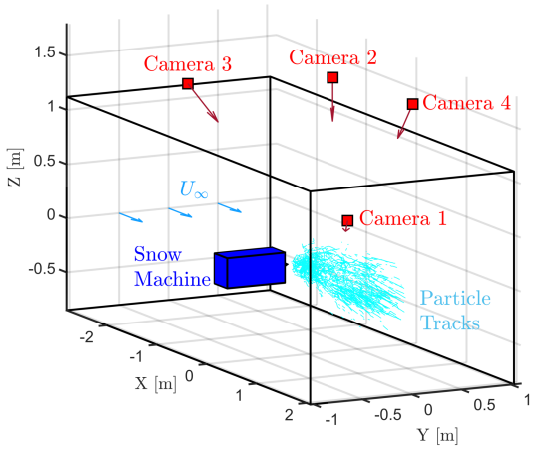

Figure C.1: Schematic of the experimental setup for snow-machine experiments. Flow is in the positive X direction, and the snow machine (blue) emits particles in the positive Y direction. Sample particle tracks (light blue) illustrate the extent of the measurement volume. The four cameras are shown in red, and arrows denote their viewing angles.

Three-dimensional PTV was used to quantify the movements of the snow particles. A wand-based calibration procedure, identical to that used in the field experiments (given in appendix C.2.1), was used to reconstruct particle tracks in three dimensions. A wand composed of a pair of LEDs spaced 10 cm apart was moved throughout the measurement volume, and the calibration utility of Theriault *et al.* (2014) established the camera positions from image coordinates of the two lights in each camera view. The wand length was reconstructed with an error of 0.75%, suggesting that the calibration was sufficiently accurate. The global coordinate system was set using a plumb line at the center of the wind tunnel, so that the nozzle was located at $(X, Y, Z) = (0, -0.2, 0)$ m. Particles were identified, triangulated in physical space, and tracked using the procedure outlined in appendix C.2.2. Because of the high seeding density of the particles, only the largest 10% by area of the identified particles in the raw images were triangulated into physical coordinates. This was done to reduce triangulation ambiguities, and to isolate the large particles that would have been observable in the field experiments for analysis. A statistical analysis of the size distributions of the particles from the two output settings was achieved by binarizing images taken by the camera positioned directly above the measurement volume (Figure C.2), and converting the pixel areas of the identified particles to effective diameters in physical dimensions. The largest 10% of the particles by area had effective diameters of $d_p = 11.2 \pm 4.2$ mm in the large-snow case and $d_p = 5.9 \pm 1.1$ mm in the small-snow case. For each experiment, at least

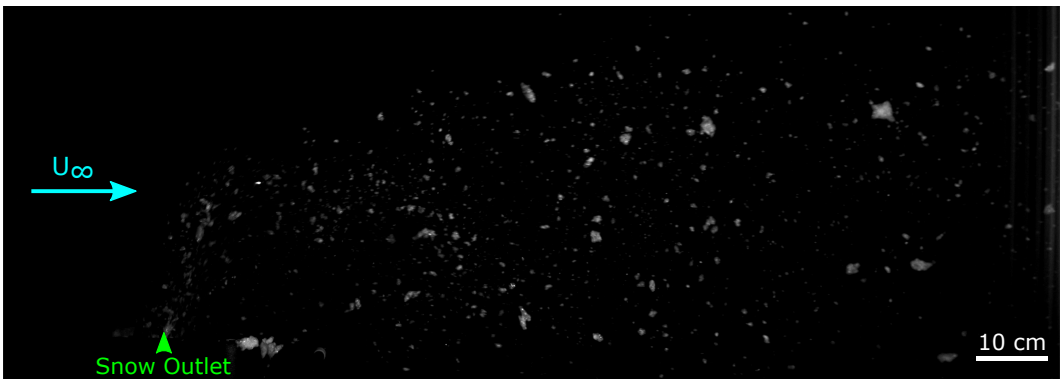

Figure C.2: Photograph of snow particles of the type used in the field experiments, viewed from above (Camera 2). Particles are generated at the nozzle at the lower left (green arrow) and are convected toward the right of the image.

120 seconds of data were recorded, corresponding to over 30,000 raw images per camera. The resulting velocity vectors were binned and time-averaged into 3-cm cubic voxels with at least 10 vectors per displayed voxel.

C.1.2 Experimental results

Particle time scales and response characteristics were computed from the data in the following manner. First, the jet in cross-flow was identified from velocity fields measured with the small snow particles. This was accomplished by applying a high-pass filter to streamwise slices of the spanwise velocity V to isolate the jet in cross-flow from the signal of the larger particle jet. A hill-climbing search algorithm was then applied within this region to find the local maximum of spanwise velocity corresponding to the center of the jet at each streamwise location. These maxima were projected into the XY plane to define the jet centerline (Figure C.3). To educe a jet profile from these data, it was assumed that the trajectory of the jet in cross-flow would follow the similarity solution given by Hasselbrink and Mungal (2001) for the region near the jet orifice

$$\frac{x}{rd} = \left(\frac{2}{c_{ej}} \frac{y}{rd} \right)^{1/2} . \tag{C.1}$$

The jet diameter d was estimated as 3 cm based on the diameter of the snow-machine particle generator, and the velocity ratio $r = \frac{V_{jet}}{U_\infty}$ was calculated based on the maximum velocity measured on the jet centerline. A single-parameter fit for the measured jet centerline was then applied to estimate the entrainment coefficient, c_{ej}. Between the two small-snow experiments (r = 0.29 and 0.36), the extracted

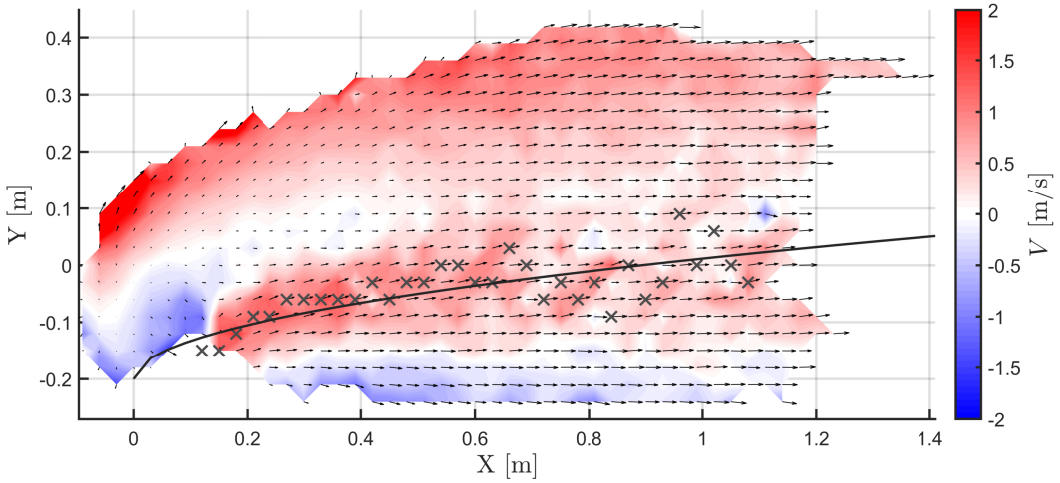

Figure C.3: Contours of spanwise velocity V at the plane $Z = 0$, for experiments with small snow particles at $U_\infty = 6.58 \pm 0.45$ ms^{-1}. Grey crosses represent the identified cross-flow jet centerline from the data, and the black curve shows the resulting fit according to the profile given by Hasselbrink and Mungal (2001). Negative velocities upstream of $X \lesssim 0.1$ m were likely spurious, as particles in this region were clumped together and thus hard to identify accurately.

entrainment coefficient was $c_{ej} = 0.39 \pm 0.01$. This was slightly larger than the value of $c_{ej} = 0.32$ given by Ricou and Spalding (1961) for a free jet in controlled conditions, likely due to the higher turbulence intensities in this experiment. The jet in cross-flow in the large-snow experiments was harder to identify in the velocity fields because of its lower velocity ratio (a consequence of the lower snow-machine blower setting), which resulted in a lower signal-to-noise ratio. The presence of instabilities in the jet at low velocity ratios likely further obscured the jet profile in the time-averaged velocity fields (Ilak *et al.*, 2012; Klotz *et al.*, 2019). Thus, for the sake of consistency across experiments, the measured value for c_{ej} from the small-snow experiments was used to infer the trajectory of the jet in cross-flow in the large-snow experiments.

The particle jet was identified using images taken from above the measurement domain (Figure C.4). The particles detected in each frame were binned into 3-cm square areas and were plotted as a 2D distribution of particles, averaged over all images in the experiment. The center of the jet was identified at each streamwise location to subpixel accuracy using a three-point parabolic fit. The results were then fitted with a two-parameter power-law fit of the form $y(x) = ax^n - 0.2$, where another parabolic fit was applied along the line $Y = -0.2$ m to fix the coordinate system with respect to the jet orifice.

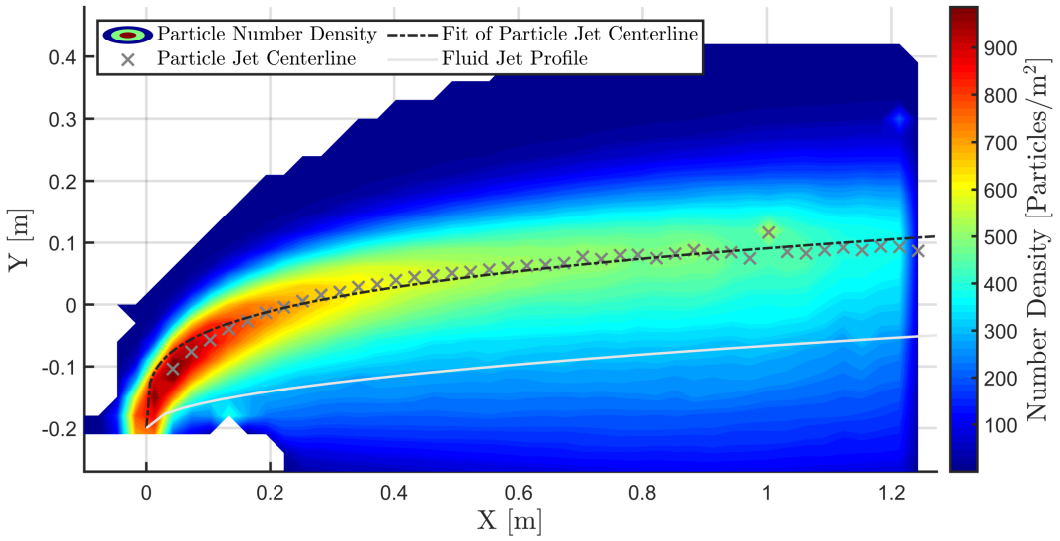

Figure C.4: Contours of 2D particle number density at the plane $Z = 0$, for experiments with large snow particles at $U_\infty = 6.58 \pm 0.45$ ms^{-1}. Grey crosses represent the identified particle-jet centerline from the data, and the black curve shows the resulting power-law fit, $y(x) = 0.291x^{0.268} - 0.2$. The profile of the jet in cross-flow ($c_{ej} = 0.39$, $r = 0.116$) is given in light grey.

Given trajectories $y(x)$ for the cross-flow and particle jets and information about the convective velocities along the trajectories, time-dependent profiles $x(t)$ and $y(t)$ could be inferred for the two jets. For the jet in cross-flow, it was assumed that ideal tracer particles would follow the velocity profile derived from the aforementioned similarity solution of Hasselbrink and Mungal (2001) as

$$U(x) = U_\infty \left(1 - \frac{c_{vj}}{c_{ej}} \frac{d}{x}\right), \tag{C.2}$$

where the profile coefficient c_{vj} was taken to be unity. A time history could then be extracted by integrating across point values of $\Delta t = \Delta x / U(x)$. For the particle jet, the streamwise velocity averaged across Y and Z at each streamwise location X was taken to represent the average convective velocity of the particles at that location. This velocity followed a nonlinear relaxation in X that was used to extract an average particle time history. The streamwise coordinates of the cross-flow and particle jets, $x_{cf}(t)$ and $x_p(t)$, were computed for a common series of time steps by interpolation. Then, the spanwise coordinates $y_{cf}(t)$ and $y_p(t)$ were computed from $x(t)$ using the corresponding fit function for each jet profile.

From the matched time histories of $y_{cf}(t)$ and $y_p(t)$, a spanwise error was defined as $\delta(t) = y_p(t) - y_{cf}(t)$. This difference represents the deviation of an inertial particle

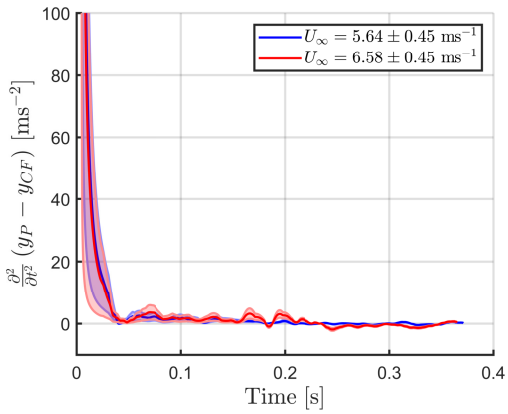

Figure C.5: Impulse response in acceleration for the artificial snow particles used in the field experiments, at two free-stream velocities. Oscillations are artifacts of numerical errors from interpolation.

from the background flow. Differentiating once with respect to time yielded the spanwise slip velocity of a particle subjected to a step change in V. Differentiating again in time gave the particle's impulse response in acceleration (Figure C.5). The reliance on numerical differentiation required smooth signals to obtain meaningful results; it is for this reason that fit functions were used instead of measured data to obtain $y(t)$. In addition, a modest smoothing was required on $x(t)$ to prevent interpolation errors from accumulating through numerical differentiation. Error bars were computed from the residuals of the fits for $y_p(x)$ and $y_{cf}(x)$. The steady-state value of the profiles was computed as the mean of the latter half of the time history of the signal. The particle-response time scale τ_p was defined as the time at which the profiles of $\frac{\partial^2 \delta}{\partial t^2}$ decayed to within one standard deviation of the converged value. The steady-state values of $\frac{\partial \delta}{\partial t}$ provided an estimation of the slip velocity V_s of the particles. Computed particle time scales and slip velocities are given for the four experimental cases in Table C.1.

C.1.3 Implications for field experiments

The small snow particles had slightly shorter timescales and smaller slip velocities than the large snow particles. For both types of particles, the particle-response timescales showed little dependence on the free-stream velocity, while the slip velocities increased modestly with U_∞, most noticeably for the large snow particles. This was a consequence of the functional difference between the impulse response in acceleration, which does not depend on the magnitude of the disturbance, and the step response in velocity, which does. The particle-response timescales for the large snow

Experimental Case	Small Snow 1	Small Snow 2	Large Snow 1	Large Snow 2
Particle Diameter, d_p (mm)	5.9 ± 1.1	5.9 ± 1.1	11.2 ± 4.2	11.2 ± 4.2
Tunnel Speed, U_∞ (ms^{-1})	5.64 ± 0.45	6.58 ± 0.45	5.64 ± 0.45	6.58 ± 0.45
Particle Time Scale, τ_p (ms)	35.5 ± 1.2	34.4 ± 2.0	39.2 ± 0.3	40.5 ± 6.7
Slip Velocity, V_s (ms^{-1})	0.019±0.013	0.025±0.017	0.088±0.004	0.101±0.030

Table C.1: Particle diameters, timescales, and estimated slip velocities for the four cases in this experiment. Uncertainties represent one standard deviation from the mean quantities.

particles were therefore representative of those expected in the field experiments. The relevant flow timescale in the field experiments was $\tau_f = D/U_\infty \approx 0.18$, resulting in a particle Stokes number of $Sk \approx 0.23$. Since $\tau_p < \tau_f$, it could be assumed that the large snow particles used in the field experiments would respond rapidly enough to resolve the flow structures of interest to this study.

Since the slip velocities showed a tendency to increase with the free-stream velocity, the particle slip velocities in the field experiments were expected to be somewhat larger than those measured in the laboratory experiments. Assuming the particle slip velocity is directly proportional to U_∞, a linear extrapolation to the average wind speed at the field site ($U_\infty = 11$ ms^{-1}) yields a worst-case particle slip velocity of $V_{s,max} = 0.170$ ms^{-1}. The acceleration-impulse condition produced in the wind-tunnel cross-flow configuration was somewhat dramatic compared to conditions encountered by the particles in the field experiments, in which the jet was aligned with the free-stream flow. Therefore, this slip velocity should be treated as an upper bound on the flow fidelity of the particles. Errors due to particle slip in the field experiments were thus estimated to be below 2% of the free-stream velocity, which was similar to the precision of the 3D-PTV measurement system (cf. appendix C.2.2).

Lastly, the effect of the snow machines on the flow incident on the wind turbine in the field experiment can be ascertained from the results of the laboratory experiments. The maximum velocity of the flow exiting the snow machine for the large-snow case was 0.993 ± 0.165 ms^{-1}. Since the snow machines expelled their particles in

the streamwise direction in the field experiments, this injection of momentum was minimal compared to the average wind speed. In addition, the particle-response time scales measured in the laboratory suggest that the particles would have equilibrated to the background flow well in advance of their approach to the turbine (on the order of 1 m from the snow-machine nozzle). Given the turbulent nature of the wind conditions at the field site, the presence of the snow machines was not expected to disrupt the inflow condition to the turbine. These considerations suggested that the effect of the snow machines on the quality and measurement of the flow conditions was negligible.

C.2 Processing procedures

C.2.1 Camera calibration

Calibrations were performed before each turbine was raised into position to facilitate wand motion throughout the measurement volume. One calibration was used for all measurements with the UGE turbine, and a second calibration was used for all measurements with the WPE turbine. A wand, consisting of two 2,000-lumen LEDs (XLamp XM-L, Cree Components) spaced 1.15 m apart, was moved throughout the measurement volume using a reach forklift. A light located in the middle of the wand was flashed to provide a synchronization signal for the cameras. Using the MATLAB tool developed by Theriault *et al.* (2014), the LED positions and wand lengths were reconstructed in an arbitrarily assigned global coordinate system. The standard deviations of the reconstructed wand lengths from the two calibrations, over all recorded images of the wand as it moved through the measurement domain, were 0.16% and 0.20% of the measured wand length. The accuracy of the calibrations was further examined by comparing the calculated and measured distances between cameras, to quantify reprojection errors. The average reprojection errors across all inter-camera distances were $0.74 \pm 0.39\%$ and $0.83 \pm 0.41\%$ for the two calibrations. These corresponded to less than 10 cm in physical space, which was within the error tolerances of the tape-based physical measurements themselves. Lastly, the two calibrations were compared by applying both calibrations to the videos of the first calibration. After matching the two coordinate systems using principal-component analysis, the average distance between corresponding LED positions in the two calibrations was 1.34 cm. This corresponded to a difference on the order of 1 pixel in the camera images, suggesting that the difference between the two calibrations was negligible. Still, for the sake of consistency, the first calibration was used for

all of the experiments with the UGE turbine, while the second calibration was used for all experiments with the WPE turbine. As a final check on the validity of the calibrations, images in which the turbines were present in the camera views were used to reconstruct the spans of the turbines. Several points along the top and bottom of each turbine were selected in several camera views, and an elliptical fit of these points identified points lying on the central axis of the turbine. Triangulating the positions of these points in 3D space (using the methods outlined later in Section 4.2.4) yielded turbine spans that differed by 0.21% and 0.32%, respectively, from the actual values. Overall, these analyses demonstrated that both calibrations were accurate and consistent in their 3D reconstruction of objects in the measurement domain.

C.2.2 3D-PTV processing and statistical convergence

To obtain accurate time-averaged velocity fields from the raw camera images, a series of processing steps were undertaken. First, for every individual data set, the images from each camera were averaged to produce a background image, which was then subtracted from each image to remove glare and stationary structures. Then, the turbine and support structures visible in each frame were masked using an intensity threshold and object-detection routine. Through this combination of background subtraction and masking, the artificial snow particles in each image were isolated. The results of these steps were checked manually for each data set to confirm that the correct regions of the flow field were isolated.

To compute the temporal offset between images from different cameras, the signal of the synchronization light on the turbine tower was tracked in each image. The mean of the pixel intensities in a small region containing the synchronization light was computed for every frame in each set of camera images. A custom edge-finding routine was then used to locate the frames in each camera view in which the light was switched on. The six sets of images were temporally aligned according to these reference frames, and the subset of time instances that were represented in all six camera views was selected for the particle-identification step.

To identify particles in this set of images, intensity thresholds were chosen for every camera in each data set. These thresholds were used to binarize the images, and were set manually by iterating on a subset of the images in a data set, so that approximately 200 particle candidates would be identified in each image. This target number of particles was found to be sufficiently high to remain sensitive

to poorly illuminated particles, while low enough to prevent false positives from obfuscating actual particles. Pixel coordinates for each particle candidate were determined by computing its centroid, which was more robust to the non-spherical nature of the particles than other measures. These identified coordinates in 2D image space were then triangulated onto 3D global coordinates based on the calibrations outlined in Section 4.2.2, using epipolar geometry (Hartley and Zisserman, 2003). To reduce the number of ghost particles (non-physical artifacts from ambiguities in epipolar geometry) detected by this triangulation approach, it was required that a particle appear in at least three camera views in order for it to be triangulated into 3D space (Elsinga *et al.*, 2010). Particle trajectories and velocities were then numerically computed from these spatial coordinates for all time instances in the data set using a multi-frame predictive-tracking algorithm developed by Ouellette *et al.* (2006) and Xu (2008). The velocity fields for three data sets with different snow-machine heights were then combined into a single unstructured 3D volume of three-component velocity vectors. This volume was rotated into the coordinate system given in Figure 4.4 from the arbitrary one assigned by the calibrations using the axis of the turbine and the tips of the snow-machine towers as references. The result of this procedure was a collection of velocity vectors distributed throughout the measurement domain, representing instantaneous velocity measurements at various time instances during the experiment.

The unstructured velocity vectors were then interpolated onto a grid of cubic voxels to produce a single time-averaged velocity field. As the choice of the voxel size influenced both the resolution and statistical convergence of the measured velocity field, statistical analyses were carried out to inform this selection. First, the effect of the number of vectors per voxel on statistical convergence was ascertained. For this analysis, the first case of the helical-bladed UGE turbine was selected. Bootstrap sampling was employed to obtain better estimates of the statistics of the population (Efron, 1979). For a voxel with a side length of 25 cm located upstream of the turbine, 9,000 bootstrap samples of N vectors were taken, and the mean and standard deviation of the velocity magnitude were computed for each sample. This process was repeated for values of N from 1 to the total number of vectors in that voxel. The standard deviation of these bootstrapped means represented the uncertainty due to computing an average from samples of the entire population. This uncertainty decreased with increasing N, and dropped below 5% of the average velocity magnitude of all samples in the voxel, $|\mathbf{U}|$, at $N \approx 25$ (Figure C.6a). The uncertainty fell below 2% at $N \approx 150$. A similar conclusion regarding the value of

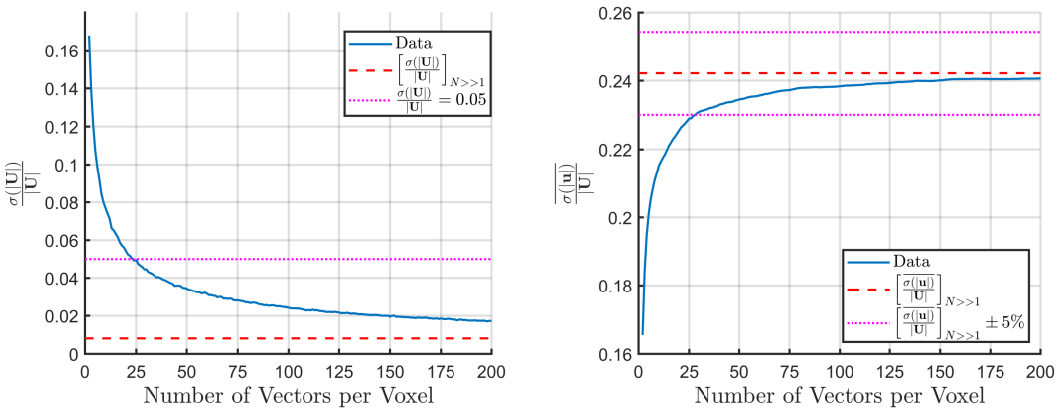

(a) (b)

Figure C.6: Statistical analysis of vectors contained in a 25-cm cubic voxel, located 1.5 D upstream of the UGE turbine. The variations of the (a) standard deviation of bootstrapped means and (b) mean of bootstrapped standard deviations of the velocity magnitude are shown against the number of vectors taken in each sample. In both figures, the converged value of each measure for $N >> 1$ is shown as a red dashed line, while bounds for acceptable convergence are given as dotted magenta lines. $N \gtrsim 25$ yields convergence within 5%, while $N \gtrsim 150$ yields convergence within 2%.

N was drawn from the average of the bootstrapped standard deviations for various values of N (Figure C.6b). Hence, subsequent analyses sought to include 25 vectors per voxel, where possible.

Given that the distribution of particle traces in the domain was not uniform, a series of voxel sizes was tested on the same data set used above to determine a voxel size that balanced spatial resolution and the target number of vectors per voxel. Voxels of various sizes were used to discretize the domain, and voxels that contained at least 3 vectors were counted toward the total number of voxels in each discretization. The fraction of these voxels that contained at least 25 vectors began to converge around a grid dimension of 30 cm (Figure C.7a). A grid dimension of 25 cm resulted in over 50% of voxels having at least 25 vectors (5% precision, according to Figure C.6a), as well as over 20% having at least 150 vectors (2% precision). In a volume encapsulating the turbine wake (bounded by $X/D > \frac{1}{2}$, $|Y/D| \leq \frac{3}{2}$, and $|Z/D| \leq \frac{3}{2}$), 87% of voxels had at least 25 vectors, and 58% of voxels had at least 150 vectors. Therefore, the level of precision of the results presented in this work, which focus on this wake volume, was comfortably below 5% in the area of interest for voxels of this size. In addition, the standard deviation of the bootstrapped means for *all* vectors within a voxel of a given size dropped below 1% of $|\mathbf{U}|$ for a grid dimension

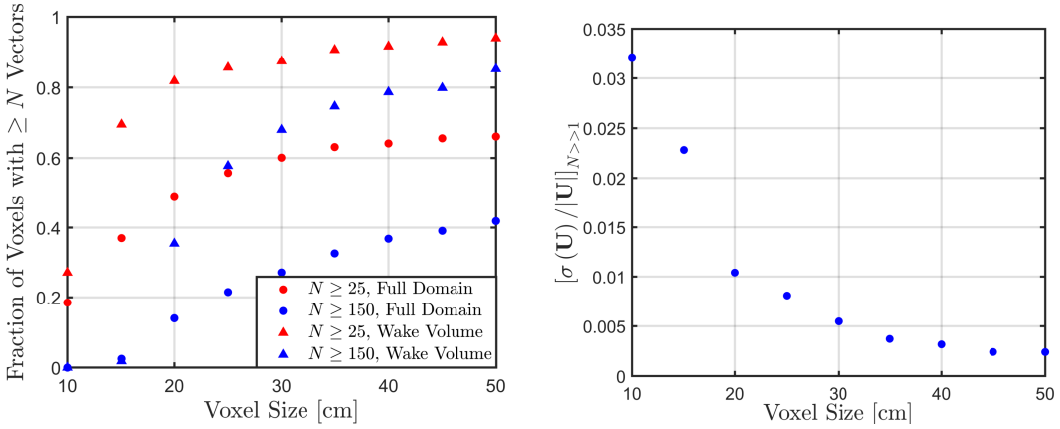

(a) (b)

Figure C.7: Measures for the determination of an appropriate voxel size for binning and averaging velocity vectors. (a) shows the fraction of voxels containing at least $N = 25$ and $N = 150$ vectors, representing the number of vectors required for 5% and 2% measurement precision, for the entire measurement domain (circles) and the wake region (triangles). (b) shows the standard deviation of bootstrapped means for all vectors in a given voxel, representing the best-case precision possible for a given voxel size. Both measures suggest that a grid dimension of 25 cm is a good compromise between spatial resolution and statistical convergence.

of 25 cm (Figure C.7b). This indicated good best-case statistical convergence for voxels of at least this size.

In light of these results, a voxel size of 25 cm was used to discretize the domain, serving as a good compromise between grid resolution and statistical convergence. At least half of all voxels in the measurement volume had standard deviations in the velocity magnitude below 5%, with 20% of these having a measurement precision below 2%. In the wake of the turbine, the precision for 87% of the voxels was below 5%, with close to 60% of this volume having a precision below 2%. The best-case precision for the most densely populated voxels was below 1%.

Once the velocity vectors had been binned and averaged into 25-cm cubic voxels, a filter developed by Schiavazzi *et al.* (2014) was employed to enforce a zero-divergence criterion on the vector fields, in keeping with the negligible Mach numbers ($Ma < 0.05$) of the experimental conditions. The effect of this filter was to attenuate unphysical deviations in the velocity fields due to spurious particle trajectories, especially near the edges of the domain where velocity vectors were more sparse (cf. Figure C.8).

From these filtered velocity fields, values for the velocity incident on the turbine and

the settling velocity of the artificial snow particles were computed by averaging all velocity vectors at least 1 D upstream of the axis of rotation of the turbine. Compared to the settling velocity of the particles measured in quiescent air, $W_s^0 = 0.60 \pm 0.18$ ms^{-1}, the observed settling velocities measured in the prevailing wind conditions at the field site were higher: $W_s = 0.89 \pm 0.12$ ms^{-1}. The discrepancy was likely due to the presence of a slight downward slope in the local topography at the site. According to data collected by Kinzel *et al.* (2012), the corresponding bias in the vertical velocity was $W \approx -0.22$ ms^{-1}, which is consistent with the discrepancy observed in the present data. It is also possible that atmospheric turbulence contributed to the increased settling velocity as well, an effect that has been observed for natural snowflakes (Nemes *et al.*, 2017) and general inertial particles (Petersen *et al.*, 2019) in turbulent conditions. Thus, the average settling velocity measured upstream of the turbine, W_s, was subtracted from the entire velocity field, so that the time-averaged vertical velocity W induced by the turbine could be isolated.

Fields of vorticity were computed from these velocity fields. Due to the relatively coarse grid size and the error associated with numerical differentiation, a $3 \times 3 \times 3$ median filter was applied to all fields involving velocity derivatives. This was mainly employed to remove unphysical results from numerical differentiation near the edges of the measurement domain, but also had a modest smoothing effect on the vortical structures present in the wake.

To demonstrate the effects of the filters applied to the velocity and vorticity fields, a single planar slice at $X/D = 1.5$ was isolated from the WPE turbine data at $\lambda = 1.20$, and the vertical vorticity component ω_z was plotted in Figure C.8. The unfiltered vorticity fields were marked by significant noise on the boundaries of the domain (Figure C.8a). Applying the solenoidal filter to the velocity fields resulted in locally smoothed velocity vectors, corresponding to slight smoothing in the vorticity fields (Figure C.8b). By contrast, applying the $3 \times 3 \times 3$ median filter to the vorticity fields removed the shot noise from the boundaries of the domain, while smoothing over the large-scale structures (Figure C.8c). The combination of the two filters resulted in smoothed velocity and vorticity fields that allowed trends in the flow fields to be identified more readily (Figure C.8d).

C.3 Velocity and vorticity fields

In this section, salient features of the velocity and vorticity fields in the wake are described and discussed. These results are compared with previous studies in the

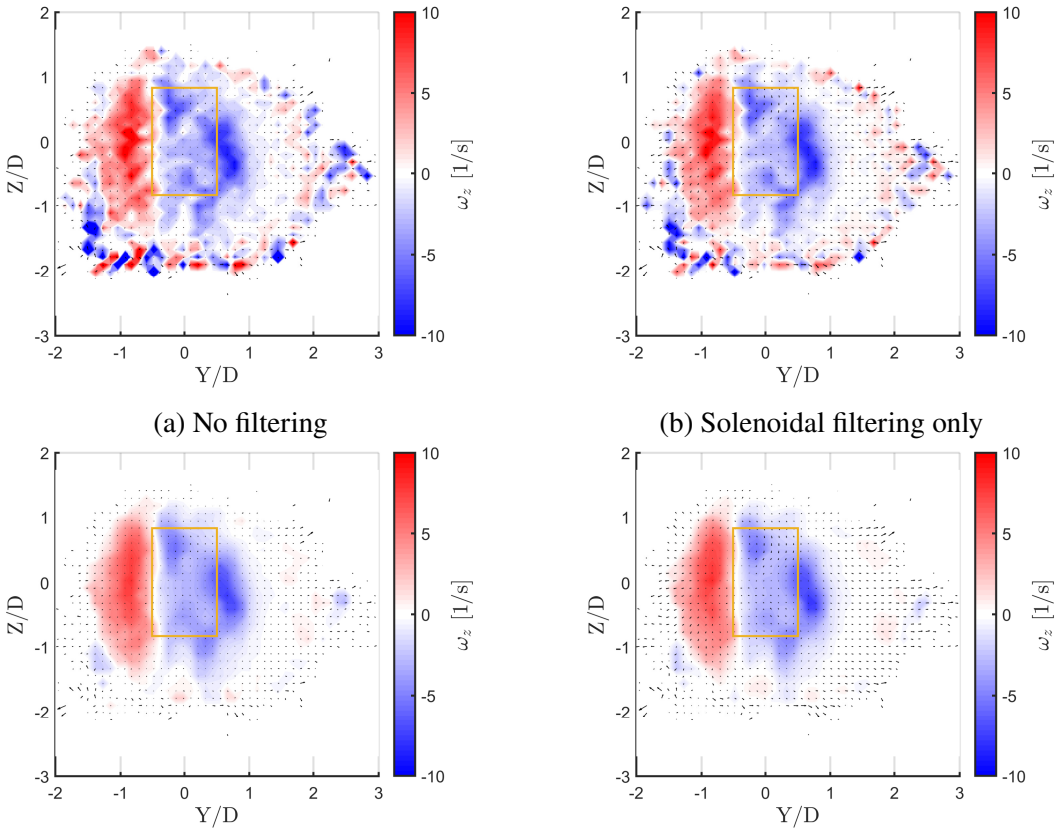

(a) No filtering

(b) Solenoidal filtering only

(c) Median filtering only

(d) Both solenoidal and median filtering

Figure C.8: Effects of the two filters applied to the voxel-averaged velocity and vorticity fields, demonstrated on a cross-section of vertical vorticity (ω_z) at $X/D = 1.5$ downstream of the WPE turbine for $\lambda = 1.20$. The solenoidal filter affects both the velocity and vorticity readings, while the median filter is only applied to the vorticity field.

literature to show that many of the trends observed in laboratory experiments at lower Reynolds numbers still apply for full-scale turbines in field conditions.

C.3.1 Velocity fields

Velocity fields for the time-averaged streamwise-velocity component U on three orthogonal planar cross-sections are given for the UGE and WPE turbines respectively, each at two tip-speed ratios, in Figures C.9 and C.10. The velocity deficit in the wakes were slightly more pronounced in the higher-λ cases, and the wake regions were shifted slightly toward the negative spanwise direction due to the rotation of the turbine. This is consistent with the wake trends observed by Parker and Leftwich (2016). The magnitude of the velocity deficit was significantly larger for the WPE turbine, consistent with its higher solidity. These flow fields qualitatively

paralleled those reported by Araya *et al.* (2017), which were recorded in a water channel at a significantly lower Reynolds number ($Re_D = 8 \times 10^4$). This supports the inference of Parker and Leftwich (2016) that the general shape of the turbine wake is not sensitive to Reynolds number in this parameter range, despite the fact that the coefficients of power only converge for $Re_D \gtrsim 1.5 \times 10^6$ (Miller, Duvvuri, Brownstein, *et al.*, 2018).

Velocity fields for the time-averaged spanwise-velocity component V, also taken at the mid-span of the turbines, are shown in Figures C.11a and C.11b for the UGE and WPE turbines at $\lambda = 1.2$. A clear upstream bifurcation of the flow due to the presence of the turbine was visible in Figure C.11a, and a negatively skewed velocity field, representing spanwise flow induced by the rotation of the turbine, was present downstream of the turbine in both cases. This region grew more rapidly in thickness behind the WPE turbine than behind the UGE turbine, again likely due to its higher solidity and correspondingly stronger flow induction.

The wake recovery of the two turbines also followed previously observed trends in the literature (cf. Ryan *et al.*, 2016; Araya *et al.*, 2017). The wake recovery was quantified by thresholding planar slices of the streamwise velocity component at various streamwise positions downstream of the turbine by the average upstream flow velocity incident on the turbine, U_0. For each slice, this thresholding procedure divided the wake region, defined as the region of flow where the local streamwise velocity component was less than U_∞, from the surrounding free-stream region. The average velocity within the wake region, $\langle U \rangle$, was taken for each streamwise slice, and was plotted against streamwise distance (Figure C.12). The analysis of these wake-recovery profiles has been undertaken comprehensively by Araya *et al.* (2017), and the trends found in these experiments show good agreement with their findings. The minimum value of $\langle U \rangle / U_0$ was observed to decrease with increasing λ and increasing σ. These differences were most prominent in the near wake ($X/D \lesssim 2$), in which vortex shedding from the turbine blades is most significant (Tescione *et al.*, 2014; Parker and Leftwich, 2016; Araya *et al.*, 2017). The streamwise extent of the measurement domain was not large enough to observe the full transition to bluff-body wake dynamics described by Araya *et al.* (2017), but the presently measured wake profiles exhibit similarity to that previous work within the domain of present interest.

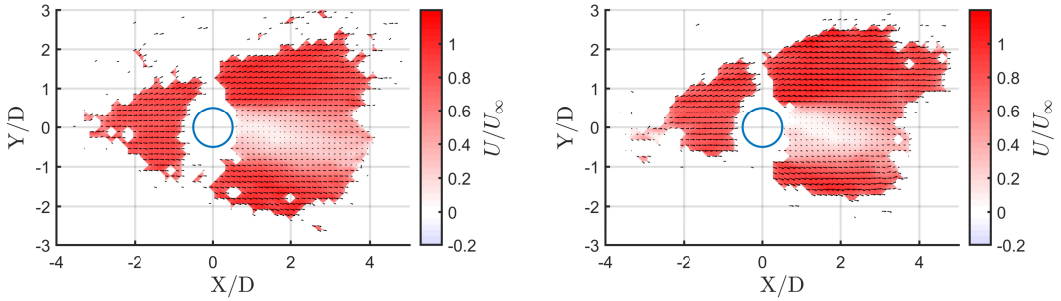

(a) (b)

Figure C.9: Time-averaged planar fields of the streamwise velocity U for the UGE turbine at (a) $\lambda = 1.19$ and (b) $\lambda = 1.40$, taken at $Z/D = 0$. The differences in the shape of the wake between the two tip-speed ratios are minor.

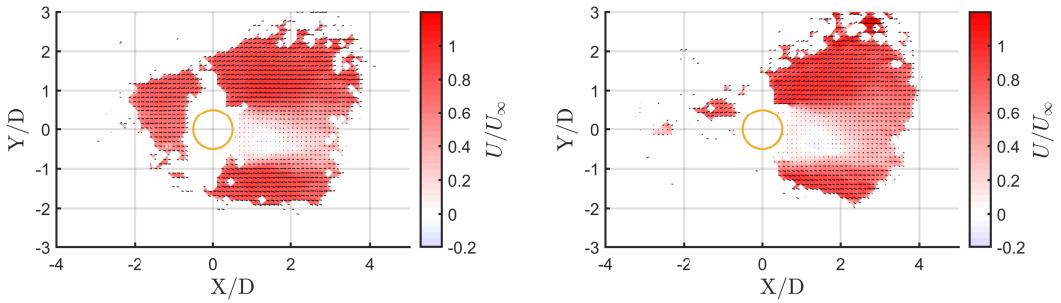

(a) (b)

Figure C.10: Time-averaged planar fields of the streamwise velocity U for the WPE turbine at (a) $\lambda = 0.96$ and (b) $\lambda = 1.20$, taken at $Z/D = 0$. As in Figure C.9, the differences in the wake between these two tip-speed ratios are minor.

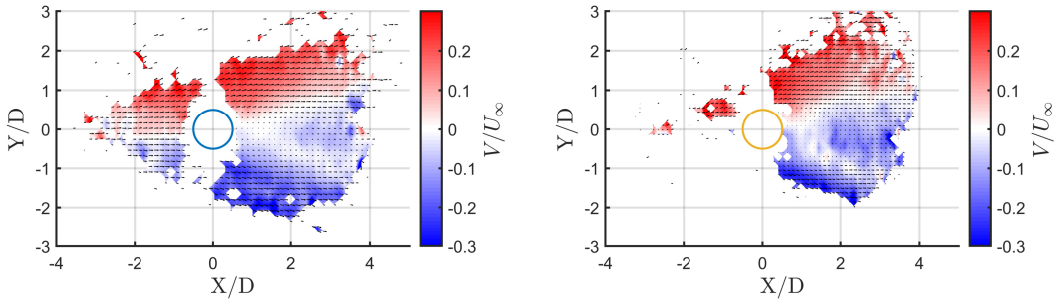

(a) (b)

Figure C.11: Time-averaged planar fields of the spanwise velocity V for (a) the UGE turbine at $\lambda = 1.19$ and (b) the WPE turbine at $\lambda = 1.20$, taken at $Z/D = 0$. The V-shaped region of negative spanwise velocity downstream of the turbines is more prominent for the WPE turbine, which has a higher solidity.

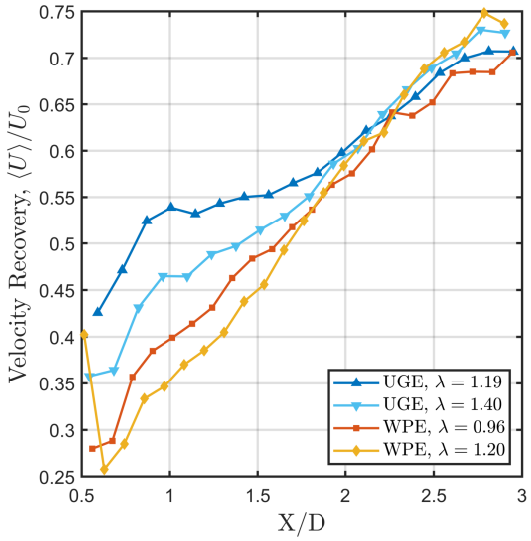

Figure C.12: Profiles of $\langle U \rangle / U_0$ versus distance downstream of the turbine for all four experimental cases. Here, angle brackets denote spatial averages across YZ-sections of the wake, and U_0 represents the velocity directly upstream of the turbine. Profile discrepancies corresponding to differences in λ and σ are present in the near wake ($X/D \lesssim 2$), whereas the wake recovery in the far wake appears to be more uniform.

C.3.2 Vorticity fields

For the sake of completeness, streamwise slices of the spanwise vorticity ω_y are provided in Figures C.13 and C.14. The time-averaged vortical structures visible in these plots represented tip vortices shed from the turbine blades (Tescione *et al.*, 2014). These structures did not display a strong degree of asymmetry, suggesting that they were relatively unaffected by the tilted-wake behavior observed in the vortical structures in ω_x and ω_z.

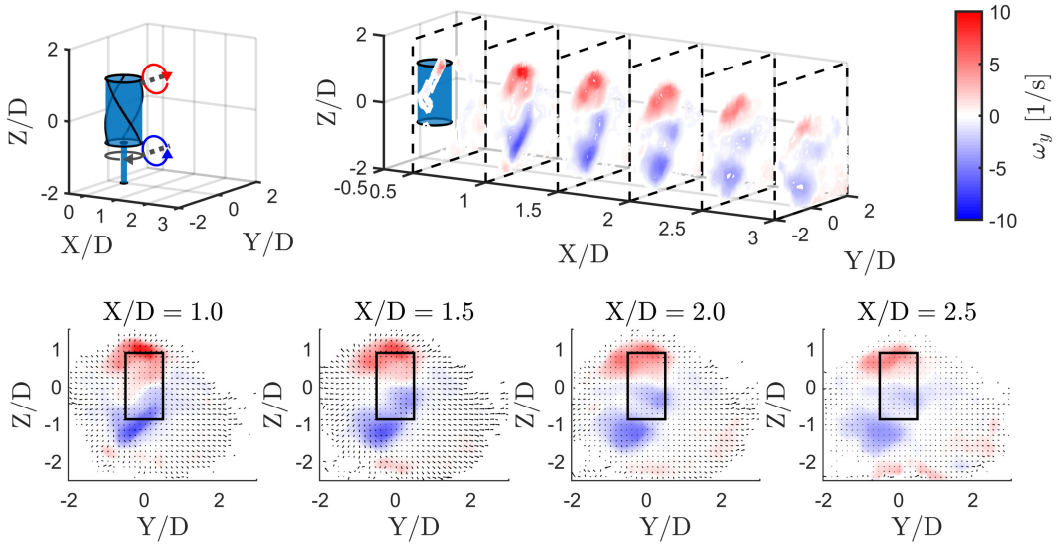

Figure C.13: Streamwise slices of the spanwise vorticity ω_y downstream of the UGE turbine for $\lambda = 1.19$. These structures are products of vortex shedding from the tips of the turbine blades (Tescione *et al.*, 2014). Note that the X-axis is stretched on $0.5 \leq X/D \leq 3$.

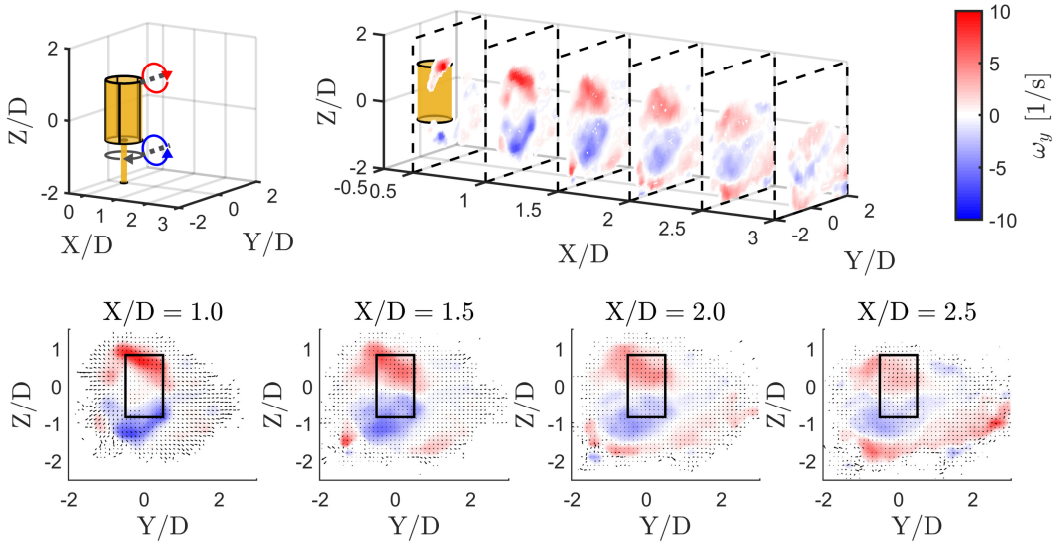

Figure C.14: Streamwise slices of the spanwise vorticity ω_y downstream of the WPE turbine for $\lambda = 1.20$. These structures are not significantly different from those shown in Figure C.13.